UNIVERSITY OF CALIFORNIA
SANTA CRUZ

UNVEILING THE HEARTS OF LUMINOUS AND ULTRA-LUMINOUS INFRARED GALAXY MERGERS WITH LASER GUIDE STAR ADAPTIVE OPTICS

A dissertation submitted in partial satisfaction of the
requirements for the degree of

Doctor of Philosophy

in

ASTRONOMY & ASTROPHYSICS

by

Anne M. Medling

June 2013

The Dissertation of Anne M. Medling
is approved:

Professor Claire E. Max, Chair

Doctor Lee Armus

Doctor Bradford Holden

Professor Piero Madau

Tyrus Miller
Vice Provost and Dean of Graduate Studies

Table of Contents

List of Figures

List of Tables

Abstract

Unveiling the Hearts of Luminous and Ultra-luminous Infrared Galaxy Mergers with Laser Guide Star Adaptive Optics

by

Anne M. Medling

Gas-rich galaxies across cosmic time exhibit one or both of two phenomena: 1) ongoing star formation, and 2) an active galactic nucleus indicating current black hole accretion. These two processes are important mechanisms through which galaxies evolve and grow, but their effects are difficult to disentangle. Both will use up some available gas, and both are capable of producing winds strong enough to eject remaining gas from the galaxy. But the systems most likely to show this kind of feedback tend to exhibit both intense star formation and black hole growth, making it impossible to distinguish each effect by looking at the systems globally. Instead, one must look at high spatial resolutions in order to separate the dynamical effects of star formation going on *near* the nucleus of a galaxy from the black hole growth going on *in* the nucleus.

We present high spatial resolution integral field spectroscopy of fifteen nearby luminous and ultra-luminous infrared galaxies. These systems are extremely bright in the infrared exactly because they host powerful starbursts and active nuclei, which in turn heat the surrounding dust. Though they are rare in the local universe and are triggered only by major mergers, there is substantial evidence that suggests they may be more typical of the activity level of galaxies at redshifts $z \sim 1 - 3$. Our data

provide resolved stellar and gaseous kinematics of the central kiloparsec of each of these systems by removing atmospheric blurring with adaptive optics, an observing technique that measures the turbulence in the Earth's atmosphere and then uses a deformable mirror to correct for the resulting distortions. This yields spatial resolutions on the order of a few tens of parsecs in these galaxies.

Our kinematic maps reveal nuclear disks of gas and stars with radii $\sim$ a few hundred parsecs surrounding the central black holes. Because the stellar and gas kinematics match well, we conclude that the stars are forming *in situ* from the gas in the disks. These disks may be the progenitors of kinematically decoupled cores seen in many isolated elliptical galaxies, and may have a significant effect on the merger rate of binary black holes. Additionally, these disks may be used to measure black hole masses during their major epoch of fueling. We measure black holes ranging from $5 \times 10^7 - 2 \times 10^9 M_\odot$ that, when combined with host galaxy properties and placed on scaling relations, indicate that black holes grow as or more quickly than their host galaxies during a merger. This suggests that a sudden burst of black hole growth at in the final stages of the merger (e.g. "quasar-mode feedback") is not likely to be responsible for shutting off star formation in these systems.

To my parents and my husband,

who always believed in me.

Acknowledgments

I owe a great deal to many people who have supported me scientifically and in every other way possible. Thank you to my parents, who didn't bat an eye when my childhood dreams transitioned suddenly from ballerina to astrophysicist, and to my grandparents, whose house on a lake provided the best viewing of the Perseids around. Thank you to Mr. Roche of High Technology High School, who brought me to my first science fair and convinced me to write my first grant proposal.

My sincerest thanks to my thesis advisor, Claire Max, whose mixture of hands-on and hands-off advising taught me to be a skilled and independent scientist. This work would not have been possible without her guidance and support, and I might have given up several times if she had not routinely remembered to offer positive feedback. Thank you also to Lee Armus, whose skeptical nature kept our science on the straight-and-narrow, and to Brad Holden, whose feedback was always productive and useful.

Throughout this project, Vivian U has been an outstanding collaborator and friend. During all the long observing nights, you are my first choice for keeping me optimistic and on-the-ball. Thank you for not making it awkward to blend catching up on science with catching up on life.

I owe many thanks to all the UC Santa Cruz graduate students who have helped me along the way in innumerable ways: to my project manager and officemate Rosalie McGurk, who kept me on track and cheered me on when I needed cheering; to Robert da Silva, who taught me everything I know about making figures with IDL; to Kevin Schlaufman for his expertise in statistics; to Mark Ammons, who molded me into

a respectable grad student; to Javiera Guedes, who kept reminding me why nuclear disks are important; to Valery Rashkov and James Guillochon for their assistance navigating graduation requirements; and to the collective grads for their supportive community. I owe a special debt of thanks to those who fed me during the last few months of crunch time: Feña Duran, Priya Kollipara, Tina Wasem, and Leila Jewell.

Even with such a supportive department, I could not have completed this without my husband Scott, who drove many miles late into the night to stock my fridge and do my laundry. Thank you for your patience with living double lives in two cities and for being on top of all the logistics when I was too focused on science to manage.

Two chapters in this thesis have been submitted as separate publications in the Astrophysical Journal. Chapter 2 was published as Medling et al. 2011, ApJ, 732, 32; I would like to thank these coauthors, Mark Ammons, Claire Max, Richard Davies, Hauke Engel, and Gabriela Canalizo, for their support and permission to include this work in this dissertation. In this paper, I was responsible for analyzing the data, creating the dynamical models and comparing them with the data and interpreting the results. I wrote the bulk of the text of this paper.

Chapter 3 has been recently submitted and is currently undergoing the referee process; I would like to also thank those coauthors, Vivian U, Dave Sanders, Claire Max, Lee Armus, Kazushi Iwasawa, Aaron Evans, Lisa Kewley, and Giovanni Fazio, for their support and permission to include this work in this dissertation. I obtained the imaging data and jointly observed the integral field data. I was also responsible for analyzing the data, implementing models of the dynamics, photoionization, and shocks,

and assisted in interpreting the results. I also acted as the main editor of the text.

I am grateful to the native peoples of Hawai'i for sharing their sacred mountain with astronomers. The observatories of Mauna Kea have contributed significantly to our understanding and wonder of the universe. My work was supported in part by a National Science Foundation Graduate Research Fellowship and an Acheivement Rewards for College Scientists Foundation Fellowship.

Chapter 1

Introduction

1.1 Galaxy Evolution: Merger-Driven or Secular?

Galaxies come in a variety of sizes and flavors, but they can be divided into two broad categories: star-forming galaxies and quiescent galaxies. Over a galaxy's lifetime, it moves between these categories according to one particular trait: how much gas is available in the system. When cold gas is present in a galaxy, two phenomena may occur: 1) if the gas is cold and dense enough, it can gravitationally collapse in on itself and form stars, and 2) the gas may fall into the black hole. When gas becomes gravitationally bound to a black hole, it forms a hot accretion disk, which radiates as a blackbody, while infalling charged particles emit X-rays. This radiation associated with a growing black hole marks it an active galactic nucleus (AGN). Star formation and AGN activity can continue until the gas reservoir is depleted; no new stars are formed and their contributions of blue light fade away, leaving the galaxy "red and dead". If the gas supply is renewed, star formation and AGN activity can resume.

Given the importance that the amount of gas has on a galaxy's life, in order to understand the evolution of galaxies, one must ask the question, "how do galaxies get their gas?" There are two mechanisms that can bring in a new supply of gas to a gas-poor galaxy. First, the galaxy may accrete gas from the surrounding intergalactic medium, potentially flowing in along filaments of dark matter in the cosmic web (Dekel & Birnboim, 2006; Dekel et al., 2009; Bournaud et al., 2011). This gas may be pristine, low-metallicity gas, or gas which has been enriched in the galaxy and ejected at an earlier time. This process is part of "secular evolution", and can occur slowly over a long period of time. The alternative is "merger-driven evolution", during which a galaxy increases its gas supply by colliding with another gas-rich galaxy. The gas will be torqued by gravitational forces and the final system can end up with a gas-rich core (Di Matteo et al., 2005; Springel et al., 2005a,b). But which of these processes dominates galactic evolution?

The answer, of course, is complicated: both processes are important pieces of the puzzle of galactic evolution. Studies of AGNs selected by different techniques obtain conflicting results: some showing a strong correlation with major galaxy mergers (Koss et al., 2010; Ellison et al., 2011), while others do not show a higher rate of merging than field galaxies (Cisternas et al., 2011b; Kocevski et al., 2012). Treister et al. (2012) combine multiwavelength studies of AGNs and their correlations with mergers and find that only 10% of AGNs are likely triggered by a major galaxy merger. However, because this 10% comprises the most luminous AGNs, they also conclude that approximately 50% of black hole growth over cosmic time is associated with major mergers. This result

is still controversial, however, because of the selection effects that may complicate the combining of varied datasets.

1.2 (U)LIRGs and Their Place in Cosmic Time

The universe is a quieter place now than it has been in the past. Studies of high redshift galaxies show that the star formation rate density peaks around $z \sim 3$ (González et al., 2010, and others). X-ray surveys can identify the levels of AGN activity as a function of redshift; Aird et al. (2010) find that AGN activity peaked at a redshift of $z \sim 1.2$. Galaxies in the local universe have less fuel to form stars and grow black holes than they did 8-12 billion years ago. Studying the most active era of cosmic history is only beginning to be possible but a detailed analysis requires the ability to spatially resolve star formation and black hole growth, a requirement only met for galaxies at low redshift.

However, the local universe does host a population of extreme systems, Ultra-Luminous and Luminous InfraRed Galaxies ((U)LIRGs), that may be analogous to normal galaxies at $z \sim 2$. In fact, analysis of the far-infrared background with Herschel shows that LIRGs account for $> 90\%$ of infrared light at $0.5 < z < 1.0$ and ULIRGs provide more than half of the background above $z = 1.0$ (Berta et al., 2011). (U)LIRGs are infrared-bright ($L_{IR} > 10^{12} L_{\odot}$ for ULIRGs, $L_{IR} > 10^{11} L_{\odot}$ for LIRGs) because they contain large quantities of gas and dust which is being funneled to the center; the gas forms stars and fuels AGN activity, which in turn heat the dust, which radiates in the infrared (Sanders & Mirabel, 1996). There is considerable evidence that infrared

luminosity is linked with merging activity: morphological analysis of LIRGs reveals an increase of strongly interacting systems with higher infrared luminosity (e.g. Ishida, 2004); (U)LIRG with double nuclei show a decreasing nuclear separation with increasing infrared luminosity (Haan et al., 2011); studies of pairs of Sloan Digital Sky Survey galaxies find an increasing fraction of LIRGs as pair separation decreases (Ellison et al., 2013); and observations of (U)LIRGs at high redshift find mergers to be a major factor, though slightly less so than at low redshift (Melbourne et al., 2005; Dasyra et al., 2008; Kartaltepe et al., 2010, 2012). Locally, the merger fraction can pass 90% at the highest luminosities (Sanders et al., 1988; Melnick & Mirabel, 1990; Clements et al., 1996; Veilleux et al., 2002; Ishida, 2004). Additionally, as infrared luminosity increases, the fraction of systems hosting AGN also increases (Veilleux et al., 1995; Ellison et al., 2013; Koss et al., 2013).

Though we understand that such interactions may not have been the most common trigger for such activity at moderate redshifts, these systems represent the only currently feasible opportunity we have to study such active systems in detail. By looking at nearby mergers in high resolution, we can study the black hole growth and map the gas kinematics as a first step towards disentangling the fueling and feedback of star formation and AGN activity.

1.3 Black Hole Scaling Relations

In order to understand what role a black hole, active or quiescent, might play in a system, it is important to first characterize its mass. Large studies of black hole

masses have shown that they correlate with properties of their host galaxies' bulges (Kormendy & Gebhardt, 2001): bulge mass (Kormendy & Richstone, 1995; Magorrian et al., 1998), bulge luminosity (Marconi & Hunt, 2003), and bulge stellar velocity dispersion (Tremaine et al., 2002; Ferrarese & Merritt, 2000; Gebhardt et al., 2000), all most recently updated by McConnell & Ma (2013). There is some evidence for an evolving $M_{BH} - \sigma_*$ relation with redshift (e.g. Zhang et al., 2012). Alternatively, the most basic scaling relation may be with total stellar mass (Jahnke et al., 2009; Cisternas et al., 2011a); in this case the evolution with redshift would indicate the changing bulge-to-disk fractions of galaxies.

These correlations were originally unexpected, since the black hole makes up less than a percent of the galaxy's mass and the volume of its gravitational influence is small compared to the galaxy's size. Why should stars across the galaxy have orbits that seemingly depend on the black holes mass? This has canonically been answered with the idea that galaxies and their black holes both grow when the system obtains additional gas. This can occur through secular evolution, when pristine gas flows in from outside of the galaxy to promote growth, or when two galaxies collide, particularly if either galaxy starts out with a supply of gas (e.g. Hopkins et al., 2006). In the latter case, gravitational torques funnel the gas into the centers of the merging galaxies, triggering two phenomena: an intense burst of star formation to feed the bulge, and accretion of gas on to the black holes in the centers of each galaxy. It has been postulated that the black hole growth can regulate this process through AGN feedback (Springel et al., 2005b), which may produce massive winds that evacuate the gas from the galaxy on

short timescales, cutting off star formation and future black hole growth. This sense of self-regulation has been confirmed observationally by Kauffmann & Heckman (2009), who find that the Eddington ratio (a measure of how much a black hole is accreting relative to its theoretical limit) of a sample of AGNs depends on the supply of cold gas in the galaxy. If there is plenty of cold gas, the accretion rate does not depend on the quantity of gas available; if the supply of cold gas is limited, the accretion rate depends on the rate at which stellar winds provide fuel for the AGN. Though the detailed mechanisms through which these correlations are formed are still unconfirmed, it is evident that star formation and black hole growth are fed by the same reservoir of inflowing gas; their growth histories are intertwined. It is likely that these two processes compete for fuel in a predictable fashion.

1.4 Measuring Black Hole Masses

A variety of methods are used to measure black hole mass, some of which we review here. One established method uses full three-integral modeling of stellar orbits; this method, most commonly used in elliptical galaxies, (see e.g. Siopis et al., 2009; Gültekin et al., 2009a, and references therein) uses line-of-sight velocity distributions and light profiles to create a detailed dynamical mass profile of the galaxy, including the black hole mass. Two- and three-integral models are also sometimes used on bulges of spirals (e.g. Davies et al., 2006; Onken et al., 2007; Cappellari et al., 2009). Reverberation mapping (e.g. Denney et al., 2009, and references therein) is a method of measuring black hole masses in AGN; it uses time-resolved brightness fluctuations in the continuum

versus lines from the broad-line region to estimate the size of the broad-line region and therefore the mass of the black hole powering the AGN. Masses measured with reverberation mapping can be calibrated to match the M_{BH}-σ_* relation (Onken et al., 2004). Black hole masses have been derived (Shields et al., 2003, and references therein) from the continuum luminosity and the width of the broad Hβ line. The masses of supermassive black holes powering quasars have been estimated using x-ray luminosity as an indicator, as in Kiuchi et al. (2009). In some cases, it is possible to measure the Keplerian rotation of ionized or molecular gas around a black hole and deduce its mass, as in Harms et al. (1994), Hicks & Malkan (2008), and Neumayer et al. (2007). In a few galaxies, masers in the disk allow precise velocity (and therefore black hole mass) measurements (Herrnstein et al., 1999; Miyoshi et al., 1995). In the Galactic Center, individual stars have been resolved and their orbits around the black hole tracked astrometrically over time to determine the black hole mass (Ghez et al., 2008; Gillessen et al., 2009). Recently, adaptive optics have been used to resolve stellar dynamics inside the sphere of influence of black holes in nearby galaxies (e.g. Davies et al., 2006; Nowak et al., 2008; McConnell et al., 2011; Gebhardt et al., 2011).

Though there are many black hole mass measurement techniques to choose from, we are limited when considering black holes in gas-rich mergers. Reverberation mapping and emission line diagnostics require observations of a broad line region, but the dust is thick enough to obscure it in gas-rich environments. Three-integral orbital superposition methods require relaxed dynamical systems, an assumption which isn't valid in ongoing mergers. Except for the rare merger which happens to have an OH

maser observable (e.g. Mrk 273; Klöckner & Baan, 2004), black hole masses in these systems have been largely uncertain.

1.5 AGN Activity and Binary Black Hole Mergers

To understand the interplay between star formation and black hole growth, it's critical to look at systems in the midst of this increased fueling. One set of such galaxies are gas-rich mergers; selected from (U)LIRGs, gas-rich mergers tend to have extreme bursts of star formation and a higher incidence of AGN activity. How do these mergers fall on black hole scaling relations? Does the black hole grow first, leaving the stars to slowly use up the remaining gas? Or is star formation cut off once the black hole reaches a bright quasar phase of extreme growth? A merger's position on black hole scaling relations would indicate the relative growth timescales, and confirm whether the putative quasar-mode feedback occurs (see Fig. 1.1). Theoretical arguments have suggested that star formation has preferential access to the available gas and that therefore a black hole would grow substantially only after star formation has quenched itself and the galaxy bulge is in place (Cen, 2012); this scenario would predict that gas-rich mergers would fall below black hole scaling relations, following the purple arrow in Fig. 1.1.

Understanding black hole fueling in the midst of mergers will also shed light on the rate of dual AGNs. Since major mergers do trigger AGN activity and all massive galaxies have a central black hole, one might assume that all gas-rich mergers ought to have two AGNs. Though dual AGNs have been seen to exist at many scales, many more mergers have one or zero AGNs. At what merger stage do we expect a black

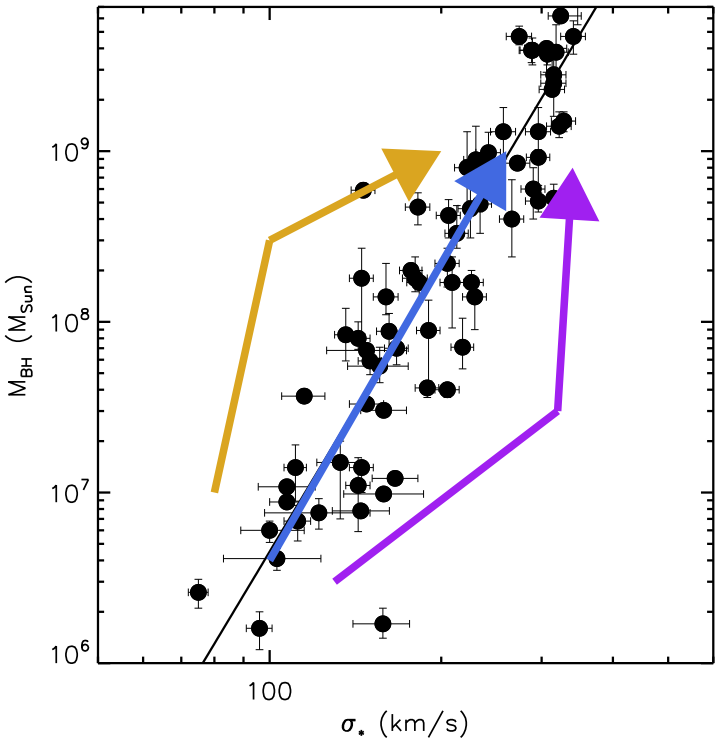

Figure 1.1: $M_{BH} - \sigma_*$ relation for isolated galaxies from McConnell & Ma (2013) (black) with three possible evolutionary tracks for merging galaxies overlaid. If the black hole grows first or more quickly than the galaxy bulge, mergers would lie above the relation (as shown by the gold arrows). If the black hole growth lags the bulge growth and is responsible for curtailing evolution (e.g. quenching through AGN feedback), mergers would lie below the relation (as shown by the purple arrows). If instead the black hole and the bulge grow in lockstep, the mergers would remain on the relation (as shown by the blue arrow).

hole to transition into an AGN? For what fraction of time is an AGN active, and does this depend on measurable quantities (e.g. gas fraction, star formation rate, etc.)? To answer these questions in detail, one needs a large well-matched sample of mergers hosting zero, one and two AGNs; this is beyond the scope of this thesis. However, studying the interplay between black hole growth and star formation is an important prerequisite to understanding dual AGN statistics.

Regardless of the rate of dual AGN, we expect all major galaxy mergers to result in a binary black hole, which may eventually merge into a single black hole. N-body numerical simulations of such mergers, however, reveal a potential difficulty present in the idea: the final parsec problem. Once the two black holes have kicked out all the stars in the loss cone, no way remains to remove angular momentum from the system and the black holes' inspiral will stall (Milosavljević & Merritt, 2003). If the binary black holes stall at ~ 1 parsec, they will never fully merge; this would effectively remove them as potential targets for gravitational wave experiments similar to LISA (the Laser Interferometer Space Antenna; Thorne, 1995; Hughes, 2002; Vecchio, 2004) and pulsar timing arrays (Lee et al., 2011) .

However with the addition of gas to numerical simulations, the scenario may have changed. High spatial resolution hydrodynamic simulations of gas-rich galaxy mergers have predicted the formation of nuclear disks on scales of a few tens to a few hundreds of parsecs (e.g. Mayer et al., 2008). These disks form as gravitational torques funnel the gas towards the nuclei of the merging galaxies, feeding gas down to the smallest resolvable scales ($\sim$ 1 pc) and likely fueling the black hole accretion

disks themselves (Kawakatu & Wada, 2008). The presence of this gas and the resulting dissipation may provide a mechanism that speeds up the formation and final coalescence of binary black holes (Kazantzidis et al., 2005; Mayer et al., 2007; Dotti et al., 2007, 2008; Chapon et al., 2013). While most current observations cannot resolve scales as small as 1 pc, the presence of significant amounts of gas on larger scales would give a strong indication that gas disks may be relevant to binary black hole mergers.

1.6 Laser Guide Star Adaptive Optics

Studying the nuclear regions of galaxies has been a challenging endeavor. The sphere of influence of a black hole is:

$$R_{infl} \sim (\frac{M_{BH}}{10^6 M_\odot})^{0.5} pc$$

(Davies, 2008), which is less than 100 pc even for the most supermassive black holes ever found. Because this is difficult to resolve (at a distance of 100 megaparsecs, 100 pc is only about $0.2''$), direct dynamical measurements of black hole masses have been limited to only the most nearby and massive galaxies or those with OH masers measurable with radio interferometry (e.g. NGC 4258; Herrnstein et al., 1999; Miyoshi et al., 1995). In the central few hundred parsecs, many AGN are dusty and contain central starbursts. These are difficult to disentangle at low spatial resolution. Until recently, studies on these topics were primarily limited to space, making use of the Hubble Space Telescope to avoid the blurring of the Earth's atmosphere. However, Hubble's resolution, ~ 0.05 $''$in the visible bands, decreases linearly with wavelength. Observing in the near-infrared,

which is less sensitive to dust, is limited by diffraction off the relatively small diameter (2.4 meters) of Hubble's primary mirror and has a resolution element closer to $0.2''$. Though much larger telescopes have been built on the ground (e.g. Keck Observatory's twin 10-meter telescopes, Gemini Observatory's twin 8-meter telescopes, and the Very Large Telescope's four 8-meter telescopes), they are all limited in resolution by the blurring due to turbulence in the Earth's atmosphere.

This turbulence is variable, and its effects are referred to as "seeing". In a turbulent atmosphere, moving air pockets of varying temperatures have slightly varying indices of refraction. When light from a star shines through the atmosphere, its wavefront is slightly distorted. As the pockets of air move through the atmosphere, this wavefront distortion varies, averaging out over time into a Gaussian seeing disk. The seeing improves at excellent observing sites and during stable weather conditions, reaching as low as $\sim 0.5\,''$in the K-band; this is still considerably worse than Hubble's resolution, even for telescopes a factor of ~ 4 larger.

The atmosphere's effects on image resolution had been a concern for the United States Department of Defense since the 1970's, and a solution, Adaptive Optics (AO), was developed. Adaptive optics systems measure the wavefront distortions caused by the atmosphere and use a deformable mirror to cancel the distortions. By sampling the wavefront and correcting it frequently (typically a few hundred times per second), diffraction-limited imaging can be achieved on the ground. In 1991, some of this research was declassified, and work began to adapt the military's techniques to astronomical purposes. For an overview of this initial work, see Collins (1992).

Today, adaptive optics systems are common among large (5-meter and above) telescopes, and take two forms: natural guide star (NGS AO) and laser guide star (LGS AO). NGS AO systems use a nearby bright star to measure turbulence in the atmosphere. The requirements for a natural guide star are usually quite strict: at Keck Observatory, this star must be brighter than ~ 13.5 magnitude and closer to the target than ~ 30 arcseconds (Wizinowich et al., 2000; van Dam et al., 2004). If the star is too faint, the system will not be able to obtain enough signal to measure the wavefront on the timescales over which the turbulence changes; if the star is bright but too far from the desired target, it will accurately measure the wavefront of the star but its distortions will not be the same as those of your target, which travels through a slightly different portion of the atmosphere.

Because these requirements severely limit the area of the sky observable with adaptive optics, the laser guide star was introduced. At Keck Observatory, the laser is tuned to the 589 nm Na D transition; the light then causes atoms in the sodium layer of the atmosphere at 95 km to fluoresce, creating a bright spot – an artificial star. This laser guide star can be used instead of a natural guide star to correct for higher order aberrations in the wavefront. However, because the laser is distorted on its way up through the atmosphere, the laser spot is not able to be used for low order aberrations such as tip and tilt – the image motion. For this purpose, even laser guide star adaptive optics require a natural star nearby, called a tip-tilt star. This star can be considerably fainter and further from the targets than in the case of NGS AO; for Keck Observatory, a tip-tilt star must be brighter than ~ 18.5 magnitude and closer to the

target than ~ 60 arcseconds (Wizinowich et al., 2006; van Dam et al., 2006). These less stringent requirements on nearby stars make a considerable fraction of the sky available to adaptive optics when a laser guide star is implemented. For extragalactic astronomy, which tends to be done far from the plane of our Milky Way Galaxy, the likelihood of a target being observable increased from $\sim 10\%$ to $\sim 50\%$ with LGS AO.

The spread of adaptive optics and the advent of LGS AO has opened up numerous fields of astronomy for study, from work characterizing extrasolar planets (Konopacky et al., 2013) or tracking stars around the black hole at the Galactic Center (SgrA* Ghez et al., 2005), to studies of the properties and dynamics of galaxies near and far (Rich et al., 2011). This thesis represents one subset of the advances made in the field of nearby gas-rich galaxies.

1.7 Outline of Remaining Chapters

In Chapters 2 and 3 we present results on individual galaxies, demonstrating our techniques to analyze integral field spectroscopy, producing kinematic maps of both emission and absorption lines. We use the test case galaxies of NGC 6240 and Mrk 273 to establish the challenges and solutions associated with the subsequent kinematic analyses; we measure black hole masses and reveal outflows likely associated with AGN feedback.

In Chapters 4 and 5 we present results associated with a population of nearby (U)LIRGs, mainly in late stages of merging. Table 1.1 contains a list of galaxies studied as part of this thesis. Chapter 4 includes the properties of nuclear disks, which appear to be extremely common in these systems, and may be the progenitors of kinematically

Table 1.1: Galaxy Sample

Galaxy Name	Redshift	Date(s) of Observation YYMMDD (UT)	Appears in Chapter
CGCG436-030	0.0312	120102	4
IRASF01364-1042	0.0490	101113,101114	4
		120102	
IIIZw035	0.0278	111210	4,5
IRASF03359+1523	0.0365	101114	4
MCG+08-11-002	0.0195	110110,120102	4
NGC 2623	0.0196	100304,100305	4,5
		110203,110110	
UGC5101	0.0390	100304,100305	4,5
		101114	
Mrk231/UGC8058	0.0433	100304,110523	4
Mrk273/UGC8696	0.0380	120522	3,4,5
IRASF15250+3608	0.0563	110523	4
NGC 6090	0.0304	100305	4
NGC 6240N	0.0244	090617	4,5
NGC 6240S	0.0244	070421	2,4,5
IRASF17207-0014	0.0432	110523,110524	4
IRAS20351+2521	0.0340	110522	4
IRASF22491-1808	0.0781	101114	4

decoupled cores in today's elliptical galaxies. In Chapter 5 we present an analysis of merging galaxies placed on black hole scaling relations, showing that black holes tend to be overmassive compared to the host galaxy's properties. This indicates that the black holes in these systems likely undergo their most major growth during early merger stages.

In Chapter 6 we describe future projects to further investigate the results presented here.

Part I

Individual Galaxy Studies

Chapter 2

The Mass of the Southern Black Hole in NGC 6240 from Laser Guide Star Adaptive Optics

Major mergers are thought to be an important factor in galaxy evolution. The scenario is as follows: when two gas-rich galaxies of comparable mass collide, large amounts of gas are funneled into the central region, fueling active star formation and nuclear activity (see e.g. Sanders & Mirabel, 1996; Barnes & Hernquist, 1996; Genzel et al., 1998; Di Matteo et al., 2005; Hopkins et al., 2006). During this phase of merging, the starbursting galaxy produces copious infrared emission from dust heated by young stars and by the active galactic nucleus (AGN). We see these galaxies in the local universe as (Ultra-)Luminous InfraRed Galaxies – (U)LIRGs. ULIRGs have infrared luminosities of more than $10^{12} L_{\odot}$. This burst of star-forming activity then uses up

much of the gas; the remainder is blown out through a combination of stellar winds and feedback from the AGN. The scenario then posits that after a major merger, gas-rich galaxies become gas-poor, star formation is largely extinguished, and eventually a "red and dead" elliptical galaxy is produced with a more massive black hole at its core.

NGC 6240 ($z = 0.0243$, $d = 98$ Mpc for $H_0 = 75$ km s^{-1} Mpc^{-1}, 1" = 470 pc), with $L_{IR} \sim 10^{11.8} L_{\odot}$ sits on the boundary between LIRGs and ULIRGs. Because of its close proximity and spectacular tidal tails and loops, it has become the prototypical example of a gas-rich system in the phase where the two nuclei are close to merging into one. It has been studied in great detail and in almost every wavelength regime (e.g. x-ray - Komossa et al. 2003; optical - Gerssen et al. 2004; near-IR - Max et al. 2005, 2007; Scoville et al. 2000; Tecza et al. 2000; Engel et al. 2010; mid-IR - Armus et al. 2006; mm - Tacconi et al. 1999; radio - Gallimore & Beswick 2004, Hagiwara et al. 2011). Near the core of NGC 6240, the nuclei of the two progenitors are visible 1.2-1.5 arcsec apart, depending on wavelength. Each of these nuclei holds an AGN; the two sources are resolved in hard x-rays by the Chandra X-Ray Observatory (Komossa et al., 2003). The AGNs are deeply obscured at optical wavelengths, however, due to large quantities of dust also present in this region. By looking into the near-infrared, Pollack et al. (2007) have seen young star clusters through some of the dust, products of the most recent close passage of the nuclei (also visible in Figure 2.1).

Supermassive black hole masses are known to scale with certain host galaxy properties, such as bulge light and mass (e.g. Kormendy & Richstone, 1995; Kormendy & Gebhardt, 2001; Magorrian et al., 1998) and bulge stellar velocity dispersion (Gebhardt

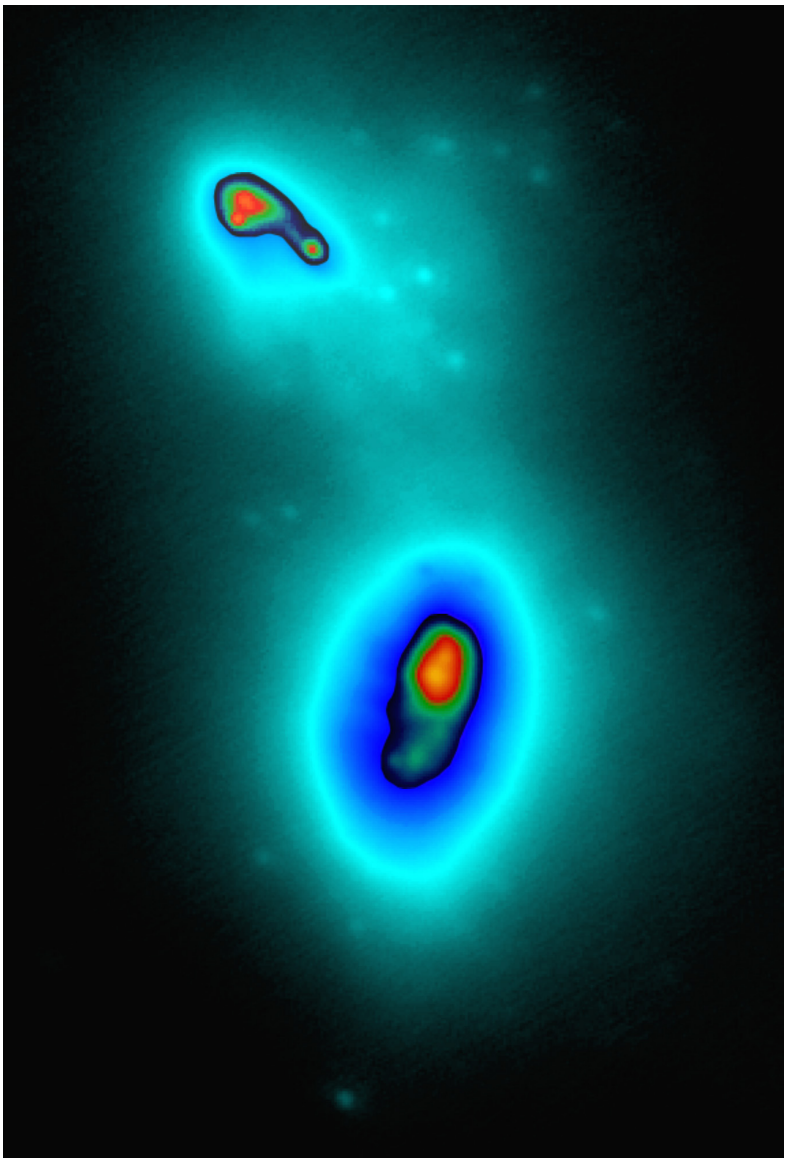

Figure 2.1: Keck adaptive optics image of NGC 6240 in K' band (data first published in Max et al., 2007). The dark-blue-enclosed regions in the north and south nuclei, which are separated by about 1.6 arcsec, have each been re-scaled to highlight their interior structure. The more diffuse image of the rest of the galaxy's nuclear region uses a logarithmic color map. Many individual young star clusters can be seen exterior to the two nuclei (Pollack et al., 2007). In this image, north is up and east is to the left.

et al., 2000; Ferrarese & Merritt, 2000). Because these quantities can evolve significantly throughout the major merger process, black hole parameters may also evolve. It is not known whether the black hole mass grows as a result of the evolution in the host's bulge, or if the bulge growth is moderated by the process of AGN feedback; indeed, it is likely a combination of feeding and feedback processes that maintains these scaling relations. In order to understand this coevolution, one needs to study systems that are currently merging and eventually to compare these observations to the most detailed merger simulations available. NGC 6240 represents the ideal candidate for such detailed observations.

One important aspect of this effort for NGC 6240 is obtaining an accurate measurement of the black hole masses. A variety of methods are used to measure black hole mass, some of which we review here. One established method uses full three-integral modeling of stellar orbits; this method, most commonly used in elliptical galaxies, (see e.g. Siopis et al., 2009; Gültekin et al., 2009a, and references therein) uses line-of-sight velocity distributions and light profiles to create a detailed dynamical mass profile of the galaxy, including the black hole mass. Two- and three-integral models are also sometimes used on bulges of spirals (e.g. Davies et al., 2006; Onken et al., 2007; Cappellari et al., 2009). Reverberation mapping (e.g. Denney et al., 2009, and references therein) is a method of measuring black hole masses in AGN; it uses time-resolved brightness fluctuations in the continuum versus lines from the broad-line region to estimate the size of the broad-line region and therefore the mass of the black hole powering the AGN. Masses measured with reverberation mapping can be calibrated to

match the M_{BH}-σ_* relation (Onken et al., 2004). Black hole masses have been derived (Shields et al., 2003, and references therein) from the continuum luminosity and the width of the broad Hβ line. The masses of supermassive black holes powering quasars have been estimated using x-ray luminosity as an indicator, as in Kiuchi et al. (2009). In some cases, it is possible to measure the Keplerian rotation of ionized or molecular gas around a black hole and deduce its mass, as in Harms et al. (1994), Hicks & Malkan (2008), and Neumayer et al. (2007). In a few galaxies, masers in the disk allow precise velocity (and therefore black hole mass) measurements (Herrnstein et al., 1999; Miyoshi et al., 1995). In the Galactic Center, individual stars have been resolved and their orbits around the black hole tracked astrometrically over time to determine the black hole mass (Ghez et al., 2008; Gillessen et al., 2009). Recently, adaptive optics have been used to resolve stellar dynamics inside the sphere of influence of black holes in nearby galaxies (e.g. Davies et al., 2006; Nowak et al., 2008; McConnell et al., 2011; Gebhardt et al., 2011), a technique which we now build upon.

In a system such as NGC 6240, we are limited in our choice of method; the black holes are obscured by dust and the general system dynamics are unrelaxed because of the ongoing merger. Keck laser guide star adaptive optics (LGS AO, Wizinowich et al., 2006; van Dam et al., 2006) enables us to address both of these challenges. By looking in the near-IR, we look through much of the dust obscuring the relevant kinematics. The high spatial resolution afforded by the adaptive optics system allows us to focus on stellar dynamics within the sphere of influence of the black hole, unconfounded by the unrelaxed dynamics of the system at large.

2.1 Observations and Data

We began by observing NGC 6240 with the W. M. Keck II 10-meter telescope using the Near InfraRed Camera 2 (NIRC2, PIs - K. Matthews & T. Soifer) and the Keck LGS AO system to obtain high-resolution imaging. Our images, taken in the K' filter and using the narrow camera (with a 0.01"/pixel plate scale), were previously published in Max et al. (2007) and Pollack et al. (2007).

We then observed NGC 6240 with the OH-Suppressing InfraRed Imaging Spectrograph (OSIRIS, Larkin et al., 2006), on the W. M. Keck II telescope using LGS AO. OSIRIS is a near-infrared integral field spectrograph with a lenslet array capable of producing up to 3000 spectra at once. The spectral resolution ranges from about 3400 in the largest pixel scale to 3800 in the three finer pixel scales; this resolution is sufficient to resolve spectral regions between the OH emission lines from Earth's atmosphere. Our data are comprised of two 600-second exposures in the Kn5 filter (2.292 μm - 2.408 μm) with the 0.035"/pixel plate scale taken on 21 April 2007. With this filter, we observe the CO (2-0) and (3-1) bandheads at 2.293 μm and 2.323 μm rest wavelength (2.345 μm and 2.380 μm observed) respectively. Figure 2.2 shows an example spectrum.

The Keck LGS AO system uses a pulsed laser tuned to the 589 nm Sodium D_2 transition, exciting atoms in the sodium layer of the atmosphere (at $\sim$95 km) and causing spontaneous emission. Thus, the laser creates a spot in the upper atmosphere which allows the AO system to monitor turbulence below the sodium layer via a Shack-Hartmann wavefront sensor and correct for it with a deformable mirror. A laser guide star enables high-order corrections to the wavefront, but relies on a natural guide star

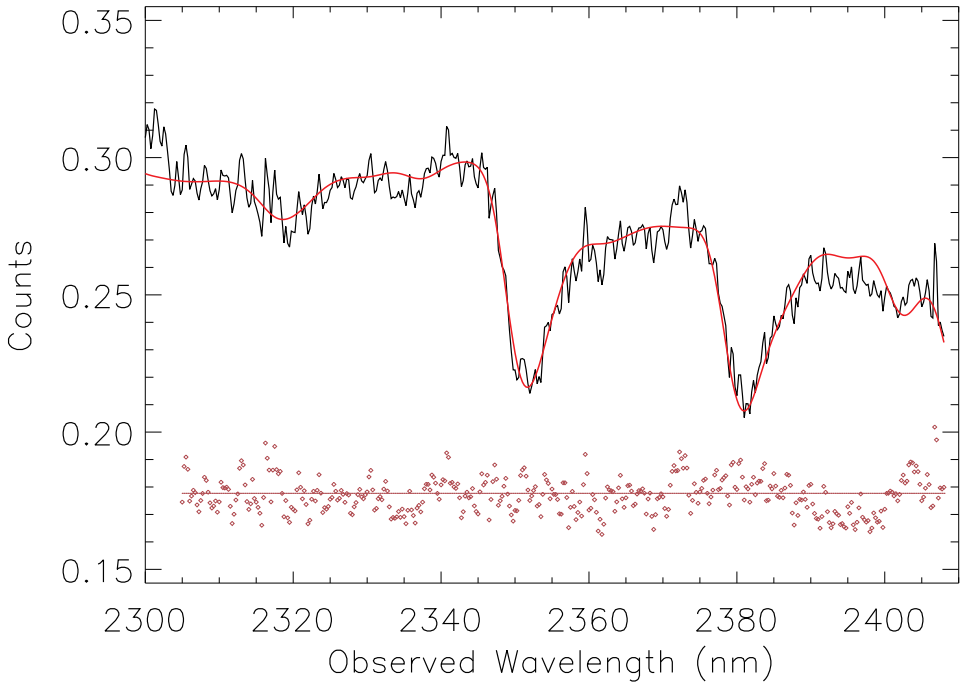

Figure 2.2: An example of the CO absorption bandheads observed in the vicinity of the southern black hole with OSIRIS. This spectrum was created by binning the light from a 3x3 pixel region around the black hole. The thick red line overplotted shows the results from template fitting to obtain kinematics, as detailed in Section 5.3. The red dots along the horizontal line show the residuals of the fit about zero, shifted upwards to fit on the same plot.

(which may be fainter and farther away from the target than if no laser were used) to make corrections to image motion (tip and tilt). Our tip-tilt star (R=13.5 mag) is 35 arcseconds to the northeast of the nuclei. To estimate the point-spread function (PSF), we took short exposures of our tip-tilt star before and after our observations; these will be described in Section 3.2.

Our OSIRIS data were reduced with the OSIRIS Data Reduction Pipeline v2.2 (available at `http://irlab.astro.ucla.edu/osiris`), which includes modules to subtract sky frames, adjust channel levels, remove crosstalk, identify glitches, clean cosmic rays, extract a spectrum for each spatial pixel, assemble the spectra into a data cube, correct for atmospheric dispersion, perform telluric corrections, and mosaic frames together.

2.2 Methods

Using the Kn5 filter, we observed the CO (2-0) and (3-1) bandheads at 2.293 μm and 2.323 μm rest wavelength respectively. These molecular features come from the atmospheres of later-type giants and supergiants. Stellar kinematics are less likely to be disrupted by non-gravitational forces than gas motions, giving us a potentially more robust measurement of the black hole mass.

2.2.1 Measuring the Kinematics

We begin by creating a signal-to-noise (S/N) map using two methods. We first calculate the S/N theoretically, by adding noise components in quadrature: photon

noise from the source, photon noise from the sky, read noise and dark current from characterizations of the detector. This produces an upper limit to the S/N because other noise sources may be present as well.

$$S/N = \frac{F\gamma t}{\sqrt{(Ft + F_S t_S (\frac{t}{t_S})^2)\gamma + (RN^2 + (\frac{\gamma}{2})^2 + Dt) n_{pix}}} \tag{2.1}$$

In this equation, F is the flux from the galaxy, F_S is the flux from the sky, γ is the detector gain, t is the exposure time of galaxy frames, t_S is the exposure time of sky frames, RN is the readnoise of the detector, D is the dark current, and n_{pix} is the number of spectral pixels. For a more thorough discussion of this equation, see Section 9.9 in McLean (2008).

It is most common to report S/N as an average signal-to-noise ratio *per spectral pixel or per resolution element.* We adjust the above equation appropriately by dividing the numerator and each variance (*not* the square-rooted noise components) by $n_{specpix}$, the number of spectral pixels included in the region of interest. In our brightest spatial pixels, we find a S/N per pixel of ~ 40.

To confirm our theoretical calculations, we calculate S/N empirically from the spectra. Bluewards of the CO (2-0) bandhead, we have a spectral region of the galaxy uncontaminated by lines. Fitting for this continuum level, we find the signal present in each spectrum. After subtracting off the continuum fit, the root mean square of the residuals gives us a representation of the noise per pixel. We find good agreement between our empirical and our theoretical estimates of signal-to-noise ratios.

Next we bin our data with optimal Voronoi tesselations using code developed

by Cappellari & Copin (2003) to improve the signal-to-noise ratio in our fainter regions. This algorithm calculates a set of bin centroids according to specific criteria on the topology, morphology, and uniformity of S/N of the final bins. That is, starting from the unbinned pixel with the highest S/N, the algorithm will include a pixel in the bin if it is adjacent to the starting pixel, does not significantly reduce the "roundness" of the bin, and, if the bin's S/N is too low, brings the S/N of the final bin closer to the chosen S/N threshold. In this way, pixels which already have a S/N at or above the chosen threshold are not binned and therefore spatial resolution is not sacrificed unnecessarily. In lower S/N regions, pixels are binned just enough to provide meaningful measurements. The morphological requirements create bins that are most likely to share similar velocities and dispersions. Following Engel et al. (2010), we choose a S/N (per spectral pixel) threshold is 20 for each bin of pixels; the optimal bins are shown in Figure 2.3.

Once we have binned our spectra appropriately, we use the Penalized Pixel Fitting code from Cappellari & Emsellem (2004) to fit radial velocities to each spectrum. This method implements a maximum penalized likelihood approach for extracting stellar kinematics from absorption-line spectra. The algorithm parametrically expands the line-of-sight velocity distribution as a Gauss-Hermite series and allows for the choice of a penalty against higher-order moments. This penalty will bias the fit against higher-order moments, so that the fit must be improved by a certain specified amount to include them. In this way, higher-order fits are possible where spectra have a high enough signal-to-noise ratio, but the fits will tend to simple Gaussians in the low signal-to-noise limit. In order to trust higher-order moments, a signal-to-noise ratio of > 50

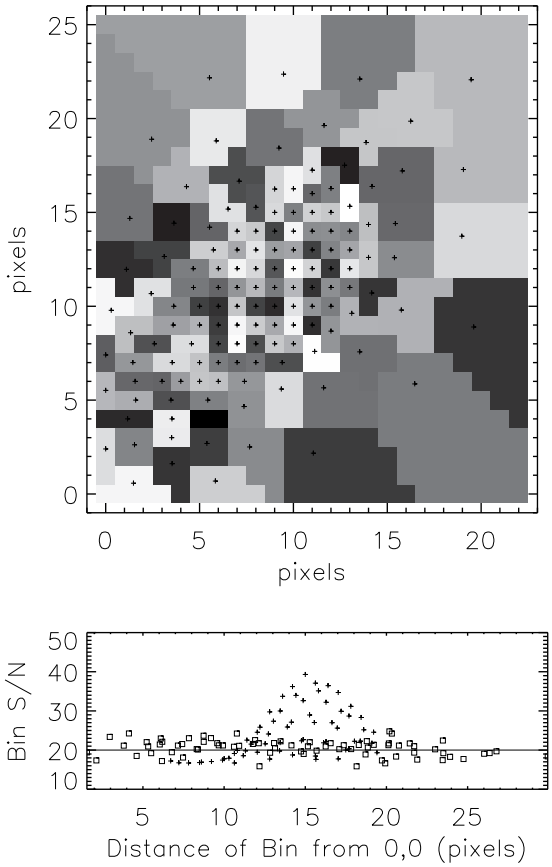

Figure 2.3: Top panel: The Voronoi tessellation bins we impose on our data to equalize to S/N of 20 in the spectrum associated with each spatial bin. The bins near the center are small (one pixel) because the flux is high enough that the S/N is already above the threshold. In the outer regions, pixels have been binned together so that the spectra have a S/N of ∼20. Bottom panel: Another representation of the S/N of bins. Each point represents a bin; the plus symbols are bins that contain only one of the original pixels – they lie above the threshold line because they had sufficient S/N initially. The open squares represent bins whose members originally had insufficient S/N; they were binned together until they approximately reach the threshold value.

(Cappellari et al., 2009) is usually required. Since binning our spectra up to a S/N of 50 would decrease our spatial resolution signficantly, we choose to fit simple Gaussians.

One key feature of this code is the option of including a set of stellar templates from which to fit the kinematics. There has been some debate on which templates most accurately represent the stellar populations of NGC 6240. Tecza et al. (2000) conclude that the bulk of the light in the near-infrared is due to late K or early M supergiants, while Engel et al. (2010) argue that late-type giants characterize the global stellar population better. With Cappellari's method, we are able to input a variety of stellar templates and allow the parametric fit to select the best combination of templates for each spectrum. In our final iteration of the code, we selected 5 stellar templates from the GNIRS library (Winge et al., 2009) that exhibited the deepest CO bandheads. The stellar templates chosen were: HD112300 (spectral type M3III), HD198700 (K1II), HD63425B (K7III), HD720, (K5III), and HD9138 (K4III). The region of these spectra around the CO bandheads is shown in Fig 2.4.

We show the measured velocity and velocity dispersion maps from OSIRIS in Figures 2.5 and 2.6, respectively. We estimate the errors in the velocity and velocity dispersion measurements by running a Monte Carlo simulation, adding the appropriate amount of random noise to each spectrum and refitting them 100 times. Formal measurement errors in our velocity and velocity dispersion measurements are ~ 10 km s^{-1} in the brightest regions, and average about 30 and 70 km s^{-1}, respectively, over the whole fitting region.

With velocity and velocity dispersion maps, it is tempting to think about the

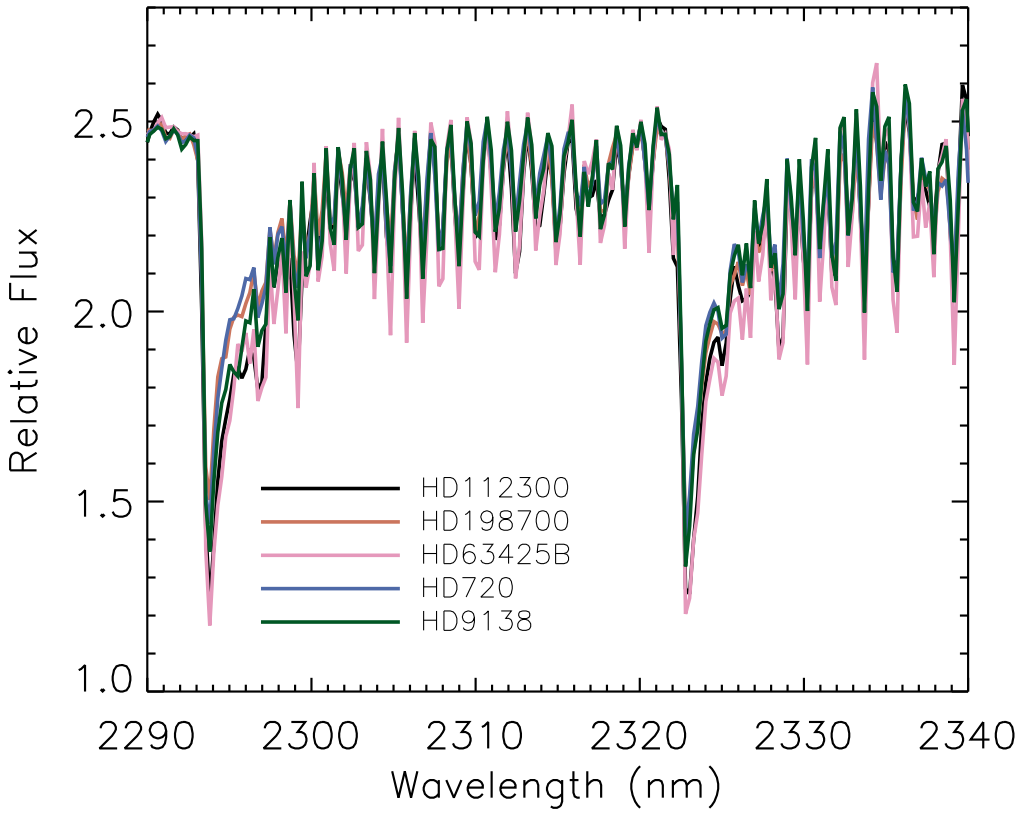

Figure 2.4: Spectra of the five late-type giants and supergiants used as stellar velocity templates in our dynamical modeling. The deep CO bandheads match those seen in our spectra (Figure 2.2). The templates were shifted in wavelength to correct for peculiar velocities of the stars, to match the CO transitions in a vacuum.

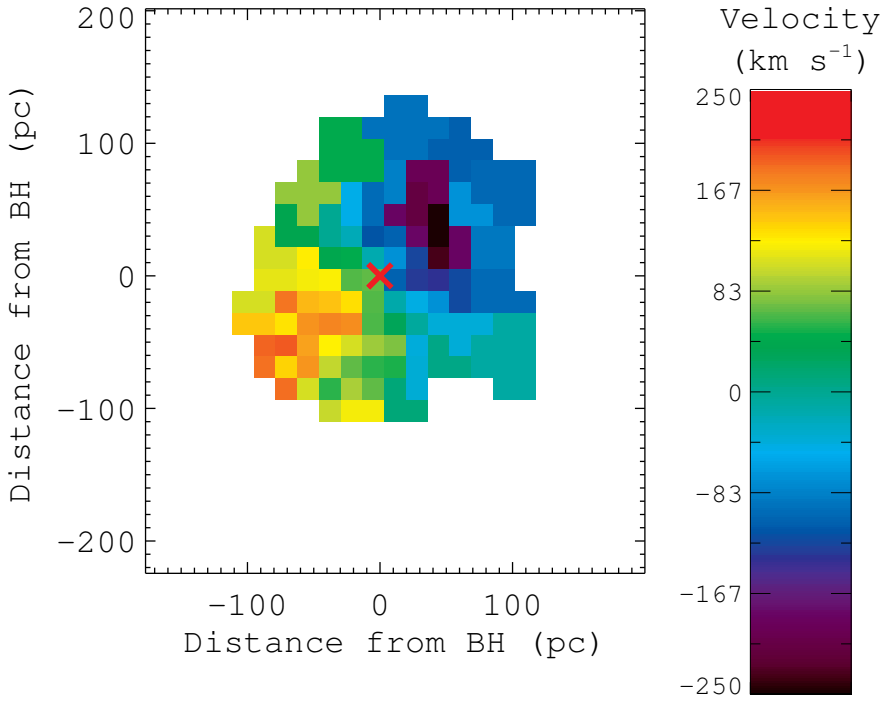

Figure 2.5: Stellar velocity field measured from the OSIRIS IFU data near the southern black hole (red x). Typical errors are ~ 10 km s^{-1} in the brightest regions and ~ 30 km s^{-1} overall. Large pixels on the periphery have been binned using Voronoi tesselation to improve S/N (see Figure 2.3). Voronoi bins with centroids further than ~ 115 pc from the black hole (in projection) have been colored white to mask out regions which are less affected by the black hole's gravity. (The data used to create this figure are available for download in the online journal.)

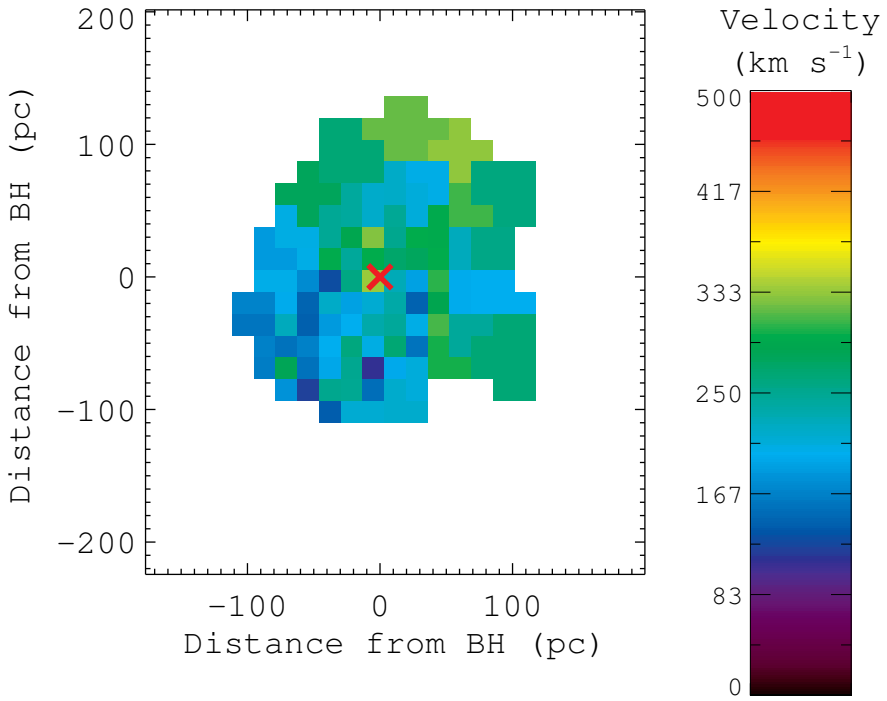

Figure 2.6: Stellar velocity dispersion measured from the OSIRIS IFU data near the southern black hole (red x). Typical errors are $\sim$ 10 km s^{-1} in the brightest regions and $\sim$ 70 km s^{-1} overall. Large pixels on the periphery have been binned using Voronoi tesselation to improve S/N (see Figure 2.3). Regions far from the black hole have been masked out, as in Figure 2.5. (The data used to create this figure are available for download in the online journal.)

measured v/σ of the system, to determine how much of the stellar dynamical energy is in rotation. However, this must be handled carefully in a system like NGC 6240. In our data, we measure velocity peaks of $\sim$ 200 km s^{-1}, and velocity dispersion that varies between roughly 200 and 300 km s^{-1}, suggesting that the energy is approximately evenly divided between ordered rotation and random orbits, with perhaps up to 50% more in the latter. However, in this region of NGC 6240, we know there are clumps of intervening material such as spiral arm remnants or tidal tails (e.g. Engel et al., 2010), which would cause an increase in the measured velocity dispersion that is not yet inherent to either the nuclear disk or the spheroid. Because we do not have a way of determining how much of the velocity dispersion measured is from relaxed material, our analysis yields only a lower bound on v/σ. We conclude that a significant fraction of the kinetic energy is in rotation.

Once we have maps of velocity and velocity dispersion, we compare our data to models that contain a black hole. Each model, of course, comes with its own set of assumptions, and in a late-stage merging system such as NGC 6240, we must think carefully about what such models can tell us. While the quality of these data is clear, understanding how to analyze them is not straightforward. Here we discuss two possible ways to measure the black hole mass from these data and compare the results of the two methods.

2.2.2 Dynamical Analysis - JAM Modeling

We begin our analysis by utilizing the JAM modeling code (Jeans Anisotropic Multi-Gaussian expansion dynamical models Cappellari, 2008), a technique based on the

two-integral axisymmetric Jeans formalism but which has been expanded to allow for anisotropy via the parameter $\beta_z = 1 - (\sigma_z/\sigma_R)^2$. JAM modeling efficiently utilizes the axisymmetric dynamics seen near the south nucleus, and does not require higher-order Hermite moments.

This method, which fits $v_{rms} = \sqrt{v^2 + \sigma^2}$, is likely to overestimate the black hole mass by assuming the dynamics measured belong to a relaxed system. In fact, an unknown fraction of the measured velocity dispersion is due to intervening material, such as tidal tails, that has not yet reached dynamical equilibrium. Additionally, this method assumes axisymmetric and smooth light and mass profiles. Finally, we assume a constant mass-to-light ratio.

The JAM modeling code requires a high-resolution light profile, which we parametrize using the Multi-Gaussian Expansion code (MGE Cappellari, 2002) designed to work with the JAM code. To fit our light profile over a larger field of view than is available in our OSIRIS data, we use our K' NIRC2 imaging and mirror it about the minor axis of the nucleus. We do this because the southeast side of the nucleus is considerably less extincted, so our signal-to-noise ratio is much improved. Once we have symmetrized the observed light profile, we then de-extinct this using the extinction map of Figure 9 in Engel et al. (2010). Using this extinction map, our recovered intrinsic brightness peaks at the same location as the kinematic center of our dynamical data, which means that in K-band the nucleus is only partially extincted. (In contrast, the extinction at visible wavelengths is so severe that the entire region surrounding the south black hole cannot even be seen (Max et al., 2005).) This is important, as most

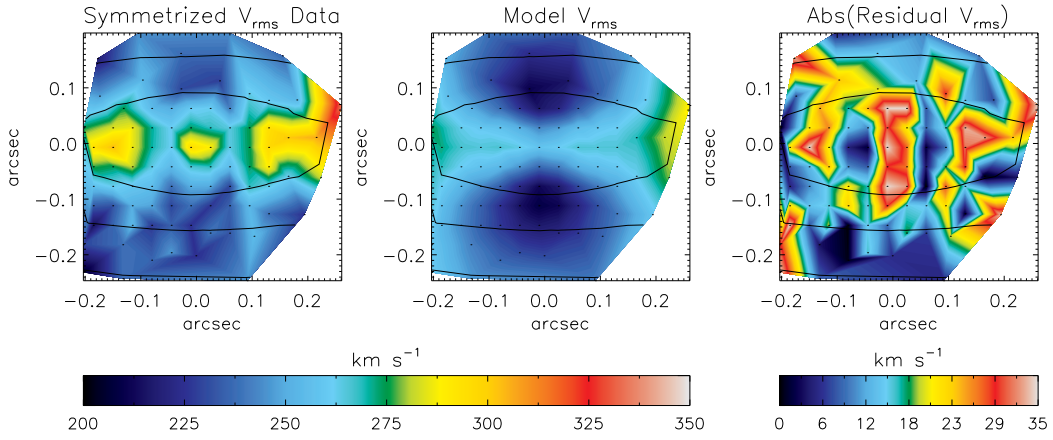

Figure 2.7: Left: Symmetrized v_{rms} map (as in Cappellari, 2008) from OSIRIS observations. Center: Best-fitting axisymmetric JAM model, on the same scale and color bar as data (left). Right: Map of residuals (absolute value of difference between left and center panels) with new color bar to the (right). In all panels, the black contours show the Gaussian expansion of the light profile, and the black dots represent the centroid of each spatially-binned spectrum, where velocity and velocity dispersion are measured. Axes show distance from the central black hole in arcseconds.

of the orbital information reported by JAM modeling is contained in the light profile. In order to determine the appropriate mass-to-light ratio, anisotropy parameter β_z and black hole mass, we compare the resulting dynamical models to those measured from our OSIRIS data in K-band.

Our best-fit models for this method measure a black hole mass of $2.0 \pm 0.2 \times 10^9 M_\odot$, and are shown, along with the symmetrized v_{rms} data for comparison, in Figure 2.7. The reduced χ^2 statistic, fitting over 120 points, is 2.21.

2.2.3 Dynamical Analysis - Thin Disk

As a sanity check on the JAM model, and to provide a lower-limit to the black hole mass, we explore a simple model comparing the velocity field to that of a thin disk

with a given enclosed mass profile exhibiting Keplerian rotation.

In this method we do not include a dispersion component because intervening material may inflate that measurement. Here we assume that the energy in intrinsic dispersion in the nuclear stellar disk is negligible compared to the energy in rotation. This should give a lower limit to the black hole mass.

We are measuring the dynamics of young stars in the very nucleus of a gas-rich merger. A thin disk of young stars may be expected because they can form out of the nuclear disks of gas and dust seen in merger simulations by, for example, Mayer et al. (2007); Kazantzidis et al. (2005); Hopkins & Quataert (2010b) and in observations by Riffel & Storchi-Bergmann (2011); Hopkins & Quataert (2010a). We clearly see in the OSIRIS velocity field a sharp steepening of the velocity gradient in the region of the black hole: a sign of strong rotation, and reminiscent of a thin Keplerian disk embedded in a larger spherical potential.

We focus our mass modeling on the region of the sphere of influence of the black hole, where the dynamics are most likely to be well-behaved. We begin with a thin Keplerian disk model, using $v = \sqrt{GM_{BH}/r}$. This will attribute all mass enclosed to the black hole, and therefore overestimate the mass; we only use this case to check the sub-pixel position of the black hole and get a rough set of parameters over which to fit a more complex model, which includes a spheroid, described in Section 2.2.3.

Once a model velocity field is constructed for a specific set of parameters, we use that information to create a synthetic datacube: for each spaxel, we use a template CO bandhead spectrum shifted in velocity space to the appropriate velocity

and weighted by the total flux in that spaxel. With this synthetic datacube we perform a wavelength-by-wavelength convolution with the PSF to simulate the residual smearing from the atmosphere and optical system. Convolving each wavelength slice with the PSF models the true image blurring, as opposed to smoothing the overall velocity field. Once the datacube has been convolved in this way, we remeasure the velocities from each spatial pixel's spectrum to derive the smoothed velocity field. We compare the resulting velocity field with the observed velocities measured by OSIRIS. We repeat this process, making models for various parameter sets, and compare each with the observed data.

Model Parameters

At these spatial scales, the velocity field of a thin Keplerian disk around the black hole can be fully described by a few parameters: black hole position, disk inclination, disk position angle, and enclosed mass. We fit the position angle of the velocity field first, as it may be fit largely independently of the other black hole parameters. Our tests indicate that the positive velocity peak falls at a PA of 130° measured counter-clockwise from north, relative to the black hole's position. We adopt this position angle in our later fits. The position of the black hole is not trivial to pinpoint. Because of 6-8 magnitudes of extinction distributed unevenly across the nucleus (Engel et al., 2010), we avoid using our K'-band isophotes to find the center of the southern nucleus, and instead use the measured velocities to determine the kinematic center. We have a close estimate of the position of the southern black hole using relative astrometry from the northern black hole, whose position is visible in our data (Max et al., 2007). To improve our positional accuracy, we allow the black hole position to vary in the fit by sub-pixel

amounts in a simple code that only takes into account the black hole mass. We then fix the position of the black hole, along with our PA, for our full suite of models.

As AO measurements can be affected by the PSF achieved in our observations, we must carefully consider the PSF used in our models. We use short exposures of our tip-tilt star bracketing our observations which are useful to characterize the performance of the AO system and the conditions during the evening. Our first PSF model is a Moffat fit of the tip-tilt star, which has a Strehl ratio of 20% and FWHM of 65 mas. We find that the north nucleus point source has a FWHM of 63 mas, consistent with that of the tip-tilt star. However, the tip-tilt star gives a lower-limit to the actual Strehl ratio since, for shorter exposure times appropriate to the tip-tilt star, the low-bandwidth wavefront sensor (Wizinowich et al., 2006) did not have time to settle into the most accurate correction. The longer exposures on NGC 6240 itself do provide sufficient settling time. This effect is partly offset by additional blurring due to the offset between the tip-tilt star and NGC 6240 (anisokineticism). Because the distance between the tip-tilt star and the nuclei is only 35", this effect is expected to be modest (van Dam et al., 2006), and does not completely counteract the aforementioned effect from the low-bandwidth wavefront sensor. We see that the AO system performs better during our longer galaxy exposures. To accommodate this, we adjust the Moffat fit coeffecients to Strehls of 25%, 30%, 35% and 40%, while maintaining the FWHM (see radial profiles in Figure 2.8). The Strehl ratio then becomes a parameter in our model-fitting procedure, in which we create models with each of these PSFs to compare with our data.

In an asymmetric, dusty system such as NGC 6240, we must also carefully

consider the region over which we compare our models to the data, masking out regions that are less important to match. We expect that our model will most accurately describe the velocities close to the black hole. At some distance from the black hole, we expect other galaxy and tidal components to dominate, which may affect the model fit. To test this concern, we use a variety of different masks to vary the distance from the black hole at which we stop our comparison. We find that the best-fitting enclosed mass is not sensitive to the mask selection.

Our mass profile includes a radially-varying contribution to the mass profile, representing a spheroidal component of the galaxy. We construct models that include both a point mass at the center and a spherically-symmetric mass profile to mimic the inner regions of the bulge. We parametrize the spheroidal component as $\rho(r) = \rho_0 r^\gamma$, where ρ is the mass density. We fit three parameters to the enclosed mass profile: the black hole mass M_{BH}, the normalization for the spheroidal compontent ρ_0, and the power-law index of the spheroidal component, γ.

Results of Thin Disk Model Fitting

Our best fit gives a black hole mass of $8.7 \times 10^8 M_\odot$ with a spheroid of $2.9 \times 10^8 M_\odot$ within 100 pc of the black hole and an index of $\gamma = 1.5$ (see velocity field of this model in Figure 2.9). The reduced χ^2 statistic for this model is 3.7, fitting over 65 velocity datapoints. To estimate the accuracy of this measurement, we perform a Monte Carlo simulation, fitting models to our observations with 100 different representations of noise added. The distribution of fitted masses can be well-fit by a Gaussian, the width of which represents our one-sigma error bars. Including this, our best fit shows a

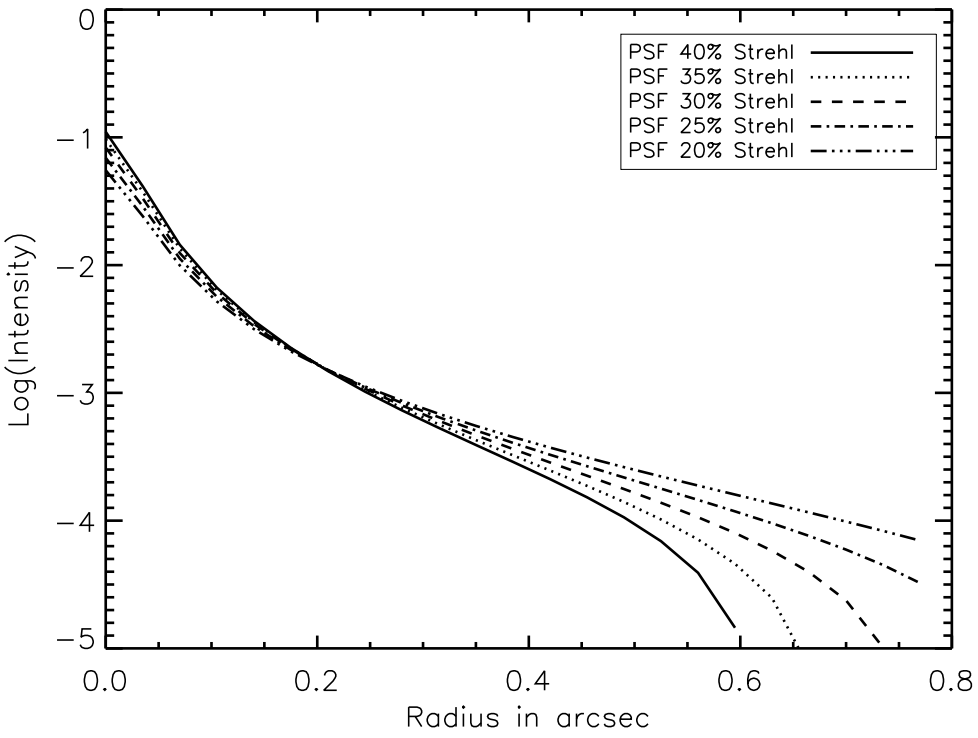

Figure 2.8: The five PSFs used by our model fitting routine. The Strehl ratio is varied as a free parameter in order to avoid systematic errors in black hole mass measurement based on PSF mismatch, while maintaining a FWHM of 65 mas, to match the FWHM measured in the data.

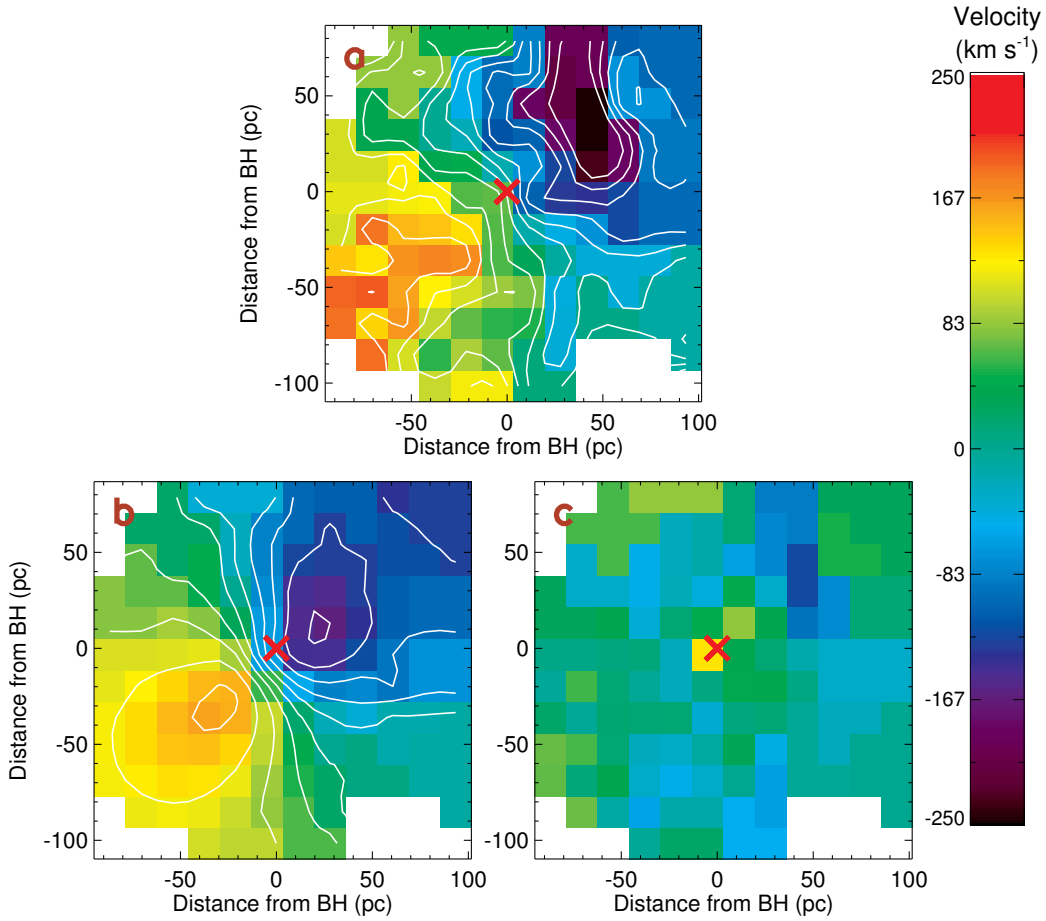

Figure 2.9: (a) The observed velocity field of our OSIRIS data for comparison with our best-fit models. (b) The best-fitting velocity field for a mass model containing a point mass and an extended, spherically-symmetric component. (c) The residuals found by subtracting the observed velocity field from the model shown in (b). Note that the model yields a good fit to the central steep velocity gradient associated with the black hole. In each panel regions far from the black hole have been masked out, as in Figure 2.5.

system with a black hole mass $8.7 \pm 0.3 \times 10^8 M_\odot$.

Trends in the Reduced χ^2 Map

It is also instructive to look at trends in the reduced χ^2 maps. The simplest example is shown in Figure 2.10, demonstrating that, for a thin disk model such as this one, the black hole must be more massive to match the velocity field when the inclination is lower, for $i < 60°$. This map also shows that the black hole mass increases again at the highest inclinations, as the model tries to match the velocity field not only along the major axis but in the surrounding spatial pixels as well (the well-known "spider diagram"). If NGC 6240 were dust-free, the morphology of the region around the south nucleus could, in principle, be used to independently measure (or constrain) the inclination. However, the northwest half of the circumnuclear disk is heavily obscured in NGC 6240. In this case, the image can only provide a lower-limit for the inclination ($\sim 55°$).

We see a demonstration of the trade-off of mass between the spheroid and black hole by looking at a 2-dimensional map of reduced χ^2 statistics (Figure 2.11), varying the amount of mass that goes into each component of our mass profile. As more mass is put in the black hole, models with less mass in the radial component fit better; as less mass is put in the black hole, the mass in the radial component must increase to best fit the data. In each case, the combined mass reaches a maximum at $\sim 2 \times 10^9 M_\odot$ within 100 pc of the black hole.

Lastly, we consider our choice of varying PSFs in our model fitting. Our best-fit models from this technique prefer PSFs with a Strehl ratio of 25%, near the lower

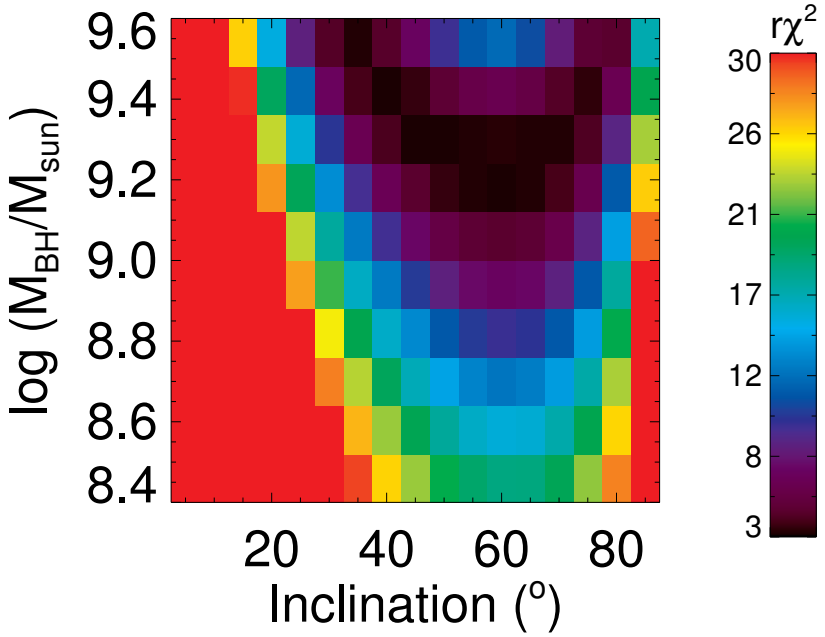

Figure 2.10: The map of reduced χ^2 statistics for our thin disk model as the black hole mass (vertical axis) and the inclination (horizontal axis) are varied. The remaining parameters (spheroid paramaters ρ_0 and γ, velocity offset, and PSF) are held fixed. We see that as the inclination decreases (the disk of stars becomes more face-on), a larger black hole mass is required to match the observed radial velocity peaks for inclinations $\lesssim 60°$. As the inclination increases beyond 60° (the disk of stars becomes more edge-on), we also see the best-fit black hole mass increase; this is likely because a larger black hole is required to affect off-axis regions of the spider diagram when the disk is more edge-on. These fits were measured with 65 datapoints.

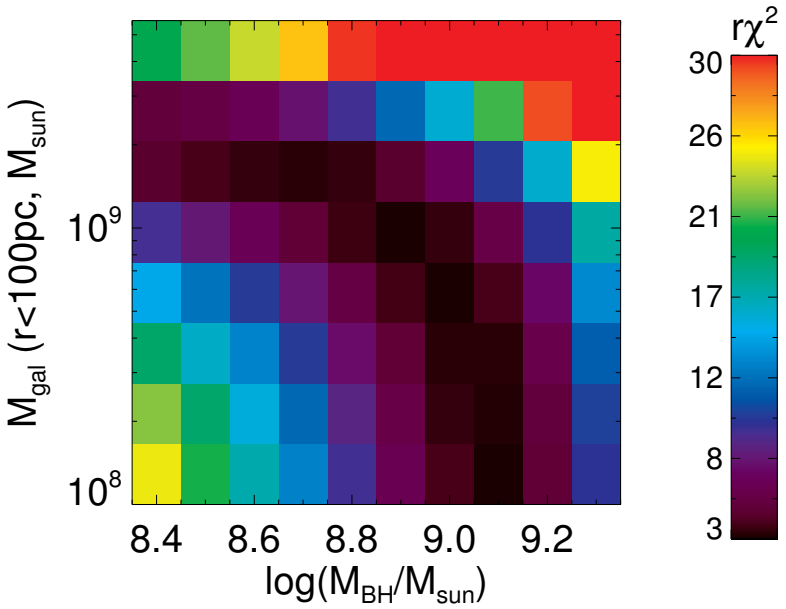

Figure 2.11: The map of reduced χ^2 statistics as the black hole mass component (horizontal axis) and the spherically-symmetric mass component (vertical axis) are varied. The other parameters (inclination, density profile index γ, and velocity offset) are held fixed. We see that on the right side (at high black hole mass), the best fitting models have less mass in the spheroidal component. On the left side (with black hole mass becoming negligible), the mass of the spheroidal component flattens out at $2 \times 10^9 M_\odot$, the total enclosed mass at our resolution limit. These fits were measured with 65 datapoints.

limit of what we would expect from our data. We compare these to models with 40% Strehl, approximately the best PSF we could hope for under the conditions of these observations. When forcing an improved PSF, the best-fitting black hole mass increases slightly, to $9.2 \times 10^8 M_\odot$. This is only slightly outside of the 1-σ range, and has a reduced χ^2 statistic of 4.8, considerably higher than our better-fitting models. While we are confident that fitting for PSF was a good choice, we also note that the black hole mass is not very sensitive to this parameter.

2.3 Discussion

2.3.1 How Much Mass Could Be Due to a Nuclear Star Cluster?

It is important to consider the limitations of our approaches. With a black-hole-only thin disk model, one does not directly measure the black hole mass; one measures the mass enclosed in the central OSIRIS pixel, 17 parsecs on a side. Including a spheroidal component implicitly assumes that the stellar mass density profile is smooth and that all other mass is due to the black hole. What fraction of this mass might be due instead to a nuclear star cluster?

To address this concern, we refer to our high-resolution NIRC2 K' imaging. Through a careful deconvolution by the PSF, we arrived at a cleaned image of the south nucleus. We flux-calibrated this image by matching the large-scale luminosity to that reported in Engel et al. (2010), and assumed their mass-to-light ratio of 1.9.

This analysis showed that there could be up to $3 \times 10^8 M_{Sun}$ of stellar mass within the sphere of influence of the black hole, consistent with the mass in our fitted

spheroidal component.

2.3.2 The $M_{BH} - \sigma_*$ Relation

With our measurement of the black hole mass, it is interesting to consider where NGC 6240 would fall on the $M_{BH} - \sigma_*$ relation, which compares the black hole mass to the stellar velocity dispersion of the bulge of the host galaxy. Because NGC 6240 is a merging system, it plausibly lacks a relaxed bulge component; therefore it is not easy to define exactly where or how the velocity dispersion should be measured to compare to the $M_{BH} - \sigma_*$ relation. Still, it is worth looking at merging active systems since they are in the process of evolving along these relations. Here we are able to take our first glimpse of where a system might fall on these relations while in the process of merging. Does the black hole grow more quickly than the larger-scale galactic properties, or must it play catch-up after the galaxy's bulge has settled back to an equilibrium state?

The $M_{BH} - \sigma_*$ relation is well-defined only in systems that are dynamically-relaxed on the large scale. In such a system, the central black hole mass can be compared to the integrated velocity dispersion of stars in the bulge within one effective radius. NGC 6240 has two black holes; here we only consider the southern one. It is not trivial to measure the equivalent stellar velocity dispersion associated only with this black hole in the southern galaxy, as the bulges of both progenitor galaxies have begun to merge. We expect the stellar velocity dispersion at this stage to be low compared to the final value; quite a bit of energy is still in ordered rotation and has yet to be randomized. As reported in Engel et al. (2010), the south nucleus shows a maximum rotational velocity of ~ 300 km s^{-1}, putting as much or more energy in ordered rotation as in dispersion.

Our spectra also give us only the dynamics of later-type giants and supergiants, via the CO bandheads. Rothberg & Fischer (2010) have suggested that this also gives an underestimate of velocity dispersion as compared to measurements made using the Ca triplet absorption lines at 8500 Å.

Our spectra also only give us dynamics very close to the nucleus. We bin our OSIRIS data into one spectrum encompassing our entire south nucleus (inside a radius of $\sim$ 300 pc); the measured velocity dispersion from the CO bandheads is 282 ± 20 km s^{-1}. For comparison, we make the same measurement using SINFONI data from Engel et al. (2010); this velocity dispersion, 310 ± 12 km s^{-1}, encompasses a wider region ($r \leq 500$ pc). We also compare these two values of stellar velocity dispersion to previous measurements from the literature. Tecza et al. (2000) measured $\sigma_* \sim 236$ km s^{-1} using the CO bandheads within 235 pc of the south nucleus. Oliva et al. (1999) measured the stellar velocity dispersion integrated over the entire system, but used three different absorption lines: Si 1.59 μm (313 km s^{-1}), CO 1.62 μm (298 km s^{-1}), and CO 2.29 μm (288 km s^{-1}). Estimates of σ_* made from integrating over a larger fraction of the galaxy could be higher because they combine multiple dynamical populations (e.g. the north and south nuclei and intervening spiral arms); however, such estimates do not distinguish between material associated with this black hole and the northern black hole, as both are partially within the seeing-limited PSF.

We plot our black hole mass measurement on the $M_{BH} - \sigma_*$ relation along with other dynamical black hole mass measurements compiled by Gültekin et al. (2009b) in Figure 5.3. We plot separate points for our black hole mass measurements under two

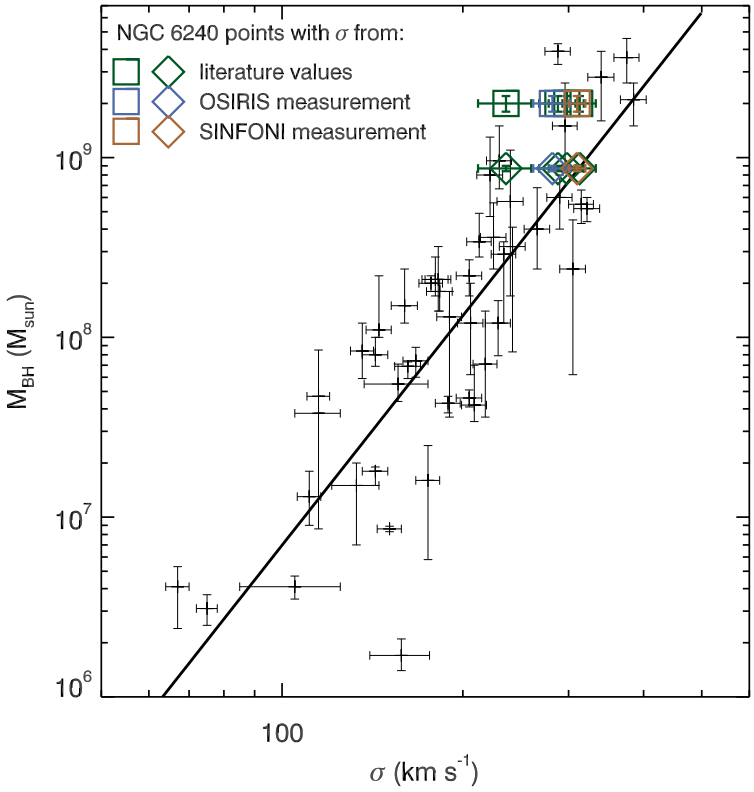

Figure 2.12: Plot of the $M_{BH} - \sigma_*$ relation as recently recalculated by Gültekin et al. (2009b). The small black points and error bars represent the black hole mass measurements from the literature. The larger colored squares and diamonds represent our black hole mass measurements in the south nucleus of NGC 6240, using different values of σ_*. Squares show the black hole mass measurement from JAM modeling, and represent an upper limit to the black hole mass. Diamonds show the black hole mass measurement from our thin disk approximation, and represent a lower limit to the black hole mass. The dark green points are our mass measurement paired with measurements of σ_* from Tecza et al. (2000) and Oliva et al. (1999). The blue and brown points plot our measurements of σ_* from OSIRIS and SINFONI respectively. See text for further details.

different assumptions. Because there is some ambiguity about the appropriate way to measure the stellar velocity dispersion in the bulge in a system such as NGC 6240, we plot our measured black hole mass with several different σ_* values from the literature as well as with our measured σ_* very close to the black hole.

NGC 6240 appears to lie well within the scatter of the $M_{BH} - \sigma_*$ relation, which may suggest that the black hole mass and the bulge velocity dispersion grow simultaneously and at similar rates during a major merger. NGC 6240 is a late-stage merger, but these data could also suggest that a system doesn't evolve along the $M_{BH} - \sigma_*$ relation until the very end stages of a merger, perhaps during nuclear coalescense. To test this, more systems at this and later stages of merging will have to be studied. This is interesting to compare to galaxy merger simulations; for example, Dasyra et al. (2006) conclude that, if the accretion efficiency stays constant, the $M_{BH} - \sigma_*$ relation should be maintained from midway between the first encounter and coalescence through to final relaxation. New higher-resolution simulations are being performed by Stickley et al. (in prep) which show that the stellar velocity dispersion stays low in the nuclear regions much longer than in the rest of the system; results will follow young and old stellar populations separately to help understand the dynamics measured from specific lines.

2.4 Conclusions

Black holes are an important ingredient in galaxy evolution, as seen by the tight correlations between black hole mass and host galaxy properties. Hydrodynamic

simulations of galaxy mergers have suggested that gas-rich mergers, which can drive galaxy evolution, can provide fuel for black hole accretion. In turn, these accreting black holes can radiate enough energy to affect the surrounding galaxy. In light of these discussions, it is particularly interesting to study systems that appear to be in the middle of such an evolutionary event. NGC 6240 represents a nearby galaxy such as this: a merging gas-rich system with two actively accreting black holes. However, such systems are notoriously difficult to study because of their unrelaxed dynamics and their dusty cores.

We have presented high-spatial resolution kinematics within the sphere of influence of the black hole in the south nucleus of NGC 6240, a nearby late-stage merger, made possible by laser guide star adaptive optics. For this test case, we have explored two possible methods for measuring black hole mass in such a system and compared their results and assumptions.

We have utilized the JAM modeling technique made public by Cappellari (2008), demonstrating that it is possible to complete such an analysis on a late-stage merger. We point out that this technique likely overestimates the black hole mass by assuming that all measured velocity dispersion is due to a relaxed system (ignoring intervening unrelaxed material, e.g. tidal tails), and therefore report an upper limit of $2.0 \pm 0.2 \times 10^9 M_\odot$. To provide a lower limit to the black hole mass, we explore the opposite assumption: that all velocity dispersion is caused by intervening material, and that the young stars sit in a thin disk around the black hole. This model of Keplerian rotation around a black hole plus smooth spheroidal mass profile suggests a black hole

which is at least $8.7 \pm 0.3 \times 10^8 M_\odot$.

We find that these two techniques provide measurements that are roughly consistent, and that follow the biases implied by their intrinsic assumptions. To determine which set of assumptions is more reliable would require a detailed study of high-resolution galaxy simulations, which is beyond the scope of this paper. Still we are encouraged that, to within a factor of about two, both measurements agree.

While we cannot make generalizations on how all black hole-galaxy coevolution must proceed, it seems that in this case, the black hole and the host galaxy parameters grow together along the $M_{BH} - \sigma_*$ scaling relation, instead of one preceeding the other. We are beginning an observing campaign to study other local merging galaxies using the same techniques, to investigate a larger sample size.

Chapter 3

The Inner Kiloparsec of Mrk 273: A Second AGN, Buried

3.1 Introduction

When gas-rich galaxies collide and merge, gaseous material can lose angular momentum and funnel towards the center of the merger system (e.g. Barnes & Hernquist, 1992). There it can feed starburst and active galactic nuclei (AGN) activities which power luminous and ultraluminous infrared galaxies ((U)LIRGs). The detailed processes of how merger dynamics contribute to AGN activity (Sanders et al., 1988; Hopkins et al., 2006; Comerford et al., 2009), how mass builds up in the central supermassive black hole (Hopkins et al., 2010; Treister et al., 2010; Rosario et al., 2011), how much energy is desposited into the system by the ionizing sources (Younger et al., 2009; Sanders & Mirabel, 1996), and when the active nuclei are triggered (Donley et al., 2010;

Hopkins, 2012; Farrah et al., 2009) are areas of active research. Because AGN have been observed in mergers with double nuclei (Komossa et al., 2003; Ballo et al., 2004; Koss et al., 2012; Fu et al., 2011; Liu et al., 2011; McGurk et al., 2011; Gerke et al., 2007; Mazzarella et al., 2012), it is known that an AGN can "turn on" before the final coalescence of the nuclei. However, many mergers do not host dual AGN (e.g. Teng et al., 2012). It is inconclusive from the models when an AGN is triggered and what dictates whether or not synchronous ignition occurs (Van Wassenhove et al., 2012).

These questions can be addressed with high-resolution observations of the nuclei in nearby luminous infrared galaxy mergers. Previous integral-field spectroscopic work on large samples of (U)LIRGs have mapped the large-scale distribution and kinematics of ionized gas, compared them to that of stellar components, determined metallicity gradients, and found evidence for galactic outflows and shocks (e.g. Westmoquette et al., 2012; Rich et al., 2011, 2012; García-Marín et al., 2009). Much of the gas is concentrated within the dusty cores of these (U)LIRGs, so longer wavelengths must be probed to understand the nuclear regions. Piqueras López et al. (2012) has presented an atlas of the 2D molecular and ionized gas structure in the southern local (U)LIRGs as probed in the near-infrared, showing the extent and kinematics of the gaseous components at $\sim$0.2 and 0.9 kpc spatial resolution. These seeing-limited observations with an average angular resolution of $\sim 0\farcs63$ full-width half-maximum (FWHM) set the framework of the large kiloparsec-scale conditions of the gas and prompt detailed high-resolution investigations of the nuclear regions.

Due to the advent of laser guide star adaptive optics (LGS AO; Wizinowich

et al., 2006; van Dam et al., 2006), black holes in local (U)LIRGs can now be examined at the sub-arcsec level (Max et al., 2007; Melbourne et al., 2008; Engel et al., 2010; Davies et al., 2010; Medling et al., 2011). In particular, the OH-Suppressing Infra-Red Imaging Spectrograph (OSIRIS; Larkin et al., 2006), an integral-field unit (IFU) with near-infrared wavelength coverage ($1\mu\text{m} < \lambda < 2.4\mu\text{m}$) on the Keck II telescope, offers imaging and kinematic information at $< 0\farcs1$ spatial resolution with LGS AO (e.g. Wright et al., 2009; Law et al., 2009; Do et al., 2009; McConnell et al., 2011; Walsh et al., 2012). NIRC2 (PIs: Keith Matthews and Tom Soifer), a diffraction-limited infrared camera also on the Keck II telescope, offers scales of $\sim$ 0.01"/pixel in the $1 - 5\mu m$ range in its narrow camera mode. They both probe the near-infrared regime where dust extinction does not pose as severe a problem.

To understand the mechanisms responsible for powering the extreme infrared luminosities in (U)LIRGs, we are conducting a survey of nearby galaxy mergers using OSIRIS to probe the gas kinematics and energetics of the nuclear regions in these systems. Observed as part of the larger campaign, Mrk 273 (= UGC 08696) is the focus of this paper as an advanced merger with infrared luminosity $L_{\text{IR}} = 10^{12.21} L_{\odot}$. At a distance of $z = 0.038$ (systemic velocity $cz = 11,400$ km s^{-1}; physical scale 0.754 kpc/$''$for $H_0 = 70$), it exhibits a prominent optical tidal tail ($\sim$40 kpc) extending to the south (Fig. 3.1). With its high infrared luminosity, this ULIRG has a heated dusty core that obscures the central ionizing sources in optical light. As one of the brightest and closest ULIRGs, Mrk 273 has been well-studied across the full wavelength spectrum, including *Spitzer*, *Hubble*, *Chandra*, and *GALEX* observations from the Great

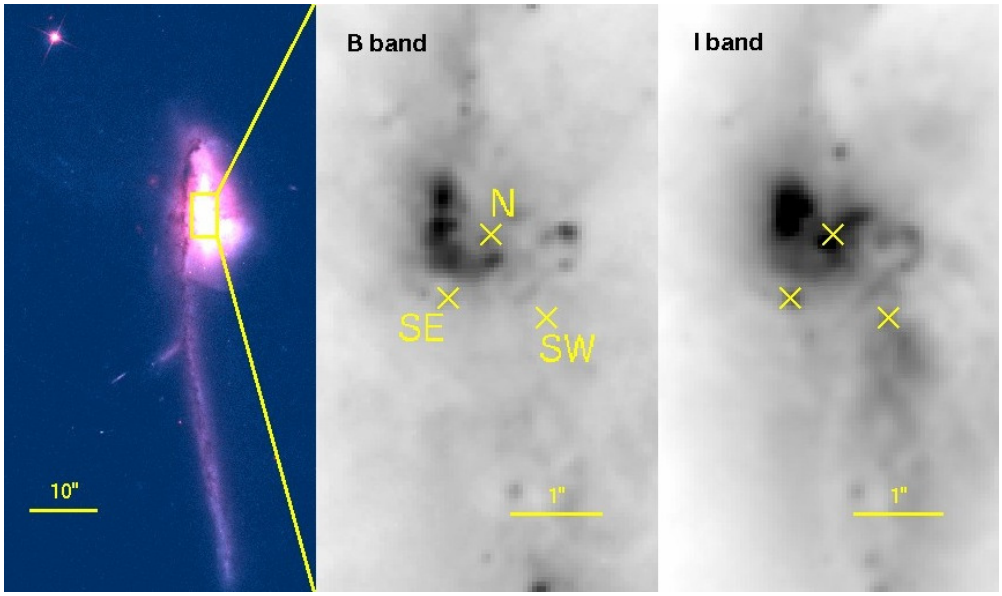

Figure 3.1: (Left) *HST* ACS $B(F435W) + I(F814W)$ composite image of Mrk 273. In these and subsequent images, north is up and east is to the left. The box indicates the zoomed in region in the grey-scale panels. (Middle) and (right) are the zoomed in B- and I-band images, respectively. The three crosses mark the N, SE, and SW sources of interest identified in radio observations (Carilli & Taylor, 2000; Bondi et al., 2005) whose measurements from near-IR imaging and spectroscopy will be presented in this paper.

Observatories All-sky LIRG Survey (GOALS; Armus et al., 2009; Howell et al., 2010; Iwasawa et al., 2011a). However, the details of its power engine remain controversial.

There is substantial evidence in the literature suggesting that at least one AGN resides within Mrk 273: Armus et al. (2007) detected the [Ne V] line in *Spitzer's* mid-infrared IRS spectrum, and measured hot gas with $T > 300$K in the continuum. PAH strength diagnostics from mid-infrared *ISO* spectroscopy classify the galaxy as an AGN (Lutz et al., 1999; Rigopoulou et al., 1999). Hard X-ray emission and the Fe K line (e.g. Xia et al., 2002; Iwasawa et al., 2011b; Ptak et al., 2003) have also been detected in support of the presence of a hard X-ray AGN, though most of the total power is likely to be from circumnuclear starbursts (Iwasawa et al., 2011b).

The status of Mrk 273 as a ULIRG and a late-stage pre-coalescence merger makes it an important galaxy for understanding the role of mergers in galaxy evolution. The specific goals of our high-resolution IFU study are to locate the nuclei of the progenitor galaxies, to determine the characteristics of any supermassive black holes, to verify their active or dormant nature, and to investigate the relative effect of AGN activity and star formation on the surrounding nuclear regions.

Multiwavelength studies have decomposed the nuclear region into multiple components. We combine our data with existing evidence to determine the likely mechanisms of emission for each source. Three main components have been identified from the detected radio continuum: north, southeast, and southwest (N, SE, SW; Condon et al., 1991; Smith et al., 1998) as indicated in Fig. 3.1. These components show dissimilar characteristics in most bands; it is not initially clear which of them may be remnant nuclei. The SE emission is only weakly detected in the near-infrared (Scoville et al., 2000) and weak or undetectable in the X-ray given the limited resolution of *Chandra* (Iwasawa et al., 2011b), but the N and SW X-ray emission coincide with peaks in the near-IR continuum flux. OH maser emission along with steep radio spectral index suggest the presence of a low-luminosity AGN with a binding mass of $1.39\pm0.16 \times 10^9 M_\odot$ in the N component (Klöckner & Baan, 2004). The N radio-1.4GHz emission is further resolved into individual compact sources thought to be clustered supernovae (Smith et al., 1998; Carilli & Taylor, 2000; Bondi et al., 2005). More recently, Iwasawa et al. (2011b) found, in *Chandra* images with improved astrometry, that the hard X-ray flux is superposed on the SW compact source, with a 6-7keV excess extending towards the

north. They determined that the known hard X-ray AGN is located at the SW component, and attributed the 6−7 keV excess to enhanced Fe K emission either from the SW source or from a heavily absorbed Compton-thick AGN at the N component.

In this paper, we present high-resolution infrared integral-field spectroscopy and imaging observations of Mrk 273 taken with the OSIRIS and NIRC2 instruments on the Keck II Telescope, probing down to the $\leq 0\farcs1$ scale. These near-infrared high-resolution maps provide great detail for identifying the location of the hardest photons from AGN and shocks as well as the dynamics of the gas. Observations and data processing are described in §3.2. Resulting spectra and images are analyzed and presented in §3.3 and §3.4; our interpretations are detailed in §3.5. Our conclusions are summarized in §3.6. We adopt $H_0 = 70\,\mathrm{km\,s^{-1}\,Mpc^{-1}}$, $\Omega_\mathrm{m} = 0.28$, and $\Omega_\Lambda = 0.72$ throughout the paper.

3.2 Observations and Data Reduction

3.2.1 OSIRIS Data Cubes

The Keck OSIRIS observations were obtained on May 22, 2011 UT under clear, dry, and stable conditions with the LGS AO system. Two filter-scale combinations were used to observe Mrk 273: the broad K-band filter ($\lambda = 1965 - 2381$nm; hereafter Kcb) at the 100mas/pixel scale (∼80pc for Mrk 273), and a narrow H-band filter ($\lambda = 1652 - 1737$nm; hereafter Hn4) at the 35mas/pixel scale (∼28pc for Mrk 273). The tip-tilt star employed for the AO corrections had R magnitude $m_R = 16.1$ at $33''$ away from the target, well within the LGS requirement constraints. We adopted a position

angle of 30° East of North and an observing scheme of object-sky-object with 10-minute integration per frame, totalling 50-minute and 60-minute on-source times for the Kcb-100mas and Hn4-35mas observations, respectively. The A0V star 81 UMa was observed at 2 different airmasses in the Kcb filter (3 in Hn4) for telluric corrections.

The data sets were processed using the OSIRIS pipeline version 2.3 (Krabbe et al., 2004). The full Astronomical Reduction Pipeline template (ARP_SPEC) incorporates dark-frame subtraction, channel level adjustment, crosstalk removal, glitch identification, cosmic ray cleaning, spectra extraction for data cube assembly, dispersion correction, scaled sky subtraction for enhanced OH-line suppression, and telluric correction. The extracted spectra were subsequently cleaned to remove bad pixels. The cleaned frames were registered using the SW peak position and combined using the pipeline's clipped mean algorithm. The final data cubes encompass signal at each pixel in the x, y, and wavelength dimensions. The FWHM of the tip-tilt star was $0\farcs05$ in the Kcb setting and $0\farcs06$ in the Hn4 setting.

The final OSIRIS Kcb and Hn4 cubes have been flux-calibrated to the respective K'- and H-band NIRC2 flux-calibrated images (see §3.2.2) in the following manner. Spatially-coincident regions were first defined within resolution uncertainties in the OSIRIS and NIRC2 images of the matching bands. Spectroscopically, the bandwidth differences between the OSIRIS data cubes and the NIRC2 images have been taken into account while integrating over the Kcb and Hn4 wavelength ranges, respectively. Conversion factors thus determined offer a calibration to absolute fluxes in physical units that allow for line ratio computations across the two bands.

It is important to understand the point-spread function (PSF) intrinsic to our OSIRIS observations before comparing them to models. We estimate our PSF by fitting a Moffat profile to images of the tip-tilt star taken right before our galaxy observation sets. However, this is a best-case limit for the PSF, because the AO correction will degrade somewhat when moving off-axis to the galaxy. The tip-tilt star provides low-order corrections, which vary on scales of the isokinetic angle. (This angle is much larger than the isoplanatic angle, which governs how wide a field-of-view a laser guide star can correct.) At Mauna Kea, the isokinetic angle is approximately 75" (van Dam et al., 2006); this represents the tip-tilt star distance at which Strehl will be degraded by $1/e$. Because our tip-tilt star is at a separation of ~ 33" from Mrk 273, we expect our Strehl to be degraded by a factor of ~ 0.6 from the tip-tilt star profile. To model this, we convolve our tip-tilt star PSF model by a Gaussian of FWHM $0\farcs05$ to estimate our true PSF.

3.2.2 NIRC2 Images

High-resolution images were also obtained with NIRC2, using the narrow camera mode ($0\farcs01\text{pixel}^{-1}$; 8 pc pixel^{-1}) and the LGS AO System, on May 20, 2012 UT. Images were taken in the H- ($\lambda_c = 1633$ nm) and K'-($\lambda_c = 2124$ nm) bands, with exposure times of 9 minutes each. Individual frames were exposed for 30 seconds for each of two coadds; frames were dithered using the standard 'bxy3' dither pattern that avoids the noisy lower-left quadrant of the chip. The same tip-tilt star used in the OSIRIS observations was used here. We reduced our images using the CfAO Treasury Survey pipeline (Glassman et al., 2002; Melbourne et al., 2005). A sky frame was

produced by combining sky regions of each dithered frame, then subtracted from each frame. A flat field was created by normalizing the constructed sky frame. This flat field was then divided out of each frame in order to correct for varying sensitivities across the detector. The sky-subtracted-and-flattened images were subsequently aligned and median-combined to obtain the final reduced image, which were then flux-calibrated using images taken of the UKIRT Faint Standard star FS 133 (Hawarden et al., 2001). Standard star exposures were 5 seconds per frame, also dithered with the 'bxy3' script; four frames were combined for the H-band standard, three for the K'-band standard. A FWHM of $\sim 0\farcs06$ has been measured from a compact source south of the SE component in both the H- and K'-band images.

3.3 Emission Line Fitting and Error Analysis

From each of the reduced OSIRIS Kcb and Hn4 data cubes, various emission lines were mapped as follows. First we extracted the continuum with power-law fits and subtracted it from the spectrum. We measured the signal-to-noise (S/N) ratio of the lines of interest based on the line flux and root-mean-square (rms) residuals of the continuum. In order to increase the S/N ratio for regions with inadequate flux, we adopted optimal Voronoi binning for the investigation of the kinematics using the Cappellari & Copin (2003) code. This algorithm bins pixels together in a region until the emission line in that region achieves sufficient S/N, which we chose here to be 3. This allows us to explore the spatial resolution in areas with high S/N and to examine those regions with low S/N in meaningful spatial regions. For morphological / size measurements, we

measured the fluxes in each pixel without binning.

In each binned or unbinned pixel, we fit the lines with a Gaussian profile to determine the flux, velocity (shift from the systemic velocity, 11,400 km s^{-1}), and velocity dispersion (sigma of the Gaussian). In order to gauge the accuracy of the line-fit parameters, synthetic data cubes were then generated using the line parameters fitted to each pixel. The S/N ratio measured above determined the random noise level added to the synthetic cube. We then refit the line parameters of the synthetic cube 500 times with random noise added. The final uncertainty in each parameter's original measurement was obtained from the distribution of that of the resulting models. The line fits for each spatial bin are fit independently from those of bins nearby.

Errors on each fit parameter were done using a Monte Carlo approach: each spatial pixel's spectrum had random noise added to it according to its measured S/N and the lines were refit 100 times. The error on each parameter is the standard deviation of each distribution of fits.

We adopted this procedure for each line species. Different lines are treated separately from each other, but all the H_2 transitions or both the Brγ and Brδ lines are fitted simultaneously. An example of the simultaneous fit of the H_2 transitions for a typical pixel in the Kcb cube is shown in Fig. 3.2. Visual inspection ensured that the line fits were sensible with appropriate continuum levels determined within each spectral window. We noted that in many of the pixels with [Si VI] detection, the fit of a single Gaussian profile resulted in large residuals. In such cases we fit a broad and a narrow Gaussian component to these lines; this significantly improved the residuals

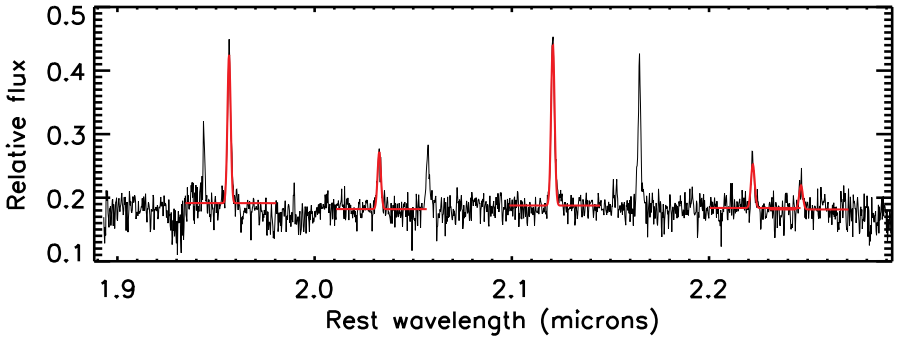

Figure 3.2: Simultaneous fitting of the different H_2 transitions for an arbitrarily-selected pixel as detected in the Kcb data cube. The black line represents the data spectrum, overplotted with model fits in red. For each spectrum, all H_2 lines are required to have the same velocity and velocity dispersion; flux is fitted separately for each line. A similar fitting routine is used for Brγ and Brδ.

(Fig. 3.3). The pixels associated with the two components appeared to be spatially segregated. The physical implication of this double-component fit is further discussed in §3.4.2.

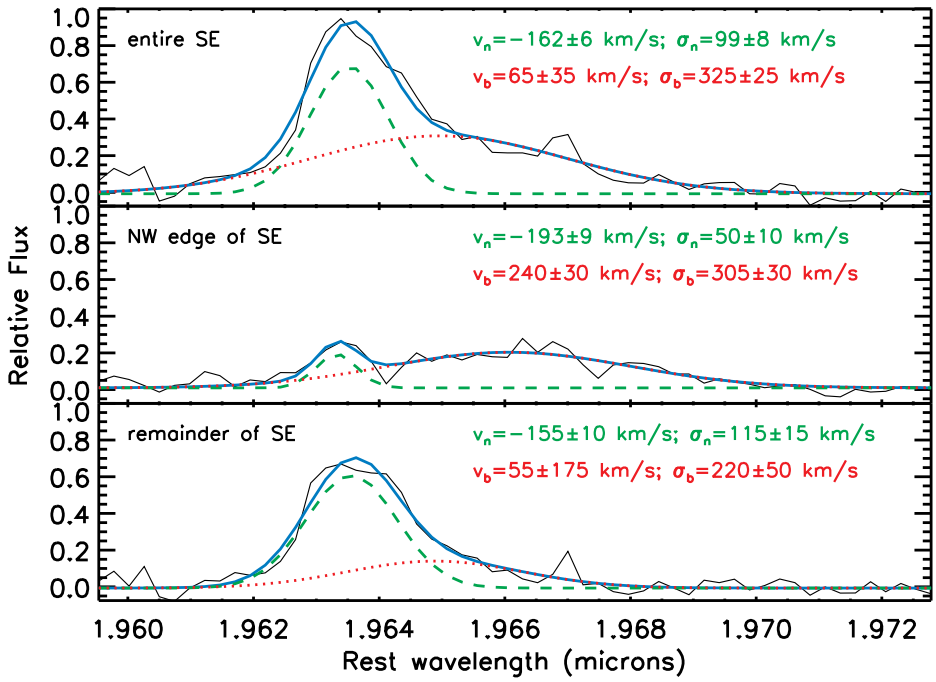

Figure 3.3: A double-Gaussian component-fit to the [Si VI] line profile in three regions of the integrated SE component. The top panel includes the entire SE component; while the middle and bottom panels split the spectrum into the northwest edge and remaining pixels. (These regions are identified in the middle panel of Fig. 3.10.) In each panel, the black line represents the data spectrum; the green dashed and red dotted lines represent the two components that contribute towards the total model fit in solid blue. In the total spectrum, the [Si VI] line clearly shows two velocity components: one with a narrow velocity dispersion and one with a broader velocity dispersion. We find by splitting the spectrum up spatially that the broader velocity component comes mainly from the northwest edge of the SE component, while the narrow portion of the line appears more heavily in the remaining section. Parameters for each fitted component are listed in each panel.

3.4 Maps and Data Cubes

3.4.1 NIRC2 Near-infrared Images

Taken at the 0.″01-per-pixel narrow-camera mode, the H- and K'-band NIRC2 images provide an unprecedented high-resolution view of the nuclear components in these wavelengths (Fig. 3.4). All three components, as denoted by the crosses corresponding to the N, SW, and SE, are distinct in both bands.

Exhibiting a disky morphology different from that seen in the optical bands, the N component is both extended and clumpy in the near-infrared. We used GALFIT (Peng et al., 2002, 2010) to quantitatively characterize its morphology and find that the underlying structure is best fit by a central point source (which we call N1) plus a Sérsic profile of index $n = 1.63$ and effective radius $r_{\rm eff} = 0.''69 \pm 0.01$, or 546±8 pc, in the H-band continuum. In order to avoid the dusty region between the nuclei, we performed the GALFIT analysis on the eastern half of the disk only (see Fig. 3.5). The residual map shows some underlying substructure in the disk, but otherwise a Sérsic disk plus central point source model (Fig. 3.5 top) were a better fit for the N component than one without the central point source (Fig. 3.5 bottom). In Fig. 3.4, approximately 0.″2 to the northeast of N1 is N2, which looks like a faint, compact clump. It is brighter in the K' band than it is in the H; the difference may be due to dust extinction. It appears distinct and could plausibly be the site of a stellar cluster. It closely coincides with the N2 as designated by Carilli & Taylor (2000), at the location of a hypothesized clump of supernovae. To the southeast of N1 at a distance of $\sim 0.''15$ is N3, which is extended and elongated in the E-W direction. It may be diffuse emission associated

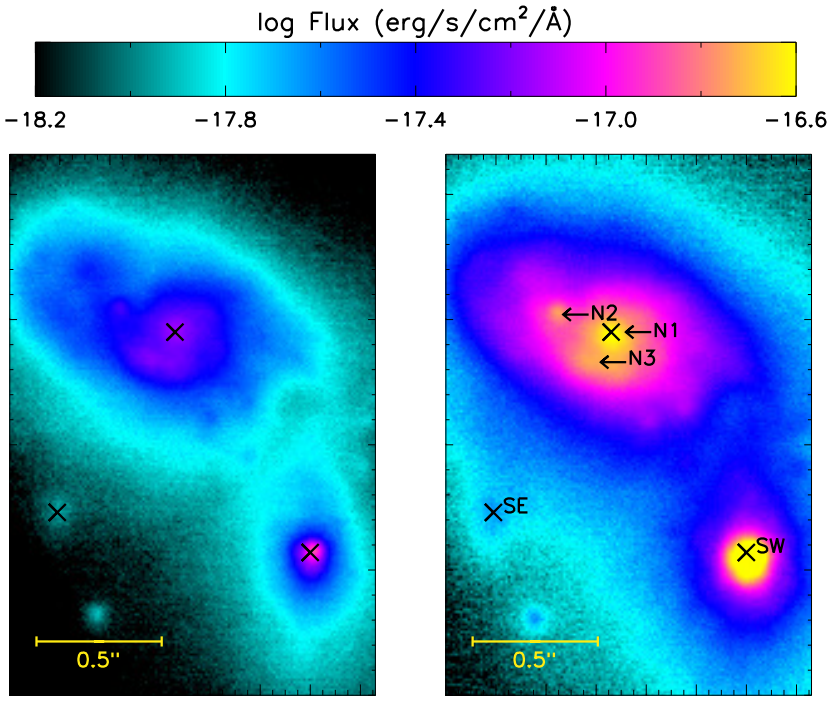

Figure 3.4: Keck NIRC2 H- (left) and K'-band (right) images taken with the narrow camera ($0\farcs01$ pixel scale). The two images are displayed in logarithmic scale in units of erg/s/cm^2/Å with north pointing up, east to the left. These images reveal clumpy structure and wispy gas in the nuclear regions of Mrk 273. Crosses denote the three components from Fig. 3.1, and the arrows point to three different clumps resolved in the N component. See text for a detailed discussion of each.

with N1 given its proximity, or it may be a separate clump. There is a larger difference in the brightness of N1 and N3 in the K'-band relative to that in the H-band, indicating that N1 is redder than N3.

Lying $\sim 1\farcs0$, or 800pc, to the southwest from N1, the SW component is also resolved at these scales with a north-south extension ($r_{\rm eff} = 71 \pm 8$ pc in the H-band and 40$\pm$8 pc in the K'-band). The high-resolution $0\farcs01$/pixel data further constrain the size of this compact emission. Detected more notably in the H-band, the north-south extended feature appears asymmetric and elongated towards the south. The northern extension resembles a tidally-disrupted feature, which suggests that it is material that has not yet settled during the course of the merger. The SW source appears the reddest in the frame, most likely due to dust. This extinction obscures it entirely in the *HST* B-band image (Fig. 3.1).

Two distinct sources can be seen in the southeast region relative to the N disk. The southernmost one is compact and appears to be a star cluster. The one denoted with a cross (see Fig. 3.4) is more diffuse and extended; it marks the site of the SE source seen in radio images (Carilli & Taylor, 2000; Bondi et al., 2005). Its spatial extent is larger than the compact source to the south from which the PSF is confirmed. This suggests that the SE component may not simply be a stellar cluster as was suggested by the NICMOS images (Scoville et al., 2000). Given its proximity to the N component and the morphology of the low surface-brightness feature between it and the N component, the SE source may be associated with the N component.

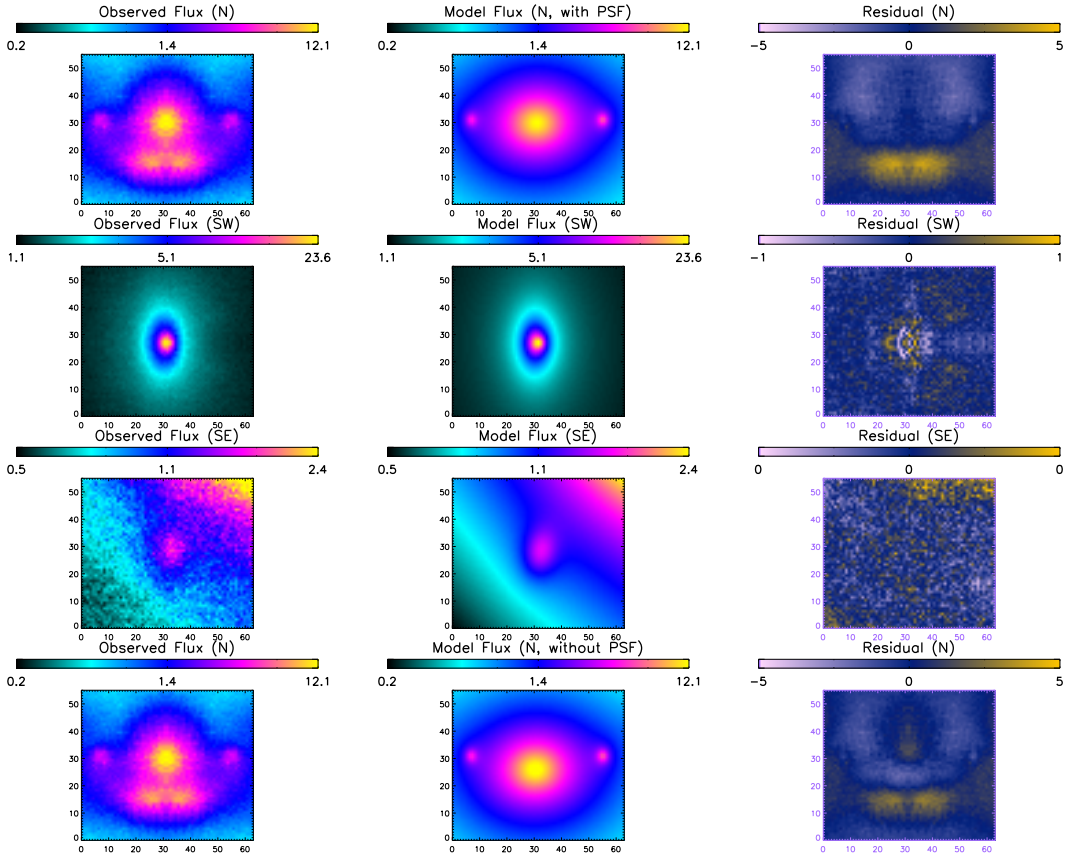

Figure 3.5: Example of fitting results of GALFIT: here, the N (top row), SW (second row), SE (third row), and N (without central PSF in model; bottom row) components in the NIRC2 H-band image have been fitted with a Sérsic, Sérsic, Gaussian, and Sérsic profile, respectively. The leftmost column shows the input data that were fed into GALFIT; the middle column demonstrates the best-fit model parameters; the rightmost column indicates the residual maps. In the case of the N and SW components, we performed GALFIT analysis on a mirrored version of the eastern and southern halves, respectively, in order to avoid the dusty region between the nuclei.

3.4.2 K Broadband Integrated OSIRIS Spectra

In the K broadband spectra ($0\farcs1$-per-pixel resolution), only two spatially-segregated components appear in the continuum of Kcb: the N extended emission and the SW compact source. The SE diffuse clump is very weak in the integrated image. Fig. 3.6 shows the integrated spectra of the N, SW, and SE components, respectively. These spectra exhibit very different features. The SW spectrum is dominated by the continuum and has strong [Si VI] 1.964 μm and H_2 emission; other emission lines are present but weak. The N spectrum features multiple extremely strong H_2 transitions along with Brγ and He I. The SE component is weak in the continuum but exhibits emission in the H_2, [Si VI], and Brackett lines as well.

Line parameters of the various regions such as the effective radii for the fitted Sérsic component or FWHM of the fitted Gaussian component, axis ratios, integrated flux ratios, mean velocities, and velocity dispersions are listed in Table 3.1. The integral-field capability of OSIRIS allows the examination of the spatial distributions and kinematics of these emission lines individually; we present these results in the following section.

H_2

Five vibrational transitions of molecular hydrogen lie within the Kcb coverage of OSIRIS: $1-0$ S(3) [$\lambda_{\rm rest} = 1.9576\mu$m], $1-0$ S(2) [$\lambda_{\rm rest} = 2.0338\mu$m], $1-0$ S(1) [$\lambda_{\rm rest} = 2.1218\mu$m], $1-0$ S(0) [$\lambda_{\rm rest} = 2.2235\mu$m], and $2-1$ S(1) [$\lambda_{\rm rest} = 2.2477\mu$m] (hereafter H_{2a}, H_{2b}, H_{2c}, H_{2d}, and H_{2e}, respectively). These vibrationally-excited emission lines

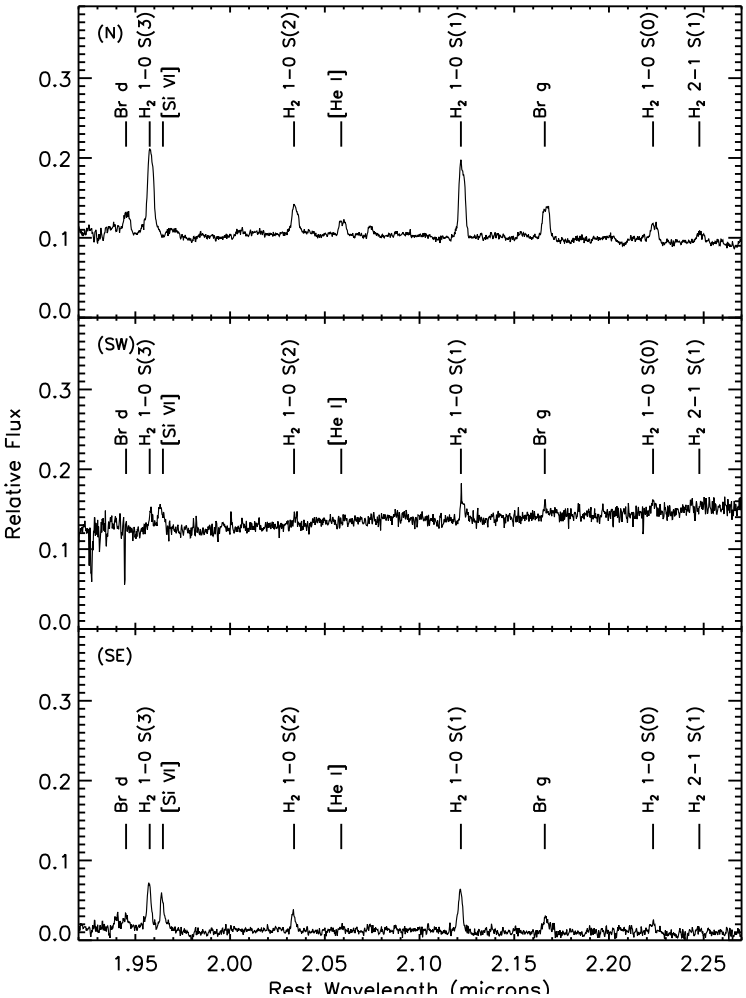

Figure 3.6: OSIRIS integrated spectra of the N component (top), the SW component (middle), and the SE component (bottom) from 50-minutes of on-source exposure, taken in K-band with the $0\farcs1$/pixel lenslet. Lines of interest are labeled. The telluric-corrected continuum in the SW still shows a steeper gradient than in the N and SE, indicating the presence of hot dust. The SE spectrum shows comparatively little continuum emission but clear evidence of line emission. Most emission lines in the SW are relatively weak. On the other hand, [Si VI] appears strongly in the SW and the SE but not in the N component.

Table 3.1: Morphological Parameters of the Different Regions in Mrk273

Region	Line	$r_{\rm eff}$ (arcsec)	$r_{\rm eff}$ (pc)	Axis Ratio	Flux Ratio	$\bar{v}$ (km/s)	σ (km/s)
N	H_{2c}	0.27±0.01	214±8	0.75±0.01	1.15±0.01	6±2	225±2
	Brγ	0.30±0.06	238±48	0.75±0.01	0.48±0.02	21±7	228±7
	He I	0.27±0.01	214±8	0.75±0.01	0.22±0.02	45±15	230±20
	[Si VI]	..	..	..	..	..	..
	[Fe II]	0.40±0.04	317±32	0.78±0.01	0.13±0.01	6±4	213±9
	H-band continuum	0.69±0.01	546±8	0.74±0.01	..	..	..
	K'-band continuum	0.80±0.01	634±8	0.88±0.01	..	..	..
SW	H_{2c}	..	..	..	0.29±0.03	50±15	180±15
	Brγ	..	..	..	..	..	..
	He I	..	..	..	..	..	..
	[Si VI]	0.14±0.02*	107±16	0.08±0.2	0.37±0.06	-290±35	220±50
	[Fe II]	..	..	..	0.04±0.04	7±30	155±45
	H-band continuum	0.09±0.01	71±8	0.41±0.01	..	..	..
	K'-band continuum	0.05±0.01	40±8	0.47±0.01	..	..	..
SE	H_{2c}	0.14±0.03*	111±24	0.56±0.05	0.59±0.02	-117±4	173±4
	Brγ	0.07±0.04*	55±28	0.42±0.05	0.30±0.03	45±20	240±20
	He I	..	..	..	..	..	..
	[Si VI]	0.16±0.02*	123±16	0.66±0.09	0.29±0.03	-125±20	150±15
	[Fe II]	0.06±0.01*	48±8	0.23±0.05	0.06±0.04	-10±40	205±60
	H-band continuum	0.6±0.01*	48±8	0.61±0.04	..	..	..
	K'-band continuum	0.13±0.01*	99±8	0.51±0.01	..	..	..
Bridge	H_{2c}	0.35±0.03*	277±24	0.68±0.04	0.73±0.02	-125±4	175±5
	Brγ	0.38±0.14*	297±107	0.16±0.06	..	..	..
	He I	..	..	..	..	..	..
	[Si VI]	0.13±0.03*	103±24	0.17±0.06	..	..	..
	[Fe II]	..	..	..	0.10±0.01	-110±15	240±20
	H-band continuum	..	..	..	..	..	..
	K'-band continuum	..	..	..	..	..	..

[1] $r_{\rm eff}$ is the effective radius for the fitted Sérsic component; in the * cases, this is the $\frac{\rm FWHM}{2}$ of the fitted Gaussian component.
[2] .. indicates weak or no detection.

trace the warm molecular gas, and result from a mixture of thermal and nonthermal components, where the excitation mechanisms may involve shock heating, UV photoioniziation by O and B stars, or X-ray ionization (Mouri, 1994). The intensity ratios among these lines can be used to distinguish between the thermal and non-thermal excitation mechanisms due to the difference in their efficiencies in populating the various vibrational levels.

Shock-excited H_2 emission has been observed in many galaxies; a notable object among these observations is the prototypical late-stage merger NGC 6240 with dual AGN at $L_{\rm IR} = 10^{11.93} L_\odot$, for which the thermal H_2 temperature was determined to be 2000 K (Mouri, 1994). Draine & Woods (1990) further proposed that most of the H_2 line emission in NGC 6240 is attributed to X-ray irradiation from either supernova

explosions or high-velocity shock waves associated with the merger. Like NGC 6240, Mrk 273 displays prominent emission in H_{2c}. Fig. 3.7 shows the unbinned flux, Voronoi-binned velocity and velocity dispersion maps of H_{2c} along with the distribution of the K band continuum in contours. The H_{2c} flux is extended in the N component. In addition, the flux bridges towards the SE component, which is the site of radio continuum emission ($\sim 1''$ southeast of the N peak).

A velocity gradient typical of an inclined rotating disk can be seen in the velocity map of H_{2c} (middle panel in Fig. 3.7). The range of the velocity is [-206, 220] km s^{-1}; the rotational axis of the rotating disk has a PA of 330°. The velocity map spans a larger region beyond the extent of the N disk. Of particular note are the negative velocities extending towards the SE component along the bridge in the emission. Along the major axis of the disk, we measure a velocity dispersion of $\sim$ 140 km s^{-1}; along the minor axis and towards the SE, this increases to $\sim$ 200 km s^{-1} (right panel in Fig. 3.7). This lends evidence to the presence of biconical collimated turbulent outflows from the center of the N source; the significance of this outflow is further discussed in §3.5.

Excitation Mechanisms of H_2

Multiple H_2 transitions are prominent in the Kcb data, particularly within the N disk. Using equations from Reunanen et al. (2002) and Rodríguez-Ardila et al. (2004, 2005) that make use of the ratios among the various H_2 transitions (e.g. H_{2e}/H_{2c} and H_{2b}/H_{2d}), we can gain insight into the temperature conditions within Mrk 273's nuclei. The rotational temperature does not vary significantly across the nuclear regions. Integrating over the regions defined by the different components, we derive for the

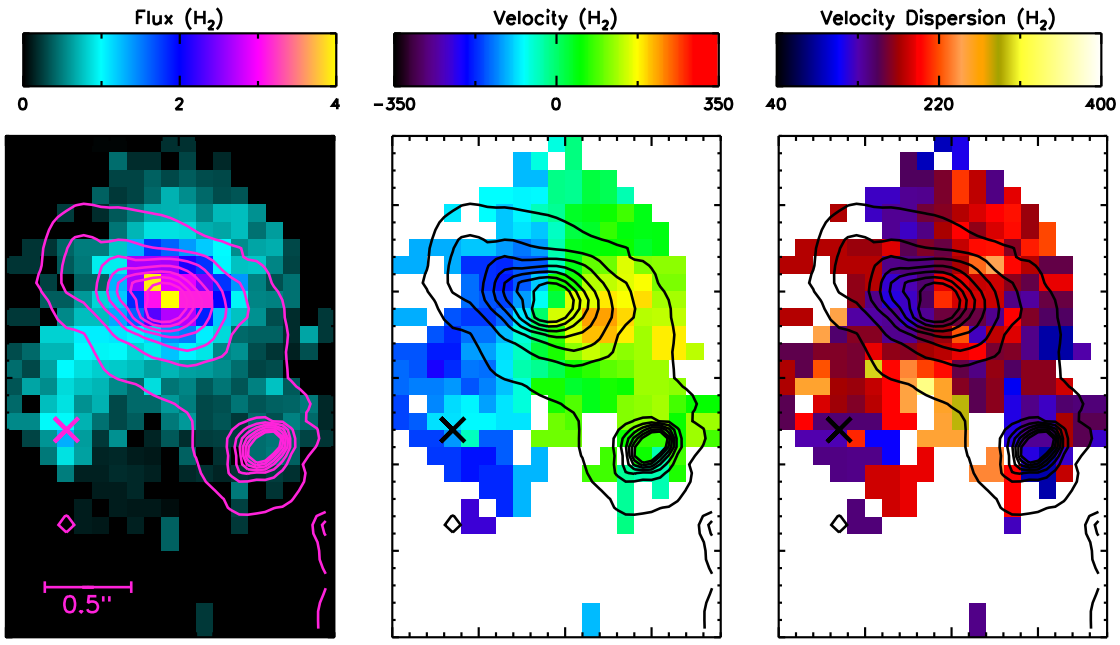

Figure 3.7: *(Left to right)* The moments 0, 1, and 2 maps corresponding to the unbinned flux, binned velocity, and binned velocity dispersion maps of H_{2c} in the central region of Mrk 273. Pixels with low signal-to-noise ratio have been removed from the kinematics maps. Contour levels represent the continuum flux, with cross marking the SE region. Bar denotes $0\farcs5$; N points up. A bridge in flux connects the N and SE components. The bridge shows negative velocities and increased velocity dispersions. The velocity map also reveals strong rotation in the N component; here, velocity dispersion increases in conical regions along the minor axis, possibly revealing biconical collimated outflows from the center of the disk.

Table 3.2: H_2 Line Ratios of Different Spatial Regions in Mrk273

Line Ratios	N	SW	SE	Bridge	Total (Mean)	Total (Median)
H_{2a}/H_{2c}	1.19±0.02	0.31±0.07	0.55±0.03	0.75±0.04	0.70	0.75
H_{2b}/H_{2c}	0.45±0.01	0.11±0.05	0.27±0.03	0.26±0.03	0.27	0.27
H_{2d}/H_{2c}	0.29±0.01	0.15±0.05	0.17±0.02	0.20±0.03	0.20	0.20
H_{2e}/H_{2c}	0.18±0.45	0.04±0.12	...	...	0.11	0.18
$T_{\rm vib}$ (K)	2590±80	2535±740	2240±230	1925±305	2325	2535
$T_{\rm rot}$ (K)	1605±115	740±150	1645±355	1230±205	1305	1605

N disk a vibrational temperature $T_{\rm vib} \simeq 2590 \pm 80$K and a rotational temperature $T_{\rm rot} \simeq 1605 \pm 115$K. The measured $T_{\rm vib}$ is consistent with that measured for a sample of Seyferts ($T_{\rm vib} \lesssim 2600$K) from Reunanen et al. (2002). In addition, the fact that the values for $T_{\rm vib}$ and $T_{\rm rot}$ differ appreciably suggests that the thermal excitation may be due to fluorescence (Rodríguez-Ardila et al., 2004). The computed H_2 line ratios along with derived temperatures for the various components are listed in Table 3.2.

H_2 gas in galaxies can be excited by a number of mechanisms in the interstellar medium: UV fluorescence, shocks, and X-ray heating (Shull & Beckwith, 1982, and others). A diagnostic involving the ratios of different H_2 transitions can be used to distinguish among the various means of exciting the gas (Rodríguez-Ardila et al., 2004). The H_{2e}/H_{2c} and H_{2a}/H_{2c} ratios in these nuclear regions are consistent with slow shocks ($v_s \sim 10 - 14$ km s^{-1}) being driven into very dense gas ($n = 10^5$ cm^{-3}; Shull & Hollenbach, 1978).

Atomic Hydrogen and Helium

After the various transitions of H_2, the Brγ line [$\lambda_{\rm rest} = 2.166\mu$m] and the He I line [$\lambda_{\rm rest} = 2.059\mu$m] are the next most prominent emission lines in the N spectrum.

Brγ is an indicator of the ionizing radiation field and stellar activity, and has been detected in many Seyfert galaxies (e.g. Riffel et al., 2006). The ionization energy of atomic helium is 24.6 eV; therefore, He I line emission is expected to originate from regions with the most massive and youngest stars (Böker et al., 2008).

Fig. 3.8 and Fig. 3.9 show the flux, velocity, and velocity dispersion of the Brγ and He I lines, respectively. The Brγ flux, and similarly the He I flux, is detected in the N disk and appears clumpy around the center; this may be due to clumpy star formation in the circumnuclear regions. The depression in flux of these atomic gases at the nucleus may suggest heavy obscuration by dust or ionization of the gas by a strong source like an AGN. The bulk of the Brγ gas coincides with the N continuum emission. There is very little Brγ emission at the SW component, but there is Brγ emission extending towards the SE source, albeit much weaker than in the H_2 lines. There is also faint He I emission in the vicinity of the SE source.

Brγ and He I also display similar kinematics. The velocity structure of a strongly rotating disk similar to that of H_2 is found for Brγ and He I. The centers of the rotating gas disks coincide with the peak of the continuum flux. The velocity dispersion at the disk is $\sim$100 km s^{-1} but increases to $\sim$ 170 km s^{-1} at the center. We see no evidence of a broad line region.

[Si vi]

[Si VI] [$\lambda_{\rm rest}$ = 1.964μm], a near-infrared tracer of AGN activity due to its high excitation potential (= 167 eV; Rodríguez-Ardila et al., 2004), has a very different spatial distribution than the other species, as seen in Fig. 3.10. A fit to the line in the

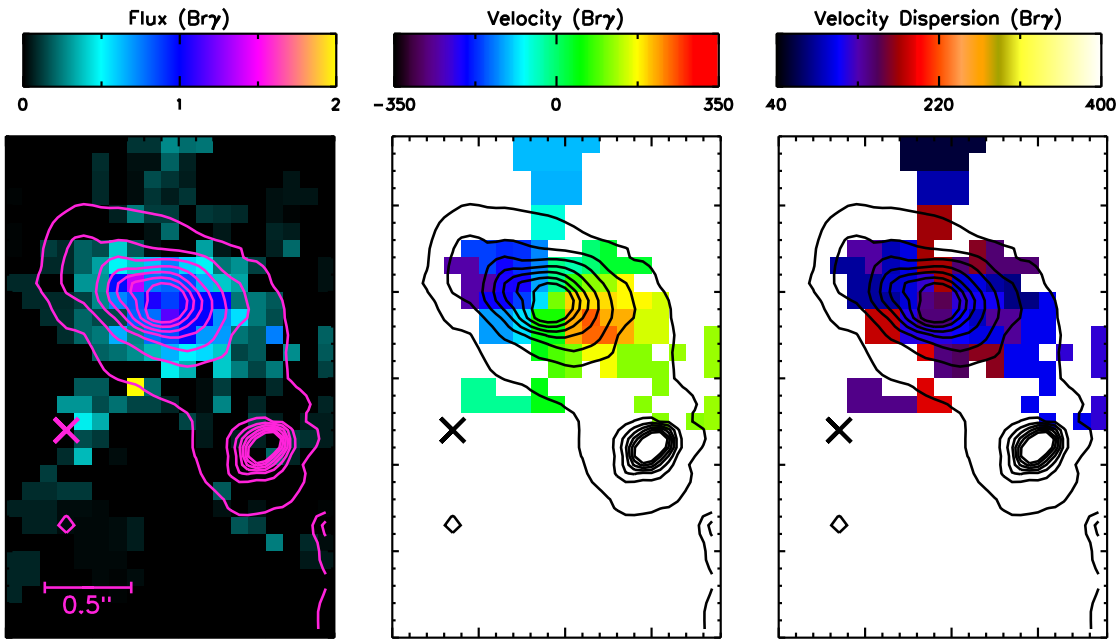

Figure 3.8: Figure similar to Fig. 3.7, but for Brγ (N points up). Brγ traces the same rotation in the N component as H_{2c}, but is much weaker along the bridge to the SE component.

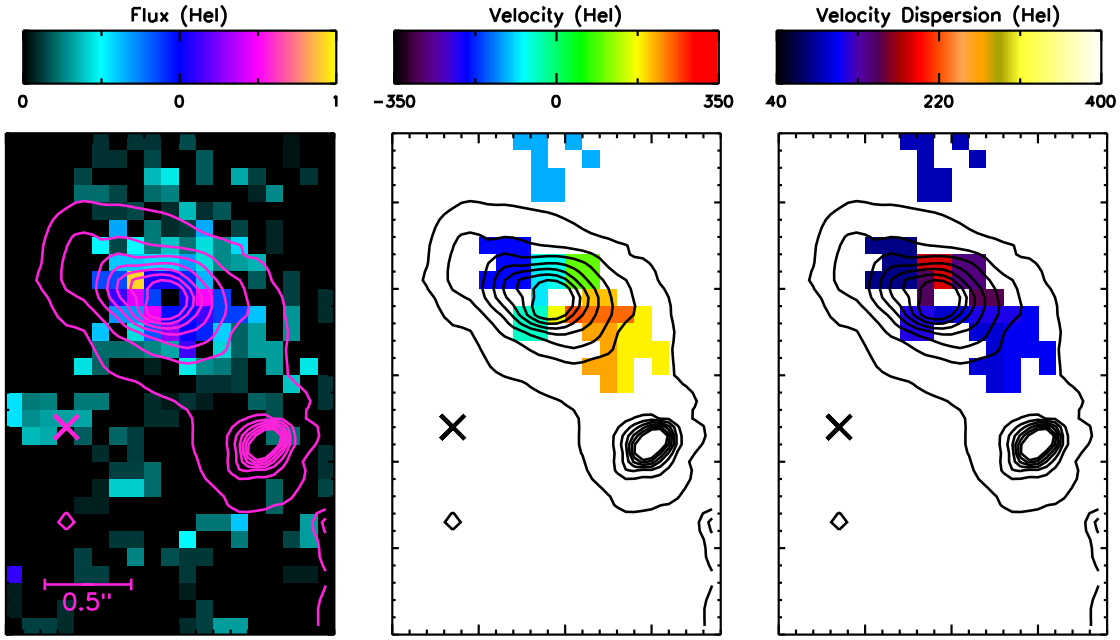

Figure 3.9: Figure similar to Fig. 3.7, but for He I (N points up). He I traces the same rotation in the N component as H_{2c} and Brγ, but is much weaker along the bridge to the SE component. As with Brγ, He I flux does not peak at the center of the N component, perhaps due to extinction or a change in the ionizing radiation.

SE region with a Gaussian profile returns poor residuals. A visual inspection prompted us to add a second velocity component which significantly improved the fit (Fig. 3.3). Two kinematically-segregated components in this region are traced by [Si VI]: a narrow component with velocity $v_n = -162 \pm 6$ km s^{-1} and velocity dispersion $\sigma_n = 99 \pm 8$ km s^{-1}; and a broad component with $v_b = 65 \pm 35$ km s^{-1} and $\sigma_b = 325 \pm 25$ km s^{-1}.

The bulk of the [Si VI] emission is found not in the N disk, likely due to heavy extinction, but at the bridge and the SE component. In the unbinned flux map (Fig. 3.10), it extends N-S and spans a $0\farcs189 \times 0\farcs163$ (150 pc $\times$ 130 pc) region. Its velocity and velocity dispersion are highest near the bridge, though its relatively low S/N ratio limits the precision with which the location of the emission can be determined. [Si VI] is also strongly detected at the SW component, the site of the hard X-ray AGN (Iwasawa et al., 2011b). The peak position of the [Si VI] flux roughly coincides with that of the continuum, with $v = -290 \pm 30$km s^{-1} and $\sigma = 222 \pm 50$km s^{-1}.

3.4.3 H Band Integrated Spectra

At a scale of $0\farcs035$ per pixel, the Hn4 continuum emission maps the resolved, clumpy N disk and compact SW component. Fig. 3.11 shows the integrated spectra of the N, SW, and SE components, respectively, highlighting the [Fe II] line found in all three regions. The [Fe II] line is typically broad ($\sigma \sim 200$ km s^{-1}) and prominent in the N and SE components, and dominated by the continuum in the SW. The SE component is weak in the continuum. Line parameters of the regions for the [Fe II] line emission can be found in Table 3.1.

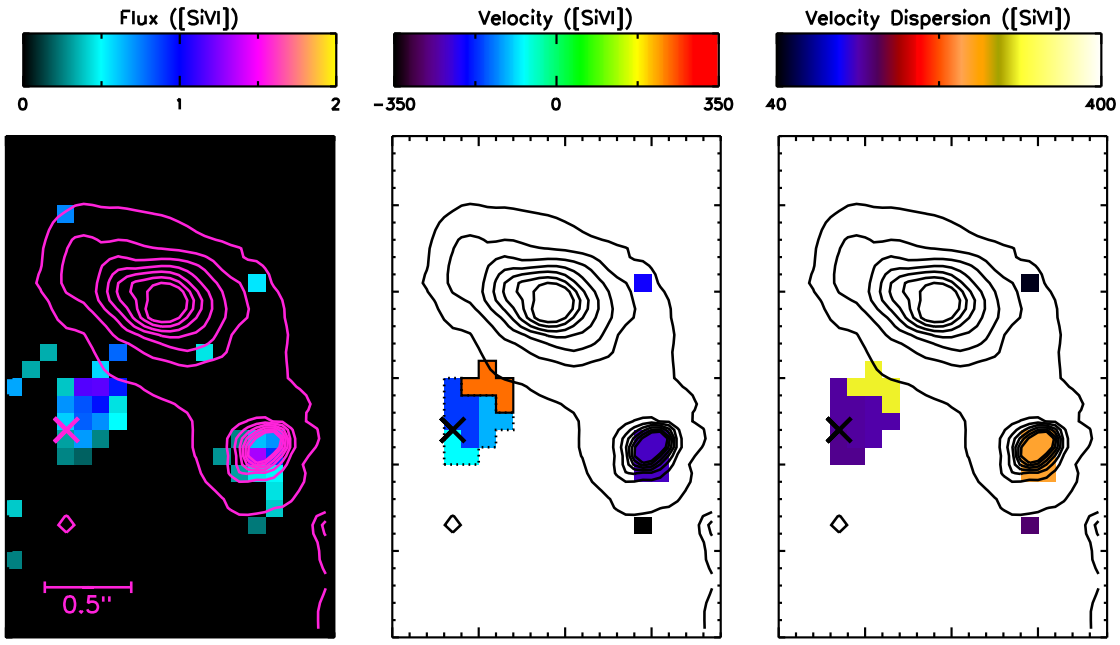

Figure 3.10: Figure similar to Fig. 3.7, but for [Si VI] (N points up). [Si VI] is undetected in the N component, but appears strongly in the SE and SW components. In the SW, [Si VI] is broad, but see Fig. 3.3 for a detailed analysis of the SE [Si VI] spectrum, which shows two kinematic components. The two kinematically and spatially segregated regions in Fig. 3.3 are marked in the center panel: the northwest edge is outlined in solid black, the remaining SE pixels are outlined in dotted black line. The northwest edge shows broader kinematics than the dotted region.

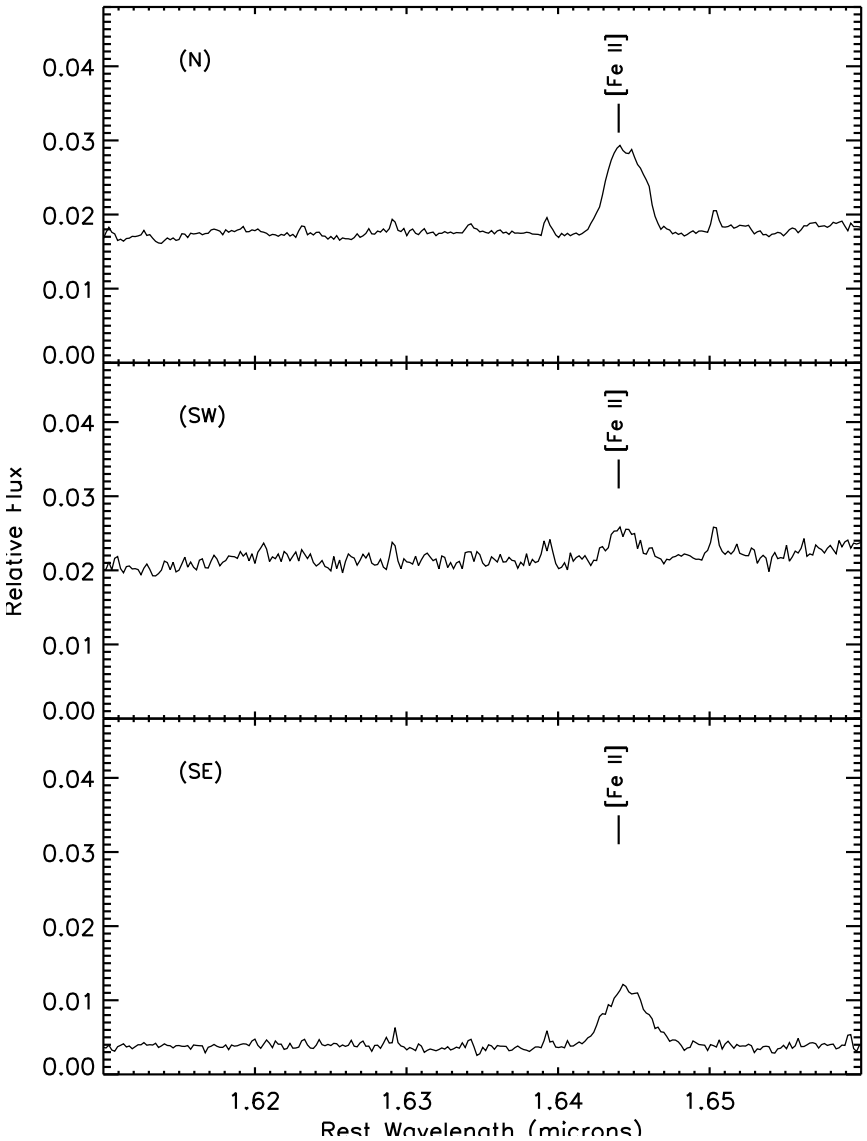

Figure 3.11: OSIRIS integrated spectra of the N (top), SW (middle), and SE components (bottom) from 60-minutes of on-source exposure, taken in H-band with the 0.″035-scale lenslet. [Fe II] is much stronger in the N and SE components than in the SW component.

[Fe ii] Emission

In the Hn4 band, the [Fe II] line at [$\lambda_{\rm rest} = 1.644\mu$m] shows strong emission in the center of Mrk 273. Because Fe is strongly depleted in the interstellar medium, gas-phase [Fe II] emission (with ionization potential of 16.2 eV; Mouri et al., 1993) in galaxies has been used as a sensitive indicator of shocks (Graham et al., 1987). The potential origins for the [Fe II] emission include regions of partially ionized gas within supernova remnants in starburst nuclei and within narrow-line regions in AGN (Mouri et al., 1993). The contribution from photodissociation regions near O and B stars is negligible. Extracting slices associated with the [Fe II] line from the Hn4 data cube, we present the flux, velocity, and velocity dispersion maps in Fig. 3.12 with continuum contours for comparison. Like the continuum, the line data are resolved into multiple clumps in the N disk, but the emission is relatively weak at the N1 site, dominant at N2, and detected at N3. The differences in the line-to-continuum flux ratios between N1 and the other clumps (N1: 0.016, N2: 0.022, N3: 0.022) may suggest that they have different origins (see §3.5). The [Fe II] line flux is negligible in the SW nucleus but very bright in the SE, with a slightly N-S elongated morphology. The N disk contains more total integrated [Fe II] flux, but the SE peak dominates the surface brightness in the entire inner kpc region. The velocity structure of the [Fe II] line also indicates strong rotation ($\pm$240 km s^{-1} centered on the systemic velocity), with high velocity dispersion near the center of the N disk and the strongest velocity dispersion at the SE component.

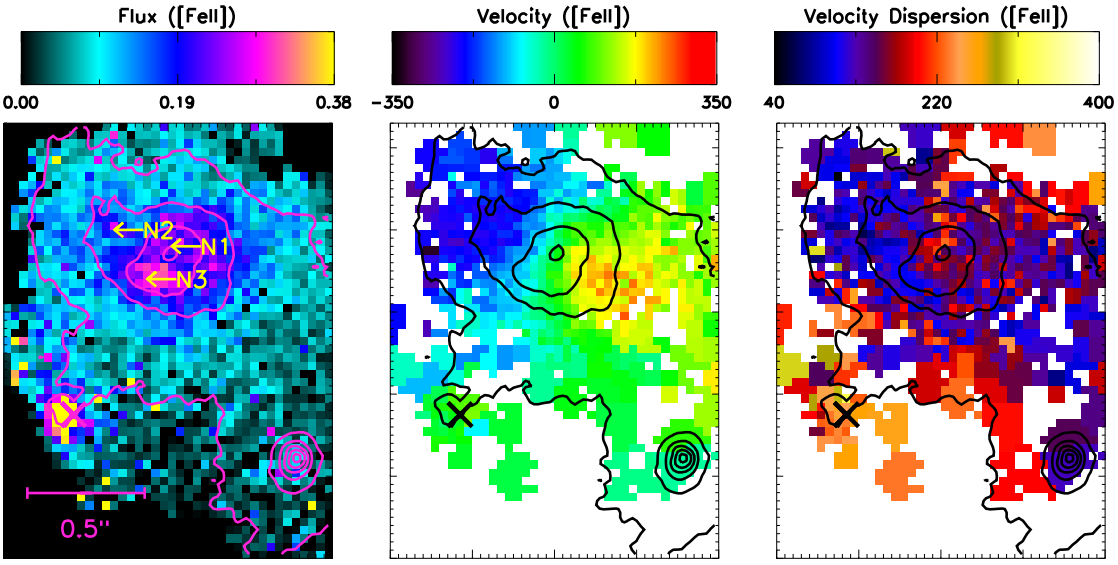

Figure 3.12: Figure similar to Fig. 3.7 but for [Fe II] ($\lambda_{\rm rest} = 1.644\mu m$) from the Hn4 band (N points up). The [Fe II] velocity map shows strong rotation about the N component, with a small increase in velocity dispersion at the center. [Fe II] flux is clumpy in the N component, resolving N1, N2, and N3 due to high resolution as in the NIRC2 images (Fig. 3.4). However, the fact that N1 is weaker than N2 and N3 could be due to extinction or to differing ionizing radiation fields. The strongest and broadest [Fe II] appears in the SE component.

3.5 Discussion

The mechanisms that power the enormous luminosities in Mrk 273 are likely to be associated with the three nuclear components situated within the dusty core. Here we discuss the nature of these regions.

3.5.1 The Northern Disk

The nature of the N component has been controversial due to different interpretations of the multiwavelength data: clustered radio supernovae (Smith et al., 1998), Seyfert 2 AGN (Xia et al., 2002), and a starburst with the possibility of an additional Compton-thick AGN from excess $6-7$ keV emission that might be associated with a high equivalent-width Fe K emission (Iwasawa et al., 2011b). The Fe K line as indicative of a heavily obscured AGN is also present in a dual-AGN LIRG merger Mrk 266, where the LINER nucleus exibits enhanced shock-excited H_2 emission and diminished coronal line compared to the Seyfert nucleus (Mazzarella et al., 2012). Here, our OSIRIS data cube provides evidence of a strongly rotating gas disk through the distribution and kinematics of the near-infrared emission line gas. The strong H_{2c} flux suggests localized shocks and fits well with the models of clustered radio supernovae (Smith et al., 1998), lending support to their hypothesis that a starburst provides much of the power. Carilli & Taylor (2000) have resolved individual compact sources that may be supernova remnants; they suggest that the diffuse emission may be a result of excitation from the remnants. Our OSIRIS data resolve the individual clumps and provide spatial information on the physical conditions of the ionizing source in the N disk. We consider the evidence in

this section.

Strong Rotation in Emission Lines

The velocity maps for the emission lines (H_2, Brγ, He I, and [Fe II]) detected in the N disk show structure consistent with a strongly rotating disk. The deprojected rotational velocity is $\sim \pm 240$ km s^{-1}, and its structure is indicative of Keplerian rotation about a large mass (see §3.5.1). We suggest that the rotating disk in the N is the remnant nucleus of a progenitor galaxy in this merger system, with its gas rotating about a central supermassive black hole or a very massive central star cluster, or a nuclear disk formed from new gas inflow during the merger. In the next section we use dynamical modeling to determine the enclosed mass.

Black Hole Mass

From the strong rotation inferred from the emission lines, we measure the kinematics to understand the underlying mass profile. Though rotation in the N disk is seen in every emission line, we focus on the [Fe II] kinematics because these data have significantly higher spatial resolution, by a factor of three, compared to the other emission lines. To measure the dynamical mass of the central source, it is crucial that we resolve within the black hole's sphere of influence. The radius of the sphere of influence is given by

$$r_{\rm BH} = \frac{GM_{\rm BH}}{\sigma^2}$$

where G is the Gravitational constant, $M_{\rm BH}$ is the mass of the black hole, and σ is the velocity dispersion. We assume a conservative estimate for the mass of the black hole to be $M_{\rm BH} \sim 10^9 M_\odot$, given that Klöckner & Baan (2004) had measured a mass of $1.39 \pm 0.16 \times 10^9 M_\odot$ from radio interferometry observations of OH masers.

The circumnuclear velocity dispersion we measure from the [Fe II] line is ∼215 km s^{-1}. Therefore, the radius of the sphere of influence is at least $r_{\rm BH} \geq 95$ pc. Since the angular resolution achieved by the [Fe II] line maps is $0\farcs035$, corresponding to ~ 28 pc/pixel spatial resolution, we do resolve within the sphere of influence of the central point source and can measure the mass dynamically via [Fe II] line kinematics.

We follow the Keplerian disk fitting method outlined in Chapter 2 to compare the measured kinematics to those of simple models. First, we create velocity maps using $v = \sqrt{GM/r}$ and assuming a central point mass; we also solve for the inclination of the disk and the position of the central point mass. We use the Levenberg-Marquardt least squares fitting routine MPFITFUN (Markwardt, 2009; Moré, 1978) to select the parameters that best fit the [Fe II] velocity map. We fix the central mass position for generalization to a more complete mass profile. In our second set of models, we estimate the stellar mass profile by fitting a disk to the continuum emission. We subtract off the central point-source from the center of the continuum light before fitting. We fit this using the simple radially-varying surface density profile $\Sigma(r) = \Sigma_0 r^{-\gamma}$, making the mass in a ring $2\pi\Sigma_0 r^{1-\gamma} dr$. We fit the inclination, γ, and Σ_0, and find that the fitted inclination is consistent with the inclination from the first dynamical model (55°); we fit a γ of 1.0. In our final set of models we adopt $v = \sqrt{GM(r)/r}$, with the mass

profile containing a single point mass plus a radially-varying disk mass of surface density $\Sigma(r) = \Sigma_0\, r^{-\gamma}$. We fix the inclination and the exponent γ from our previous two models, and vary only the point mass and the disk mass density normalization Σ_0. (Note that we allow the last to vary in order to avoid making assumptions about mass-to-light ratio. On such small scales, dark matter should be negligible, but estimating a M/L ratio for a stellar population of unknown age with unknown extinctions would introduce more uncertainties than allowing it to be a free parameter.) In each set of models, we convolve our light-weighted model with the PSF (see discussion in §3.2) before comparing it to our observations.

Errors on best-fit model parameters were estimated by using a Monte Carlo approach, varying the kinematics with random noise based on the errors determined in §3.3 and refitting the model 100 times. The final error on black hole mass is the standard deviation of the distribution of fitted masses.

A comparison between our velocity map and the final model is found in Fig. 3.13. We find that the best-fit central point mass is $1.04^{+0.10}_{-0.08}\times10^9 M_\odot$, and conclude that the N disk houses a supermassive black hole. This mass is consistent with that measured from radio interferometry of an OH maser, $1.39\pm0.16\times10^9 M_\odot$ (Klöckner & Baan, 2004), and is similar to that of the southern black hole of NGC 6240 ($8.7 \times 10^8 M_\odot < M_{BH} < 2.0 \times 10^9 M_\odot$), another late-stage galaxy merger (see Chapter 2 and Medling et al., 2011). From the kinematics, we cannot determine whether Mrk 273's N disk hosts a quiescent black hole or a Compton-thick AGN as suggested by Iwasawa et al. (2011b). In either case, the presence of the disk and supermassive black hole confirms

that this is the remnant nucleus of one progenitor galaxy.

Though we have shown from our GALFIT analysis that the infrared continuum light profile is best fit with a model of Sérsic disk along with a central point source, we note the possibility that the central mass may be a massive star cluster instead of a supermassive black hole. Given that massive star clusters found in NGC 6240 have photometric masses of $7 \times 10^5 - 4 \times 10^7 M_\odot$ (Pollack et al., 2007) and those found in the Milky Way have upper mass limits of $10^8 M_\odot$ (Murray, 2009), $\geq$10-30 of the most massive of these clusters must reside in the central $\sim$ 60 pc region to feature the observed kinematics. The two most massive clusters described in Murray (2009) have masses of $10^8 M_\odot$ and measured radii of $\sim$ 100 pc, suggesting that a cluster 10 times as massive and in a much smaller volume would be improbable. We calculate the dynamical free-fall time of such a star cluster as

$$t_{ff} = \frac{\pi}{2} \frac{R^{1.5}}{\sqrt{2GM}}$$

Taking $R = 60pc$, $M = 10^9 M_\odot$, and $G = 4.48 \times 10^{-30} pc^3 M_\odot^{-1} s^{-2}$, the resulting free-fall time is approximately 2.5×10^5 years. Such a short free-fall time indicates that such a star cluster is dynamically unstable, and we thus conclude that the central mass must be a supermassive black hole.

Spatial Distribution of Line Emission

Brγ, which traces ionized gas, and He I, which traces neutral gas, both appear in the N disk. These species both have moderately low velocity dispersion in the disk, and show no sign of being associated with a broad line region. The coronal line [Si VI] is

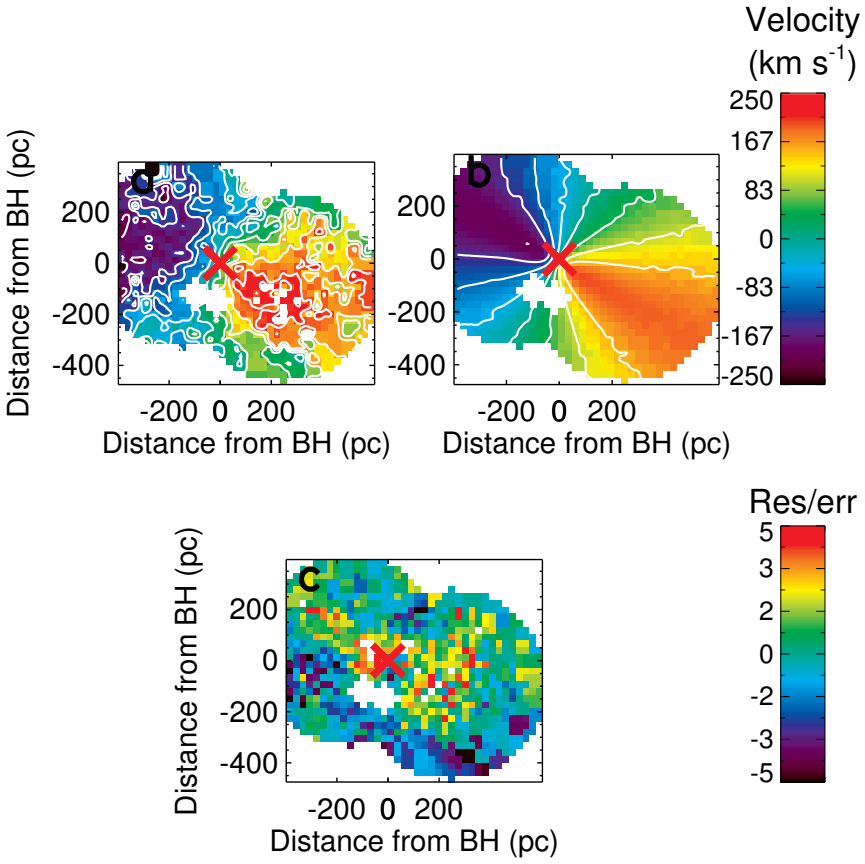

Figure 3.13: A comparison of our measured velocity map of [Fe II] (panel a) with the velocity map of a rotating disk model with a mass profile containing a radially-varying mass component plus a point mass of $M = 1.04^{+0.10}_{-0.08} \times 10^9 M_\odot$ (panel b). These kinematics are indicative of the presence of a black hole at the center of the N disk, and suggest that the N is the remnant nucleus of a progenitor galaxy. Below (panel c) is a map of the residuals of the model divided by the errors in the velocity map. N points up.

virtually non-existent in the N disk. However, 1.4GHz images from Carilli & Taylor (2000) suggested that there may be a weak AGN present near N1. Similarly, the 6−7 keV extended emission detected near around the N nucleus may be due to enhanced 6.4 keV Fe K line emission, lending support to the presence of a heavily obscured AGN (Iwasawa et al., 2011b). We measure an increase in the velocity dispersion for H_2 along the minor axis and towards the SE, which gives direct evidence for the presence of biconical collimated molecular outflows from the N source.

There is a deficiency of Brγ and He I flux near N1 compared with the rest of the N disk. This could be due to ionization caused either by an AGN or by supernovae in the center of the disk. However, we find other putative supernovae sites that do not show a deficiency in Brγ, so factors such as extinction may contribute towards this phenomenon near N1. Our Kcb line data are unable to fully resolve the individual clumps in the N disk, but the [Fe II] line and NIRC2 images resolve them at the $0\farcs035$ and $0\farcs01$ scales, respectively. In particular, N1 is bright in the K'- and H-band flux but relatively weak in [Fe II], whereas the faint clump N2 and extended clump N3 have a higher [Fe II]-to-continuum ratio. N3 has similar brightness as N1 in the H-band, but is weaker than N1 in the K'-band. The presence and clumpiness of [Fe II] may indicate regions excited by supernova remnants (Alonso-Herrero et al., 1997). However, since N1 is weak in [Fe II] and redder in color than N2 and N3, its ionizing source may be similar to the AGN in the SW component. Given that the supermassive black hole measured dynamically in §3.5.1 lies inside N1, we note the possibility that it may be an obscured AGN.

3.5.2 The Southwestern Nucleus

The SW component is the location of the hard X-ray source from an updated *Chandra* map (Iwasawa et al., 2011b). It is red and unresolved in NICMOS imaging (Scoville et al., 2000), and shows 8.4GHz flux consistent with a radio-quiet AGN (Condon et al., 1991). In our OSIRIS data, this SW region is compact and dominated by the continuum emission. It shows strong [Si VI] and moderate H_2 emission, but is weak in Brγ flux. At the $0\farcs01$ scale of the NIRC2 data, the SW source is resolved and exhibits a N-S extended, asymmetric low surface-brightness structure. The presence of hot dust as inferred from the rising continuum slope agrees with the redness seen at this source in the NICMOS JHK-band images (Scoville et al., 2000) as well as with the *Spitzer*-IRS results (Armus et al., 2007), consistent with the presence of an AGN.

The SW nucleus features low detection from H_2, Brγ, and He I, all potentially partially destroyed by a strong ionizing source. [Si VI] emission is detected in this region, but is not resolved. It usually indicates the presence of the hard ionizing spectrum of an AGN, consistent with the *Chandra* results that an AGN resides in this source (Iwasawa et al., 2011b).

3.5.3 The Southeastern Component and its Bridge

Though the SE component has been observed in several bands, the causes of its emission are unclear and controversial. From *HST* ACS and NICMOS images, the SE component resembles a star cluster (Scoville et al., 2000) and is identified as a candidate blue star cluster (CSC1; Iwasawa et al., 2011b). Radio images show prominent

emission and extended morphology consistent with AGN jets, but lack the compact core indicative of an AGN. The radio data show a steep spectrum ($\alpha = 1.4 \pm 0.2$), which could point to a starburst origin (Carilli & Taylor, 2000; Bondi et al., 2005), though the extended nature (~ 230 pc) suggests that it is larger than a single star cluster.

Our spectral decomposition of the SE component in the near-infrared adds new information. The SE component appears weak and diffuse in the NIRC2 H- and K'-band continuum images, but does appear clearly in several emission lines: H_2 (Fig. 3.7), [Si VI] (Fig. 3.10), and [Fe II] (Fig. 3.12) in our IFU data. In particular, we note the strong [Si VI] emission; as [Si VI] has the highest ionization potential of the observed lines (167 eV), its presence gives a strong clue to the origin of the SE component. The use of [Si VI] as a tracer of the coronal line region (CLR) has been demonstrated by Müller-Sánchez et al. (2011) in 7 nearby Seyfert galaxies. They found that the CLRs in these low-power Seyferts to be $\sim 80 - 150$ pc in radius and are associated with outflows, providing circumstantial evidence for the existence of extended CLRs and highly ionized gas in outflows from Seyfert nuclei like that in Mrk 273. Here we consider two possible mechanisms to ionize [Si VI]: photoionization and shock-heating. We first consider the [Si VI]/Brγ flux ratio in our models; the map of this ratio is shown in Fig. 3.14. We compare the [Si VI] flux to Brγ flux since the ratios may give clues to the ionization mechanisms involved. We find that, along the northwest boundary between the SE component and its bridge, the [Si VI]/Brγ ratio reaches 7.9 near the N nucleus, and decreases over $\sim 0\farcs3$ to 1.2 near the SE component. This gradient suggests that the origin of the ionization mechanism may be external; we consider below potential

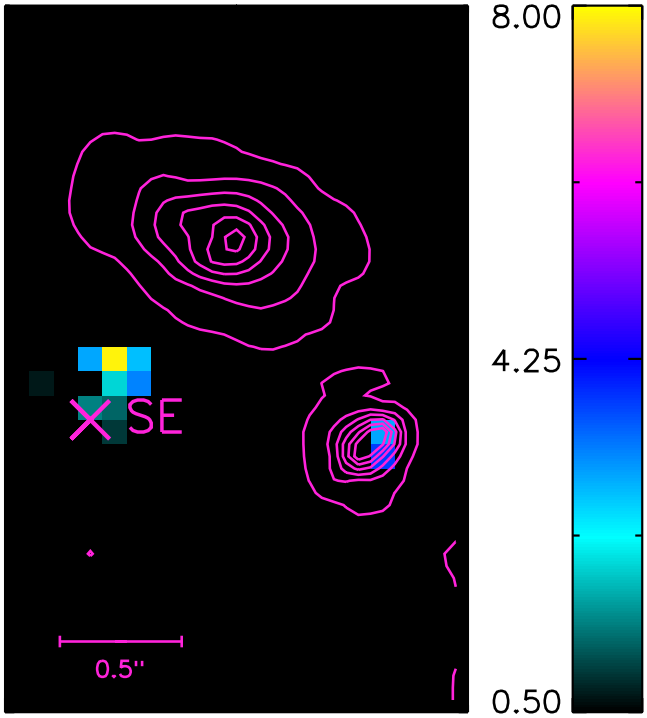

Figure 3.14: [Si VI]/Brγ ratio map. The ratio appears strongest near the N nucleus and descreases along the northwest edge of the SE component, suggesting that the origin of the ionization mechanism may be external rather than local. Bar denotes 0.″5; N points up.

sources for the ionization.

Photoionized [Si vi]

If the [Si VI] is photoionized, the hard ionizing radiation may come from either an AGN or nearby O and B stars. We compared our measured [Si VI]/Brγ flux ratio to those produced by CLOUDY models representing each scenario. We used CLOUDY version 08.00, described by Ferland et al. (1998).

First we confirmed that an AGN can plausibly produce our measured [Si VI]/Brγ flux ratio. Our incident AGN spectrum was a power-law continuum with a spectral index of -0.2, and we assumed that the gas is approximately solar metallicity (consistent with estimates from Huo et al., 2004). We varied the ionization parameter of the gas $U = Q(H^0)/(4\pi r^2 n_H c)$, where $Q(H^0)$ is the flux of ionizing photons, r is the distance between the ionizing source and the illuminated edge of the cloud, n_H is the volume density of neutral hydrogen to ionize, and c is the speed of light. We found that, in order to produce a [Si VI]/Brγ flux ratio of ~ 6, an ionization paramater U of at least $10^{-2.7}$ is required. When varying the metallicity $\log(Z/Z_\odot)$ from -0.5 to 1.0, we found that the required ionization parameter varies by less than 0.3 dex. We used $n_H \sim 10^3 cm^{-3}$ as a conservative estimate of the density in the central regions of ULIRGs (but see Davies et al., 2003, whose models suggest the densities can be as high as $10^4 - 10^5 cm^{-3}$). We found that the required $Q(H^0) \sim 4 \times 10^{54} (\frac{r}{800pc})^2 s^{-1}$. A typical $Q(H^0)$ for a quasar can reach nearly $10^{57} s^{-1}$ (Tadhunter, 1996); lower levels of AGN activity would naturally produce fewer ionizing photons. These numbers suggest that photoionization from an AGN in the N disk could plausibly produce our measured [Si VI]/Brγ flux ratios, even at a distance of 800 pc. We note that both the N and the SW components, at distances of 680 and 800 pc respectively, fall within this range. However, the spatial distribution of the [Si VI]/Brγ flux ratio (see Fig. 3.14, where the gradient seems to be higher toward the N nucleus) is more consistent with photoionization from a N AGN than from the SW unless there is variable dust extinction surrounding the SE component that alters the angle of the gradient.

We must determine if our measured [Si VI]/Brγ flux ratios could instead be produced by nearby O and B stars due to intense star formation. To test this scenario, we used an incident O star spectrum from the Tlusty models described in Lanz & Hubeny (2003). As an extreme case, we chose two of the hottest O star spectra available, with effective temperatures of 55,000K and 52,500K, at solar metallicity and with log(g) of 4.5 and 4.25, respectively. Again we varied the ionization parameter U and the metallicity of the gas to found the required $Q(H^0)$ to produce our measured [Si VI]/Brγ flux ratios. In this scenario, we find that an ionization parameter U of at least $\sim 10^{12}$ is required for our measured [Si VI]/Brγ flux ratio. This U value is much higher than is required for an AGN because the AGN spectrum is much harder than that of an O star. To produce this high of an ionization parameter from stars present within 5 pc requires $Q(H^0) \sim 8 \times 10^{64} (\frac{r}{5pc})^2 s^{-1}$. A single O star's $Q(H^0) \sim 10^{50} s^{-1}$ (see models by Sternberg et al., 2003); for this line ratio to be produced by photoionization from stars, we would need 10^{14} O stars within 5 pc – a completely unphysical scenario. We conclude that if our measured [Si VI]/Brγ flux ratios are caused by photoionization, they must be from an AGN.

Shock-Heated [Si vi]

[Si VI] may be ionized in gas heated by shocks and is sometimes observed in novae and supernova remnants (Gerardy & Fesen, 2001). Several pieces of evidence in our observations suggest the possibility of outflows that could be causing shocks near the SE component. The H_2 and [Fe II] emission bridge, the increase in H_2 velocity dispersion along the minor axis, as well as the noted [Si VI]/Brγ gradient decreasing along the

bridge from the N to the SE component, would be explained by outflows associated with the central powering source within the N nucleus in this scenario – AGN jets or stellar winds. Although the [Si VI] emission appears diffuse, the H_2 velocity map in this region shows a clear shift from the systemic velocity of the system with $\Delta v \sim -150$km s^{-1} along the bridge and $\Delta v \sim -75$km s^{-1} at the SE component. The spectrum of the H I 21 cm absorption shows a double-peaked profile suggesting infall at 200 km s^{-1} on scales $\leq$ 40 pc (Carilli & Taylor, 2000). With this evidence of gas motion, it is likely that shocks may exist; these shocks could be responsible for some or all of the measured [Si VI]/Brγ flux ratio ($\leq 7.9 \pm 3.4$).

To determine if our observed [Si VI]/Brγ flux ratio may be plausibly caused by shocks, we compared it to the shock models of Allen et al. (2008) using the IDL SHOCKPLOT widget. In particular, we adopted the radiative shock plus photoionized precursor model with solar abundance and density $n = 10^3$ cm^{-3} as a conservative estimate for a ULIRG, and calculated line ratios produced for models within a grid of parameter space. The precursor model provides most of the [Si VI]flux, so including it is important for to determine the highest [Si VI]/Brγratio obtainable. The parameter space in magnetic parameters $B/n^{1/2}$ and shock velocities v_s of the model grid is $B/n^{1/2} = 10^{-4} - 10\mu$G cm$^{3/2}$ and $v_s = 200 - 1000$ km s^{-1}. The model grid is shown in Fig. 3.15, with a green symbol marking the value of the line ratios observed in the SE component; it does not appear to converge on any shock model generated within our parameter space. The more robust [Si VI]/Brγ ratio (which is less sensitive to dust or cross-filter photometric calibrations) is only produced by models with a high $B/n^{1/2}$ value

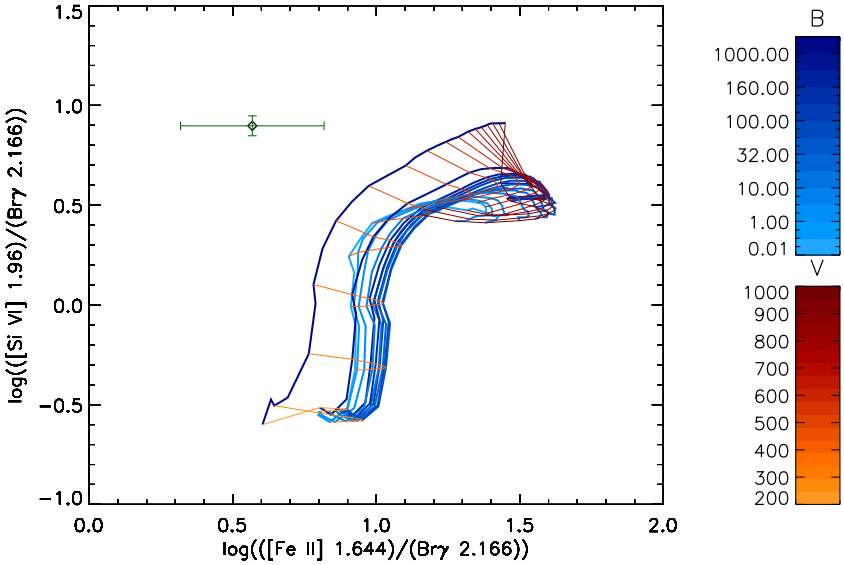

Figure 3.15: Diagnostic plot of [Si VI]/Brγ vs. [Fe II]/Brγ showing a grid of shock models with solar abundance and density $n = 10^3$ cm^{-3} (Allen et al., 2008). The parameter space spans magnetic parameters $B/n^{1/2} = 10^{-4} - 10\mu$G cm$^{3/2}$ and shock velocities $v_s = 200 - 1000$ km s^{-1}. The green symbol marks the value of the line ratios associated with the SE component; it does not appear to converge on any shock model generated within our parameter space. The more robust [Si VI]/brg ratio (which is less sensitive to dust or cross-filter photometric calibrations) is only produced by models with a high $B/n^{1/2}$ value and high shock velocity, suggesting that only fast shocks in the densest material, if at all, could be responsible for its excitation.

($> 10 - 30\mu$G cm$^{3/2}$) and a shock velocity to $v_s \geq 550$ km s^{-1}, indicating that only fast shocks in the densest material, if at all, could produce the line ratios that are observed in the SE component.

Energy Flow from N1

The [Si VI]/Brγ ratio, seen as a gradient from the N and decreasing toward the SE, in combination with the bridge between SE and N seen in the other flux maps, strongly suggest an external origin for the source of the observed energy flow, possibly

from the center of the N disk. We find that the SE component is likely to be gas from a tidal feature or stellar cluster that is being affected in one of two ways. The easiest way to ionize the [Si VI] is with a buried AGN in the N disk or the SW AGN with variable extinction. The AGN would not be isotropically obscured, and thus could photoionize gas in certain directions. However, we find that the observed [Si VI]/Brγ ratios may also be produced in extreme shock situations. Here we investigate if such shocks are consistent with our kinematic data, and whether star formation is able to provide sufficient energy to power them.

The spectral maps and kinematics in the region of the bridge suggest its origin as an outflow originating at the center of the N disk. It extends along the minor axis of the disk, following the region of increased velocity dispersion in molecular hydrogen, suggesting that a biconical turbulent outflow is present. The increased H_2 emission towards the SE has a peculiar velocity of -200 km s^{-1} relative to the systemic velocity of the system; this gas appears to be outflowing. We used simple energy arguments to estimate the amount of energy input required, to determine whether it is likely driven by stellar winds or from AGN feedback. The energy contained in the outflow is $1/2\ mv^2$, where m is the mass contained in the outflow and v is the peculiar velocity, -200 km s^{-1}. To estimate the mass contained in the outflow, we adopted solar metallicity and a density of 1000 cm^{-3} (a conservative estimate for (U)LIRGs, see Davies et al., 2003), and used the size of the extended emission (see Table 3.1) assuming an equal depth and width, resulting in a mass of 7700 $M_\odot$. To determine an energy input rate, we estimated the amount of time the outflow has been traveling from the distance between

the SE and the center of the N disk. To travel this distance of 680 pc at 200 km s^{-1}, the outflow requires $\sim$ 3.3 million years. Assuming the energy contained in the outflow was spread out over this timescale, the energy input rate required to drive this outflow is 1.3×10^{43} erg s^{-1}.

Is there enough star formation to provide this energy input in stellar winds? We estimate the available energy input from stellar winds as follows: the luminosity of Brγ in the N disk is 2.1×10^{40} erg s^{-1}, implying a star formation rate of 17 $M_{\odot}$ yr^{-1} (Kennicutt, 1998) and therefore a bolometric luminosity of 1.7×10^{11} $L_{\odot}$ (Krumholz & Tan, 2007). Approximately 1% of the bolometric luminosity of a starburst is available to drive stellar winds (Heckman, 1994), divided by an angular scale ratio of $1/4\pi$ steradians, yielding an energy input rate available from the N disk's star formation of approximately 5×10^{41} erg s^{-1}. As this is more than an order of magnitude lower than the required energy to drive this outflow, a scenario in which an AGN is contributing some or all of the energy input is likely.

It is also important to consider whether the energy available to drive outflows from star formation is sufficient to shock-heat the [Si VI] seen in the SE component. The incoming kinetic energy rate is $e_k = 1/2\ \rho v_s^3 A$, where ρ is the density (as above, 1000 cm^{-3}), v_s is the shock velocity ($\geq$ 550 km s^{-1}, calculated from the SHOCKPLOT models in §3.5.3), and A is the surface area of the gas being shocked. A lower limit on the shocked area is a hemisphere on the surface of the SE component: 2π (74 pc)^2. (In reality, the shock front would likely have structure and therefore larger surface area; this provides a conservative lower limit on the energy input required to shock this [Si

VI].) These estimates require an energy input of 1.7×10^{44} ergs^{-1}, two and a half orders of magnitude larger than 5×10^{41} erg s^{-1}, the available energy for outflows from star formation in the N disk. This suggests that the observed [Si VI] emission cannot be caused solely by shock-heating due to stellar winds. Instead, some of the [Si VI] emission must be caused in part by either AGN photoionization (as discussed in §3.5.3) or by shocks partly powered by an AGN-driven outflow.

Though photoionization from an AGN is the simplest way to produce the [Si VI] emission in the SE, it is likely produced by a combination of the two processes: e.g., a weaker AGN to photoionize some gas, and less extreme shocks to heat the rest. Our observed double-peaked [Si VI] velocity profile indicates that there are likely two kinematic components in this region — with broad and narrow velocity dispersions, respectively. The broad component contributes to roughly half the [Si VI] flux, resulting in a [Si VI]/Brγ ratio of 3.9±1.7, or $0.59^{+0.16}_{-0.25}$ dex in logarithmic units. This constrains the shock models to velocities $v_s \sim 350 - 450$ km s^{-1}, within the range of the velocity dispersion of the broad component. The two narrow and broad components may have originated from two different heating mechanisms, lending support to the combined AGN and shocks scenario. While it is plausible that the photoionization has originated from the SW AGN while the shocks are driven by the outflows from the N disk, it would require a quite specific geometry and gradient in extinction between SE and SW to produce the observed spatial gradient in the [Si VI] excitation. Since the geometry would have to be somewhat contrived, we deem more likely that the photoionization originated from a N AGN. A reasonable interpretation might involve a combination of

shocks from the outflow and photoionization by a buried AGN within the N disk, which is almost edge-on to our line of sight.

3.6 Summary

High spatial resolution imaging and integral field spectroscopy with Keck laser guide star adaptive optics has allowed us to study the properties of the atomic and molecular emission lines of Mrk 273 in the H- and K'-bands. The nuclear region is resolved into three primary components (N, SW, and SE) with a gas bridge between the N and SE components. These near-infrared high-resolution maps are well suited for investigating the gas dynamics and the location of the hardest photons from AGN and fast shocks; they complement other multiwavelength data for determining the ultimate power associated with each component.

We have shown that the N component is a rotating gaseous disk with PA $\sim 330°$. The characteristic size of the disk varies depending on the emission line studied, but the effective radius is roughly $0\farcs30$ (240 pc). Using the observed strong rotation, we measure from the kinematics of [Fe II] a central mass of $M = 1.04^{+0.10}_{-0.08} \times 10^9 M_\odot$, consistent with the mass measurement from OH maser kinematics (Klöckner & Baan, 2004). This enclosed mass likely indicates the presence of a supermassive black hole at the center of the N disk, suggesting that the N component is the remnant nucleus of a progenitor galaxy. The gaseous disk may be a remnant from the progenitor galaxy or may be recently formed with new gas from the merger. The black hole is heavily obscured and may be an AGN and/or surrounded by additional star formation, consistent

with conclusions from X-ray (Iwasawa et al., 2011b) and radio data (Carilli & Taylor, 2000; Bondi et al., 2005). An increase in the velocity dispersion of H_2 along the minor axis of the N disk and towards the SE suggests the presence of bipolar molecular outflow originating from the N source. Extended emission of shocked H_2 towards the SE also reveals the presence of a collimated outflow. Energy arguments associated with the size and kinematics of this outflow suggest that it is too massive to be produced by star formation alone, and also point towards the scenario in which the N black hole is a buried AGN. H_2 line ratios offer insight into the rotational and temperature conditions as well as their excitation mechanisms. We derived $T_{\rm vib} \simeq 2591 \pm 79$K and $T_{\rm rot} \simeq 1604 \pm 113$K, which fall within the range of temperatures for Seyfert galaxies (Reunanen et al., 2002).

The SW component is bright and compact in the K'- and H-band continua, and shows emission of the coronal line [Si VI]. We suggest that a non-thermal photon source is ionizing the silicon and producing the [Si VI] emission that we observe; it would also heat the hot dust that we observe in the continuum. Our near-IR data support the notion that the SW nucleus hosts the known hard X-ray AGN in this system (Iwasawa et al., 2011b).

The SE component presents a new piece in the puzzle of the merger's nuclear region. While it has previously been detected in the radio regime (Smith et al., 1998), it has not been detected in optical and near-IR images until now due to the dominance of the broadband continuum. With our new AO-assisted NIRC2 images and OSIRIS integral field spectroscopy, the SE component is detected in several emission lines, and is prominent in both [Fe II] and [Si VI]. The double-Gaussian fit to this [Si VI] line

indicates that there are two velocity components involved, perhaps due to outflows. We discussed several potential scenarios for the origin of the SE component: photoionization by AGN or O and B stars, shock-heating due to stellar winds or AGN-driven outflows, or a combination of both. We favor the case where the SE component is a clump of gas or tidal feature photoionized by an obscured AGN in the N disk and/or shock-heated by outflows from the same AGN and its surrounding star formation. While AGN photoionization alone could produce the observed [Si VI]/Brγ ratio, only the most extreme shocks in the shock-heated scenario could account for these [Si VI]/Brγ values. We suggest that a combination of photoionization and shocks could best produce both the observed line ratios and the two kinematic components of [Si VI].

As a late-stage gas-rich merger, Mrk 273 offers a unique time in the merger sequence where the nuclei have not completely merged and yet one AGN has already been triggered. We have identified a second black hole, located in the center of the N disk, which may be an obscured AGN with supporting evidence of outflows. The gas disk is likely the remnant nuclear disk from one of the progenitor galaxies, or perhaps a young disk formed during the merger. An understanding of the unveiling of this second black hole as an unburied AGN may lead to a deeper understanding of the frequency of dual AGNs in merging gas-rich galaxies.

Part II

Statistical Properties of a Sample of Merging (U)LIRGs

Chapter 4

Stellar and Gaseous Nuclear Disks in Nearby Gas-Rich Major Mergers

4.1 Introduction

High spatial resolution hydrodynamic simulations of gas-rich galaxy mergers have predicted the formation of nuclear disks on scales of tens to hundreds of parsecs (e.g. Mayer et al., 2008). These disks form as gravitational torques funnel the gas towards the nuclei of the merging galaxies, feeding gas down to the smallest possible scales resolved in the simulations ($\sim$ 1 pc). The presence of this gas and the resulting dissipation may provide a mechanism that speeds up the formation and final coalescence of binary black holes (Kazantzidis et al., 2005; Mayer et al., 2007; Dotti et al., 2007,

2008; Chapon et al., 2013).

To date, nuclear disks of varying scales (a few to a few hundred pc) have been found in a handful of nearby isolated galaxies, both spirals (e.g. Zasov & Moiseev, 1999; Pizzella et al., 2002) and ellipticals (e.g. Scorza & van den Bosch, 1998; Krajnović & Jaffe, 2004). These nuclear disks are identified using one or both of high-resolution imaging and spectroscopy to identify disky isophotes and Keplerian-like rotation curves. Kinematically decoupled cores and nuclear disks have been discovered in a number of early-type galaxies in the SAURON survey (de Zeeuw et al., 2002; McDermid et al., 2004; Emsellem et al., 2004; McDermid et al., 2006a; Krajnović et al., 2008). McDermid et al. (2006b) suggest that the most compact of these decoupled cores are linked with recent star formation. Their formation is likely to be caused by a galaxy merger (Kormendy, 1984; Bender, 1988; Balcells & Quinn, 1990; Hernquist & Barnes, 1991) or interaction (Bender, 1988; Hau & Thomson, 1994). This hypothesis has been supported by the case of NGC 5953, whose kinematically decoupled core may have been caused by the current inflow of cold gas from its neighbor, NGC 5954 (Falcón-Barroso et al., 2006, 2007). Recently, Hicks et al. (2013) have shown that active galactic nuclei (AGN) are likely to host nuclear disks on scales of a few hundred parsecs, and that these disks are absent in similar quiescent galaxies; this suggests that disks may be an important mechanism for transporting fuel inwards to power AGN. Bender et al. (2005) find a nuclear disk of stars in M31 of radius ~ 8 pc, and Lu et al. (2009) find a nuclear disk of young stars around the Galactic Center of radius ~ 0.4 pc.

In order to understand the origins of kinematically decoupled galaxy cores, and

to estimate the effect nuclear disks may have on black hole merger rates, it is important to search for and characterize nuclear disks in nearby merging galaxies, or galaxies which have undergone recent mergers.

We selected our sample of gas-rich merging galaxies from the Great Observatory All-sky LIRG Survey (GOALS; Armus et al., 2009). This survey consists of the brightest infrared galaxies at redshifts $z < 0.1$ and provides imaging and spectroscopic observations with the Hubble Space Telescope, the Galaxy Evolution Explorer (GALEX), the Chandra X-Ray Observatory, and the Spitzer Space Telescope. Though the GOALS survey spans all nuclear spectral types and merger stages, we selected targets primarily from later stages of mergers, in which the two nuclei are within $\sim 5''$ (2-7 kpc at these redshifts).

The existing Hubble ACS images of these merging galaxies have sufficient spatial resolution to detect the disky isophotes commonly associated with nuclear disks (Kim et al., 2013). However, because (U)LIRGs exhibit high levels of extinction due to dust (Scoville et al., 2000), the nuclear regions are too obscured in the optical bands to detect them. High spatial resolution observations in the near-infrared have been difficult to obtain from space due to the limiting size of space telescope primary mirrors; such observations from the ground are subject to blurring from turbulence in the Earth's atmosphere. In the past decade, laser guide star adaptive optics (LGS AO) systems have been developed to measure the atmospheric turbulence and to correct for it, providing diffraction-limited imaging for large ground-based telescopes.

In this paper, we present high spatial resolution integral field spectroscopy of

the nuclear regions of 15 (U)LIRGs in late stages of merging. In §5.2 we describe our observations and data processing. The resulting spectra are analyzed using a procedure described in §4.3 to produce flux and velocity maps, which are presented in §5.4. In §4.6 we compare our results to disks found in high-resolution merger simulations. Our conclusions are summarized in §5.5. We adopt $H_0 = 70\,\mathrm{km\,s^{-1}\,Mpc^{-1}}$, $\Omega_\mathrm{m} = 0.28$, and $\Omega_\Lambda = 0.72$ throughout the paper. Physical scales were calculated using Ned Wright's Cosmology Calculator (available at `http://www.astro.ucla.edu/~wright/CosmoCalc.html`; Wright, 2006).

4.2 Observations and Data

We observed the nuclei of 15 (U)LIRGs undergoing major mergers with the OH-Suppressing InfraRed Imaging Spectrograph (OSIRIS, Larkin et al., 2006), on the W. M. Keck II telescope using LGS AO between April 2007 and January 2012. OSIRIS is a near-infrared integral field spectrograph with a lenslet array capable of producing up to 3000 spectra at once. The spectral resolution ranges from about 3400 in the largest pixel scale to 3800 in the three finer pixel scales. This resolution is sufficient to resolve spectral regions between the OH emission lines from Earth's atmosphere, and enables improved sky subtraction.

OSIRIS sits behind the Keck Observatory AO System (Wizinowich et al., 2000; van Dam et al., 2004; Wizinowich et al., 2006; van Dam et al., 2006), which measures wavefront distortions due to atmospheric turbulence and corrects for them using a deformable mirror. This technique enables spatial resolutions in the near-infrared match-

ing those of the Hubble Space Telescope at visible wavelengths ($\sim 0.05''$). OSIRIS observations may be taken at $0.02''$, $0.035''$, $0.05''$or $0.1''$per pixel. In order to measure distortions, AO systems require either a natural guide star (NGS) or a laser guide star (LGS) plus a tip-tilt star. NGS AO at Keck Observatory requires a guide star brighter than ∼13th magnitude and within $\sim 30''$of the target. For all of our systems except IRASF01364-1042, we used the Keck LGS AO system, since the required tip-tilt star can be up to an arcminute away and as faint as ∼18th magnitude. In this case, the Keck LGS AO system uses a pulsed laser tuned to the 589 nm Sodium D_2 transition, exciting atoms in the sodium layer of the atmosphere (at ∼95 km) and causing spontaneous emission. Thus, the laser creates a spot in the upper atmosphere which allows the AO system to monitor turbulence below the sodium layer via a Shack-Hartmann wavefront sensor and correct for it with a deformable mirror. This laser guide star enables high-order corrections to the wavefront, but low-order corrections for image motion are corrected using the tip-tilt star.

Our OSIRIS observations usually consisted of ten minute exposures taken in sets of three, using the pattern object-sky-object. Total exposure times on each target and their relevant sky frames are listed in Table 5.1. In each case we also observed the tip-tilt star to use in our estimates of the point-spread function (PSF). We selected filters and plate scales based on the redshift of each target, also listed in Table 5.1. We employed a combination of broadband observations (Kbb and Kcb: 1.965 μm - 2.381 μm) and narrowband observations (Hn4: 1.652 μm - 1.737 μm; Kn5: 2.292 μm - 2.408 μm). For each galaxy, observations include a subset of the following emission and

absorption features: Brγ 2.16 μm, H_2 2.12 μm, Paα 1.875 μm, and the CO (2-0) and (3-1) bandheads at 2.293 μm and 2.323 μm.

We reduced our OSIRIS observations using the OSIRIS Data Reduction Pipeline version 2.3 (available at `http://irlab.astro.ucla.edu/osiris/pipeline.html`), which includes modules to subtract sky frames, adjust channel levels, remove crosstalk, identify glitches, clean cosmic rays, extract a spectrum for each spatial pixel, assemble the spectra into a data cube, correct for atmospheric dispersion, perform telluric corrections, and mosaic frames together. For some cases we utilized the Scaled Sky Subtraction module based on the technique outlined in Davies (2007), which scales the thermal continuum and OH line groups separately to provide optimal sky subtraction; we modified the module to include a smoother subtraction of the thermal continuum.

We imaged the tip-tilt stars for each galaxy during the observations in order to provide an estimate for the PSF. A Moffat profile was fit to each tip-tilt star and then broadened according to the distance between the galaxy and the tip-tilt star. At Mauna Kea, the isokinetic angle is $\sim 75''$(van Dam et al., 2006); this represents the on-sky distance from the tip-tilt star at which the Strehl will be degraded by $1/e$. Each galaxy's tip-tilt star was therefore broadened by a Gaussian broad enough to decrease the tip-tilt star's peak flux to match the predicted degradation based on the distance to the target. Because most tip-tilt stars are significantly closer than $75''$, this correction was usually small, about 10-30%.

Table 4.1: Details of OSIRIS Observations for Disk Studies

Galaxy Name	Redshift	UT Date(s) YYMMDD	Filter	Plate Scale $''$/ pixel	Exp Time on Target, Sky (min)	Tip-tilt Star R Mag[a]	Tip-tilt Star Separation ($''$)
CGCG436-030	0.0312	120102	Kcb	0.1	30, 10	11.2	33.1
IRASF01364-1042	0.0490	101113	Kcb	0.1	130, 80	10.3	30.0
		101114					
		120102					
IIIZw035	0.0278	111210	Kbb	0.035	100, 50	12.6	44.3
IRASF03359+1523	0.0365	101114	Kcb	0.1	60, 30	17.4	30.0
MCG+08-11-002	0.0195	110110	Kcb	0.1	60, 30	16.4	17.6
		120102					
NGC 2623	0.0196	110110	Kcb	0.1	50, 25	16.9	55.4
		110203					
UGC5101	0.0390	101114	Kcb	0.1	30, 20	14.7	35.4
UGC5101	0.0390	100304	Kn5	0.035	80, 50	14.7	35.4
		100305					
Mrk231/UGC8058	0.0433	110523	Kbb	0.035	36, 18	10.	0.0
Mrk231/UGC8058	0.0433	100304	Kn5	0.035	57, 30	10.	0.0
Mrk273/UGC8696[b]	0.0380	120522	Kcb	0.1	50, 30	16.1	33.1
IRASF15250+3608	0.0563	110523	Kbb	0.05	80, 40	15.6	53
NGC 6090	0.0304	100305	Kcb	0.1	30, 10	15.7	36.5
NGC 6240N	0.0244	090617	Kn5	0.035	210, 75	12.0	35.8
NGC 6240S[c]	0.0244	070421	Kn5	0.035	20, 10	12.0	35.8
IRASF17207-0014	0.0432	110523	Kcb	0.1	60, 30	14.1	25.6
IRASF17207-0014	0.0432	110523	Hn4	0.035	40, 20	14.1	25.6
		110524					
IRAS20351+2521	0.0340	110522	Kcb	0.1	30, 20	12.2	18.1
IRASF22491-1808	0.0781	101114	Kcb	0.1	20, 10	16.4	43.0

[a]Taken from the USNO B1 Catalog
[b]Originally presented in Chapter 3
[c]Originally presented in Chapter 2

4.3 Methods and Analysis

The OSIRIS data cubes capture both gas emission lines and stellar absorption features, which are analyzed separately in the following two sections. In each case, the data were binned using optimal Voronoi tessellations according to the code described in Cappellari & Copin (2003), which is available at `www-astro.physics.ox.ac.uk/~mxc/idl/`. The signal-to-noise ratio in each pixel was calculated using one of two methods. For emission lines, a single Gaussian function was fit to the data; the continuum-subtracted area under this curve is the signal. The corresponding noise is the root-mean-squared residual of the nearby continuum. For absorption lines, the signal-to-noise ratio was calculated as described in Chapter 2, using flux in the continuum for signal and calculating the noise theoretically using published values of readnoise and

dark current and Poisson noise for the galaxy and sky fluxes. The theoretical noise estimates match well with other empirical noise measurements.

We then used the signal-to-noise ratio calculations to spatially bin the data to obtain regions of a sufficient minimum signal-to-noise ratio. To measure an emission line, the pixels were Voronoi binned to provide a signal-to-noise ratio of at least 3 per bin. For stellar absorption line fitting, the pixels were Voronoi binned to a signal-to-noise ratio threshold of 20.

4.3.1 Probing the Gas

Emission lines were fit using the methods outlined in Chapter 3. First the cubes were continuum-subtracted, by fitting a power law continuum to each pixel's spectrum. Then the pixels were binned according to the optimal Voronoi tessellations. The binned, continuum-subtracted spectra were then fed into the appropriate line-fitting codes. When a species had only one line falling within a band (e.g. Paα), that line was fit with a single Gaussian function. The Brackett series of lines (Brγ and Brδ) are frequently both observable in K-band; these two lines were fit simultaneously, requiring that the velocity and velocity dispersion be consistent between the two lines. Similarly, the OSIRIS K broadband hosts five molecular hydrogen lines which all have the same line profiles. We simultaneously fit the five lines, allowing the fluxes in each line to vary but constraining the velocities and velocity dispersions to be the same.

4.3.2 Probing the Stars

Stellar kinematics were fit using the Penalized Pixel Fitting routine (pPXF; Cappellari & Emsellem, 2004), which produces a line-of-sight velocity distribution using a maximum penalized likelihood approach and a library of stellar templates. In the same manner as in Chapter 2, the routine was adapted to low signal-to-noise spectra by setting the BIAS keyword to 1000; this biases the code against fitting higher order moments (h_3 and h_4) and instead only fits the velocity and velocity dispersion of the stars in each bin, effectively shutting off h_3 and h_4. Due to the recent star formation in these galaxies, the CO absorption bandheads are the most prominent stellar feature in the K-band. Therefore, to further improve the signal-to-noise of the fits, the spectral regions around the CO bandheads were weighted more heavily. For K-band spectra, we used a selection of late-type giant and supergiant spectral templates from the GNIRS (Winge et al., 2009) library. Late-type giant and supergiant stars have been shown to be a good fit for starbursting galaxies (e.g. Engel et al., 2010, and Chapter 2) and host deep CO bandheads, excellent for fitting kinematics.

4.4 Results

4.4.1 Modeling the Flux Distribution with GALFIT

To quantify the characteristic sizes of the flux profiles, we modeled the continuum and emission line flux maps with GALFIT (Peng et al., 2002, 2010) using multiple components. In each case, a Sérsic profile was fit, centered on the kinematic center of the galaxy with the position angle constrained to match the kinematic major axis

(see §4.4.2). Because these galaxies frequently show substructure in the nuclear regions, additional components (Gaussians, PSFs, and Sérsics) were added to the fit until the disk's properties stabilized. This enabled us to fit the nuclear disks without confusion by spiral arms, tidal streams, on- and off-nuclear star clusters. For galaxies in which two Sérsics were fit, the disk was always the Sérsic with the smaller radius and smaller Sérsic index. For each galaxy (except Mrk 231, due to contamination from the central quasar), the continuum image was fit first; then certain disk parameters were kept fixed in emission line maps: coordinates of the center, the position angle, and the axis ratio of the disk. In some cases, the center and position angle of the continuum were constrained to the kinematic center from velocity maps; in most cases, this lines up with the photometric center and isophote contours as expected.

Many nuclei's GALFIT decompositions revealed extended H_2 emission along the minor axis of the disk. Because H_2 is likely shock-heated, these patches may be indicative of turbulent polar outflows. They will be studied in detail in a future paper; for now they are simply fit with Gaussians and removed. Evidence of these components can easily be noted by comparing the apparent position angle of H_2 emission to that of the continuum and Brγ emission; in many cases the H_2's longer axis is offset by 90°. These components are also noted for individual galaxies in §4.5.

In Table 4.2, we include the GALFIT parameter results for each nucleus. Note that the errors listed are the formal errors reported by GALFIT, and do not include systematic errors associated with GALFIT fits. Figure 4.4 shows the flux map, GALFIT model and residual for each galaxy. The flux profiles show an average Sersic index of

1.1 ± 0.1 for stars, 0.9 ± 0.2 for H_2, and 0.9 ± 0.1 for atomic hydrogen line emission, suggestive of disky structure. The average effective radius is 288 ± 12 pc for stars, 310 ± 20 for H_2, and 320 ± 35 for atomic hydrogen line emission. We exclude from this average the nuclei which are not confirmed by rotation (see next section) or higher resolution imaging. We also exclude NGC 6090 and IRAS03359+1523, which appear to be at such an early stage of merger that the disk measured is actually a remnant disk from the progenitor rather than a nuclear disk formed during the merger.

To estimate how much mass may be in these disks, we use the average surface mass density for (U)LIRGs calculated by Bryant & Scoville (1999), $< \Sigma_g >= 10^4 M_\odot pc^{-2}$, and multiply it by the area of the each disk. Though the surface density was calculated for cold gas using interferometric observations, we still consider this a lower limit to the mass because the cold gas disk may cover a larger area than is traced by the H_2 line. These derived masses are listed in Table 4.3 and range from $6.3 \times 10^8 - 3.8 \times 10^{10} M_\odot$. We also make use of the high spatial resolution kinematic modeling presented in Chapter 5 for some of these galaxies, and report their dynamical mass profiles in Table 4.3. Briefly, the kinematics were modeled as $M(r) = \rho_0 r^\gamma + M_{BH}$. Generally, the inclination and γ were constrained using the light profile, assuming that the disk mass profile is smooth and follows the K-band light profile form; the remaining parameters, ρ_0 and M_{BH}, were fit from the kinematics. These disk mass profiles encompass not just the molecular gas mass but all components of the disk. The dynamical estimate is a factor of a few higher than the molecular gas mass in two out of the four galaxies with both estimates.

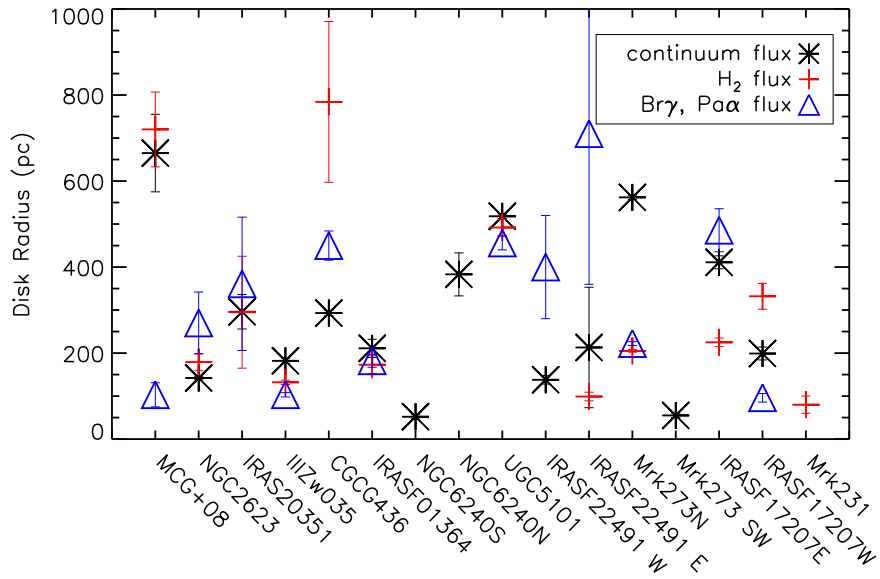

Figure 4.1: Radii of nuclear disks, as measured from GALFIT parameters. Galaxies are sorted according to infrared luminosity. Points represent the disk sizes measured from the continuum flux map (black asterisks), the H_2 flux map (red crosses), and the Brγ or Paα flux map (blue trianges).

The sizes of nuclear disks do not appear to be correlated with infrared luminosity (see Figure 4.1 and Figiure 4.2). We also include a plot of disk size for different redshift bins (Figure 4.3) in order to determine if our modeling is limited by resolution; it does not appear to affect our results.

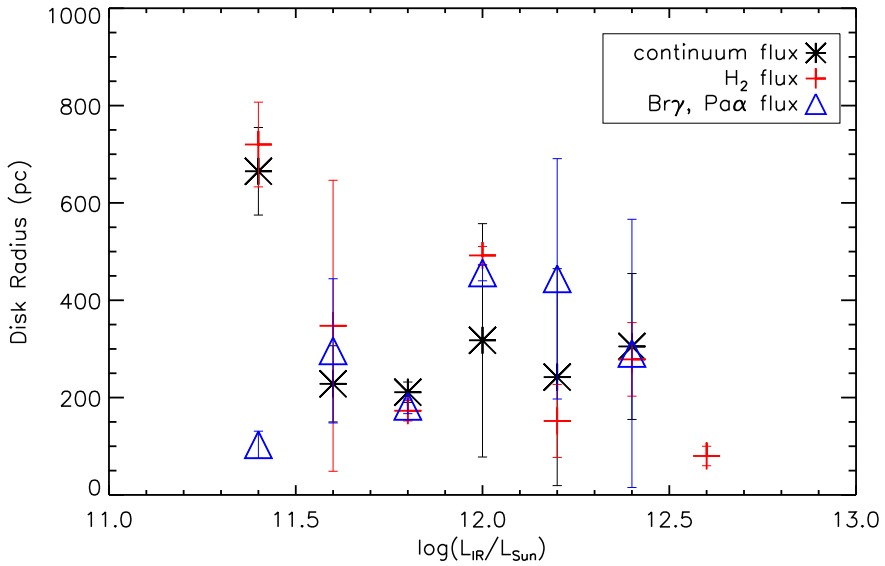

Figure 4.2: Radii of nuclear disks, as measured from GALFIT parameters. Galaxies are binned according to infrared luminosity. Points represent the disk sizes measured from the continuum flux map (black asterisks), the H_2 flux map (red crosses), and the Brγ or Paα flux map (blue trianges). The error bars show the standard deviation of the disk sizes within each bin.

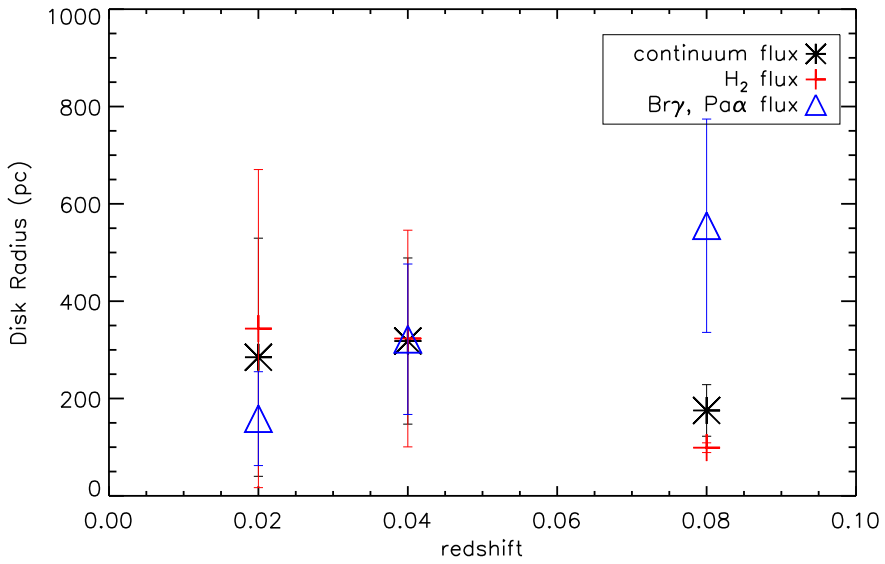

Figure 4.3: Radii of nuclear disks, as measured from GALFIT parameters. Galaxies are binned according to redshift. The lack of trend confirms that our disk size measurements are not merely a function of resolution. Points represent the disk sizes measured from the continuum flux map (black asterisks), the H_2 flux map (red crosses), and the Brγ or Paα flux map (blue trianges). The error bars show the standard deviation of the disk sizes within each bin.

Table 4.2: Measured Disk Morphologies

Galaxy Name	Tracer	Effective Radius (pc)	Sérsic Index n	Axis Ratio[a] (b/a)	Central PSF?
CGCG436-030	continuum	293 ± 6	0.6 ± 0.05	0.76 ± 0.01	off-center
	H_2	775 ± 200	0.42 ± 0.17	0.76	off-center
	Brγ	450 ± 30	0.87 ± 0.1	0.76	off-center
IRASF01364-1042	continuum	211 ± 21	0.4 ± 0.2	0.49 ± 0.03	Y
	H_2	173 ± 20	1.2 ± 0.5	0.49	N
	Paα	182 ± 15	0.75 ± 0.25	0.49	Y
IIIZw035	continuum	182 ± 6	0.67 ± 0.04	0.51 ± 0.01	Y
	H_2	132 ± 5	0.45 ± 0.04	0.51	off-center
	Brγ	103 ± 5	0.5 ± 0.1	0.51	Y
IRASF03359+1523	continuum	1850 ± 280	2.7 ± 0.4	0.24 ± 0.02	Y
	H_2	725 ± 25	0.4 ± 0.1	0.24	N
	Brγ	370 ± 250	3.1 ± 1.7	0.24	N
MCG+08-11-002	continuum	665 ± 90	1.6 ± 0.1	0.4 ± 0.02	Y
	H_2	720 ± 85	0.4 ± 0.1	0.4	N
	Brγ	105 ± 30	0.8 ± 0.3	0.4	off-center
NGC 2623	continuum	142 ± 3	2.0 ± 0.1	0.8 ± 0.01	Y
	H_2	180 ± 20	1.25 ± 0.15	0.86 ± 0.01	N
	Brγ	270 ± 70	1.64 ± 0.24	0.72 ± 0.01	N
UGC5101	continuum	518 ± 5	0.6 ± 0.01	0.44 ± 0.01	Y
	H_2	492 ± 18	0.6 ± 0.1	0.44	Y
	Brγ	455 ± 15	0.3 ± 0.1	0.44	N
Mrk231	H_2	80 ± 20	3.0 ± 2.5	1.0 ± 0.1	N
Mrk273 N[b]	continuum	562 ± 3	2.1 ± 0.5	0.75 ± 0.1	Y
	H_2	205 ± 3	0.64 ± 0.02	0.75	N

Table 4.2 (cont'd): Measured Disk Morphologies

Galaxy Name	Tracer	Effective Radius (pc)	Sérsic Index n	Axis Ratio[a] (b/a)	Central PSF?
	Brγ	220 ± 5	0.43 ± 0.03	0.75	N
Mrk273 SW[b]	continuum	55 ± 2	1.6 ± 0.5	0.44 ± 0.03	Y
IRASF15250+3608 NW[c]	continuum	246 ± 41	1.9 ± 0.3	0.78 ± 0.01	off-center
	H_2	220 ± 10	2.0 ± 0.9	0.78	off-center
	Paα	135 ± 30	2.2 ± 0.7	0.78	off-center
NGC 6090	continuum	780 ± 50	1.5 ± 0.1	0.74 ± 0.01	Y
NGC 6240N	continuum	383 ± 50	1.1 ± 0.1	0.49 ± 0.01	Y
NGC 6240S	continuum	52 ± 5	0.5 ± 0.1	0.54 ± 0.01	N
IRASF17207-0014 E	continuum	410 ± 15	0.8 ± 0.05	0.4 ± 0.01	Y
	H_2	225 ± 10	0.2 ± 0.1	0.41	N
	Brγ	485 ± 50	1.1 ± 0.2	0.041	N
IRASF17207-0014 W	continuum	200 ± 15	0.9 ± 0.05	0.85 ± 0.05	N
	H_2	330 ± 30	1.2 ± 0.2	0.85	N
	Brγ	96 ± 7	0.75 ± 0.24	0.85	N
IRAS20351+2521	continuum	296 ± 40	1.4 ± 0.2	0.81 ± 0.1	N
	H_2	295 ± 130	0.85 ± 0.4	0.81	N
	Brγ	360 ± 155	1.1 ± 0.4	0.81	N
IRASF22491-1808 E	continuum	213 ± 137	1.8 ± 1.6	0.9 ± 0.1	N
	H_2	100 ± 10	1.0 ± 0.9	0.85	N
	Paα	710 ± 350	1.2 ± 0.07	0.85	Y
IRASF22491-1808 W	continuum	138 ± 10	1.0 ± 0.2	0.6 ± 0.1	N
	Paα	400 ± 120	1.2 ± 0.8	0.6	N

[a]For galaxies with continuum and line emission maps, the axis ratio was fit using the continuum, then fixed to this best-fit value for additional line fits.

[b]Originally presented in Chapter 3

[c]Note that kinematic analysis of this galaxy does not show evidence of a disk (see §4.4.2), but GALFIT parameters were included here for completeness.

Table 4.3: Disk Mass Estimates

Galaxy Name	Tracer	$M_{H_2,disk}$[a] ($10^9 M_\odot$)	$M_{dyn,disk}(r)$[b] ($M_\odot$)	$M_{dyn,disk}$[b] ($10^9 M_\odot$)
CGCG436-030	H_2	38 ± 20		
IRASF01364-1042	H_2	1.9 ± 0.4		
IIIZw035	continuum		$1.0 \times 10^3 r_{pc}^2$	0.07 ± 0.01
	H_2	1.1 ± 0.1		
	Brγ		$1.9 \times 10^4 r_{pc}^2$	0.4 ± 0.03
IRASF03359+1523	H_2	33 ± 2		
MCG+08-11-002	H_2	33 ± 8		
NGC 2623	continuum		$1.1 \times 10^4 r_{pc}^2$	0.42 ± 0.07
	H_2	2.0 ± 0.5		
UGC5101	continuum		$9.5 \times 10^4 r_{pc}^2$	51 ± 1
	H_2	15 ± 1		
Mrk231	H_2	0.4 ± 0.2		
Mrk273 N	H_2	2.6 ± 0.1		
	[Fe II]		$1.1 \times 10^7 r_{pc}$	7.0±0.8
IRASF15250+3608 NW[c]	H_2	3.0 ± 0.3		
NGC 6240N	continuum		$9.7 \times 10^3 r_{pc}^2$	2.8 ± 0.4
NGC 6240S	continuum		$2.9 \times 10^5 r_{pc}^{1.5}$	0.2 ± 0.04
IRASF17207-0014 E	H_2	3.2 ± 0.3		
IRASF17207-0014 W	H_2	6.8 ± 1.2		
IRAS20351+2521	H_2	5.5 ± 4.8		
IRASF22491-1808 E	H_2	0.63 ± 0.13		

[a] $M_{H_2,disk} = 2\pi R_{eff}^2 < \Sigma_g >$, with $< \Sigma_g >= 10^4 M_\odot pc^{-2}$ from Bryant & Scoville (1999). Though we use the cold gas surface density, this is still likely a lower limit to the cold gas mass because we use the effective radius calculated from warm H_2, which may not trace the entire cold H_2 disk. Consider also, however, that there may be considerable variance in the parameter Σ_g not accounted for in this average value or error bars.

[b] Dynamical disk masses were calculated using kinematic fits fully presented in Chapter 5 for galaxies with high spatial resolution data, and are presented here for comparison. These masses do not include black hole or other central masses. In column 5, $M_{dyn,disk} = 2M(r_{eff})$ using the equation in column 4 and the appropriate r_{eff} from GALFIT results.

[c] Note that kinematic analysis of this galaxy does not show evidence of a disk (see §4.4.2), but GALFIT parameters were included here for completeness.

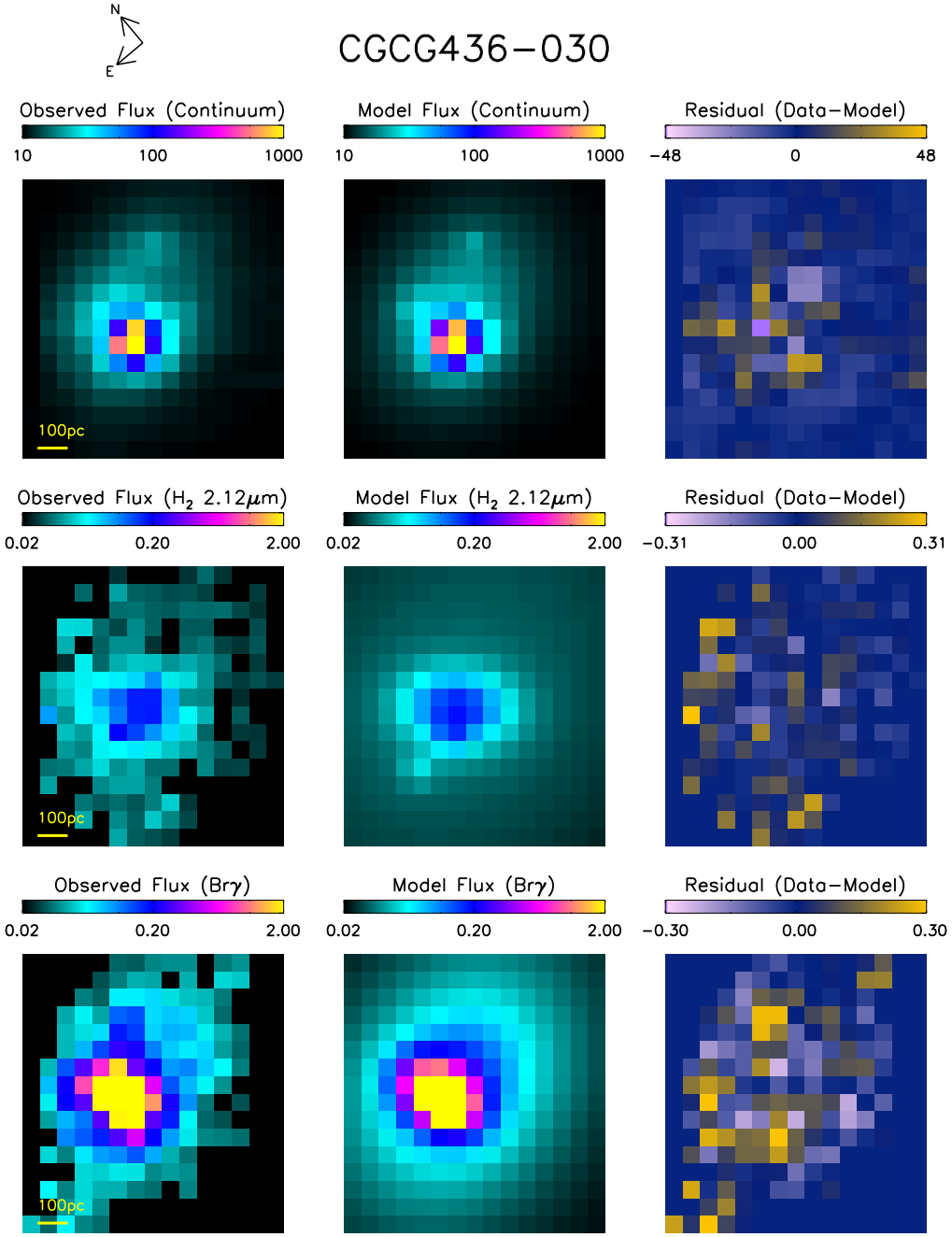

Figure 4.4: Flux map (left panel), GALFIT model (center panel) and residual (right panel) for each galaxy. Where three rows are present, the top row is the continuum flux, the middle row is H_2 flux, and the bottom row is Brγ or Paα flux.

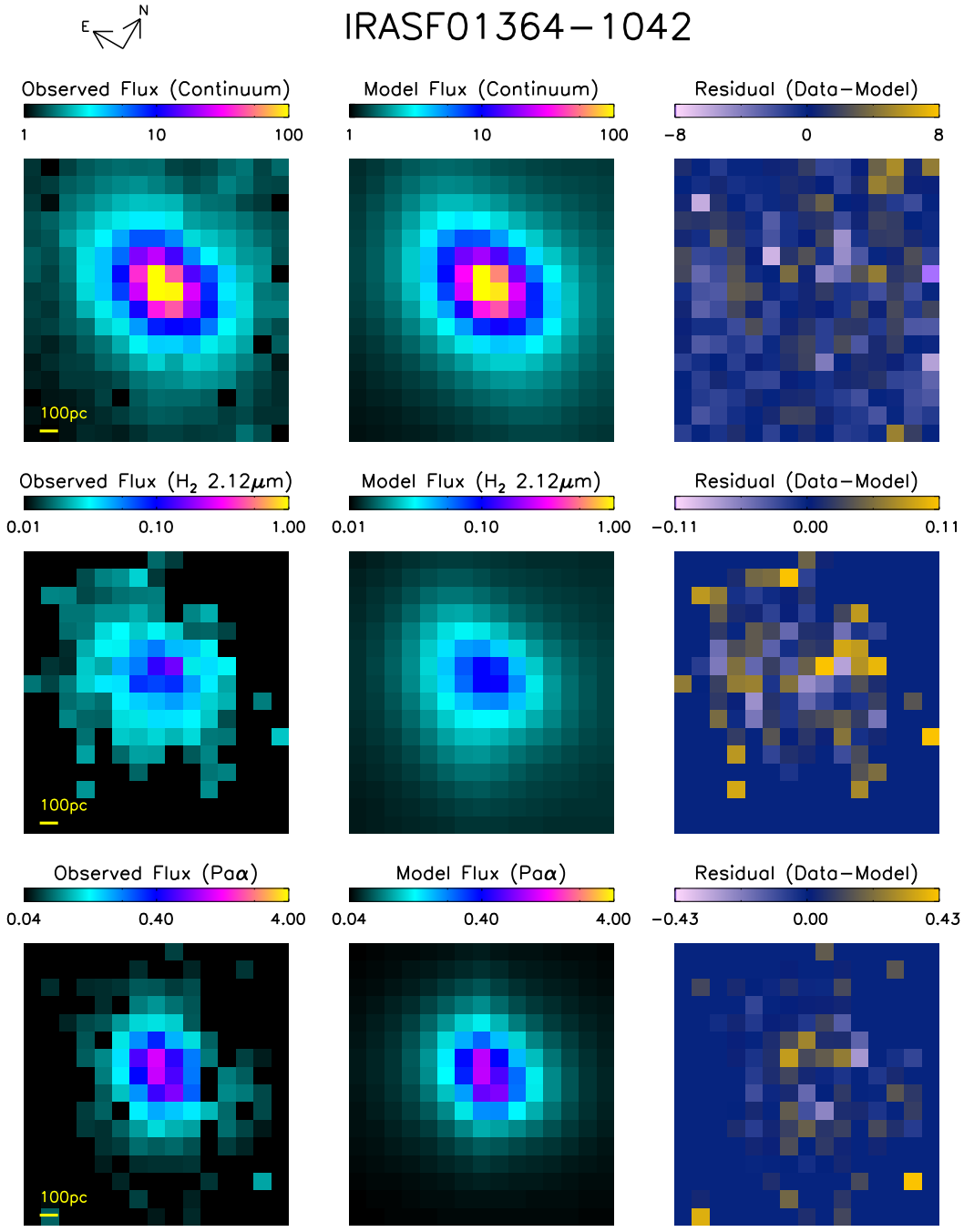

Figure 4.4: Flux map (left panel), GALFIT model (center panel) and residual (right panel) for each galaxy in different tracers.

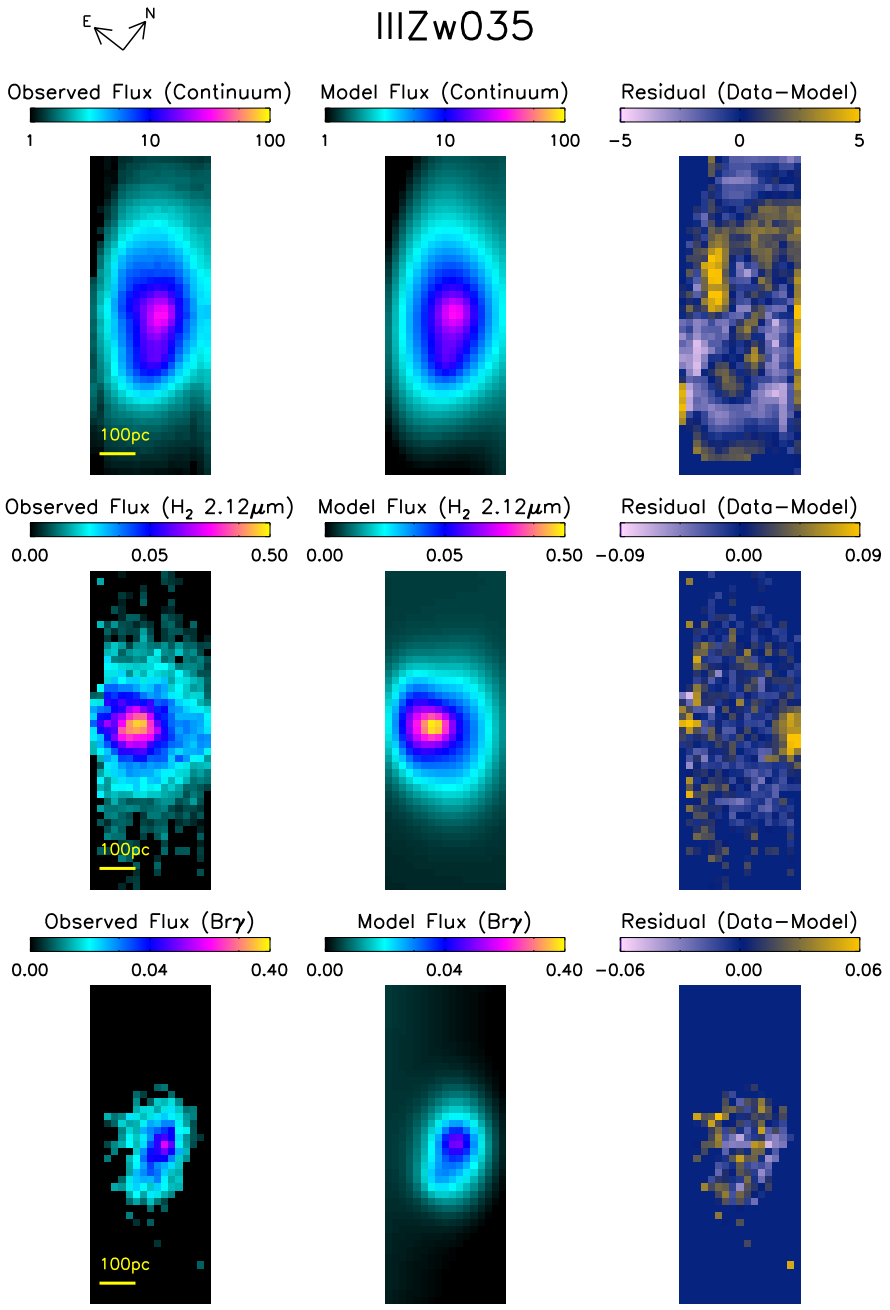

Figure 4.4: Flux map (left panel), GALFIT model (center panel) and residual (right panel) for each galaxy in different tracers.

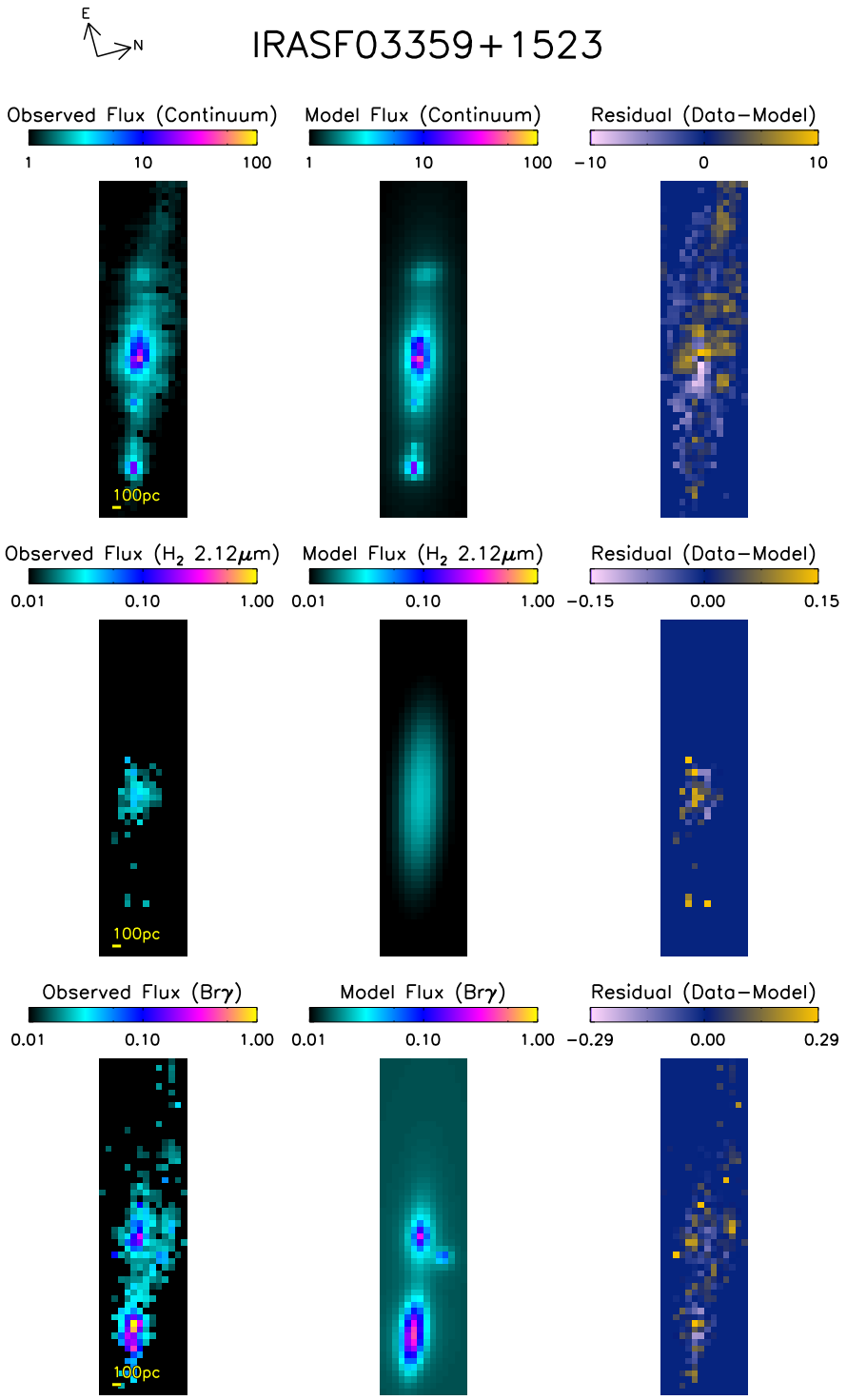

Figure 4.4: Flux map (left panel), GALFIT model (center panel) and residual (right panel) for each galaxy in different tracers.

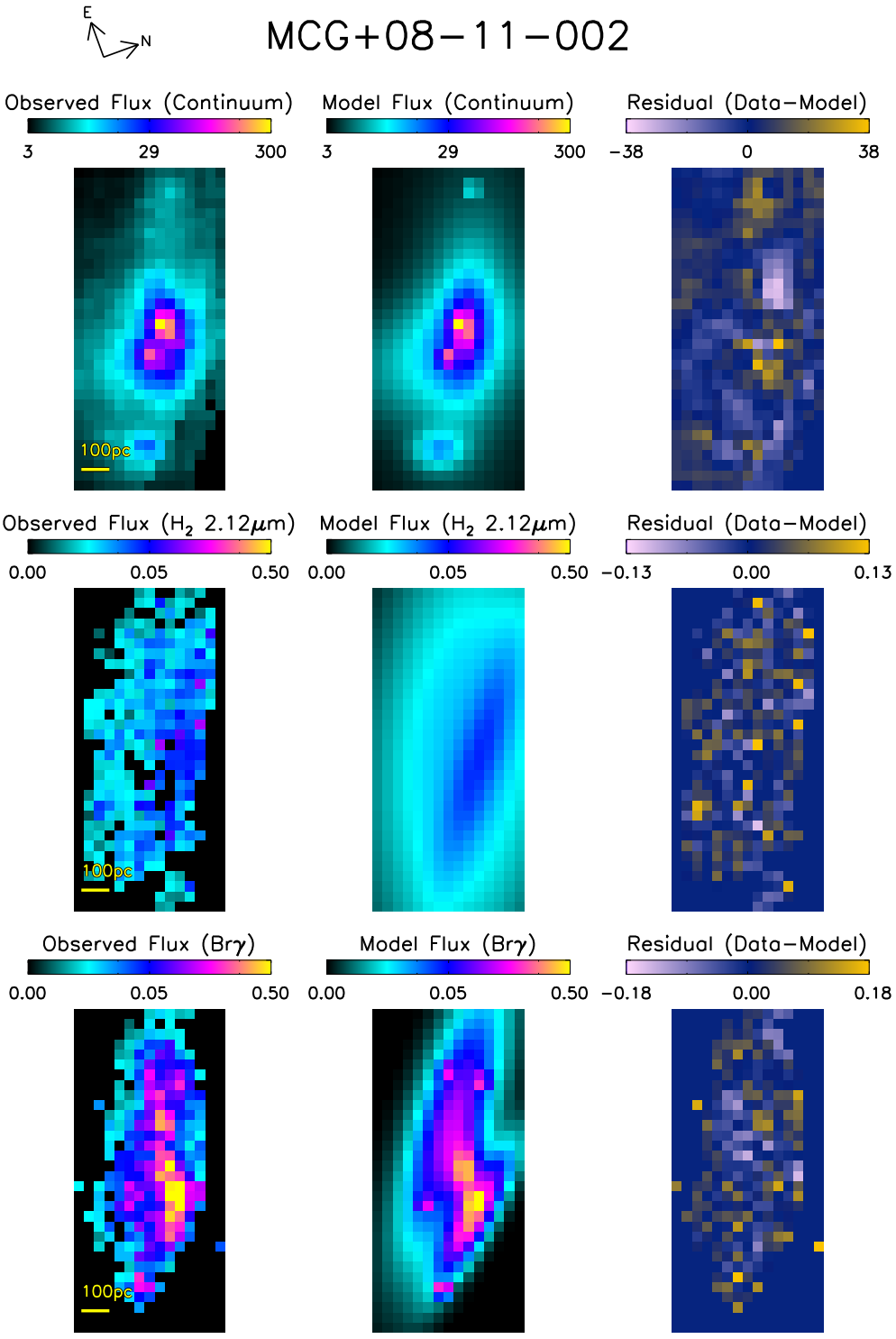

Figure 4.4: Flux map (left panel), GALFIT model (center panel) and residual (right panel) for each galaxy in different tracers.

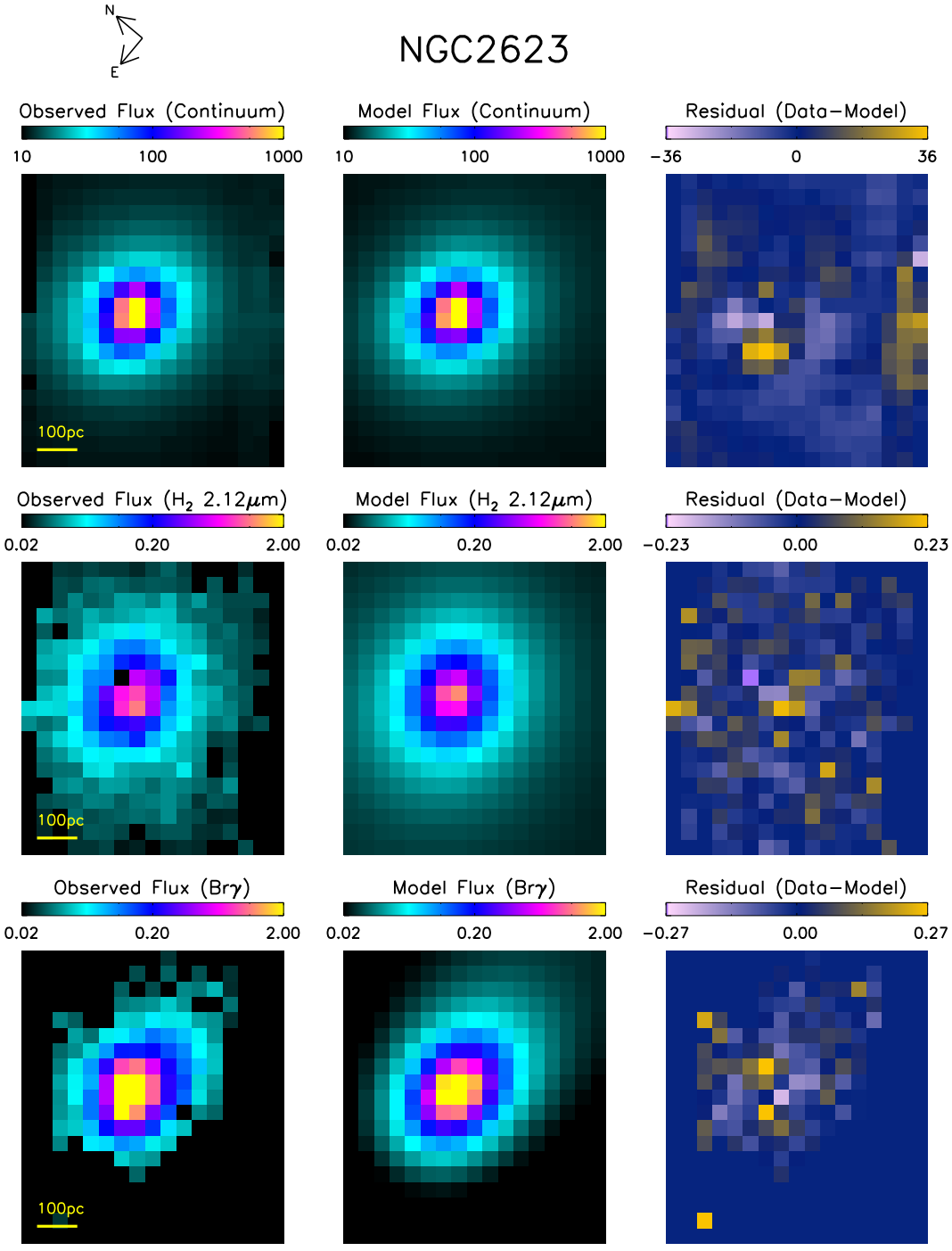

Figure 4.4: Flux map (left panel), GALFIT model (center panel) and residual (right panel) for each galaxy in different tracers.

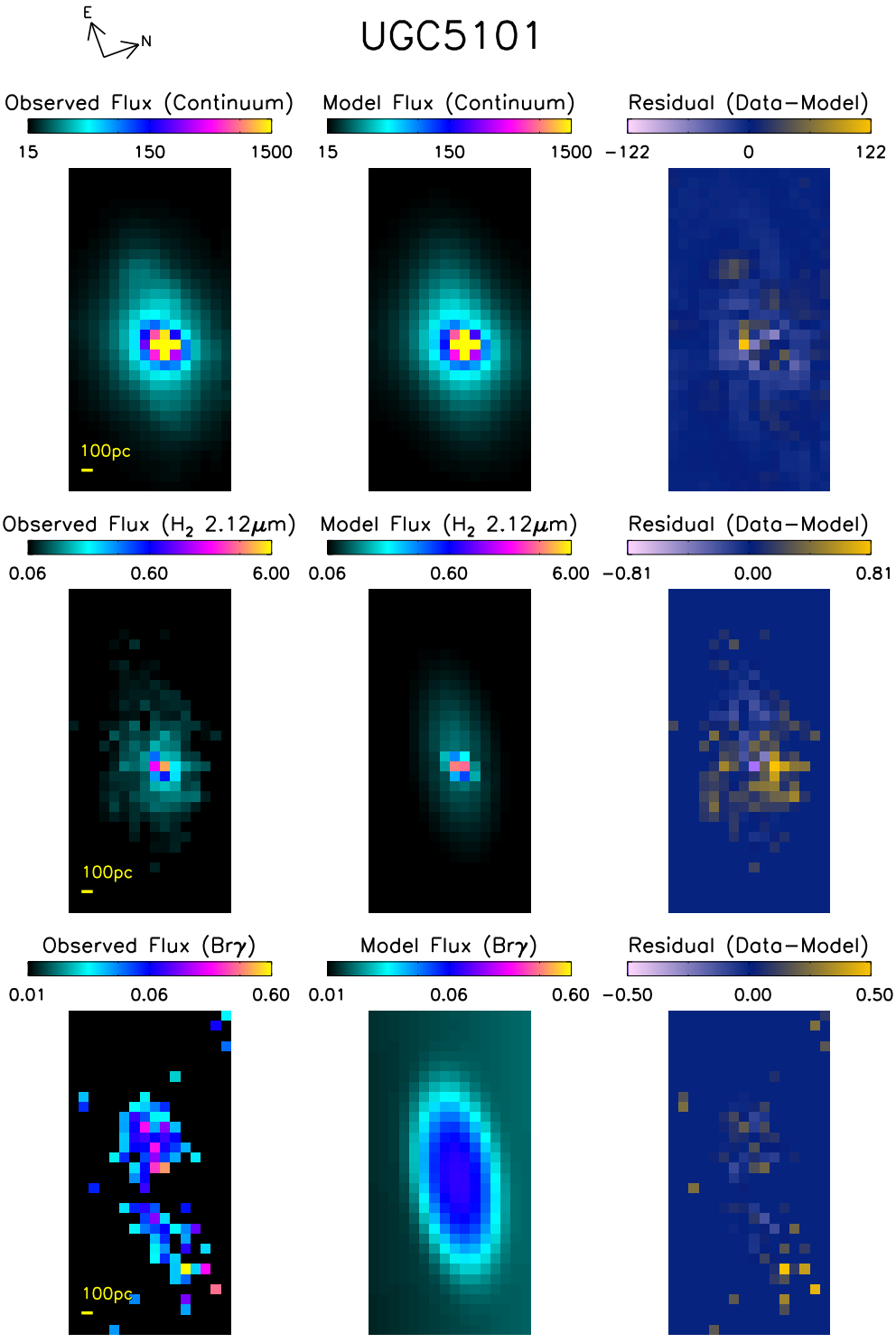

Figure 4.4: Flux map (left panel), GALFIT model (center panel) and residual (right panel) for each galaxy in different tracers.

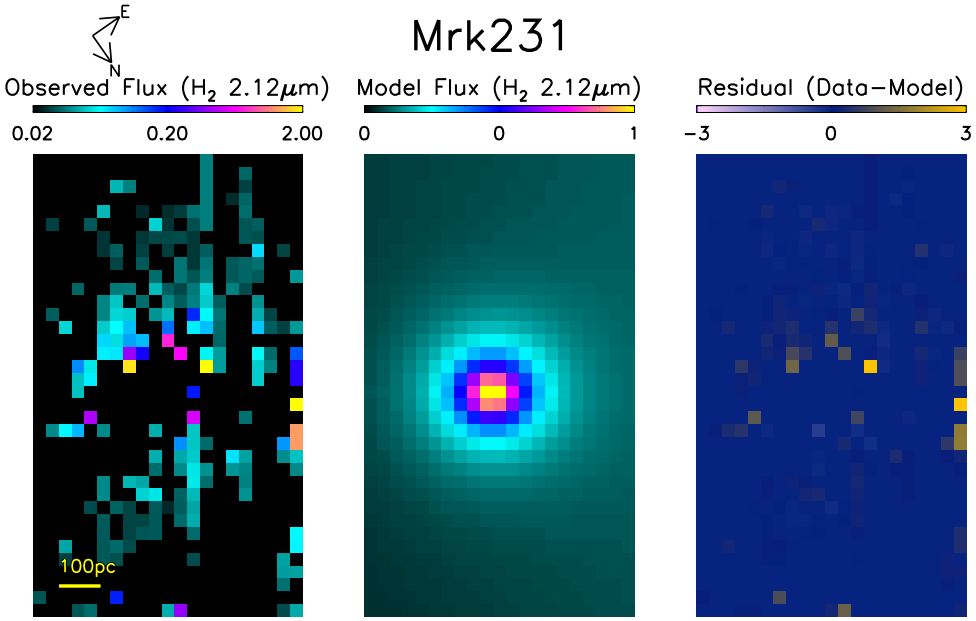

Figure 4.4: Flux map (left panel), GALFIT model (center panel) and residual (right panel) for each galaxy in different tracers.

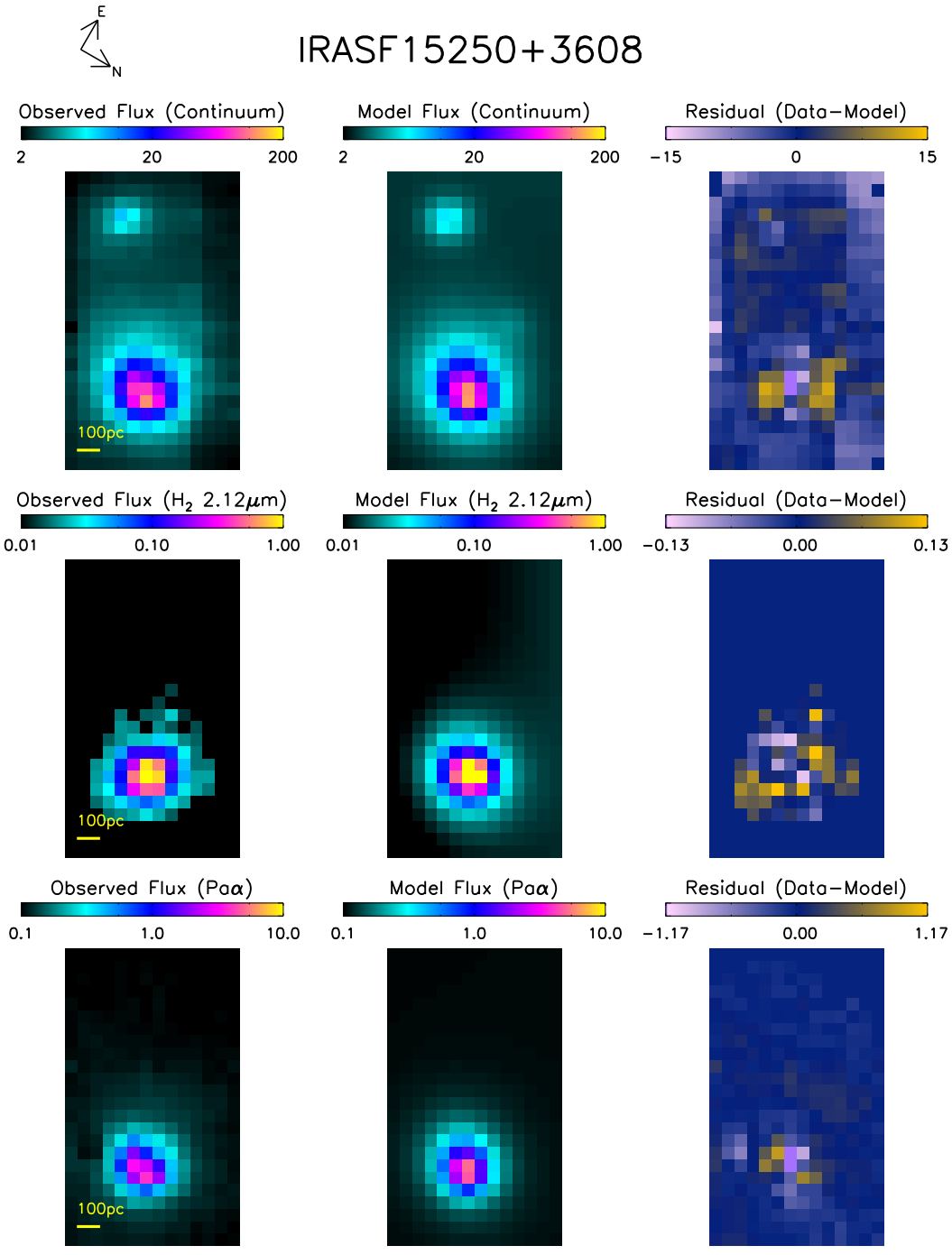

Figure 4.4: Flux map (left panel), GALFIT model (center panel) and residual (right panel) for each galaxy in different tracers.

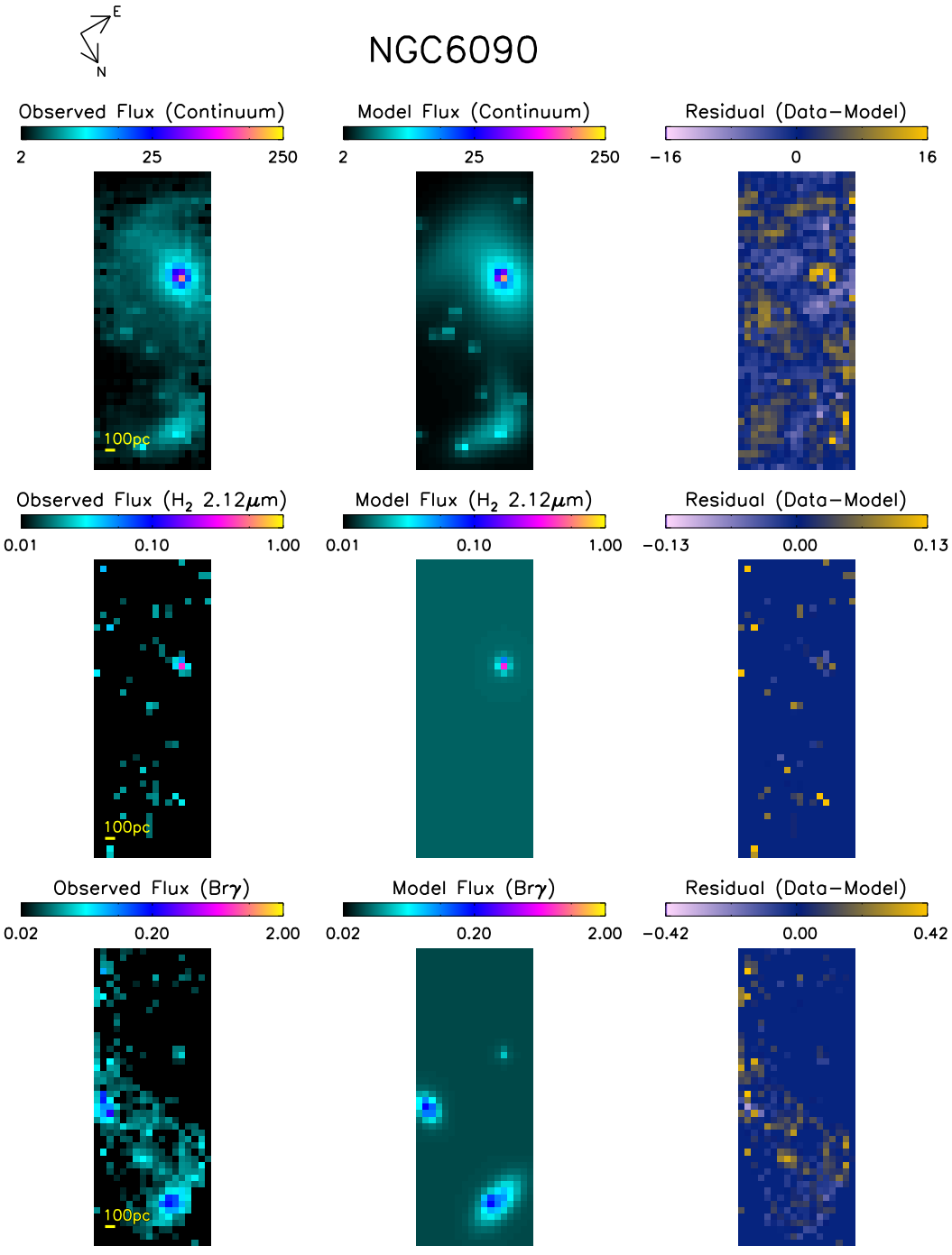

Figure 4.4: Flux map (left panel), GALFIT model (center panel) and residual (right panel) for each galaxy in different tracers.

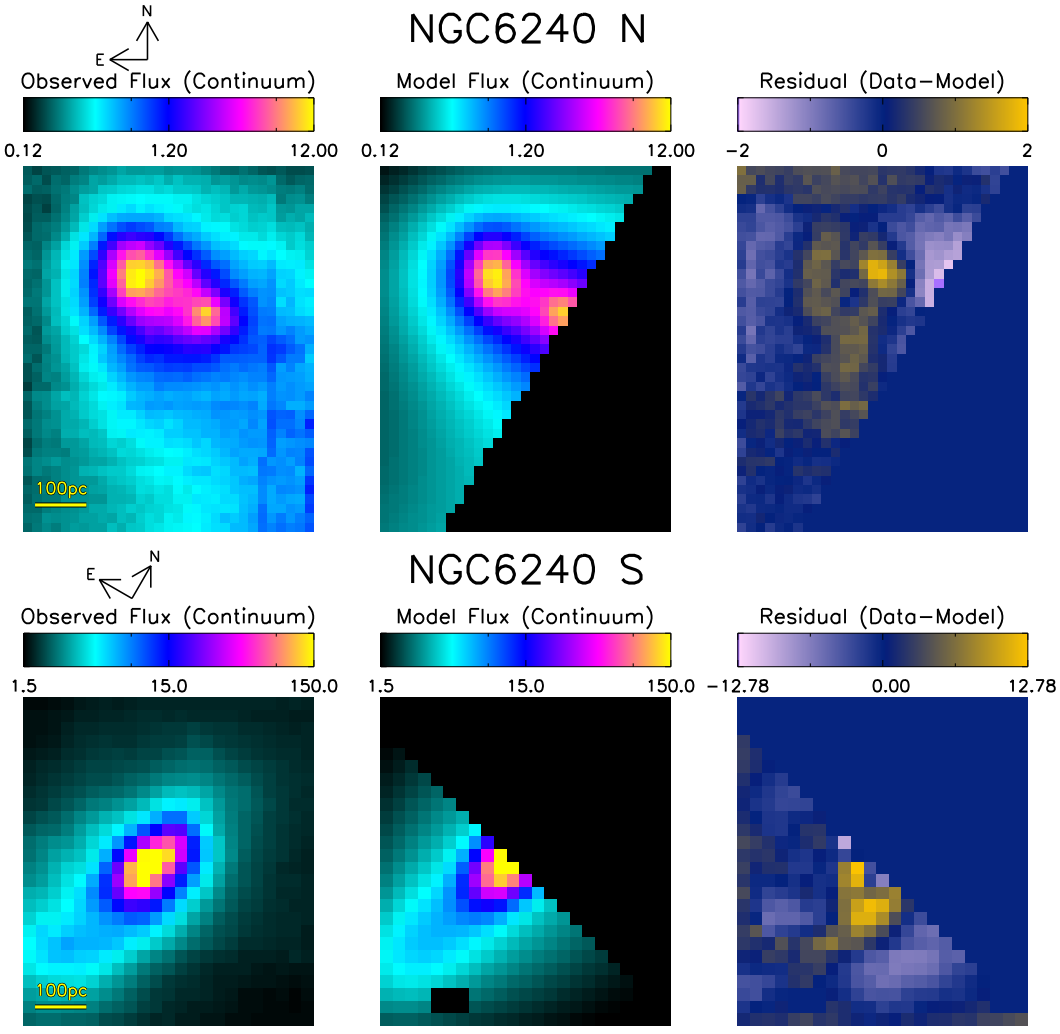

Figure 4.4: Flux map (left panel), GALFIT model (center panel) and residual (right panel) for each galaxy in different tracers. Here the two nuclei are separated by an extremely dusty region, which was masked out in the model and residuals.

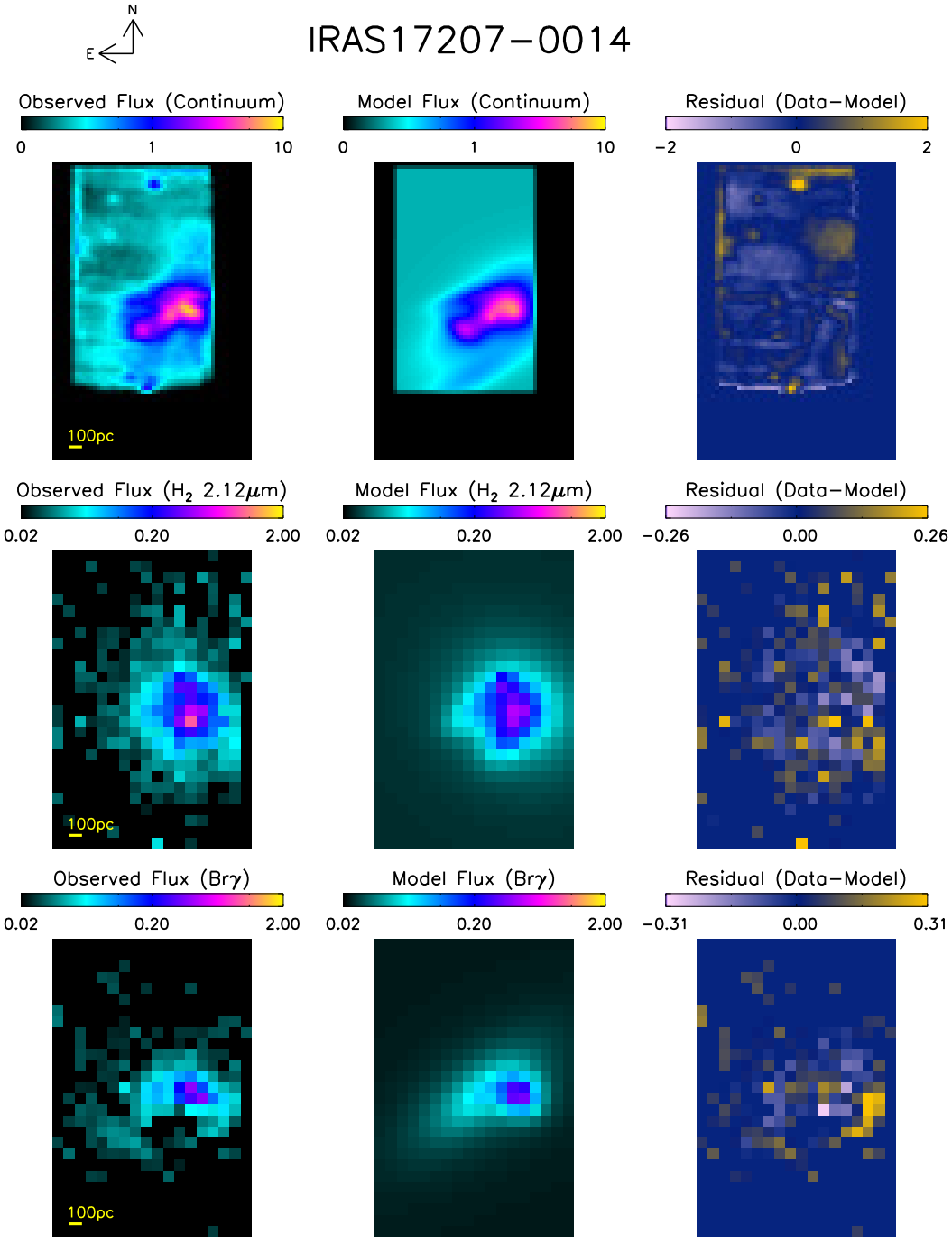

Figure 4.4: Flux map (left panel), GALFIT model (center panel) and residual (right panel) for each galaxy in different tracers.

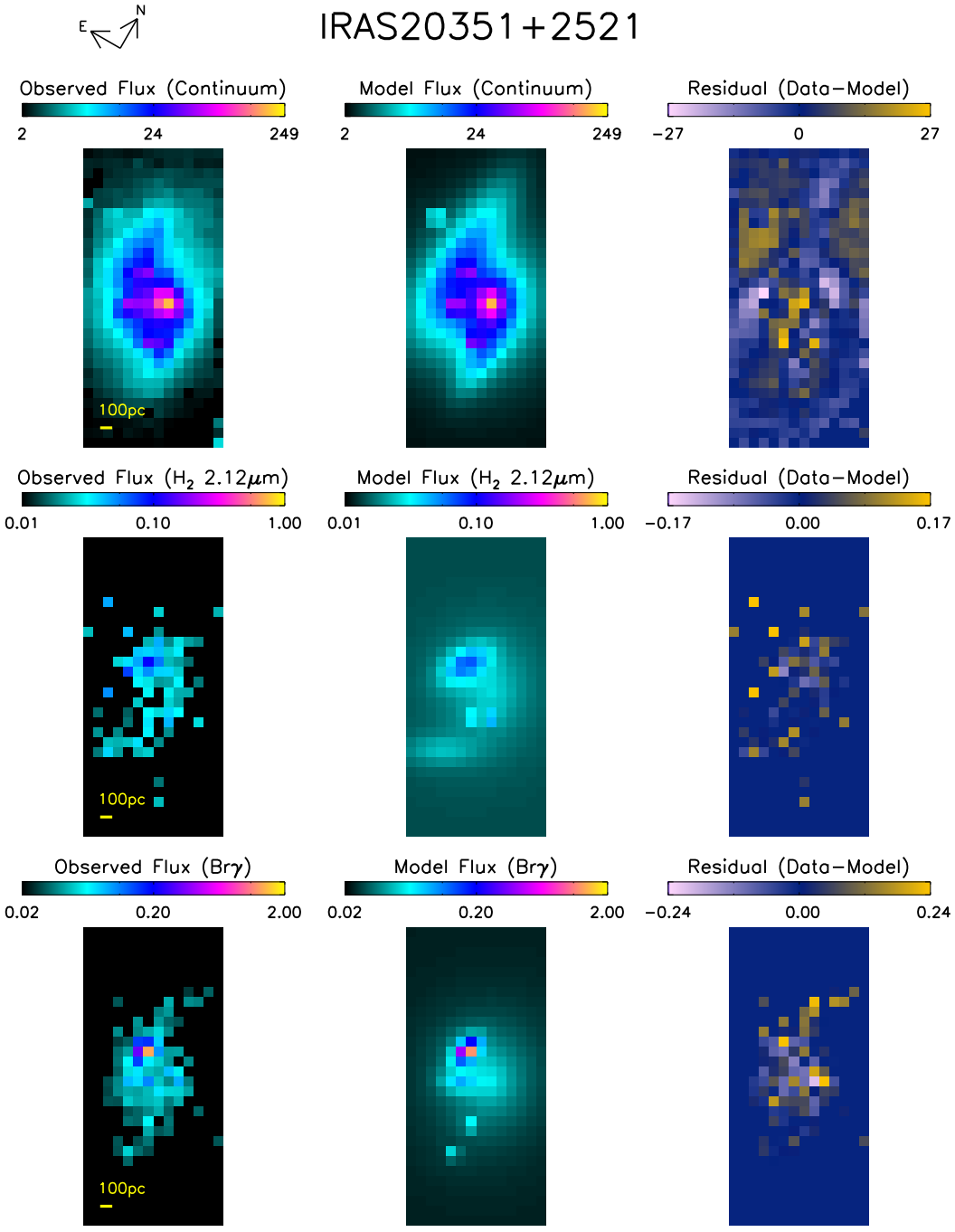

Figure 4.4: Flux map (left panel), GALFIT model (center panel) and residual (right panel) for each galaxy in different tracers.

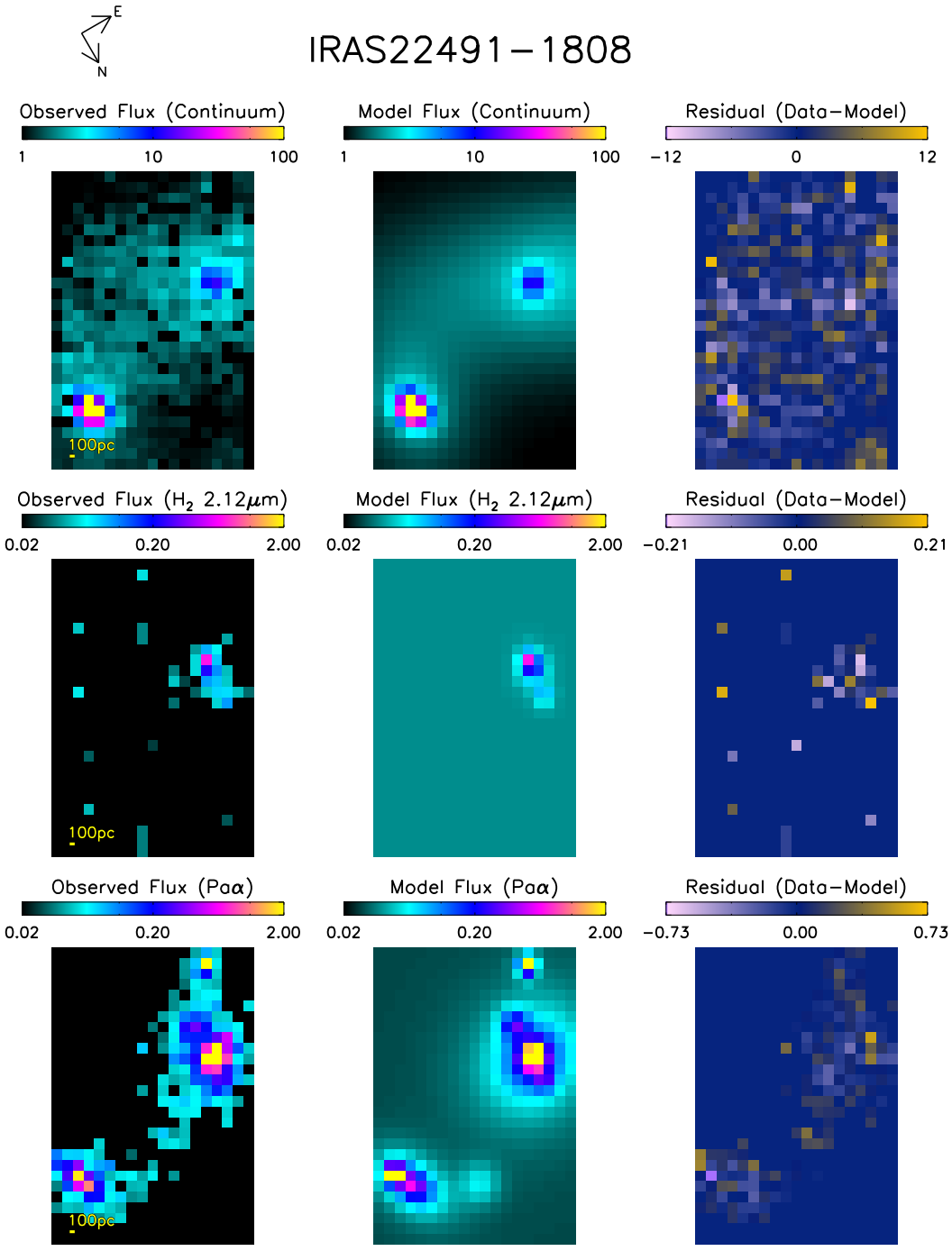

Figure 4.4: Flux map (left panel), GALFIT model (center panel) and residual (right panel) for each galaxy in different tracers.

4.4.2 Disk Kinematics

We find that in 17 of 19 nuclei (from 15 merger systems, 4 of which show confirmed dual nuclei), there is strong rotation seen in stars, molecular hydrogen and/or atomic hydrogen, evidenced by steep velocity gradients across the major axis. Velocity maps and a one-dimensional velocity profile across the major axis are shown for each galaxy nucleus in Figure 4.5. In most cases, the kinematics from different tracers (stars, molecular gas, ionized gas) are similar. This suggests that the stars likely formed *in situ* from the gas disks.

To test the hypothesis that these are young stars forming *in situ*, we measure the equivalent width W_{CO} of the 2.292 μm absorption feature for galaxies with that feature. Because these features are deepest in giants and supergiants, which evolve more quickly than their lower-mass siblings, W_{CO} can be correlated with the age of a stellar population. We compare our measurements to a fiducial model of an instantaneous starburst from Figure 101b of Leitherer et al. (1999a) to determine the corresponding starburst age. It is important to note that hot dust in the nuclear regions can produce nonstellar continuum that will dilute the W_{CO} measurements. As such, our W_{CO} measurements are lower limits to the actual W_{CO} of the stars in the nucleus. This then corresponds only to an upper limit to the age of the stars. Our measurements of W_{CO} and the corresponding ages are listed in Table 4.4. We find that our CO bandheads are quite deep, with an average equivalent width exceeding 12.5 Å. The two galaxies with markedly lower W_{CO} measurements, NGC 6090 and UGC5101, are both known to have a central AGN and are likely more contaminated than the others. This evidence

Table 4.4: CO 2.292 μm Equivalent Widths

Galaxy Name	W_{CO} (Å)[a]	Starburst Age (yr)[a,b]
CGCG436-030	18.65	1×10^7
IIIZw035	13.29	2.5×10^7
MCG+08-11-002	16.43	1×10^7
NGC 2623	12.52	3×10^7
UGC5101	5.75[c]	6×10^8
NGC 6090	7.54	2×10^8
NGC 6240N	13.53	2.5×10^7
NGC 6240S	12.24	3×10^7

[a]The presence of nonstellar continuum may confound some or all of these measurements; for that reason, these should be considered a lower limit to the W_{CO} values and an upper limit to the stellar population ages.

[b]Starburst ages were estimated using Figure 101b from Leitherer et al. (1999a).

[c]To attempt to minimize the nonstellar continuum, the central 3x3 pixel region was excluded for this calculation.

supports the idea that the stars were formed quite recently in the disks.

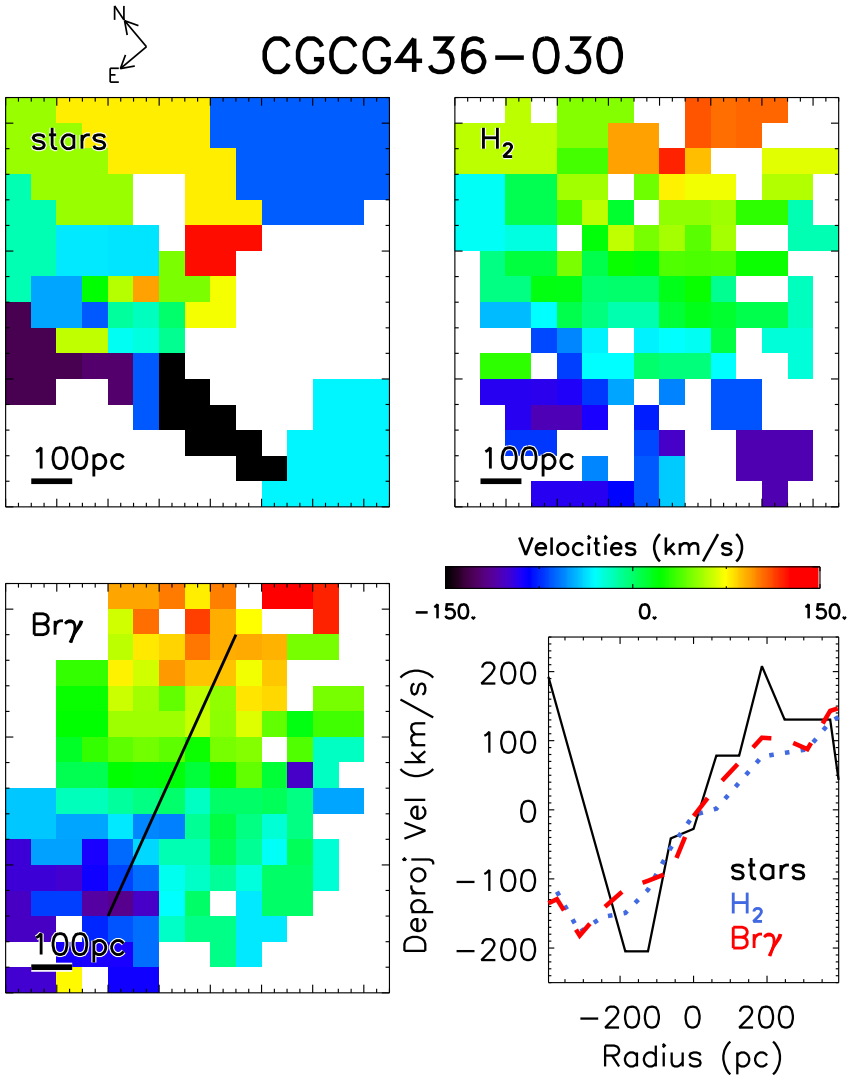

Figure 4.5: Observed velocity maps of stars (top left), molecular gas in H_2 (top right), and ionized gas in Brγ or Paα (bottom left) for each galaxy. All velocity maps use the same color bar; white pixels do not have sufficient signal to measure velocities accurately. Bottom right panel shows the reprojected velocity profile cut through the major axis for each of the 3 tracers: stars (solid black), H_2 (dotted blue), Brγ or Paα (dashed red). The major axis cut is indicated in black on the bottom left map for clarity.

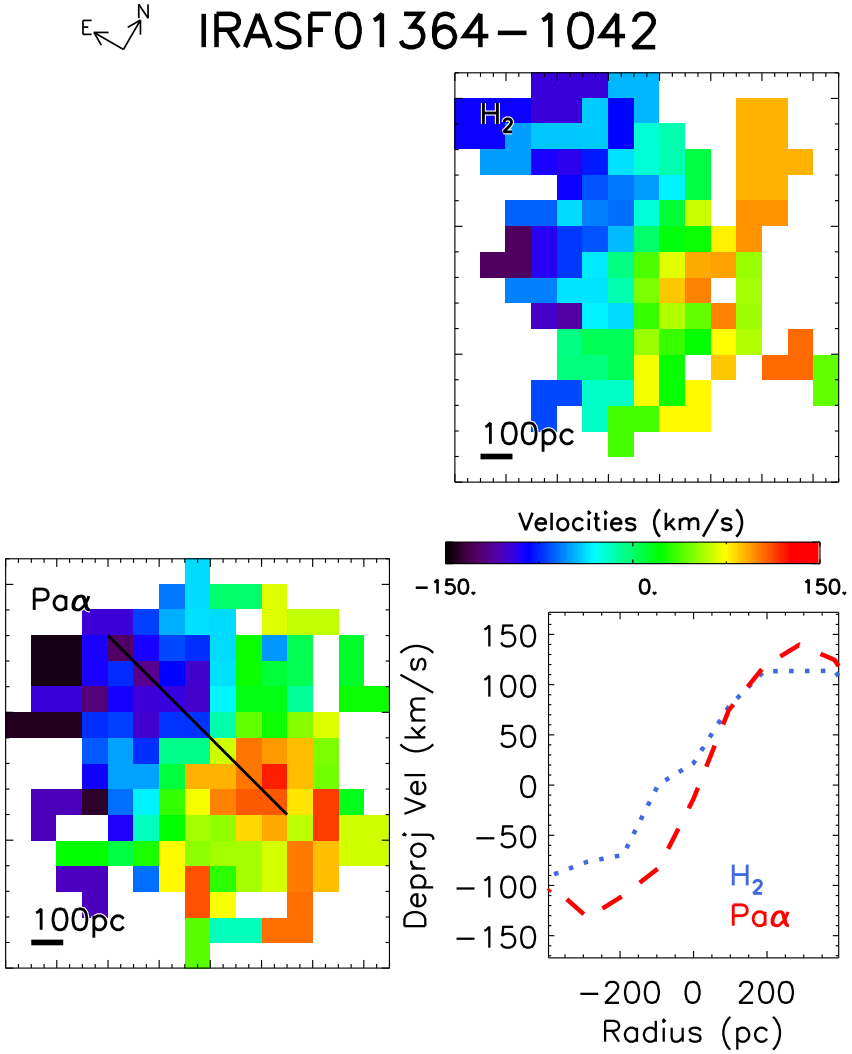

Figure 4.5: Observed velocity maps of stars (top left), molecular gas in H_2 (top right), and ionized gas in Brγ or Paα (bottom left) for each galaxy.

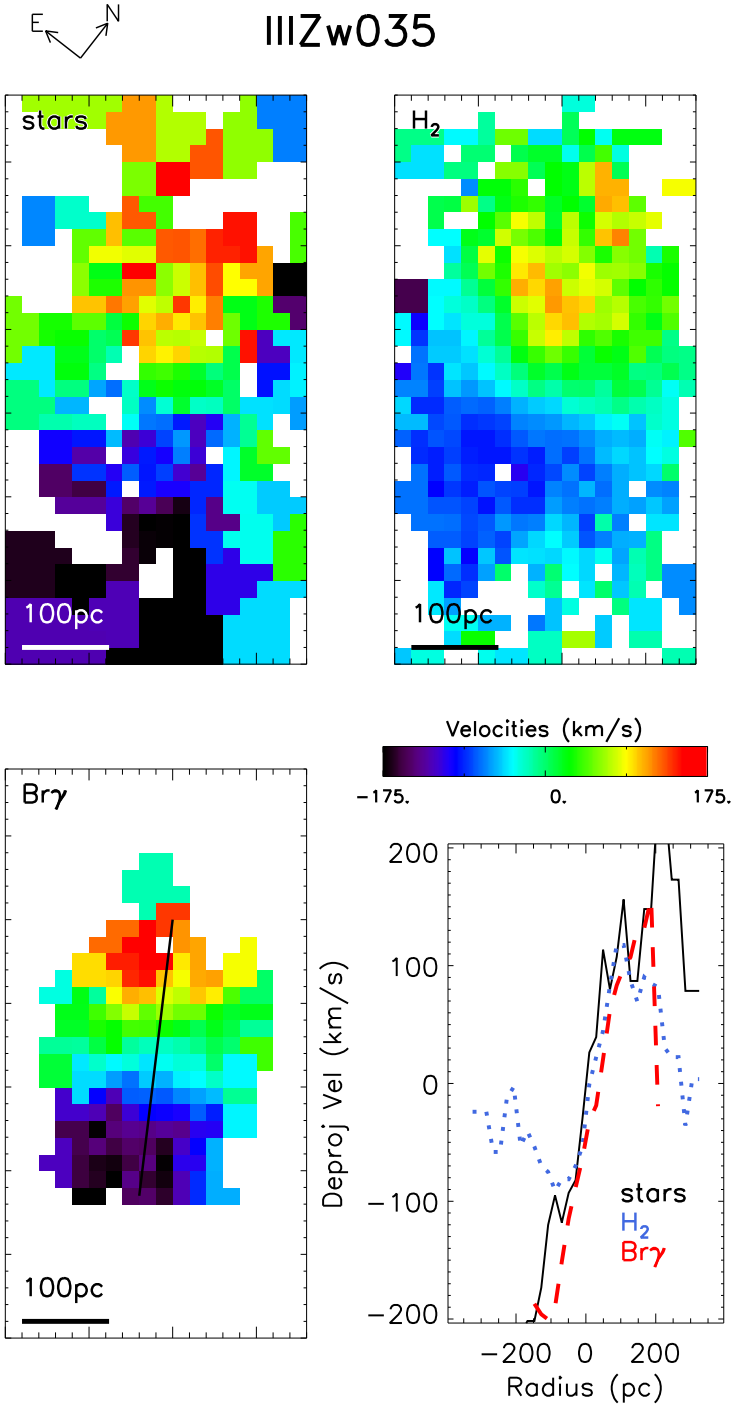

Figure 4.5: Observed velocity maps of stars (top left), molecular gas in H_2 (top right), and ionized gas in Brγ or Paα (bottom left) for each galaxy.

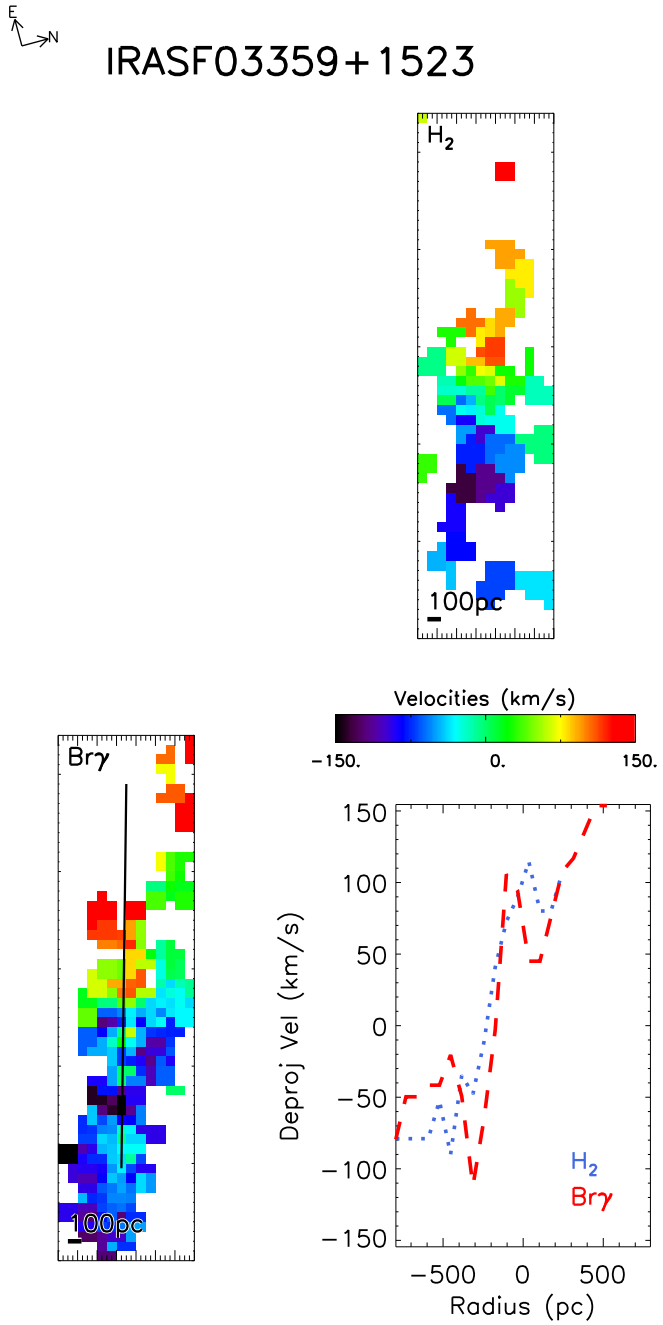

Figure 4.5: Observed velocity maps of stars (top left), molecular gas in H_2 (top right), and ionized gas in Brγ or Paα (bottom left) for each galaxy.

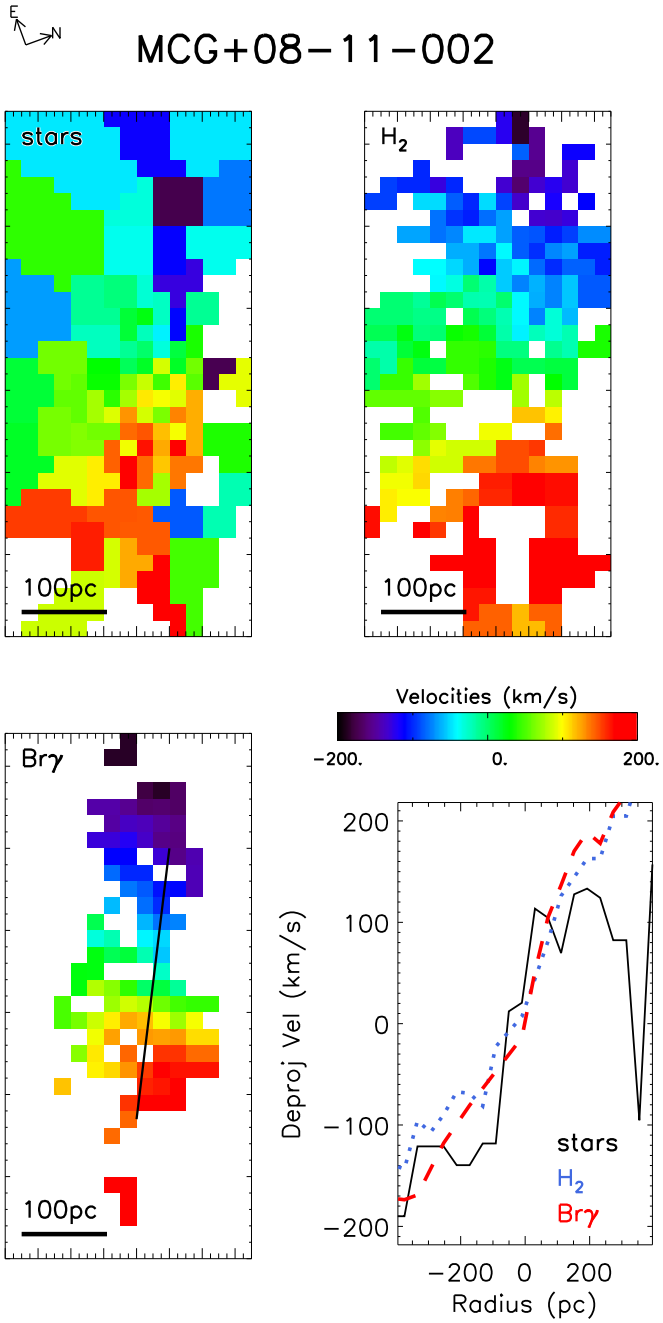

Figure 4.5: Observed velocity maps of stars (top left), molecular gas in H_2 (top right), and ionized gas in Brγ or Paα (bottom left) for each galaxy.

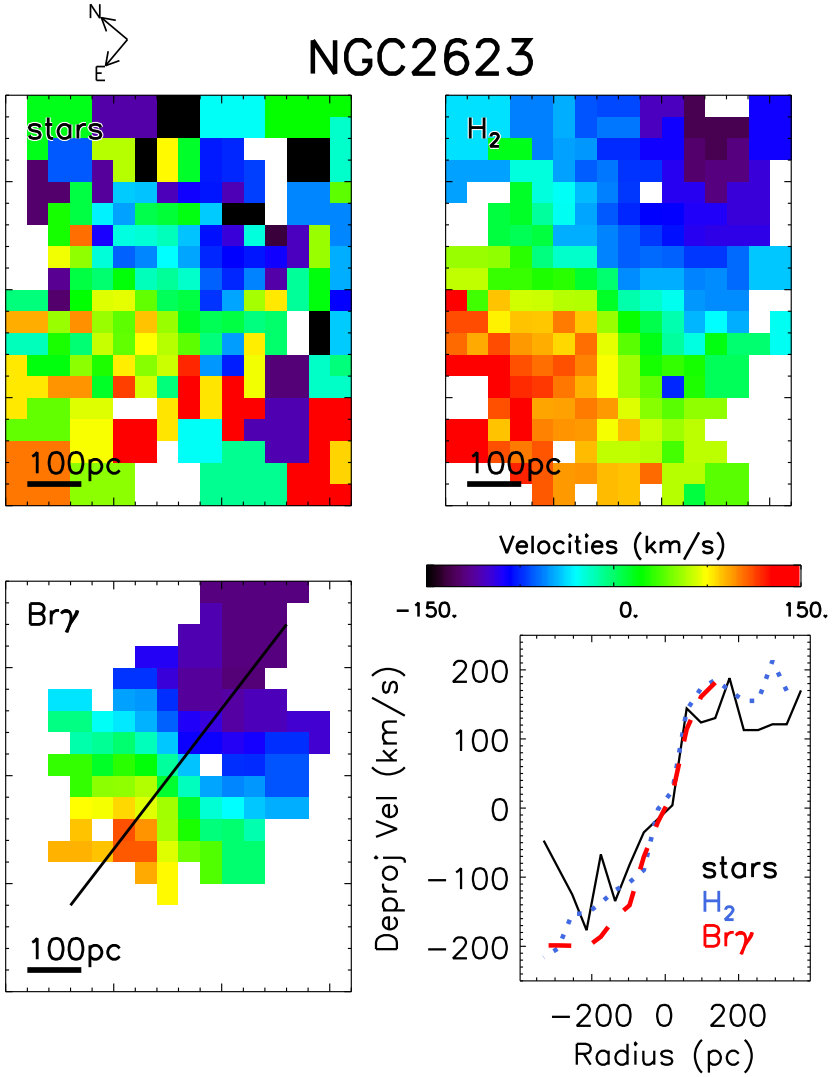

Figure 4.5: Observed velocity maps of stars (top left), molecular gas in H_2 (top right), and ionized gas in Brγ or Paα (bottom left) for each galaxy.

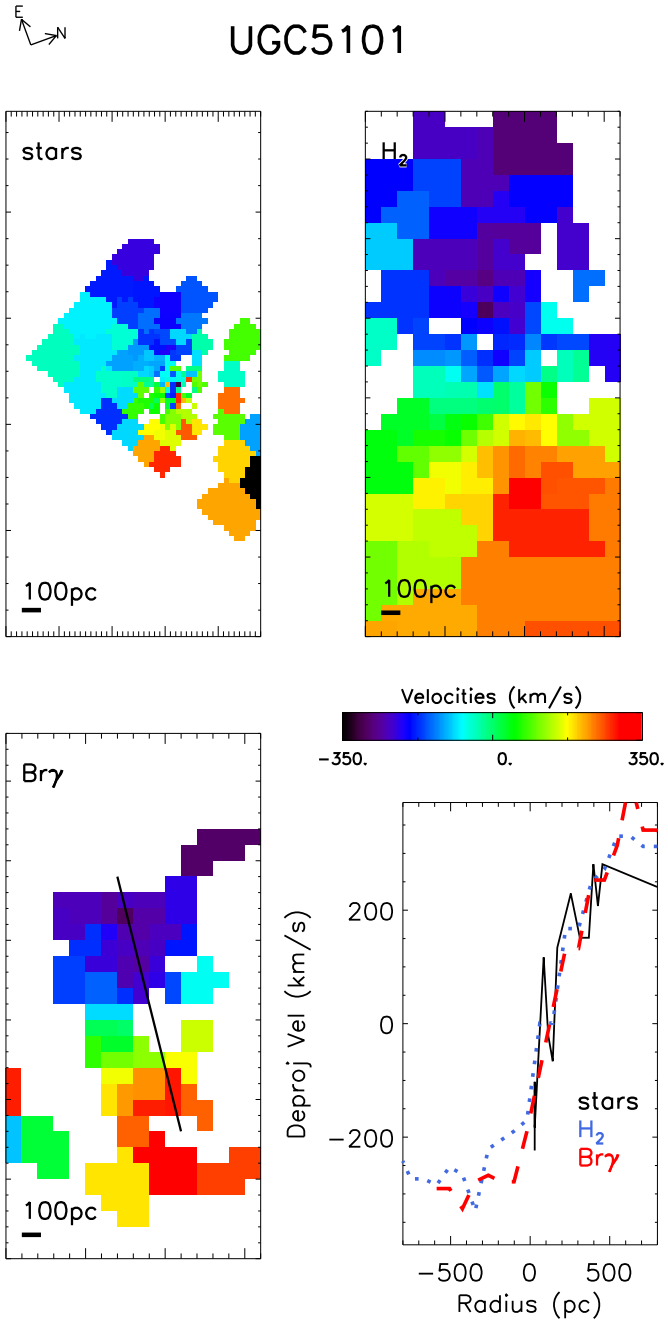

Figure 4.5: Observed velocity maps of stars (top left), molecular gas in H_2 (top right), and ionized gas in Brγ or Paα (bottom left) for each galaxy.

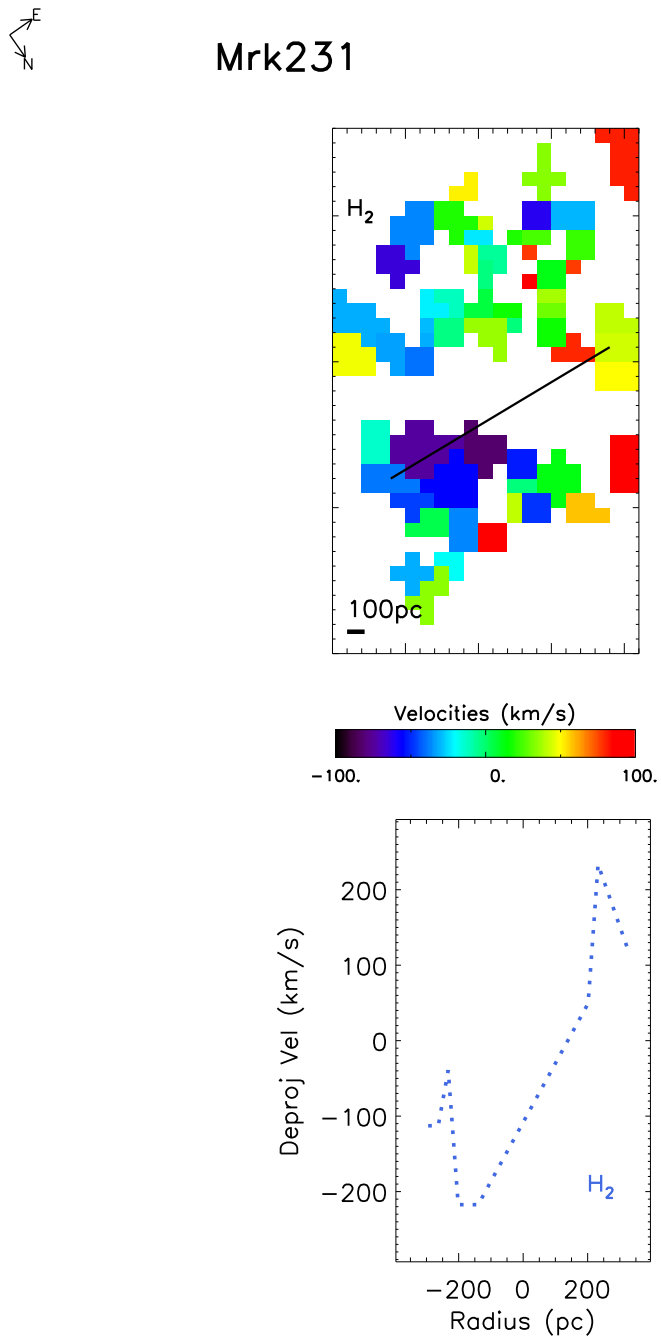

Figure 4.5: Observed velocity maps of stars (top left), molecular gas in H_2 (top right), and ionized gas in Brγ or Paα (bottom left) for each galaxy.

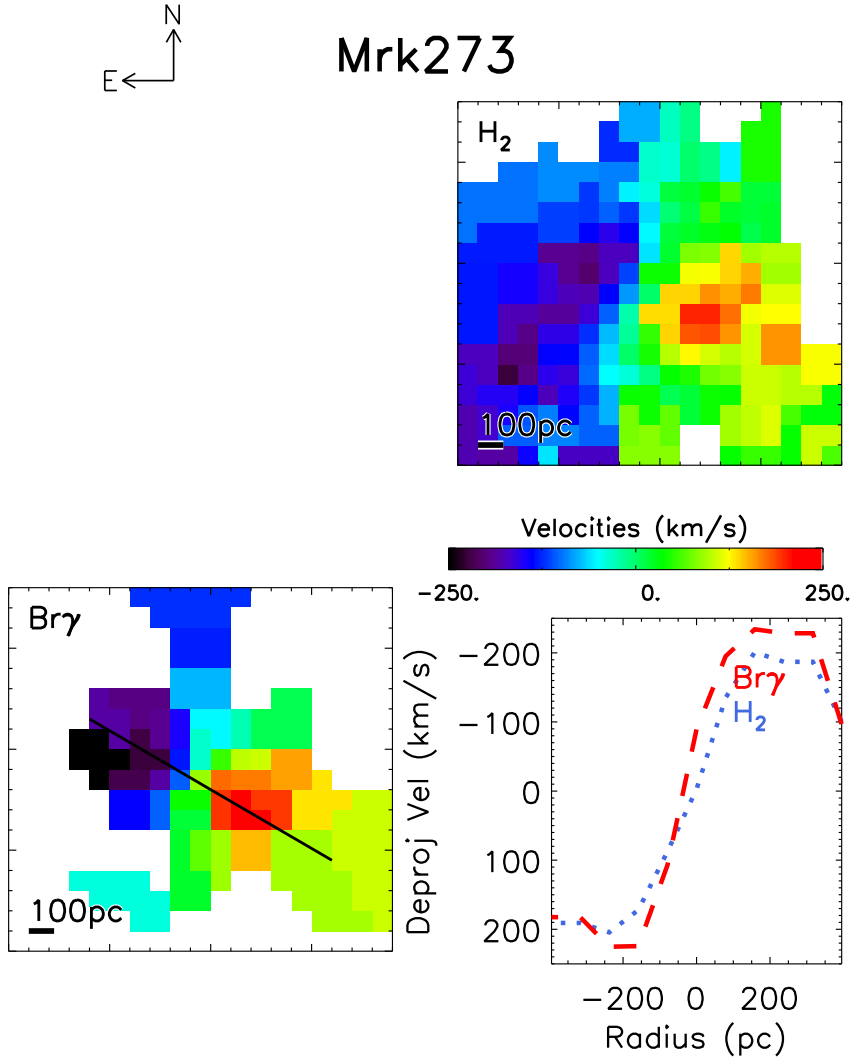

Figure 4.5: Observed velocity maps of stars (top left), molecular gas in H_2 (top right), and ionized gas in Brγ or Paα (bottom left) for each galaxy.

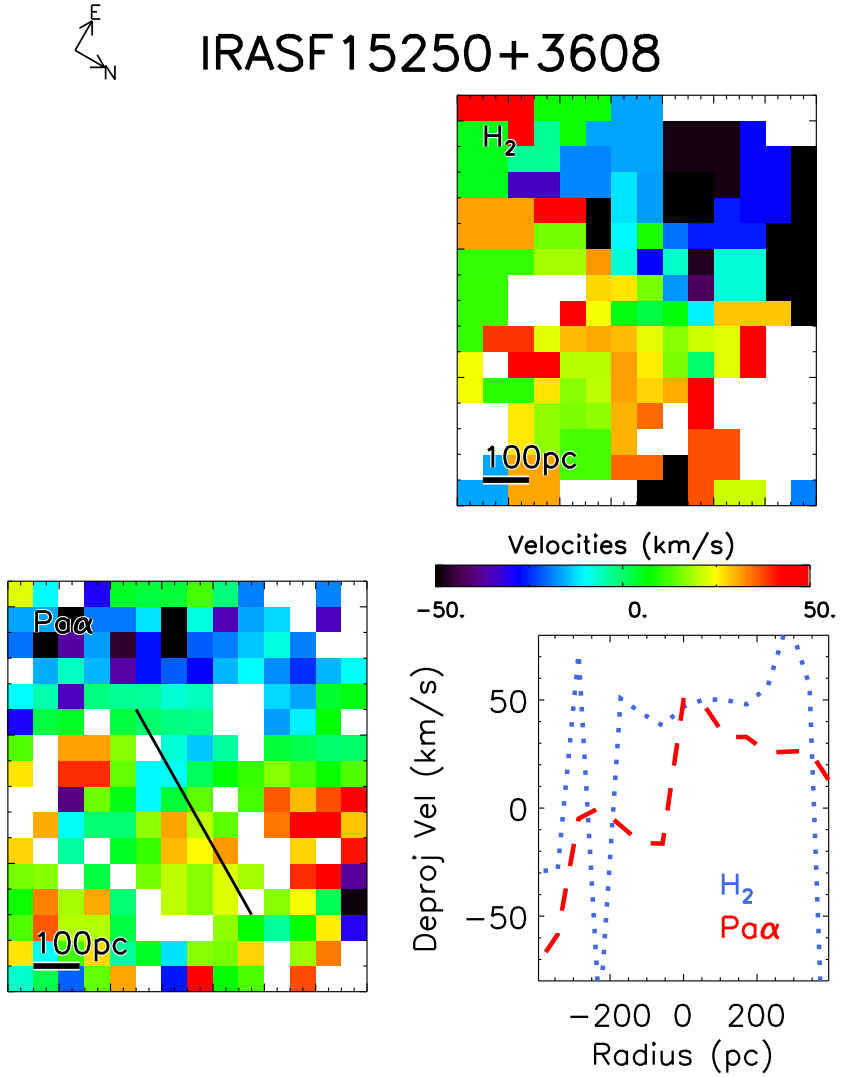

Figure 4.5: Observed velocity maps of stars (top left), molecular gas in H_2 (top right), and ionized gas in Brγ or Paα (bottom left) for each galaxy.

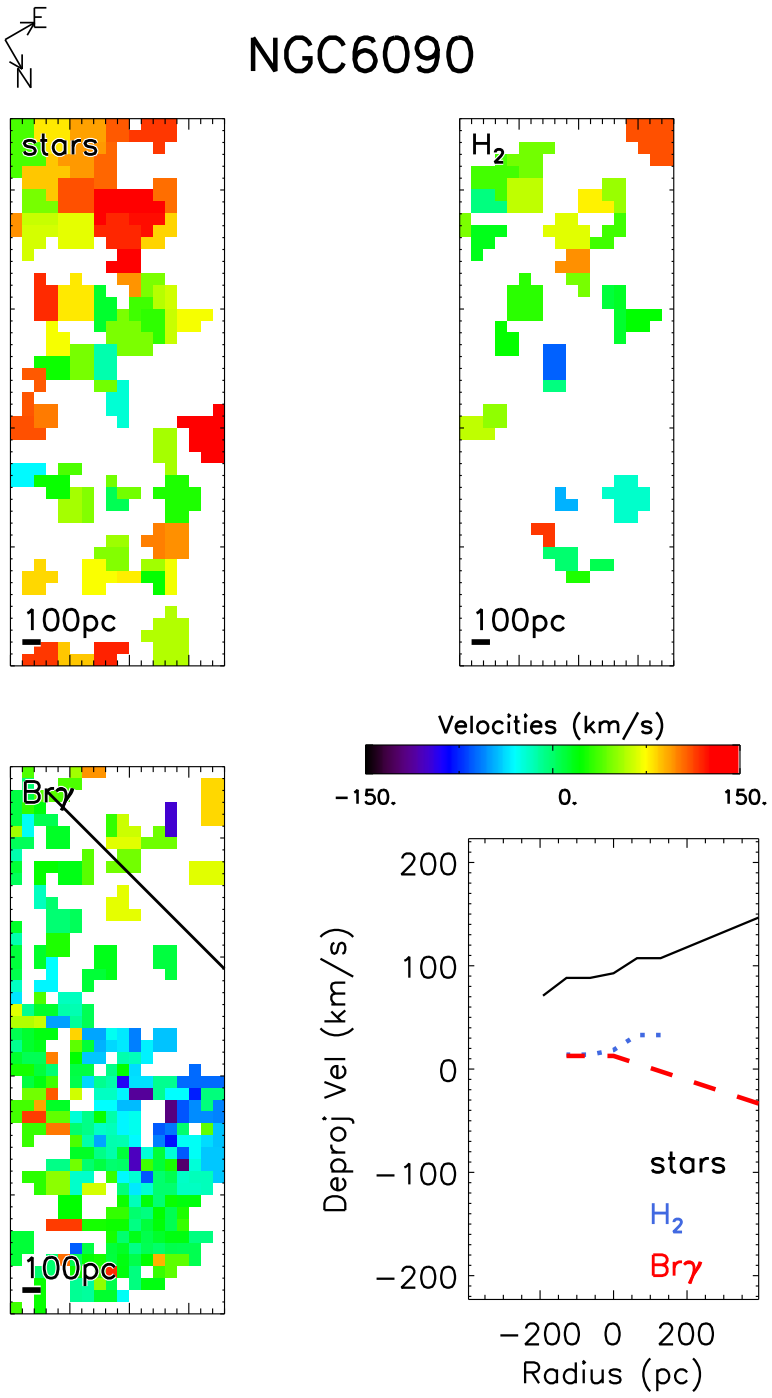

Figure 4.5: Observed velocity maps of stars (top left), molecular gas in H_2 (top right), and ionized gas in Brγ or Paα (bottom left) for each galaxy.

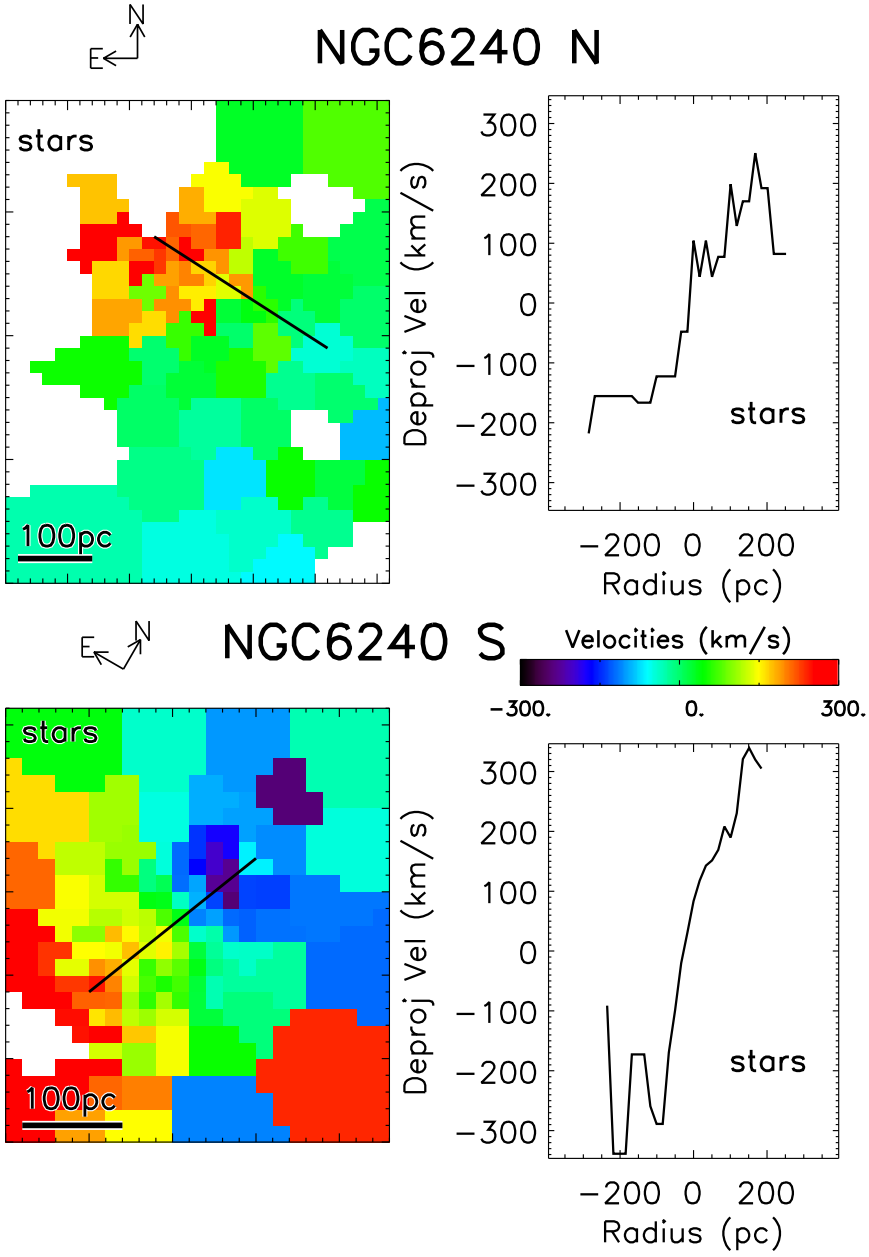

Figure 4.5: Observed velocity maps of stars (top left), molecular gas in H_2 (top right), and ionized gas in Brγ or Paα (bottom left) for each galaxy.

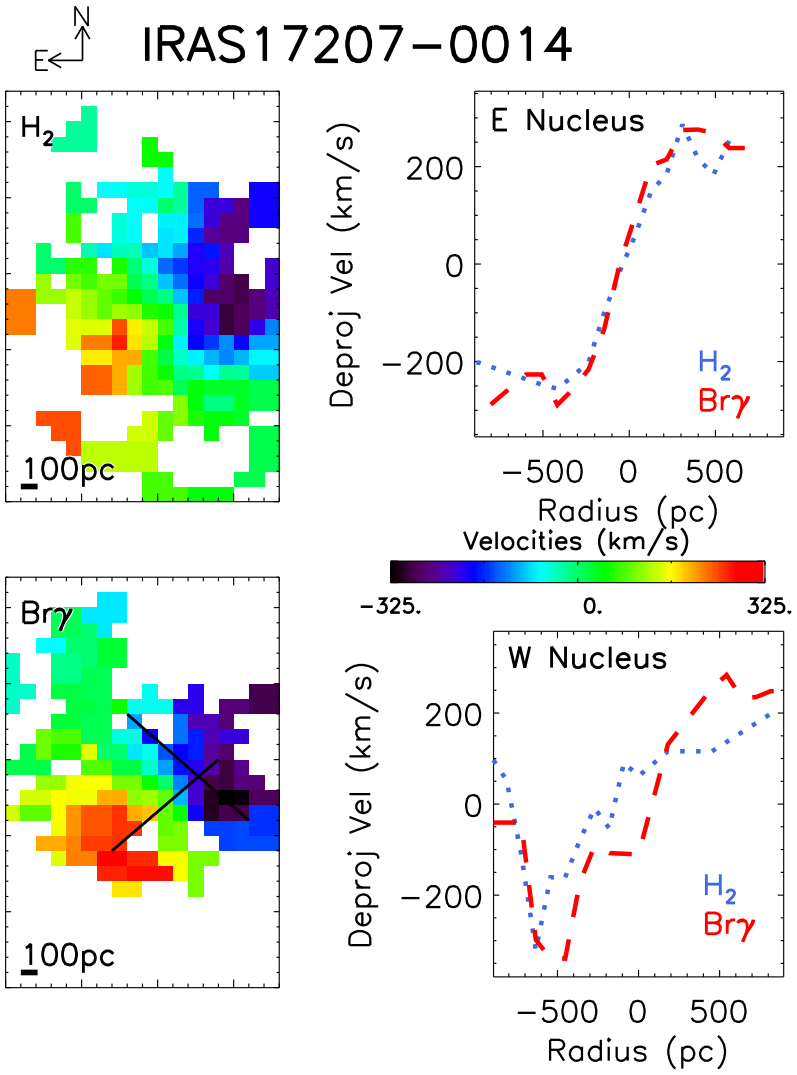

Figure 4.5: Observed velocity maps of stars (top left), molecular gas in H_2 (top right), and ionized gas in Brγ or Paα (bottom left) for each galaxy.

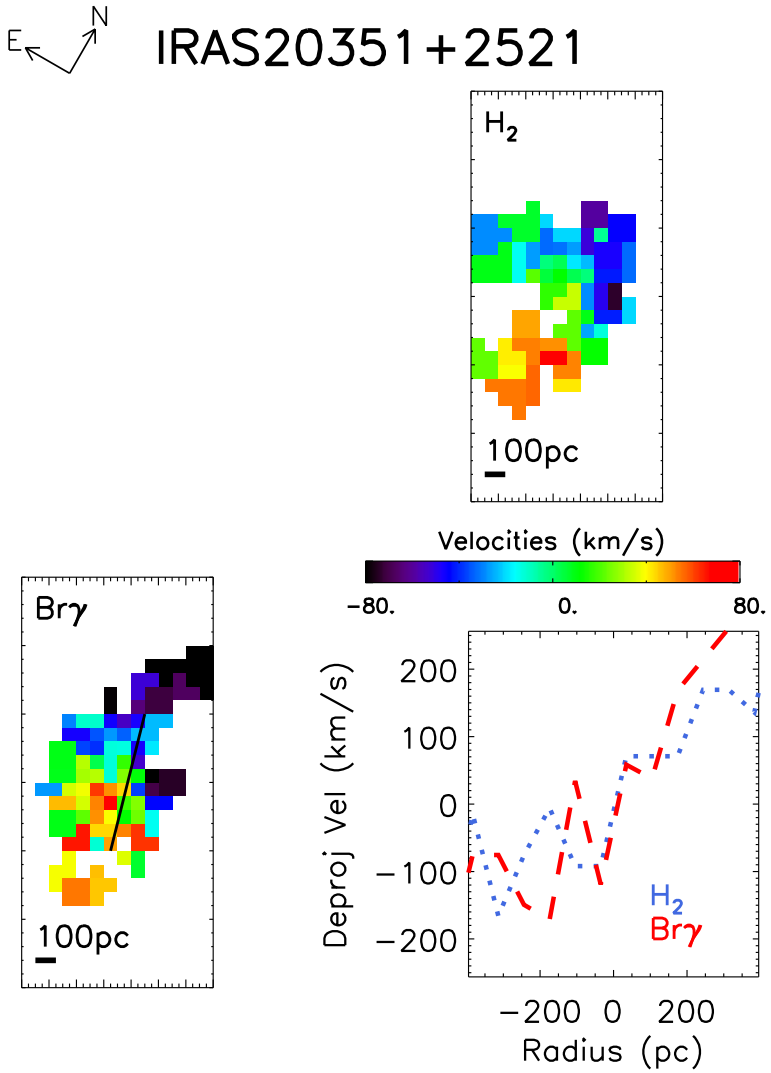

Figure 4.5: Observed velocity maps of stars (top left), molecular gas in H_2 (top right), and ionized gas in Brγ or Paα (bottom left) for each galaxy.

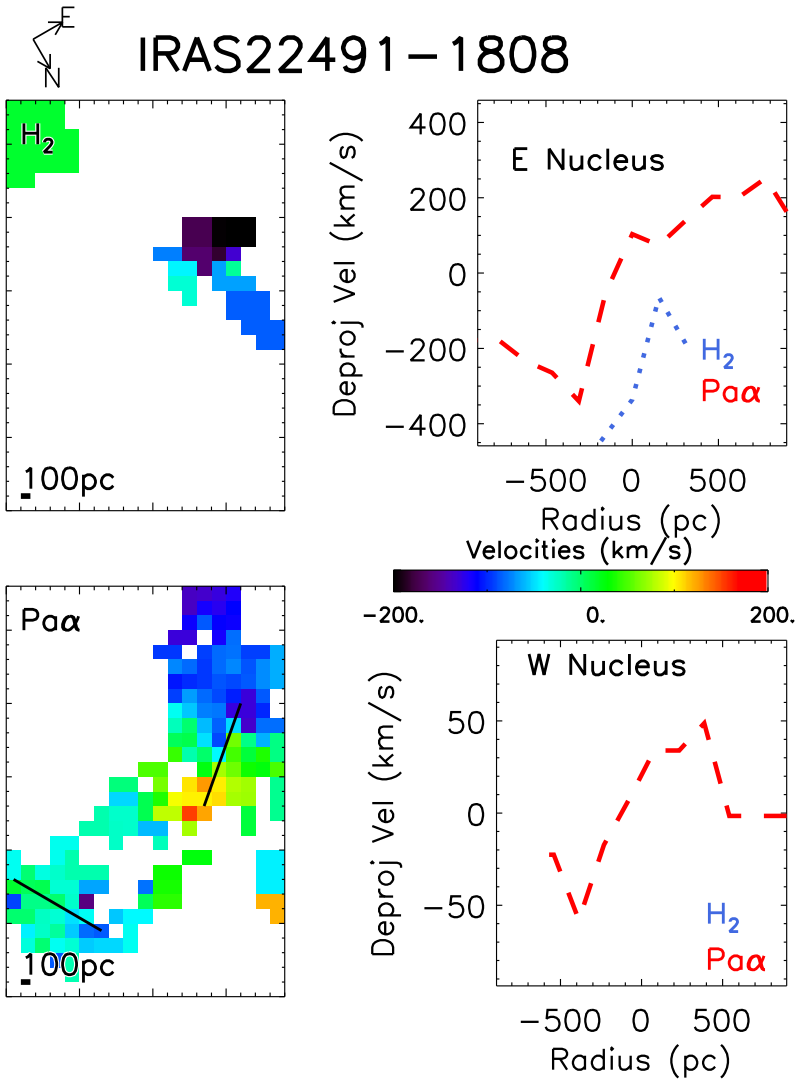

Figure 4.5: Observed velocity maps of stars (top left), molecular gas in H_2 (top right), and ionized gas in Brγ or Paα (bottom left) for each galaxy.

An interesting parameter to measure is v/σ, the ratio of peak velocity to velocity dispersion, which indicates how dynamically cold the orbits are. For a thin disk, $v/\sigma >> 1$. In turbulent or thick disks, this ratio can be closer to 1. However, measuring the intrinsic σ is difficult, because the measured width of a line includes peculiar velocity motions (Kang et al., 2013). In an unresolved disk spectrum, the width of the line is a light-weighted combination of velocity and dispersion at each point: $v_{rms} = \sqrt{v^2 + \sigma^2}$. As one resolves the disk better, this width will shrink as the velocity motions are split into separate pixels. To avoid confusion from this resolution effect, we calculate the intrinsic σ backwards from the v_{rms}. We subtract off the light-weighted contribution from velocity for each spatial pixel using the equation:

$$\sigma^2 = v_{rms}^2 - \frac{\sum(velocitymap * fluxmap)^2}{\sum(fluxmap)^2}$$

This is then reported in Table 4.5.

The average v/σ of these disks is 1.3 ± 0.1 for stars, 1.7 ± 0.2 for H_2, and 1.8 ± 0.2 for atomic hydrogen emission. On average, the gas disks are dynamically colder than the stellar disks by a small margin. The v/σ does not appear to correlate with the infrared luminosity of the host galaxy (see Figure 4.6 and Figure 4.7).

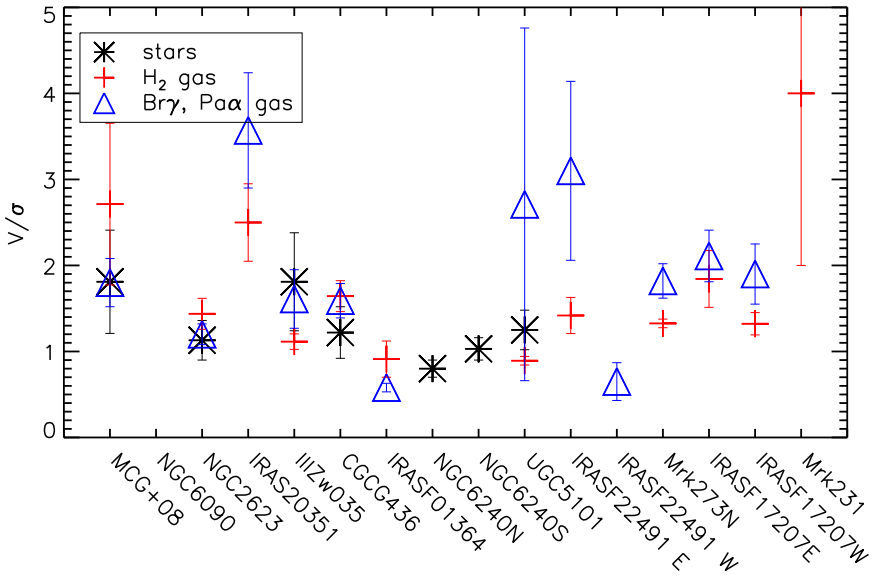

Figure 4.6: v/σ for nuclear disks, sorted according to infrared luminosity of the host galaxy. Points represent the kinematics measured from the stars (black asterisks), the H_2 emission (red crosses), and the Brγ or Paα emission (blue trianges). A horizontal dotted line has been drawn for $v/\sigma = 1$ to show the value at which pressure support and rotational support are equal.

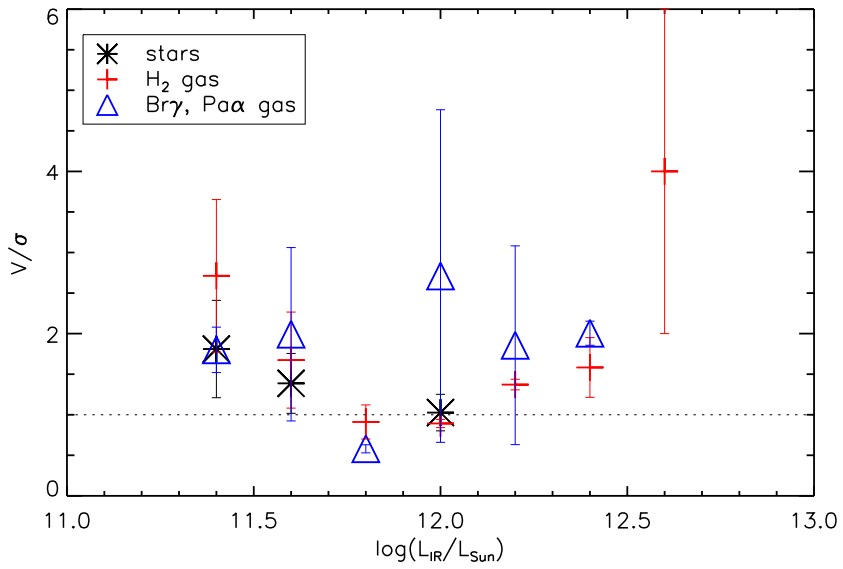

Figure 4.7: v/σ for nuclear disks, binned according to infrared luminosity of the host galaxy. Points represent the kinematics measured from the stars (black asterisks), the H_2 emission (red crosses), and the Brγ or Paα emission (blue trianges). The error bars indicate the standard deviation of the v/σ for each bin. A horizontal dotted line has been drawn for $v/\sigma = 1$ to show the value at which pressure support and rotational support are equal.

Table 4.5: Measured Disk Kinematics

Galaxy Name	Tracer	Peak Velocity (Deprojected; km/s)	Velocity Dispersion (km/s)	v/σ
CGCG436-030	stars	165 ± 25	135 ± 20	1.2 ± 0.3
	H_2	165 ± 9	100 ± 10	1.6 ± 0.2
	Brγ	189 ± 12	120 ± 10	1.6 ± 0.2
IRASF01364-1042	H_2	110 ± 20	121 ± 16	0.9 ± 0.2
	Paα	107.5 ± 10	213 ± 7	0.6 ± 0.05
IIIZw035	stars	240 ± 25	130 ± 40	1.8 ± 0.6
	H_2	127 ± 7	114 ± 7	1.1 ± 0.1
	Brγ	190 ± 15	120 ± 20	1.6 ± 0.3
IRASF03359+1523	H_2	152 ± 35	115 ± 45	1.3 ± 0.6
	Brγ	160 ± 20	120 ± 25	1.3 ± 0.3
MCG+08-11-002	stars	200 ± 20	110 ± 30	1.8 ± 0.6
	H_2	200 ± 10	75 ± 25	2.7 ± 0.9
	Brγ	230 ± 10	125 ± 20	1.8 ± 0.3
NGC 2623	stars	190 ± 35	165 ± 10	1.1 ± 0.2
	H_2	195 ± 15	135 ± 15	1.4 ± 0.2
	Brγ	165 ± 10	137 ± 10	1.2 ± 0.1
UGC5101	stars	272 ± 25	220 ± 35	1.25 ± 0.2
	H_2	367 ± 15	410 ± 15	0.9 ± 0.1
	Brγ	370 ± 20	137 ± 100	2.7 ± 2.0
Mrk231	H_2	168 ± 15	40 ± 20	4 ± 2
Mrk273 N	H_2	247 ± 5	186 ± 6	1.3 ± 0.1
	Brγ	306 ± 6	170 ± 20	1.8 ± 0.2
Mrk273 SW	H_2	...[a]	...	...
	Brγ	...	...	...

Table 4.5 (cont'd): Measured Disk Kinematics

Galaxy Name	Tracer	Peak Velocity (Deprojected; km/s)	Velocity Dispersion (km/s)	v/σ
IRASF15250+3608 NW	H_2	...	...	...
	Brγ	...	...	...
NGC 6090	stars			
NGC 6240N	stars	210 ± 20	255 ± 20	0.8 ± 0.1
NGC 6240S	stars	345 ± 20	340 ± 40	1.0 ± 0.1
IRASF17207-0014 E	H_2	280 ± 15	150 ± 25	1.8 ± 0.3
	Brγ	310 ± 10	150 ± 20	2.1 ± 0.3
IRASF17207-0014 W	H_2	230 ± 15	175 ± 12	1.3 ± 0.1
	Brγ	225 ± 15	120 ± 20	1.9 ± 0.4
IRAS20351+2521	H_2	250 ± 20	100 ± 15	2.5 ± 0.5
	Brγ	345 ± 15	96 ± 18	3.6 ± 0.7
IRASF22491-1808 E	H_2	210 ± 20	150 ± 17	1.4 ± 0.2
	Paβ	325 ± 25	105 ± 35	3.1 ± 1.04
IRASF22491-1808 W	Paβ	65 ± 20	100 ± 10	0.7 ± 0.2

[a]Some nuclei show disky morphology but do not exhibit rotation in the velocity maps; or show rotation in some lines but not others. These cases are indicated by '...'.

4.5 Notes on Individual Galaxies

CGCG436-030: This galaxy shows slight evidence for extended H_2 emission along the minor axis of the disk. Though the stellar kinematics are noisy, they appear to be consistent with the motions of the gas.

IRASF01364-1042: This galaxy shows slight evidence of extended H_2 emission to the south; this extension is between the major and minor axis of the disk. Though a similar velocity gradient appears in H_2 and Paα here, the differences may be related to outflowing structure traced by H_2 and not by Paα.

IIIZw035: This galaxy shows strong extensions in H_2 flux along the minor axis of the galaxy. The bend in the continuum emission may be evidence of a warped disk, which is not modeled here. It should also be noted that the rotation of stars and Brγ match well over most of our field of view, but the H_2 kinematics only match over $\lesssim 200$ pc. Because the GALFIT models do not indicate that the H_2 disk is smaller

in flux, we suggest that the velocity discrepancy may be due to additional H_2 emission that is outflowing, or otherwise not part of the disk, along the line of sight. We see no sign of structure associated with the 22 pc OH maser ring offset in position angle by 40° (Pihlström et al., 2001).

IRASF03359+1523: This galaxy has a large, nearly-edge on disk with a string of star clusters along it. Taking this in conjunction with previous estimates of the merger stage, we suggest that this disk is not a nuclear disk formed during the merger, but is more likely galactic-scale progenitor galaxy's disk that has not yet been disrupted. As such, its parameters are left out of the average nuclear disk calculations.

MCG+08-11-002: The extended bright Brγ emission shows that star formation in the nucleus of this galaxy is considerably strong and clumpy. The flux map of Brγ also suggests the presence of spiral arms which aren't apparent in the continuum map.

NGC 2623: This galaxy has smooth flux profiles and similar kinematics in all tracers.

UGC5101: The residuals of the continuum fit in this galaxy show faint structures resembling spiral arms. Additionally, this galaxy is the only one in our sample to require a central PSF in the H_2 flux GALFIT model.

Mrk231: The central quasar in this galaxy produced an excess of noise in the central regions, making GALFIT models of the continuum emission impossible. Indeed, even the H_2 map is quite noisy. However, the results found here are consistent with the H_2 disk measured by Davies et al. (2004). Binning the data in a 2x2 pattern may be

sufficient to improve estimates.

Mrk273: A thorough analysis of this galaxy was presented in Chapter 3. Though rotation is seen in the northern nucleus, the southwestern nucleus shows none. However, their high resolution NIRC2 images ($0.01''$pixel$^{-}1$) reveal a morphological disk on scales unresolvable by OSIRIS' kinematics. Here we include the southwest nucleus as a disk in Table 4.2 even though these OSIRIS data cannot provide a kinematic confirmation.

IRASF15250+3608: The continuum image reveals a second clump to the southeast of the main nucleus. However, due to the lack of emission line detections, it is not clear whether or not this is a second nucleus or an off-nuclear clump. Velocity maps focus on the main component. This is the only galaxy in our sample for which we see no rotation in either stars or gas. GALFIT model residuals show that multiple components may be present in the main nucleus, but because no kinematic angle has been measured, constraints for additional components are not present. Since the velocity maps do not confirm rotation, even the morphological parameters are left out of the final nuclear disk averages. However, these parameters are included in Table 4.2 for completeness.

NGC 6090: This galaxy's continuum map shows a low-inclination disk with large spiral arms and possibly a bar. As with IRASF013359+1523, the size of the disk and previous estimates of the merger stage suggest that this disk was not formed during the merger, but rather is a large galactic disk that has not yet been disturbed. As such, its parameters are left out of the average nuclear disk calculations. It is also interesting to note that, while the nucleus shows strong continuum, minimal line flux is seen at

the nucleus of the disk. Brγ flux is, however, strong in the spiral arms. Because of this lack of flux, and the limited field of view of these OSIRIS data, obtaining velocity information for the gas across the major axis of the disk is difficult, and provides little insight.

NGC 6240: Masks shown in GALFIT fits were implemented due to the excess of dust present between the two nuclei (Max et al., 2007). Though the narrow-band OSIRIS data presented here do not include emission lines with which to measure gas kinematics, we note that the SINFONI data presented by Engel et al. (2010) suggests that the gas kinematics are dominated by disrupted tidal streaming and shocks, not disks. However, their stellar kinematics are consistent with those presented here.

IRASF17207-0014: This galaxy shows two overlapping disks. They are likely overlapping in superposition rather than actually colliding; such collisions would presumably disrupt the disks. Here as well the H_2 flux map shows morphologies that do not match continuum emission; this may be signs either of outflows or of collisional shocks related to the larger nuclear orbits.

IRAS20351+2521: The clumpy nature of this nucleus is reminiscent of spiral arms; with a large clump of emission appearing in continuum and both line emission maps. The H_2 and Brγ velocity maps show similar kinematics.

IRASF22491-1808: This galaxy also shows two nuclei; in Paα, the strongest emission line, both disks appear to show rotating kinematic signatures. However, though H_2 is detected in the E disk, it does not appear to share the kinematics of Paα. A velocity gradient is seen, but because it isn't centered about the same velocity as Paα, it is more

likely to be due to streaming shocked gas.

4.6 Comparing to Simulations

Recent high resolution hydrodynamical galaxy merger simulations (e.g. Kazantzidis et al., 2005; Mayer et al., 2007, 2008; Callegari et al., 2009; Chapon et al., 2013) have shown that when two gas-rich galaxies merge, gaseous disks will form, providing one possible mechanism for removing angular momentum from the binary black hole system, allowing it to reach final coalescence in less than a Hubble time. With the first integral field survey of observed nuclear disks in nearby gas-rich galaxy mergers, we have the ability to compare important parameters and test the predictions of these simulations against real nuclear disks.

Since studying these disks was not the initial purpose of these merger simulations, a full prescription for star formation was not included in the highest resolution zone at the end of the merger. As such, though gas disks do form in the simulations, stars do not form within them like we observe in our sample. Figure 4.8 shows the v/σ profile for the disks in two simulations: a major gas-rich merger and a minor gas-rich merger. We see that the disk is much larger and diskier in the major merger. We see as noted above that the stellar v/σ profiles are very low, indicating that stars are not forming within the disk. A comparison of disk radii between observations and simulations will require a full radiative transfer treatment in order to conquer the complicating factors of dust and ionizing flux.

Simulations are currently running that include star formation in the highest

resolution setting and can be compared to our observed stellar disks. Additionally, future investigations will explore the dependence of measured morphology and kinematics on viewing angle and merger stage.

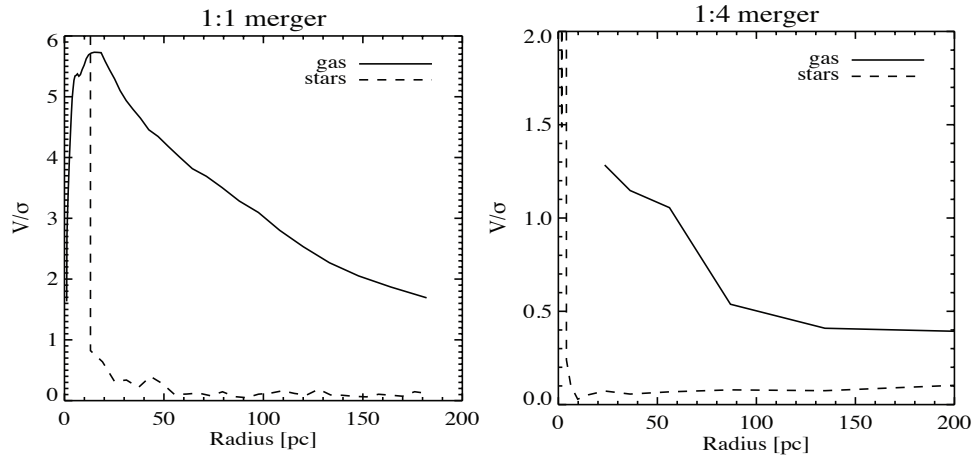

Figure 4.8: Maps of stellar and gas v/σ from two simulations. Kinematics are diskier in the major merger (left); in both cases the gas is dynamically colder than the stars.

4.7 Conclusions

Additional data for this project may be obtained at the end of May 2013 and will be included in the final paper. For now we make conclusions based on the current sample.

The formation of nuclear gas disks has been predicted by hydrodynamical simulations of gas-rich galaxy mergers. In simulations, gas present in the progenitor galaxies is funneled towards the nuclei and forms a disk on scales of a few to a few hundred pc. Stellar disks on these scales have been seen in a number of isolated galaxies, including our own (Lu et al., 2009) and our neighbor M31 (Bender et al., 2005). We

present the first high spatial resolution integral field spectroscopy of a survey of 15 nearby gas-rich major mergers, providing observational evidence of these nuclear disks in both gas and stars. Because the stellar and gas kinematics match well in most cases, we suggest that the stars formed in situ, from cold gas present in the disks.

The formation of these disks seems to be a common occurrence in these gas-rich galaxy mergers. We find gas disks in 15 out of 18 nuclei, and stellar disks in 8 out of 12 nuclei. These disks have radii ranging from 50 to 1850 pc, and have v/σ of generally between 1 and 2. This is in qualitative agreement with nuclear disks seen in simulations. More detailed comparisons with simulations will be presented in a future paper. We find stellar and gas disks both around individual nuclei before coalscence (e.g. IR17207-0014) and in the final coaelsced nuclei (e.g. NGC 2623). Though the disks may be disrupted during the final stages of the merger, they appear to reform quickly.

The near-ubiquitousness of disks in these gas-rich major mergers suggests that galaxy interactions may be a source of the kinematically decoupled cores seen in isolated galaxies, supporting the conclusions of previous authors (e.g. Kormendy, 1984; Bender, 1988; Balcells & Quinn, 1990; Hernquist & Barnes, 1991; Bender, 1988; Hau & Thomson, 1994). These kinematically decoupled cores exist on scales of a few hundred parsecs, which is similar to the disk sizes formed here. Though these data only show that disks exist during mergers, their stellar components at least are likely to persist and may become the dynamically-cold cores seen in isolated galaxies. In a future paper, we intend to expand this observational sample to include galaxies at a wider range of

merger stage to trace the evolution of these nuclear disks. The disks seen here do not appear to be significantly decoupled from their host galaxies in position angle on the sky. Studying the kinematics on larger scales throughout the merger stage is necessary to determine if and when these disks decouple from the larger system.

Finally, the presence of these nuclear disks during galaxy mergers is likely to assist in the final coalescence of binary black holes. Though these data with resolutions of tens of parsecs do not directly confirm the presence of gas in the final parsec, simulations of these disks show that gas disks at tens or hundreds of parsecs funnel gas effectively to parsec scales (Mayer et al., 2007; Chapon et al., 2013). Our observations reveal that star formation is occurring in these disks as well; it may be that star formation in these disks can replenish the region of stars ejected by the binary black holes (the so-called "loss cone") sufficiently to conquer the last parsec problem. Future simulations that include star formation in the disks are underway.

Chapter 5

Black Hole Scaling Relations During Galaxy Mergers

5.1 Introduction

Virtually every massive galaxy hosts a supermassive black hole in its core. These central black holes are known to correlate well with properties of their host galaxies's bulges (Kormendy & Gebhardt, 2001): bulge mass (Kormendy & Richstone, 1995; Magorrian et al., 1998), bulge luminosity (Marconi & Hunt, 2003), and bulge stellar velocity dispersion (Tremaine et al., 2002; Ferrarese & Merritt, 2000; Gebhardt et al., 2000), all most recently updated by McConnell & Ma (2013). There is some evidence for an evolving $M_{BH} - \sigma_*$ relation with redshift (e.g. Zhang et al., 2012). Alternatively, the most basic scaling relation may be with total stellar mass (Jahnke et al., 2009; Cisternas et al., 2011a); in this case the evolution with redshift indicates

the changing bulge-to-disk fractions of galaxies.

The mechanism through which black hole masses correlate with galaxy properties has been attributed to gas-rich galaxy mergers (e.g. Hopkins et al., 2006). In this scenario, gravitational torques funnel the gas into the galaxies' centers, triggering two phenomena: an intense burst of star formation to feed the bulge, and accretion of gas on to the black holes in the centers of each galaxy. It has been postulated that the black holes' growth can regulate this process through AGN feedback (Springel et al., 2005b), through massive winds that evacuate the gas from the galaxy on short timescales, cutting off star formation and future black hole growth. This sense of self-regulation has been confirmed observationally by Kauffmann & Heckman (2009), who find that the Eddington ratio of a sample of AGNs depends on the supply of cold gas in the galaxy. If there is plenty of cold gas, the accretion rate does not depend on the quantity of gas available; if the supply of cold gas is limited, the accretion rate depends on the rate at which stellar winds provide fuel for the AGN. Though the detailed mechanisms through which these correlations are formed are still unconfirmed, star formation and black hole growth are fed by the same reservoir of inflowing gas; their growth histories are intertwined. It is likely that these two processes compete for fuel in a predictable fashion.

To understand this interplay, it is critical to look at systems in the midst of this increased fueling. One set of such galaxies are gas-rich mergers, which tend to have extreme bursts of star formation and a higher incidence of AGN activity. How do these mergers fall on black hole scaling relations? Does the black hole grow first,

leaving the stars to slowly use up the remaining gas? Or is star formation cut off once the black hole reaches a bright quasar phase of extreme growth? A merger's position on black hole scaling relations would indicate the relative growth timescales, and confirm whether the putative quasar-mode feedback occurs (see Fig. 1.1). Theoretical arguments have suggested that the starburst has preferential access to the available gas and that therefore a black hole would grow substantially only after star formation has quenched itself and the galaxy bulge is in place (Cen, 2012); this scenario would predict that gas-rich mergers would fall below black hole scaling relations.

Merger-driven galaxy evolution is not a complete explanation, however. Though some AGN studies find a correlation with major mergers (Koss et al., 2010; Ellison et al., 2011), AGNs found with other selection techniques and at different redshift ranges do not show a higher rate of merging than field galaxies (Cisternas et al., 2011b; Kocevski et al., 2012). Instead of mergers bringing in gas, these systems with low-level activity probably are undergoing secular evolution, accreting their gas directly from the cold intergalactic medium. The dividing line between these two processes is not yet well understood; here we focus on understanding the evolution due to major mergers.

In Chapter 4, we have studied the kinematics of both gas and stars in the inner kiloparsecs of a sample of (U)LIRGs, finding that nuclear disks on scales of a few tens to hundreds of parsecs are common. In Chapters 2 and 3, we demonstrate a technique that uses high spatial resolution integral field spectroscopy to measure black hole masses. With kinematic maps that resolve inside the sphere of influence of a black hole, the complex and unrelaxed large-scale dynamics are less important, and black hole

masses can be measured to within a factor of a few. In Chapter 3, the black hole mass measured with this technique was consistent with the measurement made by OH maser kinematics (Klöckner & Baan, 2004).

Using a novel technique such as this to measure black hole masses in these gas-rich mergers is important because more traditional methods of black hole mass measurements rely on assumptions that aren't valid here. Three-integral orbital superposition models (as in Gültekin et al., 2009a; Siopis et al., 2009) are able to use large-field kinematics to separate different components to the galaxy's mass profile; however, this approach requires a dynamically relaxed system and is used therefore in isolated galaxies. Another successful black hole mass measurement technique is reverberation mapping (e.g. Denney et al., 2009, and references therein), which measures the time lag between flux variations of the continuum and the lines in the broad line region. Since (U)LIRGs are so dusty, the broad line regions are too obscured to view.

Obtaining data at spatial resolutions sufficiently high to resolve inside the sphere of influence of a supermassive black hole at the typical redshifts of local (U)LIRGs ($z \lesssim 0.1$) requires adaptive optics systems, which are becoming available at an increasing number of ground-based observatories. Though the Hubble Space Telescope has excellent resolution in the visible bands, its relatively small mirror size limits the resolution at longer wavelengths, necessary to look through the dust in these galactic nuclei; and even at the longest wavelength available to the Wide Field Camera 3 (H-band), these nuclei are still obscured. In order achieve high spatial resolution in the K band, large ground-based telescopes have employed adaptive optics systems which measure

turbulence in the Earth's atmosphere and use a deformable mirror to correct for the resulting distortions. These distortion measurements require references, either a natural guide star (NGS AO) or a laser guide star plus a fainter natural "tip-tilt" star (LGS AO). The addition of laser guide star adaptive optics has increased the area of the sky observable with this technique.

Throughout this paper we have adopted a cosmology of $H_0 = 70\,\mathrm{km\,s^{-1}\,Mpc^{-1}}$, $\Omega_\mathrm{m} = 0.28$, and $\Omega_\Lambda = 0.72$. In §5.2 we present our data and reduction techniques. In §5.3 we briefly describe the kinematic fitting techniques demonstrated in Chapters 2 and 3. In §5.4 we present the black hole masses measured from several tracers and compare them to black hole scaling relations. §5.5 contains our conclusions.

5.2 Observations and Data

We obtained near-infrared integral field spectroscopy of the central kiloparsec of 6 galaxies with OSIRIS, the OH-Suppressing InfraRed Imaging Spectrograph (Larkin et al., 2006) on the W. M. Keck II 10-meter telescope. These data were taken using the 0.035 arcsec pixel^{-1} plate scale. This high spatial resolution is enabled by the Keck Observatory laser guide star adaptive optics system (LGS AO; Wizinowich et al., 2000; van Dam et al., 2004; Wizinowich et al., 2006; van Dam et al., 2006). The system uses a nearby star and a laser spot projected on the sodium layer of the Earth's atmosphere to measure the blurring caused by turbulence; once measured, the system uses a deformable mirror to correct for the distortions in the wavefront and produce diffraction-limited images.

Our OSIRIS observations were comprised of observing sets of object-sky-object; typically each exposure was ten minutes. Observations were taken either in the broad-band K filter (Kbb: 1.965 μm - 2.381 μm) or in a narrow band targeting specific lines (Hn4: 1.652 μm - 1.737 μm; Kn5: 2.292 μm - 2.408 μm). When possible, the primary target lines were the CO (2-0) and (3-1) bandheads at 2.293 μm and 2.323 μm in K or the CO (5-2), (6-3), and (8-5) bandheads at 1.598 μm, 1.6189 μm, and 1.661 μm in H, which trace the kinematics of young stars. We also compare the stellar kinematics in some cases to those of various emission lines: [Fe II] 1.644 μm, Brγ 2.16 μm, H_2 2.12 μm. For some galaxies, stellar kinematics were not available, and we rely on the aforementioned emission lines for this analysis. Total exposure times, observed filters, and parameters of the observed galaxies are listed in Table 5.1. Some of these data were presented in previous chapters, these are indicated in Table 5.1 as well.

Additionally, we have obtained similar data for five other galaxies: Mrk231, MCG+08-11-002, NGC 6090, IRASF17207-0014, and IRAS20351+2521. Their analysis has not yet been completed, but will be done before publication. With luck, the sample will be increased further in our observing run at the end of May 2013.

We reduced our OSIRIS observations using the OSIRIS Data Reduction Pipeline version 2.3 (available at `http://irlab.astro.ucla.edu/osiris/pipeline.html`), which includes modules to subtract sky frames, adjust channel levels, remove crosstalk, identify glitches, clean cosmic rays, extract a spectrum for each spatial pixel, assemble the spectra into a data cube, correct for atmospheric dispersion, perform telluric corrections, and mosaic frames together. For some cases we utilized the Scaled Sky Subtraction

Table 5.1: Details of OSIRIS Observations for Black Hole Studies

Galaxy Name	Redshift	Date(s) YYMMDD (UT)	Filter	Exp Time on Target (minutes)	Exp Time on Sky (minutes)
IIIZw035[a]	0.0278	111210	Kbb	100	50
NGC 2623	0.0196	100304, 100305	Kn5	100	50
UGC5101[a]	0.039	100304, 100305	Kn5	80	50
Mrk273/UGC8696[b]	0.038	120522	Hn4	60	30
NGC 6240N[a]	0.0232	090617	Kn5	210	75
NGC 6240S[c]	0.0232	070421	Kn5	20	10

[a]Originally presented in Chapter 4
[b]Originally presented in Chapter 3
[c]Originally presented in Chapter 2

module based on the technique outlined in Davies (2007), which scales the thermal continuum and OH line groups separately to provide optimal sky subtraction; we modified the module to include a smoother subtraction of the thermal continuum, as in Chapter 4.

We imaged the tip-tilt stars for each galaxy during the course of the observations in order to obtain an estimate of the point-spread function (PSF). A Moffat function was fit to each tip-tilt star and then broadened according to the distance between the target and the tip-tilt star. This broadening accounts for differential image motion between the tip-tilt star and the galaxy; the further a target is from its tip-tilt star, the worse its PSF will be. The isokinetic angle for the Keck II AO system, at which the Strehl ratio is reduced to 37% of its peak value, is approximately 75 arcseconds.

5.3 Kinematic Fitting

We measured the kinematics following the methods presented in detail in Chapter 2 for stellar kinematics and Chapter 3 for emission line kinematics. We briefly describe these techniques here.

For each measurement, we first calculate the signal-to-noise ratio in each pixel and bin them using optimal Voronoi tesselations (Cappellari & Copin, 2003) in order to require a certain signal-to-noise ratio for reliable measurements. We used signal-to-noise ratio thresholds of 20 and 3 for stellar kinematics and emission line kinematics, respectively. Once binned, stellar kinematics were fit using the penalized pixel fitting routine (Cappellari & Emsellem, 2004, available at `http://www-astro.physics.ox.ac.uk/~mxc/idl/`) and using K-band templates of late-type giants and supergiants from GNIRS (Winge et al., 2009) and unpublished H-band templates provided by Nate McCrady (private communication). Emission lines were fit with Gaussian profiles to determine the flux, velocity, and velocity dispersion in each bin. For emission lines where multiple lines exist in a specific band (the 5 H_2 transitions in the K-band, or Brδ and Brγ), those lines were fit simultaneously, requiring that the velocity and velocity dispersion be consistent between lines.

5.4 Black Hole Masses

Our black hole mass measurement techniques have been demonstrated in two prior chapters. In Chapter 2, we place limits on the mass of the black hole in the south nucleus of NGC 6240 using 2-D stellar kinematic maps and two methods. We calculate the lower limit to the mass by assuming the stars lie in a thin Keplerian disk, and fit a density profile including a black hole and a smoothly-varying spheroidal mass component: $\rho(r) = M_{BH} + \rho_0 r^{-\gamma}$. Because of the high spatial resolution of our data, we probe radii small enough that the first term dominates over the second. The measured

black hole mass here is a lower limit because this method ignores velocity dispersion (assuming that all measured velocity dispersion is due to material along the line of sight, not intrinsic to the disk). Any intrinsic velocity dispersion in the disk will require that there be extra mass in the black hole. In the second technique, we obtain an upper limit on the black hole mass by assuming the opposite: that all measured velocity dispersion is intrinsic to the disk. Because the system is unrelaxed, there is unvirialized material along the line of sight increasing the velocity dispersion but not knowing about the central black hole mass. To find this limit, we use Jeans Axisymmetric Mass models (JAM; Cappellari, 2008).

In Chapter 3, we measure the mass of the black hole in the north nucleus of Mrk273 in a similar manner. Since no stellar kinematics were available, the JAM models are not feasible. When only gas kinematics are available, we model the gas as a thin Keplerian disk and proceed as in the first case above. The black hole mass measured for this galaxy agrees well with the measurement made using the kinematics of an OH maser (Klöckner & Baan, 2004), and therefore provide independent validation for this technique. We note that the thin Keplerian disk approximation provides reasonable agreement even though the disks analyzed in Chapter 4 are thick rather than thin, with $v/\sigma \sim$1-2.

In each case, errors on the black hole mass measurement were obtained using a Monte Carlo approach. We created a model datacube and added random noise appropriate to the signal-to-noise of each spectrum and then refit the black hole mass for 100 iterations. The width of the resulting mass distribution is the error on the measurement.

We have repeated the above analysis for the systems listed in Table 5.1, and include their fits in Figure 5.2. JAM results for UGC5101 and NGC 6240N require a more detailed analysis to correct for the central PSF and extinction, respectively, and so are not included in these results. It is interesting to note that NGC 2623 and NGC 6240S show black hole masses that are relatively consistent for both stellar disk and stellar JAM models; IIIZw035 instead shows more than an order of magnitude variation between methods. It is perhaps surprising that two of the three with multiple methods show such consistent results; the implication would be that the disks are indeed thin, which is at odds with the $v/\sigma \sim 1$ measured in Chapter 4. IIIZw035's v/σ is in fact slightly higher, but not by much. IIIZw035's discrepancy may be due to extinction, can play a large role in confounding the JAM models. It is encouraging that the Brγ models produce a black hole mass which is between the upper and lower limits produced by the stellar measurements.

The black hole mass measurements from our sample are listed in Table 5.2, along with parameters useful for black hole scaling relations from the literature: the stellar velocity dispersion of the bulge, the stellar mass of the bulge, and the total stellar mass of the galaxy. Though consistent treatment of such parameters when drawing from the literature is difficult, care was taken to select measurements most appropriate to the scaling relation. The bulge luminosities and total stellar masses were taken from the GOALS papers Haan et al. (2011) and U et al. (2012), respectively. These survey papers allow us to be confident that the bulge luminosities and total stellar masses were measured consistently across our sample. However, no such survey paper exists

currently to measure the stellar velocity dispersions of the bulges. Instead, we selected the stellar velocity dispersion measurement from the aperture that most closely aligned with the size of the bulge.

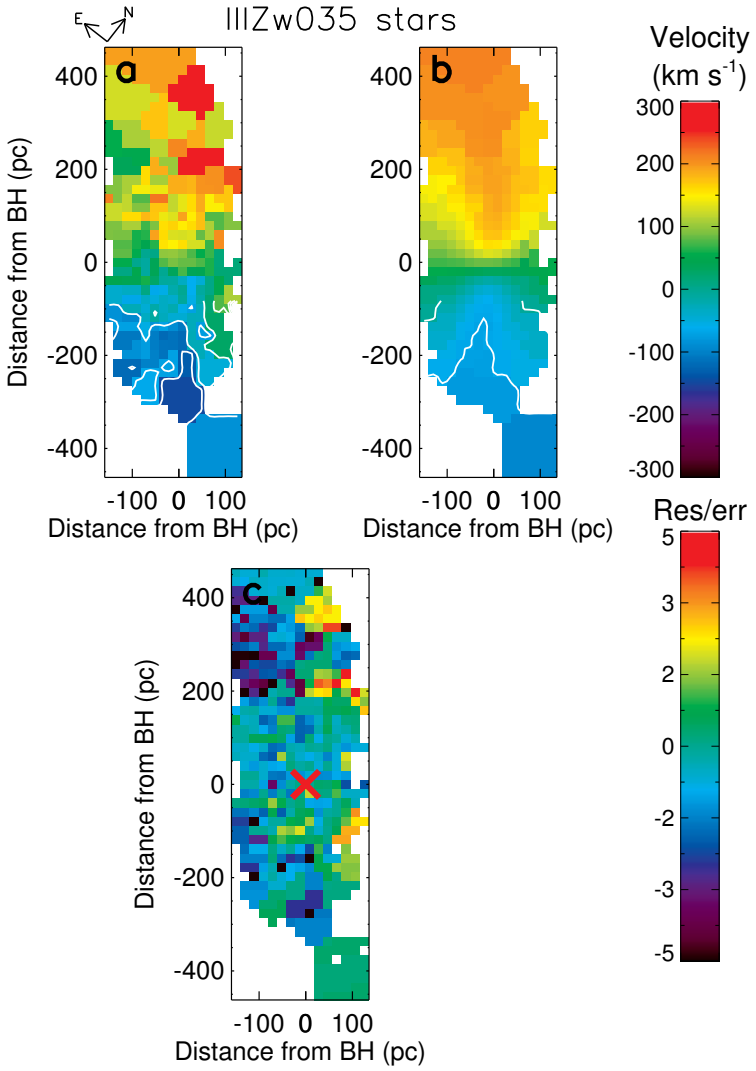

Figure 5.1: a) Map of stellar velocities of the inner region of IIIZw035. b) Map of model stellar velocities of best fit black hole model. c) Residual map of best-fit model divided by errors in velocity. In panels a) and b), velocity contours are marked in white. In each panel, a red X marks the position of the black hole.

Using these results, we place the galaxies on several black hole scaling relations.

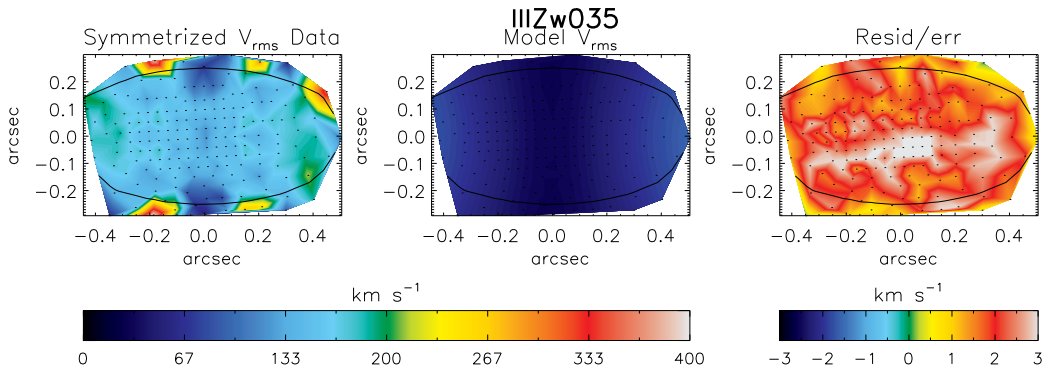

Figure 5.1: Left: Map of the symmetrized $v_{rms} = (v^2 + \sigma^2)^{0.5}$ of IIIZw035. Center: Model v_{rms} of galaxy with black hole. Right: Residual map of model - data divided by errors in v_{rms}. All three panels are centered on the black hole and have been rotated so the major axis is horizontal.

In Figure 5.3 we show the $M_{BH} - \sigma_*$ relation from McConnell & Ma (2013) with our points overlaid. They lie on or above the relation, suggesting that black holes may grow before the bulges are virialized. However, measuring the velocity dispersion of stars in the bulge can be difficult to define when bulges are not yet finally formed, or when two bulges overlap. To truly consider these effects, studies with simulations need to be done to determine what sort of corrections can be made.

In Figure 5.4, we show the $M_{BH} - L_{H,bulge}$ relation. The background galaxies were plotted using $L_{H,bulge}$ from Marconi & Hunt (2003), with updated black hole masses from McConnell & Ma (2013). We have updated the best-fit line with these numbers, producing the relation:

$$log(\frac{M_{BH}}{M_\odot}) = 7.58 + 1.06\ log(\frac{L_{H,bulge}}{10^{10.8} L_\odot})$$

Table 5.2: Measured Black Hole Masses

Galaxy Name	Tracer[a]	M_{BH} ($M_\odot$)	$\sigma_{*,bulge}$ (km s^{-1})	$\log(\frac{L_{H,bulge}}{L_\odot})$	$M_{*,total}$ ($M_\odot$)	Galaxy References[b]
IIIZw035	stars - disk	$> 5.4^{+0.9}_{-0.1} \times 10^7$	...	11.15 ± 9.11	1.8×10^{10}	1,2
	stars - JAM	$< 2.0^{+0.5}_{-0.7} \times 10^9$				
	Brγ	$3.4^{+0.4}_{-0.6} \times 10^8$				
NGC 2623	stars - disk	$> 3.1^{+0.1}_{-0.5} \times 10^8$	95 ± 13	10.61 ± 8.57	2.4×10^{10}	1,2,3
	stars - JAM	$< 4.7^{+1.2}_{-2.6} \times 10^8$				
UGC5101	stars - disk	$> 6.5^{+3.5}_{-2.1} \times 10^8$	287 ± 11	11.58 ± 9.75	1.7×10^{11}	1,2,4
Mrk273N	[Fe II]	$1.0 \pm 0.1 \times 10^9$	285 ± 30	...	6.9×10^{11}	1,5
NGC 6240N	stars - disk	$> 8.8^{+0.7}_{-0.1} \times 10^8$	174 ± 54	10.81 ± 9.38	3.9×10^{11}	2,6,7
NGC 6240S	stars - disk	$> 8.7 \pm 0.3 \times 10^8$	236 ± 24	11.29 ± 10.25	3.9×10^{11}	2,6,7
	stars - JAM	$< 2.0 \pm 0.2 \times 10^9$				

[a]All measurements with gas tracers use the thin disk method, those with stellar tracers use the disk or JAM method as marked.

[b]Galaxy parameters in columns 4-6 taken from the following references: 1 - U et al. (2012), 2 - Haan et al. (2011), 3 - Shier et al. (1996), 4 - Rothberg & Joseph (2006), 5 - Dasyra et al. (2006), 6 - Howell et al. (2010), 7 - Tecza et al. (2000)

Our merging galaxies fall above this relation, suggesting that either stars have not been forming in the bulge as quickly as the black holes have been growing, or that a large mass of stars are still strewn about in tidal tails and unrelaxed features that will eventually become part of the bulge.

In Figure 5.5, we plot $M_{BH} - M_*$ using points from from Bennert et al. (2011) and Cisternas et al. (2011a). These authors suggest that higher redshift galaxies sit on the local $M_{BH} - M_{*,bulge}$ relation if you include total stellar mass instead of only bulge mass. In this way, they attribute evolution in the black hole scaling relation to the evolution of the bulge/disk fraction with redshift. We include as a solid line the updated fit to the $M_{BH} - M_{*,bulge}$ from McConnell & Ma (2013), and find that our merging galaxies fall on or above this relation, but still within the scatter. The one point that falls below the relation, the red circle Mrk273N, represents the mass in only one out of two black holes. Because this relation takes into account the entirety of

stellar mass, it suggests that star formation is truly not outpacing black hole growth during these mergers.

These results differ from the claims made by Kormendy & Ho (2013), who in section 6.4 show five merging galaxies falling below the $M_{BH} - \sigma_*$ and $M_{BH} - L_{K,bulge}$ relations. It is important to note the differing samples when considering these discrepant results. Our sample of merging galaxies are major gas-rich mergers; the merging galaxies considered in Kormendy & Ho (2013) are mainly minor mergers and/or gas-poor mergers. It is not unreasonable to imagine that such different types of mergers would have different effects on their central black holes. In particular, a minor or gas-poor merger might use up all incoming new gas in star formation before it reaches the central black hole, causing a delay in black hole accretion until stellar feedback produces new gas to fuel it. We can perhaps conclude that when a merger has a sufficiently high gas-fraction, no such delay exists. Alternatively, the delay could exist between mass reaching the central $\sim$ 10 parsecs and actually accreting on to the black hole. If the accretion timescale were long (e.g. due to viscosity in the accretion disk, as suggested by Power et al., 2011), this could reconcile late-stage AGN feedback with the early mass growth seen here.

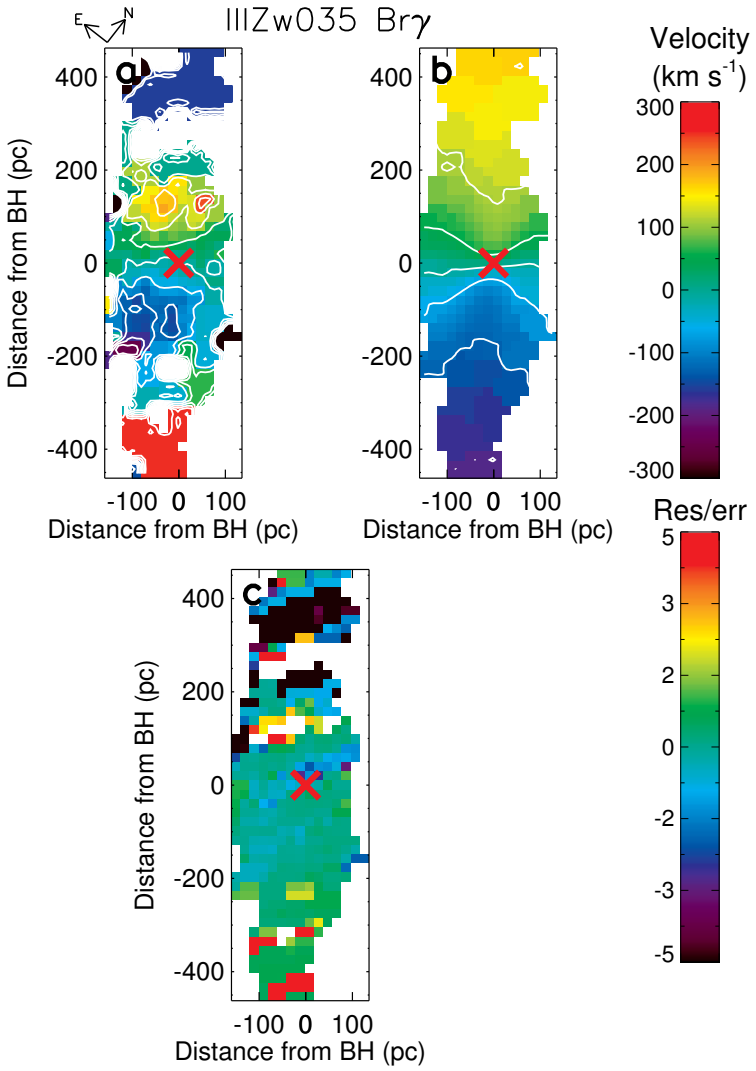

Figure 5.2: a) Map of Brγ velocities of the inner region of IIIZw035. b) Map of model velocities of best fit black hole model. c) Residual map of best-fit model divided by errors in velocity. In panels a) and b), velocity contours are marked in white. In each panel, a red X marks the position of the black hole.

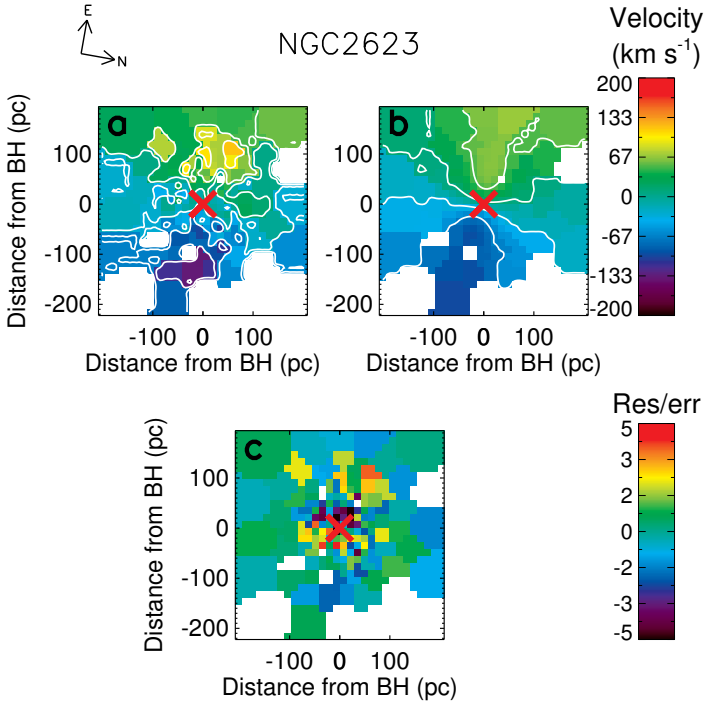

Figure 5.2: a) Map of stellar velocities of the inner region of NGC2623. b) Map of model stellar velocities of best fit black hole model. c) Residual map of best-fit model divided by errors in velocity. In panels a) and b), velocity contours are marked in white. In each panel, a red X marks the position of the black hole.

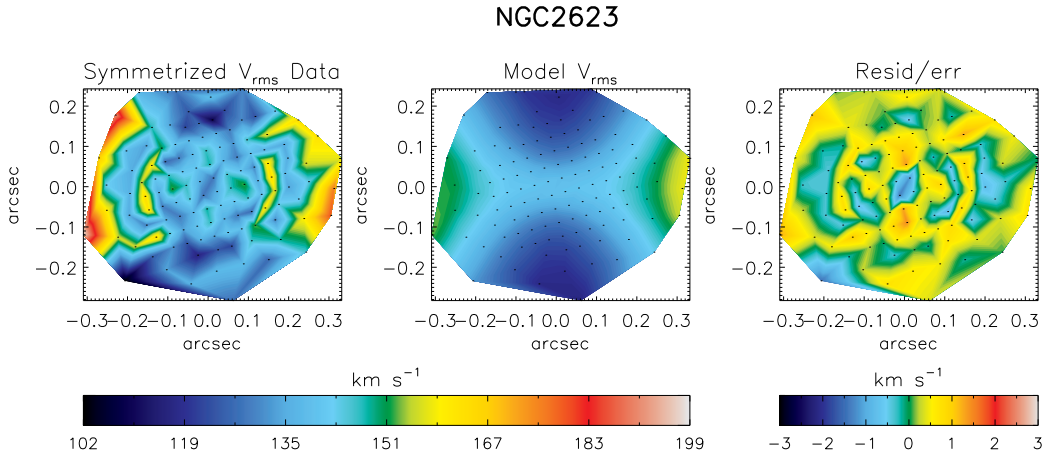

Figure 5.2: Left: Map of the symmetrized $v_{rms} = (v^2 + \sigma^2)^{0.5}$ of NGC2623. Center: Model v_{rms} of galaxy with black hole. Right: Residual map of model - data divided by errors in v_{rms}. All three panels are centered on the black hole and have been rotated so the major axis is horizontal.

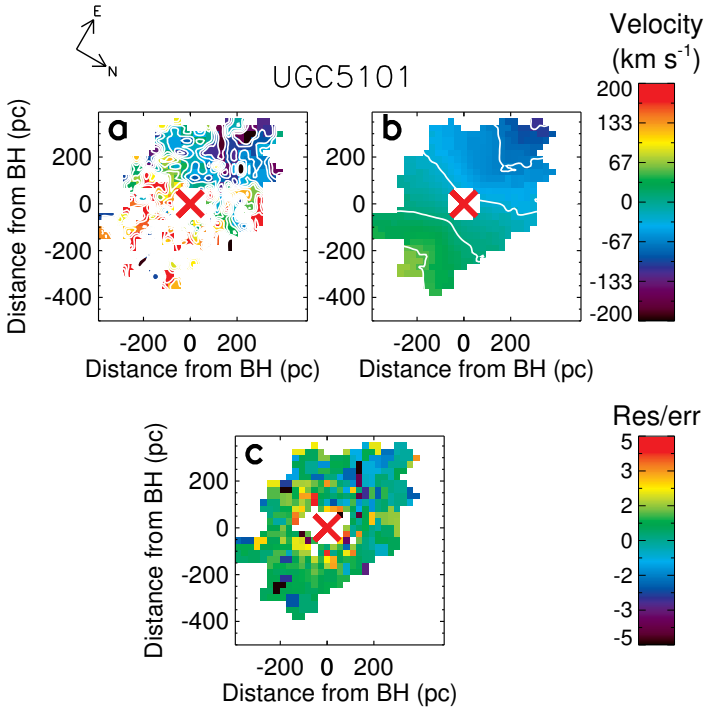

Figure 5.2: a) Map of stellar velocities of the inner region of UGC5101. b) Map of model stellar velocities of best fit black hole model. c) Residual map of best-fit model divided by errors in velocity. In panels a) and b), velocity contours are marked in white. In each panel, a red X marks the position of the black hole.

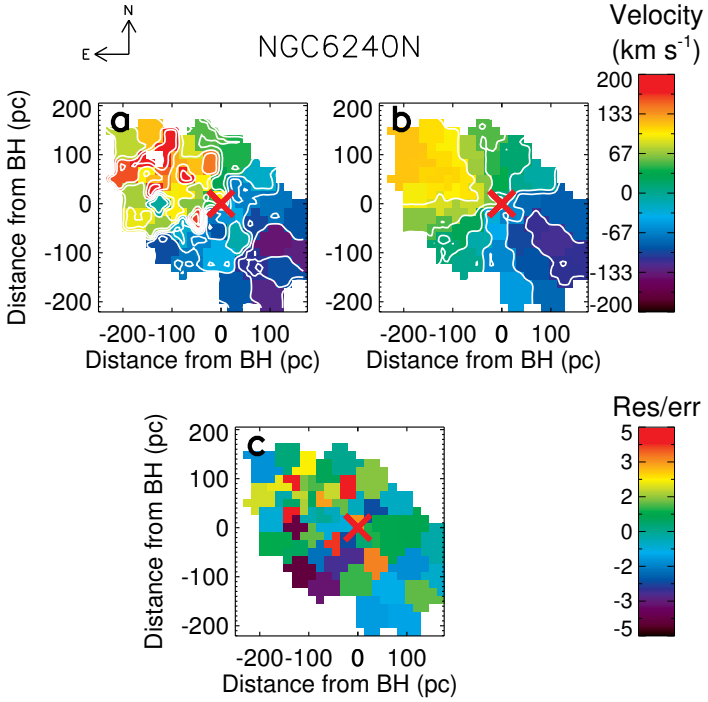

Figure 5.2: a) Map of stellar velocities of the inner region of NGC 6240N. b) Map of model stellar velocities of best fit black hole model. c) Residual map of best-fit model divided by velocity errors. In panels a) and b), velocity contours are marked in white. In each panel, a red X marks the position of the black hole.

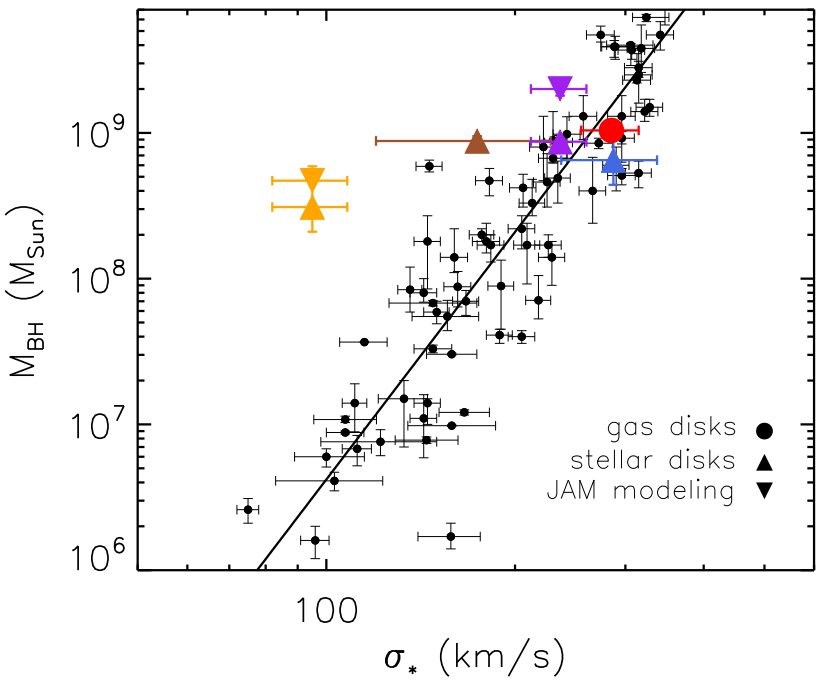

Figure 5.3: The $M_{BH} - \sigma_*$ relation for isolated galaxies from McConnell & Ma (2013) (black data and best-fit line) with our merging galaxies marked in large colored points. Symbols indicate which method was used for that mass determination: gas disk modeling in circles, stellar disk modeling in upward triangles, and JAM modeling in downward triangles. Stellar disk models represent lower limits to the black hole mass, while JAM models represent upper limits; see text for details. Galaxies presented here have parameters listed in Table 5.2, and are NGC 2623 (orange), UGC5101 (blue), Mrk273N (red), NGC 6240N (purple), and NGC 6240S (brown). Mrk273N's point (red) is the mass measurement for only the north black hole, though there is a second in the system (see Chapter 3).

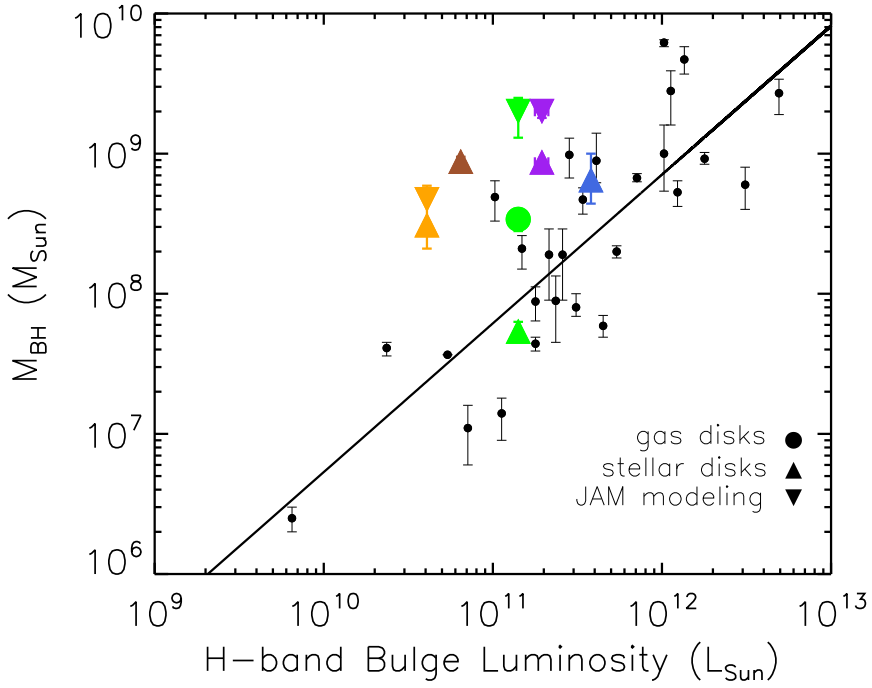

Figure 5.4: The $M_{BH} - L_{H,bulge}$ relation. The black points have luminosities taken from Marconi & Hunt (2003) and updated black hole masses from McConnell & Ma (2013). The dashed line shows the best-fit line originally presented by Marconi & Hunt (2003); the solid line is a log-log fit to the updated data: $log(\frac{M_{BH}}{M_{\odot}}) = 7.58 + 1.06\ log(\frac{L_{H,bulge}}{10^{10.8} L_{\odot}})$. Galaxies presented here are indicated by large colored points, with parameters listed in Table 5.2, and are IIIZw035 (green), NGC 2623 (orange), UGC5101 (blue), NGC 6240N (purple), and NGC 6240S (brown). Symbols indicate which method was used for that mass determination: gas disk modeling in circles, stellar disk modeling in upward triangles, and JAM modeling in downward triangles. Stellar disk models represent lower limits to the black hole mass, while JAM models represent upper limits; see text for details.

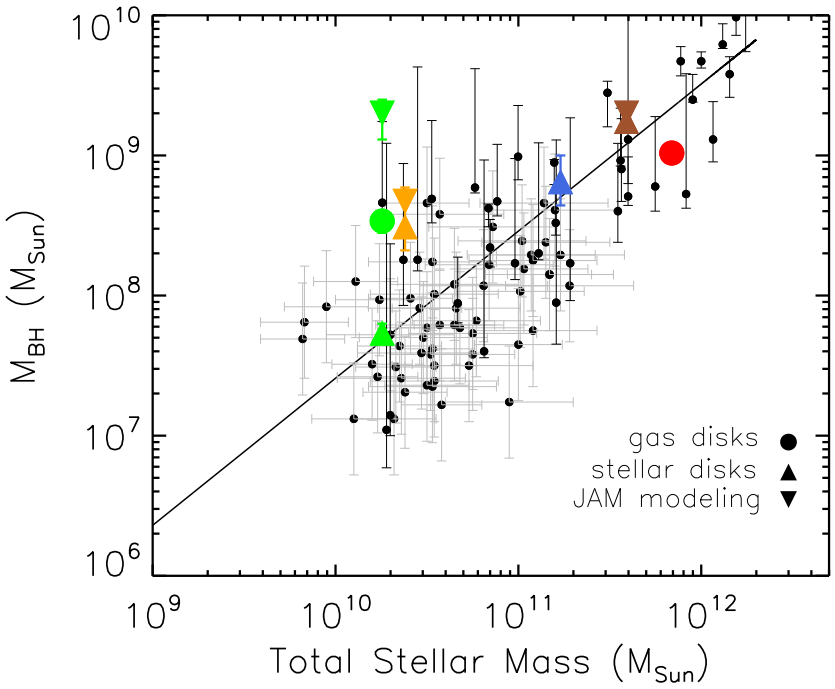

Figure 5.5: The $M_{BH} - M_*$ relation. The black points with grey error bars have luminosities and total stellar masses from Bennert et al. (2011) and Cisternas et al. (2011a), who suggest that higher redshift galaxies sit on the local $M_{BH} - M_{*,bulge}$ relation if you include total stellar mass instead of only bulge mass. In this way, they attribute evolution in the black hole scaling relation to the evolution of the bulge/disk fraction with redshift. We include also black points for local elliptical galaxies and the fit to for $M_{BH} - M_{*,bulge}$ from McConnell & Ma (2013). Merging galaxies from this work are indicated by large colored points, with parameters listed in Table 5.2, and are IIIZw035 (green), NGC 2623 (orange), UGC5101 (blue), Mrk273N (red), and NGC 6240 (brown). Symbols indicate which method was used for that mass determination: gas disk modeling in circles, stellar disk modeling in upward triangles, and JAM modeling in downward triangles. Stellar disk models represent lower limits to the black hole mass, while JAM models represent upper limits; see text for details. NGC 6240's two nuclei were summed together and appear as one point (dark brown) on this plot, paired with the entire system's total stellar mass. Mrk273N's point (red) is the mass measurement for only one black hole, though there is a second in the system (see Chapter 3).

5.5 Conclusions

Additional data for this project may be obtained at the end of May 2013 and will be included in the final paper. For now we make conclusions based on the current sample.

We have presented high spatial resolution near-infrared integral field spectroscopy of nuclear disks in nearby merging (U)LIRGs. These gas-rich mergers funnel gas to the galaxies' centers where the gas forms disks; stars then form *in situ*, creating a stellar disk as well. These disks, which were described in more detail in Chapter 4, provide an alternative method to measuring black hole masses. Three-integral orbital superposition models rely on an assumption of virialization and emission line black hole mass diagnostics require broad lines; neither of these methods are feasible in such systems. However, with adaptive optics, we have produced two-dimensional kinematic maps at spatial resolutions close to or better than radius of the sphere of influence of the black hole. Because the dynamical timescale this close to a black hole is short, the material quickly becomes virialized, and models are possible.

We implemented two different techniques using these kinematic maps, originally presented in Chapters 2 and 3, to measure 6 new black hole masses. Gaseous disks are likely thin Keplerian disks, and are therefore modeled as such. Stellar disks are more likely to have pressure support, but measuring this is not straightforward, so we place bracketing measurements using two assumptions. To provide a lower limit to the black hole mass, we assume the stars are also in a thin Keplerian disk; any pressure support would increase the black hole mass. We also use Jeans Axisymmetric Mass models to

take into account the velocity dispersion; since this velocity dispersion may be inflated by intervening unvirialized material along the line of sight, this mass measurement is an upper limit.

We have placed these black hole masses on three local black hole scaling relations, $M_{BH} - \sigma_*$, $M_{BH} - L_{H,bulge}$, and $M_{BH} - M_*$, using host galaxy parameters from the literature. We find that the majority of our sample falls on or above these scaling relations. Under the assumption that these galaxies follow black hole scaling relations before and after their mergers, this suggests that black holes grow more quickly than stars form during a major gas-rich merger. This does not line up with theoretical reasoning that star formation has easier access to inflowing gas (e.g. Cen, 2012) or that a final burst of black hole growth is likely to shut off star formation ("quasar-mode feedback"; Hopkins et al., 2005; Springel et al., 2005b), unless that feedback is delayed due to viscosity in the accretion disk (Power et al., 2011) or similar. Instead we conclude that AGN growth and feedback must be a more gradual process in some galaxies.

Chapter 6

Future Work

6.1 Comparing Nuclear Disks to Simulations

In Chapter 4, we qualitatively compare the nuclear disks seen in nearby gas-rich major mergers to those found in high-resolution hydrodynamical simulations. However, many more and detailed comparisons can and should be done, both to currently existing simulations and to a suite of simulations that could be run.

6.1.1 More Detailed Comparisons with Existing Simulations

Nuclear disks in galaxy mergers are relatively simple structures embedded in a complicated mess. The two most common ways of identifying nuclear disks observationally are through kinematic maps and morphology; both of these methods can be deceiving at times.

Nuclear disks are locally relaxed, but lie in an unrelaxed system. Observations of the inner dynamics, both for stars and for gaseous emission lines, actually recover

the line-of-sight velocity distribution. The rest of the galaxy, lying in between Earth and the nucleus, can wash out features of the disk that otherwise would be clear. Spiral arms, tidal tails, clumps of material have peculiar velocities that are difficult to predict and to account for. Using simulations of such mergers, it's possible to compare the intrinsic dynamics of the disk to those that would be measured from a line-of-sight velocity distribution; a Monte Carlo approach using thousands of sightlines in a single simulation would provide a better estimate of this effect. These line-of-sight effects are probably most likely to hide the dynamical signatures of disks but they might also provide false positives in some situations.

The second major issue with finding nuclear disks is the quantity of dust that permeates the nucleus of a gas-rich galaxy merger. Even in the K-band ($\sim 2.2\mu$m), some nuclei are obscured (e.g. the south nucleus of NGC 6240, see Chapter 4 and Max et al., 2007). If dust were an even screen across the front of a galaxy, it would be easy to compensate for. However, since dust is clumpy and occurs in, around, and/or in front of the nuclear regions, it can complicate both morphological and dynamical studies. Morphologically, dust can obscure parts of the disk, causing us to measure an artificially small size or an incorrect Sérsic index, possibly masking the disk entirely. Additionally, all dynamical measurements made observationally are light-weighted along the line-of-sight. If certain parts of the disk are more obscured, intervening material may contribute more to the measurement in that area, leading to incorrect velocity or velocity dispersion measurements. By using radiative transfer codes such as SUNRISE (Jonsson, 2006) and RADMC-3D (Dullemond, 2012), the effects of dust on the detection

and characterization of disks can be properly determined. These codes enable mock observations of simulations, allowing the comparison of light to light, instead of light to mass.

Additionally, the history and evolution of these disks can be studied in these simulations. Rather than looking at a single time-step, it's possible to compare the evolution of sizes and structures of these disks within a simulation over time. By matching the observed disk properties with a more precise merger stage (§6.2), we can compare the evolution of disks in simulations to those in galaxies. Comparing the latest stages of mergers to local ellipticals showing kinematically decoupled cores may indicate whether or not these disks are likely to be the progenitors of such systems.

6.1.2 Running a Suite of New Simulations for Comparison

Hydrodynamical simulations are continually improving, adding new physics and probing higher spatial resolutions. Even recently, the highest spatial resolution simulations (Chapon et al., 2013) have not implemented appropriate prescriptions for star formation and a multiphase interstellar medium in the regions of highest spatial resolution. This work is ongoing, and is extremely important for understanding the formation and evolution of nuclear disks. Indeed, our observations show that stars form in these disks and tend to maintain the cold kinematics. Simulations must be able to provide the appropriate physics.

However, the future is bright, and new simulations with more complete physical prescriptions are being run. Still, galaxy mergers come in many flavors, with different gas fractions, mass ratios, and orbital parameters. In order to understand the effects

these characteristics have on the formation and evolution of nuclear disks, a small suite of simulations should be run. Variations in disk parameters across parameter space, at varying stages of the merger, and from observations along different lines-of-sight all contribute to the cosmic variance seen in an large sample of nuclear disks. A small suite of simulations would determine how these parameters affect disk properties.

6.2 Studying Star Clusters

The ages of the stellar populations in the nucleus are a key piece of information to indicate the time since the major starburst – a reliable feature in major mergers' evolution, relative to which we can measure their progress. With these ages, and comparing the system's morphology to the GalMer database of galaxy merger configurations (Chilingarian et al., 2010), we would be able to constrain the time since first passage or final coalescence of the merging galaxies.

To date, merger stages are usually classified in a broad-brush approach; Surace et al. (1998); Surace (1998) first proposed a classification scheme ranging from 1-6 which can be summarized by: (1) two galaxies that will interact but are still pre-merger and undisturbed, (2-4) galaxies currently merging and still showing two distinct nuclei, and (5-6), galaxies which have coaelsced into a single nucleus but still show disturbed morphologies indicative of a recent merger. However, distinguishing the chronological differences between systems can be important for understanding the evolution of both nuclear disks (see Chapter 4) and black hole growth (see Chapter 5). By combining morphological evidence with the ages of the most recent starburst, a quantitative evolutionary

track of these systems can be built up with regards to any property studied.

We plan to measure the starburst ages of these galaxies using high spatial resolution AO-assisted images, which can resolve individual young star clusters in the nuclei of nearby major gas-rich mergers (see Fig. 6.1). Though understanding the complex stellar populations in starbursts is difficult, it is made much easier by the ability to narrow each measurement down to a single simple stellar population. We have obtained near-infrared images of more than a dozen of these systems in the J and K' bands with NIRC2 (the Near InfraRed Camera 2; PI: K. Matthews) on the Keck II telescope. Details of these observations are listed in Table 6.1. Analysis of these images can provide information about the local star formation as well as enable an independent estimate of the stage of merger. Without analysis, these images also can show where the bulk of star formation occurs. Large-scale images of (U)LIRGs taken with the Hubble Space Telescope's *Advanced Camera for Surveys* reveal star clusters in streams reaching several kpc from the nucleus of NGC 2623 (Evans et al., 2008). These images, taken in the B and I bands as part of the GOALS survey (Armus et al., 2009), miss star clusters in the dusty nuclear regions; these stars clusters will be revealed by images of similar resolution taken in the near-infrared.

Multiband photometry enables the application of stellar population synthesis using a series of models, stellar templates that combine to produce an integrated spectrum (e.g. Fioc & Rocca-Volmerange, 1997; Leitherer et al., 1999b; Bruzual & Charlot, 2003; Conroy & van Dokkum, 2012). The models which combine to provide the best fit to the observed spectrum can indicate properties of the underlying stellar population,

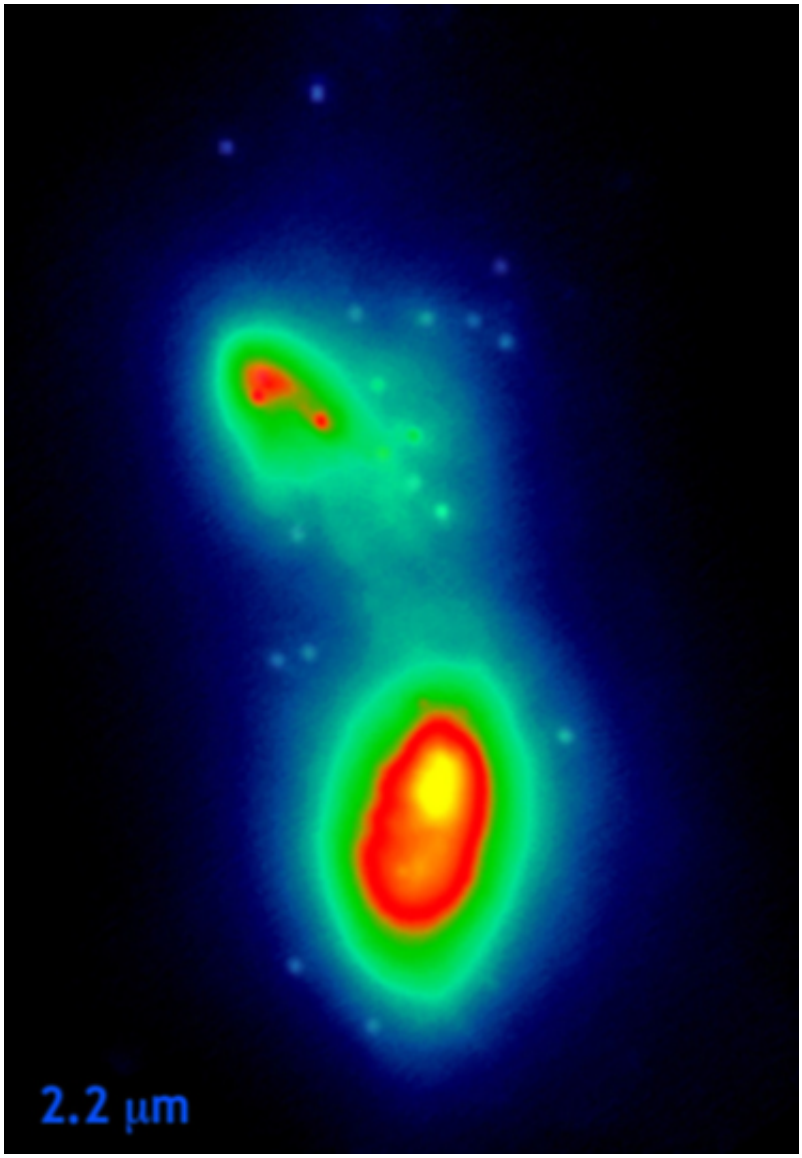

Figure 6.1: NIRC2 K'-band narrow camera image (with a plate scale 0.01 arcsec/pixel) taken of NGC 6240's two nuclei. This image clearly resolves individual star clusters surrounding the nuclei.

Table 6.1: Details of NIRC2 Observations of Star Clusters

Galaxy Name	Redshift	UT Date(s) YYMMDD	Filter	Exp Time on Target (minutes)	Exp Time on Sky (minutes)
CGCG436-030	0.0313	121225, 121226	J	19	19
CGCG436-030	0.0313	121225, 121226	K'	21	21
IRASF01364-1042	0.0490	121223,121224	K'	28	28
IRASF03359+1523	0.0355	121222	J	25	9
IRASF03359+1523	0.0355	121222	K'	19	18
MCG+08-11-002	0.0195	121224, 130206	J	20	26
MCG+08-11-002	0.0195	121223, 121225	K'	11	15
NGC 2623	0.0196	121222	J	21.5	21.5
NGC 2623	0.0196	121222	K'	14	14
UGC5101	0.0413	121222, 130206	J	37	37
UGC5101	0.0413	121222	K'	13.1	13.1
Mrk231	0.0448	121222	J	20.83	20.83
Mrk231	0.0448	121222	K'	25.3	25.3
Mrk273	0.038	120520	H	9	9
Mrk273	0.038	120520	K'	9	9
IRASF19297-0406	0.0922	120806	J	25	25
IRASF19297-0406	0.0922	120806	K'	14	14
IRAS20351+2521	0.0353	120806	J	15	15
IRAS20351+2521	0.0353	120806	K'	21	21
IRAS23436+5257	0.0348	120806	J	25	25
IRAS23436+5752	0.0348	120806	K'	11	11

including masses, ages, initial mass functions, and metallicities.

B and I band photometry from the Hubble Space Telescope's *Advanced Camera for Surveys*, combined with new J and K' or H and K' band photometry from NIRC2 with LGS AO, provide a sufficient baseline with which to measure some stellar population properties. This has been done for NGC 6240 (Pollack et al., 2007): they found ~ 30 clusters, most of which are consistent with ages of ~ 15 million years and masses ranging from 7×10^5 to $4 \times 10^7 M_\odot$.

6.3 Full Range of Merger Stages

In Chapters 4 and 5, we investigate two phenomena associated with gas-rich major mergers: the presence of nuclear disks and the growth of black holes. Our sample mainly focuses on the late stages of such mergers, but the techniques can easily be

applied to a full range of merger stages. By increasing the sample, and combining this with precise estimates of merger stage (see §6.2), it would be possible to trace a population of merging galaxies along black hole scaling relations. In Chapter 5 we see that the black hole begins to grow early; that is, that it is keeping pace with the galaxy (and sometimes outpacing it) by the time these systems reach their current state. A more complete range of merger stages would reveal just how early the major epoch of black hole growth occurs, and confirm that such systems begin and end on black hole scaling relations. Such conclusions may also depend on the masses or types of galaxies, but with a large enough sample, that can be determined. We plan to expand our sample of black hole masses, both to improve statistics in the later stages of mergers and to extend our results to earlier merger stages, potentially tracing deviations from scaling relations as they happen.

6.4 Cataloging H_2 Tracers of Outflows

The topics presented in this thesis come from a dataset rich with additional science. In particular we mention the presence of H_2 as a tracer of shocks resulting from outflows. Many of the galaxies studied here reveal an increase in velocity dispersion of the H_2 line along the disk's minor axis, as shown in Fig. 3.7. These are reminiscent of turbulent polar outflows.

Perhaps more striking is the frequent incidence of extended H_2 flux extending along the minor axis of nuclear disks. This is revealed in the GALFIT models detailed in Chapter 4, though not explored. Fig. 6.2 shows an example of one galaxy, IIIZw035,

with the nuclear disk removed and the minor axis H_2 extensions apparent.

By studying these extensions in more detail, and by decomposing the H_2 kinematics into rotation and outflowing components, the strength and frequency of outflows from nuclear disks can be determined. Additionally, it may be possible to determine whether these shocks are caused by AGN feedback or by stellar winds.

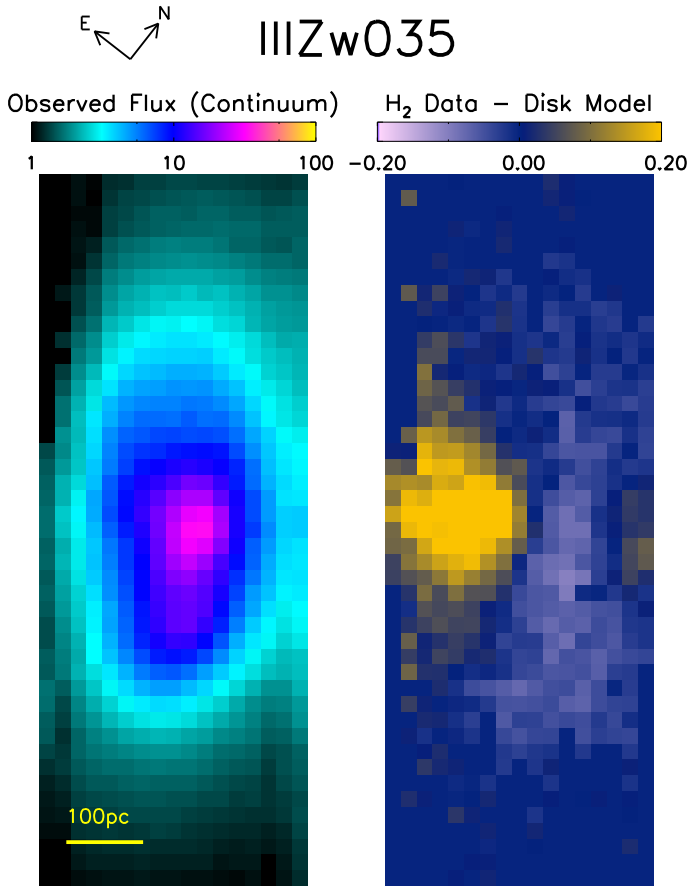

Figure 6.2: The H_2 extensions along the minor axis of IIIZw035's nuclear disk. The left panel shows the continuum flux map; the right panel shows the H_2flux map with the best fit disk subtracted. The leftover extensions appear yellow in the residual map, right.

6.5 Connecting Inner Kinematics to the Galactic Scale

The high spatial resolution kinematic maps developed as part of this thesis have revealed organized rotation in the form of nuclear disks, often combined with small-scale outflows and/or irregularities in the kinematics of some gas tracers. Meanwhile, massive outflows have been observed on larger scales in systems such as these, traced by neutral absorption (as in Mrk 231, Rupke & Veilleux, 2005), by the K-band warm excited H_2 2.12 μm line, and by CO emission with mm interferometry (as in M82, Mrk273, and NGC 1266: Veilleux et al., 2009; U et al., 2013; Alatalo et al., 2011, respectively). Additionally, galactic-scale shocks have been identified in LIRGs (Rich et al., 2011).

Because these galaxies often involve both an AGN and a starburst, it isn't immediately clear what drives their outflows; the starbursts are so massive that stellar winds can plausibly produce sufficient energy to disrupt the gas. Does that mean that AGN feedback isn't a factor in the kinematics of their host galaxies? The only way to tell – aside from systems with radio jets – is by spatially resolving the outflows near their start. In Chapter 3, we demonstrate this with the outflows seen in H_2 in Mrk273 towards the southeast from the northern black hole. Since we can conclude that the outflow begins in the center of the north nucleus, we only need to calculate how much energy is available from star formation in that nucleus to determine if star formation is a plausible driver. Energy arguments reveal that it isn't, ruling out stellar winds as the cause, and leaving AGN-driven outflows as the cause.

However, revealing AGN-powered shocks and outflows on sub-kiloparsec scales does not indicate how likely or able they are to affect the rest of the galaxy. In order

to determine this, it is necessary to combine high spatial resolutions with large fields of view for the sample sample. Such a dataset would enable the tracing of outflows near the black hole to those seen on galactic scales.

Bibliography

Aird, J., Nandra, K., Laird, E. S., et al. 2010, MNRAS, 401, 2531

Alatalo, K., Blitz, L., Young, L. M., et al. 2011, ApJ, 735, 88

Allen, M. G., Groves, B. A., Dopita, M. A., Sutherland, R. S., & Kewley, L. J. 2008, ApJS, 178, 20

Alonso-Herrero, A., Rieke, M. J., Rieke, G. H., & Ruiz, M. 1997, ApJ, 482, 747

Armus, L., Charmandaris, V., Bernard-Salas, J., et al. 2007, ApJ, 656, 148

Armus, L., Mazzarella, J. M., Evans, A. S., et al. 2009, PASP, 121, 559

Balcells, M., & Quinn, P. J. 1990, ApJ, 361, 381

Ballo, L., Braito, V., Della Ceca, R., et al. 2004, ApJ, 600, 634

Barnes, J. E., & Hernquist, L. 1992, ARA&A, 30, 705

—. 1996, ApJ, 471, 115

Bender, R. 1988, A&A, 202, L5

Bender, R., Kormendy, J., Bower, G., et al. 2005, ApJ, 631, 280

Bennert, V. N., Auger, M. W., Treu, T., Woo, J.-H., & Malkan, M. A. 2011, ApJ, 726, 59

Berta, S., Magnelli, B., Nordon, R., et al. 2011, A&A, 532, A49

Böker, T., Falcón-Barroso, J., Schinnerer, E., Knapen, J. H., & Ryder, S. 2008, AJ, 135, 479

Bondi, M., Pérez-Torres, M.-A., Dallacasa, D., & Muxlow, T. W. B. 2005, MNRAS, 361, 748

Bournaud, F., Dekel, A., Teyssier, R., et al. 2011, ApJ, 741, L33

Bruzual, G., & Charlot, S. 2003, MNRAS, 344, 1000

Bryant, P. M., & Scoville, N. Z. 1999, AJ, 117, 2632

Callegari, S., Mayer, L., Kazantzidis, S., et al. 2009, ApJ, 696, L89

Cappellari, M. 2002, MNRAS, 333, 400

—. 2008, MNRAS, 390, 71

Cappellari, M., & Copin, Y. 2003, MNRAS, 342, 345

Cappellari, M., & Emsellem, E. 2004, PASP, 116, 138

Cappellari, M., Neumayer, N., Reunanen, J., et al. 2009, MNRAS, 394, 660

Carilli, C. L., & Taylor, G. B. 2000, ApJ, 532, L95

Cen, R. 2012, ApJ, 755, 28

Chapon, D., Mayer, L., & Teyssier, R. 2013, MNRAS, 546

Chilingarian, I. V., Di Matteo, P., Combes, F., Melchior, A.-L., & Semelin, B. 2010, A&A, 518, A61

Cisternas, M., Jahnke, K., Bongiorno, A., et al. 2011a, ApJ, 741, L11

Cisternas, M., Jahnke, K., Inskip, K. J., et al. 2011b, ApJ, 726, 57

Clements, D. L., Sutherland, W. J., McMahon, R. G., & Saunders, W. 1996, MNRAS, 279, 477

Collins, G. P. 1992, Physics Today, 45, 17

Comerford, J. M., Gerke, B. F., Newman, J. A., et al. 2009, ApJ, 698, 956

Condon, J. J., Huang, Z.-P., Yin, Q. F., & Thuan, T. X. 1991, ApJ, 378, 65

Conroy, C., & van Dokkum, P. 2012, ApJ, 747, 69

Dasyra, K. M., Yan, L., Helou, G., et al. 2008, ApJ, 680, 232

Dasyra, K. M., Tacconi, L. J., Davies, R. I., et al. 2006, ApJ, 651, 835

Davies, R. 2008, New A Rev., 52, 307

Davies, R., Engel, H., Hicks, E., et al. 2010, in Society of Photo-Optical Instrumentation Engineers (SPIE) Conference Series, Vol. 7736, Adaptive Optics Systems II

Davies, R. I. 2007, MNRAS, 375, 1099

Davies, R. I., Sternberg, A., Lehnert, M., & Tacconi-Garman, L. E. 2003, ApJ, 597, 907

Davies, R. I., Tacconi, L. J., & Genzel, R. 2004, ApJ, 613, 781

Davies, R. I., Thomas, J., Genzel, R., et al. 2006, ApJ, 646, 754

de Zeeuw, P. T., Bureau, M., Emsellem, E., et al. 2002, MNRAS, 329, 513

Dekel, A., & Birnboim, Y. 2006, MNRAS, 368, 2

Dekel, A., Birnboim, Y., Engel, G., et al. 2009, Nature, 457, 451

Denney, K. D., Watson, L. C., Peterson, B. M., et al. 2009, ApJ, 702, 1353

Di Matteo, T., Springel, V., & Hernquist, L. 2005, Nature, 433, 604

Do, T., Ghez, A. M., Morris, M. R., et al. 2009, ApJ, 703, 1323

Donley, J. L., Rieke, G. H., Alexander, D. M., Egami, E., & Pérez-González, P. G. 2010, ApJ, 719, 1393

Dotti, M., Colpi, M., Haardt, F., & Mayer, L. 2007, MNRAS, 379, 956

Dotti, M., Colpi, M., Haardt, F., & Mayer, L. 2008, in IAU Symposium, Vol. 245, Formation and Evolution of Galaxy Bulges, ed. M. Bureau, E. Athanassoula, & B. Barbuy, 241–242

Draine, B. T., & Woods, D. T. 1990, ApJ, 363, 464

Dullemond, C. P. 2012, RADMC-3D: A multi-purpose radiative transfer tool, astrophysics Source Code Library, ascl:1202.015

Ellison, S. L., Mendel, J. T., Scudder, J. M., Patton, D. R., & Palmer, M. J. D. 2013, MNRAS, 430, 3128

Ellison, S. L., Patton, D. R., Mendel, J. T., & Scudder, J. M. 2011, MNRAS, 418, 2043

Emsellem, E., Cappellari, M., Peletier, R. F., et al. 2004, MNRAS, 352, 721

Engel, H., Davies, R. I., Genzel, R., et al. 2010, A&A, 524, A56

Evans, A. S., Vavilkin, T., Pizagno, J., et al. 2008, ApJ, 675, L69

Falcón-Barroso, J., Bacon, R., Bureau, M., et al. 2006, MNRAS, 369, 529

Falcón-Barroso, J., Bacon, R., Bureau, M., et al. 2007, in Science Perspectives for 3D Spectroscopy, ed. M. Kissler-Patig, J. R. Walsh, & M. M. Roth, 111

Farrah, D., Connolly, B., Connolly, N., et al. 2009, ApJ, 700, 395

Ferland, G. J., Korista, K. T., Verner, D. A., et al. 1998, PASP, 110, 761

Ferrarese, L., & Merritt, D. 2000, ApJ, 539, L9

Fioc, M., & Rocca-Volmerange, B. 1997, A&A, 326, 950

Fu, H., Myers, A. D., Djorgovski, S. G., & Yan, L. 2011, ApJ, 733, 103

García-Marín, M., Colina, L., Arribas, S., & Monreal-Ibero, A. 2009, A&A, 505, 1319

Gebhardt, K., Adams, J., Richstone, D., et al. 2011, ApJ, 729, 119

Gebhardt, K., Bender, R., Bower, G., et al. 2000, ApJ, 539, L13

Genzel, R., Lutz, D., Sturm, E., et al. 1998, ApJ, 498, 579

Gerardy, C. L., & Fesen, R. A. 2001, AJ, 121, 2781

Gerke, B. F., Newman, J. A., Lotz, J., et al. 2007, ApJ, 660, L23

Ghez, A. M., Salim, S., Hornstein, S. D., et al. 2005, ApJ, 620, 744

Ghez, A. M., Salim, S., Weinberg, N. N., et al. 2008, ApJ, 689, 1044

Gillessen, S., Eisenhauer, F., Trippe, S., et al. 2009, ApJ, 692, 1075

Glassman, T. M., Larkin, J. E., & Lafrenière, D. 2002, ApJ, 581, 865

González, V., Labbé, I., Bouwens, R. J., et al. 2010, ApJ, 713, 115

Graham, J. R., Wright, G. S., & Longmore, A. J. 1987, ApJ, 313, 847

Gültekin, K., Richstone, D. O., Gebhardt, K., et al. 2009a, ApJ, 695, 1577

—. 2009b, ApJ, 698, 198

Haan, S., Surace, J. A., Armus, L., et al. 2011, AJ, 141, 100

Harms, R. J., Ford, H. C., Tsvetanov, Z. I., et al. 1994, ApJ, 435, L35

Hau, G. K. T., & Thomson, R. C. 1994, MNRAS, 270, L23

Hawarden, T. G., Leggett, S. K., Letawsky, M. B., Ballantyne, D. R., & Casali, M. M. 2001, MNRAS, 325, 563

Heckman, T. M. 1994, in Mass-Transfer Induced Activity in Galaxies, ed. I. Shlosman, 234

Hernquist, L., & Barnes, J. E. 1991, Nature, 354, 210

Herrnstein, J. R., Moran, J. M., Greenhill, L. J., et al. 1999, Nature, 400, 539

Hicks, E. K. S., Davies, R. I., Maciejewski, W., et al. 2013, ArXiv e-prints, arXiv:1303.4399

Hicks, E. K. S., & Malkan, M. A. 2008, ApJS, 174, 31

Hopkins, P. F. 2012, MNRAS, 420, L8

Hopkins, P. F., Hernquist, L., Cox, T. J., et al. 2005, ApJ, 630, 705

—. 2006, ApJS, 163, 1

Hopkins, P. F., & Quataert, E. 2010a, MNRAS, 407, 1529

—. 2010b, MNRAS, 405, L41

Hopkins, P. F., Bundy, K., Croton, D., et al. 2010, ApJ, 715, 202

Howell, J. H., Armus, L., Mazzarella, J. M., et al. 2010, ApJ, 715, 572

Hughes, S. A. 2002, Phys. Rev. D, 66, 102001

Huo, Z. Y., Xia, X. Y., Xue, S. J., Mao, S., & Deng, Z. G. 2004, ApJ, 611, 208

Ishida, C. M. 2004, PhD thesis, Institute for Astronomy, University of Hawaii, 2680 Woodlawn Dr. Honolulu, HI 96822

Iwasawa, K., Sanders, D. B., Teng, S. H., et al. 2011a, A&A, 529, A106

Iwasawa, K., Mazzarella, J. M., Surace, J. A., et al. 2011b, A&A, 528, A137

Jahnke, K., Bongiorno, A., Brusa, M., et al. 2009, ApJ, 706, L215

James, P., Bate, C., Wells, M., Wright, G., & Doyon, R. 1999, MNRAS, 309, 585

Jonsson, P. 2006, MNRAS, 372, 2

Kang, W.-R., Woo, J.-H., Schulze, A., et al. 2013, ArXiv e-prints, arXiv:1302.4742

Kartaltepe, J. S., Sanders, D. B., Le Floc'h, E., et al. 2010, ApJ, 721, 98

Kartaltepe, J. S., Dickinson, M., Alexander, D. M., et al. 2012, ApJ, 757, 23

Kauffmann, G., & Heckman, T. M. 2009, MNRAS, 397, 135

Kawakatu, N., & Wada, K. 2008, ApJ, 681, 73

Kazantzidis, S., Mayer, L., Colpi, M., et al. 2005, ApJ, 623, L67

Kennicutt, Jr., R. C. 1998, ARA&A, 36, 189

Kim, D.-C., Evans, A. S., Vavilkin, T., et al. 2013, ArXiv e-prints, arXiv:1303.3977

Kiuchi, G., Ohta, K., & Akiyama, M. 2009, ApJ, 696, 1051

Klöckner, H.-R., & Baan, W. A. 2004, A&A, 419, 887

Kocevski, D. D., Faber, S. M., Mozena, M., et al. 2012, ApJ, 744, 148

Komossa, S., Burwitz, V., Hasinger, G., et al. 2003, ApJ, 582, L15

Konopacky, Q. M., Barman, T. S., Macintosh, B. A., & Marois, C. 2013, Science, 339, 1398

Kormendy, J. 1984, ApJ, 287, 577

Kormendy, J., & Gebhardt, K. 2001, in American Institute of Physics Conference Series, Vol. 586, 20th Texas Symposium on relativistic astrophysics, ed. J. C. Wheeler & H. Martel, 363–381

Kormendy, J., & Ho, L. C. 2013, ArXiv e-prints, arXiv:1304.7762

Kormendy, J., & Richstone, D. 1995, ARA&A, 33, 581

Koss, M., Mushotzky, R., Baumgartner, W., et al. 2013, ArXiv e-prints, arXiv:1302.0850

Koss, M., Mushotzky, R., Treister, E., et al. 2012, ApJ, 746, L22

Koss, M., Mushotzky, R., Veilleux, S., & Winter, L. 2010, ApJ, 716, L125

Krabbe, A., Gasaway, T., Song, I., et al. 2004, in Society of Photo-Optical Instrumentation Engineers (SPIE) Conference Series, Vol. 5492, Society of Photo-Optical Instrumentation Engineers (SPIE) Conference Series, ed. A. F. M. Moorwood & M. Iye, 1403–1410

Krajnović, D., & Jaffe, W. 2004, A&A, 428, 877

Krajnović, D., Bacon, R., Cappellari, M., et al. 2008, MNRAS, 390, 93

Krumholz, M. R., & Tan, J. C. 2007, ApJ, 654, 304

Lanz, T., & Hubeny, I. 2003, ApJS, 146, 417

Larkin, J., Barczys, M., Krabbe, A., et al. 2006, in Society of Photo-Optical Instrumentation Engineers (SPIE) Conference Series, Vol. 6269, Ground-based and Airborne Instrumentation for Astronomy

Law, D. R., Steidel, C. C., Erb, D. K., et al. 2009, ApJ, 697, 2057

Lee, K. J., Wex, N., Kramer, M., et al. 2011, MNRAS, 414, 3251

Leitherer, C., Schaerer, D., Goldader, J. D., et al. 1999a, ApJS, 123, 3

—. 1999b, ApJS, 123, 3

Liu, X., Shen, Y., Strauss, M. A., & Hao, L. 2011, ApJ, 737, 101

Lu, J. R., Ghez, A. M., Hornstein, S. D., et al. 2009, ApJ, 690, 1463

Lutz, D., Veilleux, S., & Genzel, R. 1999, ApJ, 517, L13

Magorrian, J., Tremaine, S., Richstone, D., et al. 1998, AJ, 115, 2285

Marconi, A., & Hunt, L. K. 2003, ApJ, 589, L21

Markwardt, C. B. 2009, in Astronomical Society of the Pacific Conference Series, Vol. 411, Astronomical Data Analysis Software and Systems XVIII, ed. D. A. Bohlender, D. Durand, & P. Dowler, 251

Max, C. E., Canalizo, G., & de Vries, W. H. 2007, Science, 316, 1877

Max, C. E., Canalizo, G., Macintosh, B. A., et al. 2005, ApJ, 621, 738

Mayer, L., Kazantzidis, S., & Escala, A. 2008, Mem. Soc. Astron. Italiana, 79, 1284

Mayer, L., Kazantzidis, S., Madau, P., et al. 2007, Science, 316, 1874

Mazzarella, J. M., Iwasawa, K., Vavilkin, T., et al. 2012, AJ, 144, 125

McConnell, N. J., & Ma, C.-P. 2013, ApJ, 764, 184

McConnell, N. J., Ma, C.-P., Graham, J. R., et al. 2011, ApJ, 728, 100

McDermid, R., Emsellem, E., Cappellari, M., et al. 2004, Astronomische Nachrichten, 325, 100

McDermid, R. M., Bacon, R., Kuntschner, H., et al. 2006a, New A Rev., 49, 521

McDermid, R. M., Emsellem, E., Shapiro, K. L., et al. 2006b, MNRAS, 373, 906

McGurk, R. C., Max, C. E., Rosario, D. J., et al. 2011, ApJ, 738, L2

McLean, I. S. 2008, Electronic Imaging in Astronomy: Detectors and Instrumentation (Second Edition)

Medling, A. M., Ammons, S. M., Max, C. E., et al. 2011, ApJ, 743, 32

Melbourne, J., Wright, S. A., Barczys, M., et al. 2005, ApJ, 625, L27

Melbourne, J., Ammons, M., Wright, S. A., et al. 2008, AJ, 135, 1207

Melnick, J., & Mirabel, I. F. 1990, A&A, 231, L19

Milosavljević, M., & Merritt, D. 2003, in American Institute of Physics Conference Series, Vol. 686, The Astrophysics of Gravitational Wave Sources, ed. J. M. Centrella, 201–210

Miyoshi, M., Moran, J., Herrnstein, J., et al. 1995, Nature, 373, 127

Moré, J. 1978, The Levenberg-Marquardt Algorithm: Implementation and Theory, Vol. 630 (Berlin: Springer-Verlag), 105

Mouri, H. 1994, ApJ, 427, 777

Mouri, H., Kawara, K., & Taniguchi, Y. 1993, ApJ, 406, 52

Müller-Sánchez, F., Prieto, M. A., Hicks, E. K. S., et al. 2011, ApJ, 739, 69

Murray, N. 2009, ApJ, 691, 946

Neumayer, N., Cappellari, M., Reunanen, J., et al. 2007, ApJ, 671, 1329

Nowak, N., Saglia, R. P., Thomas, J., et al. 2008, MNRAS, 391, 1629

Oliva, E., Origlia, L., Maiolino, R., & Moorwood, A. F. M. 1999, A&A, 350, 9

Onken, C. A., Ferrarese, L., Merritt, D., et al. 2004, ApJ, 615, 645

Onken, C. A., Valluri, M., Peterson, B. M., et al. 2007, ApJ, 670, 105

Peng, C. Y., Ho, L. C., Impey, C. D., & Rix, H.-W. 2002, AJ, 124, 266

—. 2010, AJ, 139, 2097

Pihlström, Y. M., Conway, J. E., Booth, R. S., Diamond, P. J., & Polatidis, A. G. 2001, A&A, 377, 413

Piqueras López, J., Colina, L., Arribas, S., Alonso-Herrero, A., & Bedregal, A. G. 2012, A&A, 546, A64

Pizzella, A., Corsini, E. M., Morelli, L., et al. 2002, ApJ, 573, 131

Pollack, L. K., Max, C. E., & Schneider, G. 2007, ApJ, 660, 288

Power, C., Nayakshin, S., & King, A. 2011, MNRAS, 412, 269

Ptak, A., Heckman, T., Levenson, N. A., Weaver, K., & Strickland, D. 2003, ApJ, 592, 782

Reunanen, J., Kotilainen, J. K., & Prieto, M. A. 2002, MNRAS, 331, 154

Rich, J. A., Kewley, L. J., & Dopita, M. A. 2011, ApJ, 734, 87

Rich, J. A., Torrey, P., Kewley, L. J., Dopita, M. A., & Rupke, D. S. N. 2012, ApJ, 753, 5

Riffel, R., Rodríguez-Ardila, A., & Pastoriza, M. G. 2006, A&A, 457, 61

Riffel, R. A., & Storchi-Bergmann, T. 2011, MNRAS, 411, 469

Rigopoulou, D., Spoon, H. W. W., Genzel, R., et al. 1999, AJ, 118, 2625

Rodríguez-Ardila, A., Pastoriza, M. G., Viegas, S., Sigut, T. A. A., & Pradhan, A. K. 2004, A&A, 425, 457

Rodríguez-Ardila, A., Riffel, R., & Pastoriza, M. G. 2005, MNRAS, 364, 1041

Rosario, D. J., McGurk, R. C., Max, C. E., et al. 2011, ApJ, 739, 44

Rothberg, B., & Fischer, J. 2010, ApJ, 712, 318

Rothberg, B., & Joseph, R. D. 2006, AJ, 131, 185

Rupke, D. S., & Veilleux, S. 2005, ApJ, 631, L37

Sanders, D. B., & Mirabel, I. F. 1996, ARA&A, 34, 749

Sanders, D. B., Soifer, B. T., Elias, J. H., et al. 1988, ApJ, 325, 74

Scorza, C., & van den Bosch, F. C. 1998, MNRAS, 300, 469

Scoville, N. Z., Evans, A. S., Thompson, R., et al. 2000, AJ, 119, 991

Shields, G. A., Gebhardt, K., Salviander, S., et al. 2003, ApJ, 583, 124

Shier, L. M., Rieke, M. J., & Rieke, G. H. 1996, ApJ, 470, 222

Shull, J. M., & Beckwith, S. 1982, ARA&A, 20, 163

Shull, J. M., & Hollenbach, D. J. 1978, ApJ, 220, 525

Siopis, C., Gebhardt, K., Lauer, T. R., et al. 2009, ApJ, 693, 946

Smith, H. E., Lonsdale, C. J., & Lonsdale, C. J. 1998, ApJ, 492, 137

Springel, V., Di Matteo, T., & Hernquist, L. 2005a, ApJ, 620, L79

—. 2005b, MNRAS, 361, 776

Sternberg, A., Hoffmann, T. L., & Pauldrach, A. W. A. 2003, ApJ, 599, 1333

Surace, J. A. 1998, PhD thesis, Institute for Astronomy, University of Hawaii, 2680 Woodlawn Dr. Honolulu, HI 96822

Surace, J. A., Sanders, D. B., Vacca, W. D., Veilleux, S., & Mazzarella, J. M. 1998, ApJ, 492, 116

Tadhunter, C. 1996, Optical spectroscopy of Cygnus A: mixed evidence for a hidden quasar (Cambridge University Press), 33

Tecza, M., Genzel, R., Tacconi, L. J., et al. 2000, ApJ, 537, 178

Teng, S. H., Schawinski, K., Urry, C. M., et al. 2012, ApJ, 753, 165

Thorne, K. S. 1995, in Annals of the New York Academy of Sciences, Vol. 759, Seventeeth Texas Symposium on Relativistic Astrophysics and Cosmology, ed. H. Böhringer, G. E. Morfill, & J. E. Trümper, 127

Treister, E., Natarajan, P., Sanders, D. B., et al. 2010, Science, 328, 600

Treister, E., Schawinski, K., Urry, C. M., & Simmons, B. D. 2012, ApJ, 758, L39

Tremaine, S., Gebhardt, K., Bender, R., et al. 2002, ApJ, 574, 740

U, V., Sanders, D. B., Mazzarella, J. M., et al. 2012, ApJS, 203, 9

U, V., Medling, A. M., Sanders, D., et al. 2013, submitted to ApJ, XXX

van Dam, M. A., Le Mignant, D., & Macintosh, B. A. 2004, Appl. Opt., 43, 5458

van Dam, M. A., Bouchez, A. H., Le Mignant, D., et al. 2006, PASP, 118, 310

Van Wassenhove, S., Volonteri, M., Mayer, L., et al. 2012, ApJ, 748, L7

Vecchio, A. 2004, Phys. Rev. D, 70, 042001

Veilleux, S., Kim, D.-C., & Sanders, D. B. 2002, ApJS, 143, 315

Veilleux, S., Kim, D.-C., Sanders, D. B., Mazzarella, J. M., & Soifer, B. T. 1995, ApJS, 98, 171

Veilleux, S., Rupke, D. S. N., & Swaters, R. 2009, ApJ, 700, L149

Walsh, J. L., van den Bosch, R. C. E., Barth, A. J., & Sarzi, M. 2012, ApJ, 753, 79

Westmoquette, M. S., Clements, D. L., Bendo, G. J., & Khan, S. A. 2012, MNRAS, 424, 416

Winge, C., Riffel, R. A., & Storchi-Bergmann, T. 2009, ApJS, 185, 186

Wizinowich, P. L., Acton, D. S., Lai, O., et al. 2000, in Society of Photo-Optical Instrumentation Engineers (SPIE) Conference Series, Vol. 4007, Adaptive Optical Systems Technology, ed. P. L. Wizinowich, 2–13

Wizinowich, P. L., Le Mignant, D., Bouchez, A. H., et al. 2006, PASP, 118, 297

Wright, E. L. 2006, PASP, 118, 1711

Wright, S. A., Larkin, J. E., Law, D. R., et al. 2009, ApJ, 699, 421

Xia, X. Y., Xue, S. J., Mao, S., et al. 2002, ApJ, 564, 196

Younger, J. D., Hayward, C. C., Narayanan, D., et al. 2009, MNRAS, 396, L66

Zasov, A. V., & Moiseev, A. V. 1999, in IAU Symposium, Vol. 194, Activity in Galaxies and Related Phenomena, ed. Y. Terzian, E. Khachikian, & D. Weedman, 279

Zhang, X., Lu, Y., & Yu, Q. 2012, ApJ, 761, 5